Microstructural and Optical Properties of Sputter-Deposited Ga_2O_3 Films

by

Eduardo Vega Lozada

Submitted in Partial Fulfillment of the Requirements

for the Degree of

Doctor of Philosophy

in the

Materials Science and Engineering
Program

YOUNGSTOWN STATE UNIVERSITY

May, 2024

Microstructure and Optical Properties of Sputter-Deposited Ga_2O_3 Films

Eduardo Vega Lozada

I hereby release this dissertation to the public. I understand that this dissertation will be made available from the OhioLINK ETD Center and the Maag Library Circulation Desk for public access. I also authorize the University or other individuals to make copies of this thesis as needed for scholarly research.

Signature:

Eduardo Vega Lozada, Student Date

Approvals:

Tom. N. Oder, Ph.D., Thesis Advisor Date

Clovis Linkous, Ph.D., Committee Member Date

Constantin Solomon, Ph.D., Committee Member Date

Michael Crescimanno, Ph.D., Committee Member Date

Donald Prior, Ph.D., Committee Member Date

Salvatore A. Sanders, Ph.D., Dean, College of Graduate Studies Date

ABSTRACT

Semiconductor materials have played a huge role in advancing today's technology through the electronic and photonic devices ushered in over the years. The advancement has been driven in part by society's growing need for electronic devices capable of handling higher power, higher temperature, and higher frequency. Current research efforts are expanding to ultra-wide bandgap semiconductors such as gallium oxide (Ga_2O_3). The principal goal of this dissertation is to obtain high quality β-Ga_2O_3 films with controlled conductivity by magnetron sputtering deposition. The specific objectives are the following: To grow β-Ga_2O_3 films on sapphire substrates (section 5.2) and on native β-Ga_2O_3 by rf sputtering (section 5.3), to produce doped and undoped β-Ga_2O_3 films (Section 5.4). Additionally, to grow Lu_2O_3/ Ga_2O_3 and B_2O_3/Ga_2O_3 alloy films on $(\bar{2}\ 0\ 1)$ UID or Sn-doped Ga_2O_3 and Al_2O_3 substrates to tune Ga_2O_3 original bandgap (Section 5.5). To obtain microstructural, morphological, compositional, and optical data from XRD, AFM, SEM, EDS, and UV-Vis characterization methods for all the experiments mentioned above. From this data, correlate the effects of the varying parameters for the optimization of the films, to use the developed films to fabricate Schottky barrier diodes and proceed with the electrical characterization of the fabricated devices (section 5.6).

DEDICATION

In loving memory of my dear grandmother, Ana Luisa Castro Martínez (1943-2023), whose unwavering love, wisdom, and strength continue to inspire me every day. Your kindness and guidance have shaped me into the person I am today, and I dedicate this dissertation to you with heartfelt gratitude and profound love. Though you may no longer be with us in person, your spirit and legacy live on in my heart, guiding me through every challenge and milestone. Thank you for being my pillar of support and for instilling in me the values of perseverance and determination. This accomplishment is a tribute to your enduring influence and the everlasting bond we share.

ACKNOWLEDGMENT

I gratefully acknowledge the support received for this research from the University Research Council, the College of STEM, and the College of Graduate Studies at Youngstown State University. I also wish to acknowledge funding support from the National Science Foundation (Grant No. HRD-1432950). Various pieces of equipment used in this work were acquired with funds from the National Science Foundation (Grant Nos. DMR-1229129, DMR-337296, DMR-1006083, and ECCS-0622086). Additionally, I extend my appreciation to Dr. Merrett from the Air Force Research Laboratory at Dayton, OH, for providing materials essential to this dissertation work.

A special acknowledgment is owed to Dr. Oder, my Principal Research Advisor, whose exceptional guidance was instrumental in shaping this research. Without his expertise and mentorship, this dissertation would not have been possible. I am deeply grateful for his support not only in my academic journey but also in my personal growth. I would also like to express my heartfelt gratitude to my committee members, Dr. Crescimanno, Dr. Solomon, Dr. Priour, and Dr. Linkous, for their invaluable feedback and guidance throughout the dissertation process. Their insights and constructive criticism have significantly enriched my work and contributed to my development as a researcher. I am thankful for their time, expertise, and unwavering support.

Special thanks go to Mr. Ray Hoff from the Department of Chemistry for his assistance with instrumentation and data collection. Furthermore, I extend my gratitude to Dr. Sturrus and members of the Department of Physics, Astronomy, Geology, & Environmental Sciences at Youngstown State University, for allowing me to work as a part-time faculty member during my doctoral studies at this institution.

Contents

List of Tables

List of Figures

This page intentionally left blank

1. Introduction

1.1 Background

Currently, 40% of the total primary energy consumption in the United States is attributable to electrical energy. Power electronics play a key role in the conversion of the electrical energy produced in power plants by reducing the high voltage generated to one that can utilize. Approximately 30% of total electrical energy currently flows through power electronics, with projections indicating a substantial increase to possibly reach 80% over the next decade. In modern systems, this conversion is performed by the switching and rectifying characteristics of semiconductor devices such as diodes, thyristors, and power transistors. When the electrical energy passes through these components, it inherently experiences an energy loss, creating an opening for researchers to introduce new materials with enhanced properties leading to high conversion efficiency. The power conversion sector is expected to expand from $52 billion to $71 billion by 2023, driven by the increasing consumption of electrical energy [1]. Figure 1.1 depicts a schematic highlighting the significance of power electronics in the process of power conversion, especially considering that since 30% of the total energy in the form of electricity passes through power electronics.

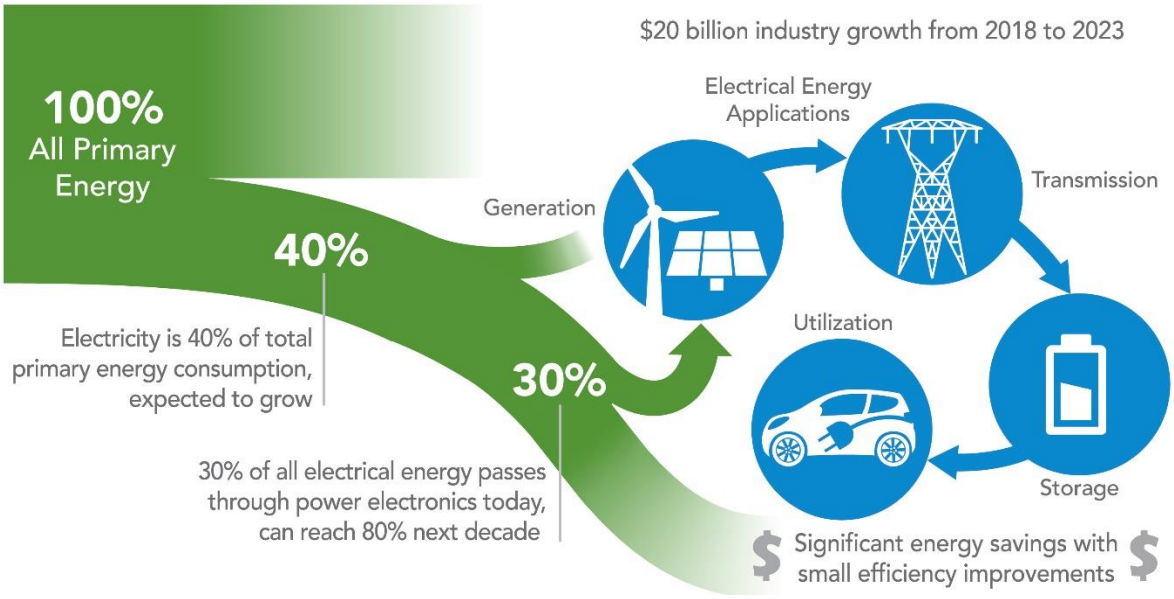

Figure 1.1 Importance of Power Electronics in our daily energy consumption [1].

Recent advancements in silicon (Si) semiconductor technology have brought it closer to the theoretical limits of silicon material. However, the power demands of many applications have reached a level that current silicon-based power devices are incapable of meeting [2]. One of the most crucial parameters in semiconductors is the bandgap, which in turn determines a semiconductor device's photonic and electronic performance. The introduction of a new semiconductor with a higher energy bandgap leads to a new generation of devices with improved performance. Silicon (Si) with a larger bandgap (E_g=1.1 eV) has replaced germanium with bandgap (E_g=0.65 eV). Subsequently the development of compound materials such as gallium arsenide (E_g=1.45 eV), gallium nitride (E_g=3.40 eV), and silicon carbide (E_g=3.25 eV) have been used as a more robust alternative to Si [2]. Current requirements include higher blocking voltages, switching frequencies, energy efficiency, improved reliability, reduced thermal waste, cost, and device dimensions.

Wide-bandgap (WBG) materials such as silicon carbide (SiC) and gallium nitride (GaN) have been used in ultrahigh-voltage power switching applications as a better alternative to Si [1-3]. These WBG SiC and GaN semiconductors can tolerate a much higher breakdown electric field (E_c) at a comparable dielectric constant (ε) and similar charge carrier mobility (μ), which translates into a larger figure of merit ($BFOM=\varepsilon\mu E_c^3$) [6], compared to Si. One of the main downsides of these materials is the higher cost of the single crystal substrate wafer production, due to the complexity of the crystal growth chemistry and the smaller scale of the crystal growth industry. Researchers worldwide have extensively explored semiconducting metal oxides due to their appealing attributes, including exceptional transparency, wide band gap, and their applicability in power electronic devices. High-quality gallium oxide (Ga_2O_3) wafers can be fabricated using simple metal-based crystal growth processes used in the fabrication of inexpensive Si or sapphire (Al_2O_3) crystals [7]. Furthermore, epitaxial growth of high quality Ga_2O_3 thin films has been demonstrated by various methods including chemical vapor deposition, pulsed lased deposition, molecular beam epitaxy, metal-organic chemical vapor deposition and magnetron sputtering [9-16]. Among the different fabrication methods for depositing oxide thin films, magnetron sputtering is the preferred method in many industrial processes because it is an established technique, suitable for large area fabrication and roll-to-roll processing [16]. The advancing Ga_2O_3 based power electronic technology has the potential to address the trade-off between cost and performance effectively by offering an enhanced performance at a lower cost. Figure 1.2 shows the results of techno-economic modeling for 6 in wafers and indicates that the cost of wafers will drop significantly in the future as more large-size and high-volume manufacturing processes are introduced.

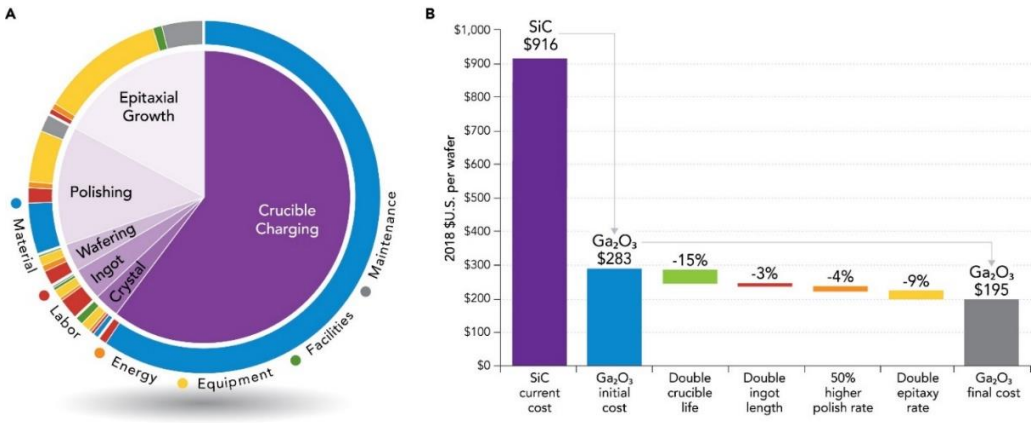

Figure 1.2 (a) Modeled Ga_2O_3 wafer manufacturing cost as a function of the fabrication process step (inner circle) and cost type (outer ring). The total cost is dominated by Iridium (Ir) material used in Ga_2O_3 crystal growth crucible. (b) Modeled 6 in wafer costs comparison for Ga_2O_3 and SiC wafers, and the Ga_2O_3 cost reduction potential. The Ga_2O_3 cost is >3x less compared to SiC and can be further reduced by better iridium (Ir) crucible utilization and faster polishing and epitaxy processes [17].

This dissertation focuses on gallium oxide semiconductor materials, specifically the thermodynamically stable polymorph of monoclinic, β-Gallium Oxide (β-Ga_2O_3). The unique properties of β-Ga_2O_3 make it a promising material for a new generation of power and optoelectronic devices. Due to its wide bandgap (4.9 eV), high transparency, and thermal stability, β-Ga_2O_3 has been of primary interest for use in power devices, solar-blind UV photodetectors, photocatalysts, gas sensors, solar cells, as well as phosphor, and transparent conducting films for electrodes on many optoelectronic devices. Controlled growth and characterization of the properties of the new material is a necessary step in bringing the material into use. As our understanding of gallium oxide's properties improves, it has the potential to replace them in various applications, provided certain limitations can be addressed.

1.2 Problem Statement

During the process of device fabrication, thin films of controlled conductivity and structure are deposited on a wafer. Epitaxial growth of high quality Ga_2O_3 has been demonstrated by various methods, including chemical vapor deposition, pulsed laser deposition, molecular beam epitaxy, metal organic chemical vapor deposition, and rf magnetron sputtering [9,18,19]. However, the quality of the films produced by each method differ due to the introduction of defects such as oxygen vacancies and different parameters used [20,21]. In addition, each existent polymorph of Ga_2O_3 could exhibit different defects and properties that require further identification. In the first part of the dissertation, rf sputtering is used as the primary method for the deposition of Ga_2O_3 films deposited on both Al_2O_3 and Ga_2O_3 substrates. It is crucial to follow a systematic study of parameters such as deposition temperature, annealing gas, annealing temperature, annealing time, along with the optical, electrical, and structural properties for the optimization of the produced films. The second part of the dissertation focuses on the doping of the films grown on its native Sn-doped Ga_2O_3 substrate, particularly, Hall measurements were performed along with annealing of the films to achieve an optimized doping concentration which preserves the crystal structure of the produced films. The third section of the dissertation, alloying of the Ga_2O_3 films with two other oxides, i.e., B_2O_3 and Lu_2O_3. The goal was to modify the optical bandgap of the films, while maintaining stoichiometry and crystal structure. Finally, the last section in this dissertation aims to demonstrate a Ga_2O_3-based Schottky diode device, characterizing its performance parameters such as ideality factor and Schottky barrier height to demonstrate the practical applications of the optimized films. By addressing these challenges comprehensively, the dissertation aims to contribute to the advancement of Ga_2O_3 thin film technology, enabling improved performance and reliability in various electronic and optoelectronic devices.

1.3 Significance of the Study

Ultra-wide bandgap semiconductor materials such as Ga_2O_3 are becoming a foundational technology for optical and electronic devices due its outstanding capabilities. These materials allow for the fabrication of smaller, faster, and more reliable power electronics, making a positive impact on the cost and energy utilization for such devices. The development of efficient high-power devices capable of operating at higher temperatures, voltages, and frequencies than those made of conventional semiconductor materials could lead to the ultimate elimination of expensive cooling systems used in elevated temperature electronics operation. This in turn will enable the development of lighter designs with reduced volume, which will have a beneficial impact on the industrial process and on the environment in general. However, fundamental understanding of these materials is still at an early stage. The introduction of defects during the growth of these materials and the parameters required to grow high quality films will determine the performance of the devices. In this dissertation, the focus is on the structural and optical characterization of rf sputter deposited Ga_2O_3 films by the used of analytical techniques from the materials science realm. The characterization of the films is utilized to find the ideal parameters to grow Ga_2O_3 films by the magnetron sputtering deposition technique, along with methods to reduce defects and improve the quality of these films. This dissertation also delves into the optimization of the doping concentration and post deposition annealing parameters, particularly while preserving the original crystal structure of the films. Additional efforts are directed towards alloying Ga_2O_3 films with other oxides mentioned above, to modify the optical bandgap of the film, expanding its potential to optoelectronic devices. Lastly, this dissertation highlights the functionality of the optimized Ga_2O_3 films through the demonstration of a simple device, highlighting the practical implication and relevance of the research findings.

1.4 Properties of β-Ga_2O_3

1.4.1 Structural Properties

At least five different polymorphs (forms) of Ga_2O_3 have been reported, namely, rhombohedral (α), monoclinic (β), defective spinel (γ), cubic (δ), and orthorhombic (ε) structures, and a transient κ- Ga_2O_3 [22, 23]. Of all its polymorphs, the β-Ga_2O_3 structure has shown to be the most stable under normal conditions of temperature and pressure. The other polymorphs can be either conductors or insulators, depending on the growth conditions, and will transform to the β-phase at sufficiently high temperatures up to its melting point 1900 °C [8]. These polymorphs not only differ in their crystal space, but also in their coordination number for Ga ions, and can be synthesized under specific conditions of pressure and temperature. For instance, the α-phase is rhombohedral with space group $R\bar{3}c$, and can be obtained at temperatures of 1000 °C and pressures of 4.4 GPa [24]. The β-phase, which holds a monoclinic structure with space group C2/m [25], can be obtained from any other polymorph by heat treatment (Fig. 1.3) in air at sufficiently high temperatures ranging from 500-700 °C [27, 28].

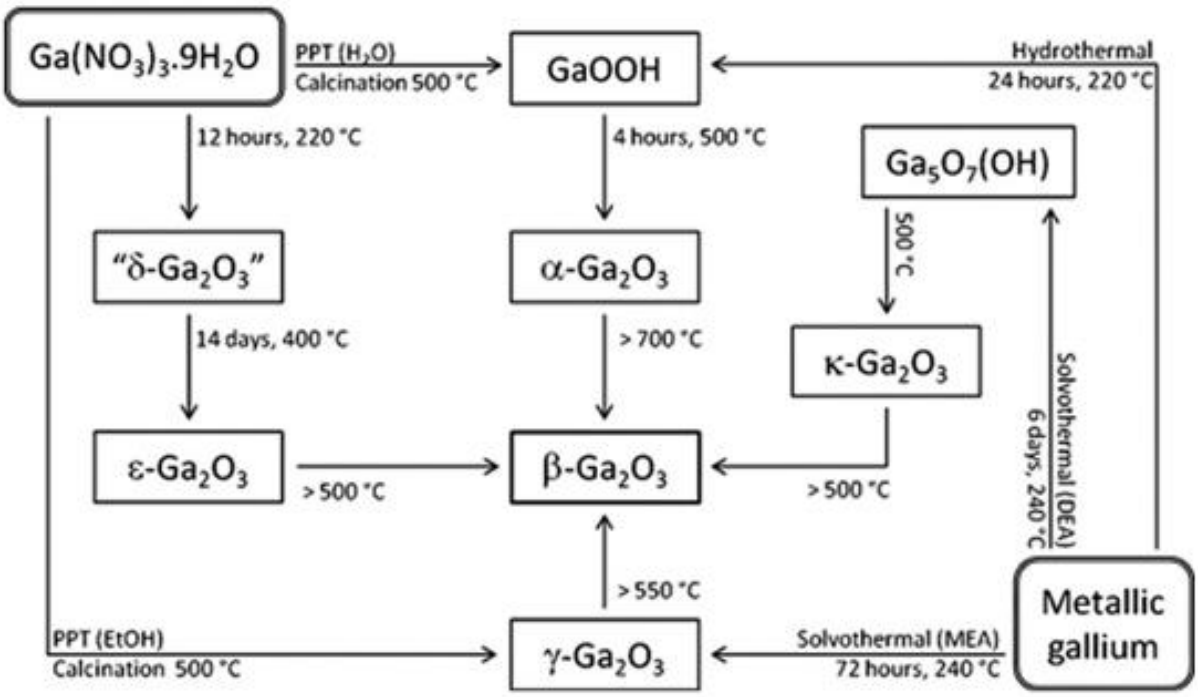

Figure 1.3 Summary of the synthesis and interconversion of the polymorphs of Ga_2O_3 and related phases. Depending on the initial phase, temperatures in the range of 500-700 °C are sufficient to allow a transformation to the β-phase [23].

The thermal stability of β-Ga_2O_3 allows the production of bulk single crystal and epitaxial films via heat treatment processes such as crystallization from melt grow or vapor phase epitaxy [26]. There is little experimental data for the other polymorphs due to the difficulty of isolating them in a pure crystalline form; therefore, much of the properties known for the other phases of gallium oxide have been produced from theoretical simulations, specifically from density functional theory [20,28–30]. Lattice parameters, space group, and volume expansivity have been calculated theoretically, and normalized to room temperature for the different polymorphs. The results showed an increase in volume expansivity in the following order: β, ε, α, δ, with the β phase having the lowest volume expansion [31].

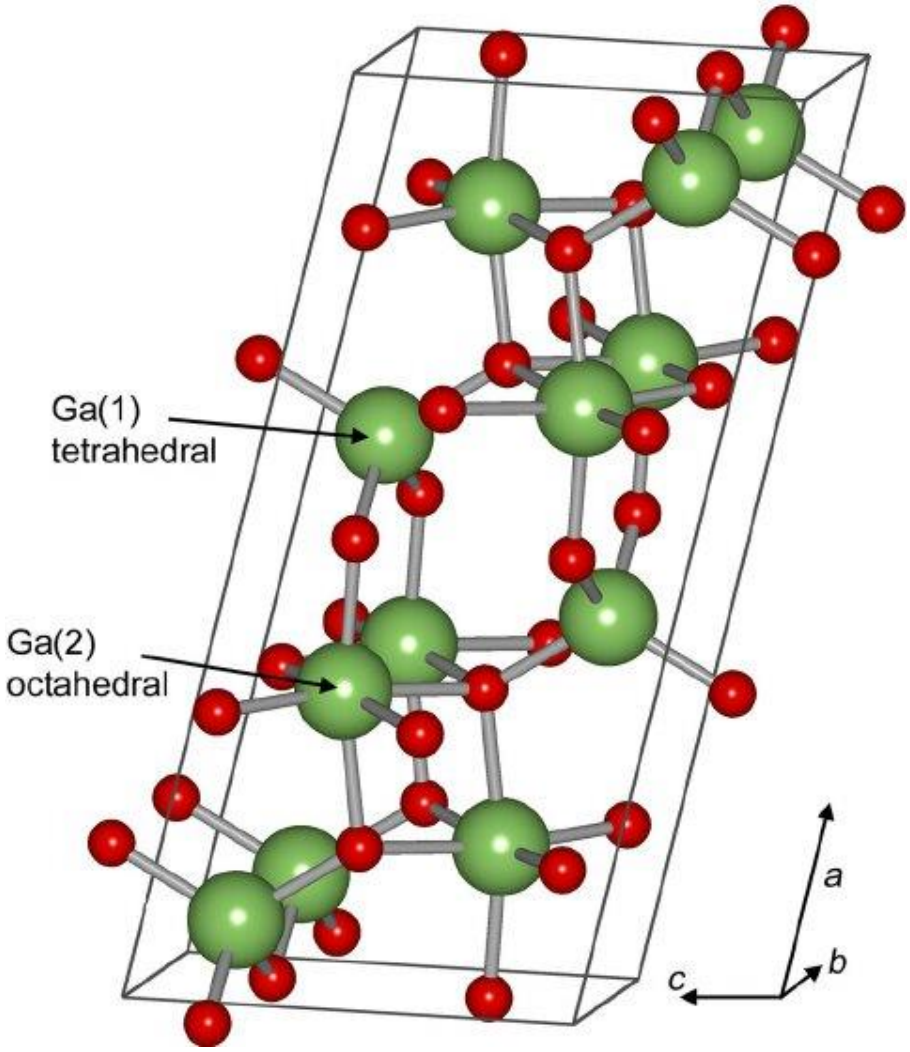

Figure 1.4 Monoclinic crystal structure of β-Ga_2O_3 [32].

Crystallographic studies performed by Ahman et al, indicate that the unit cell of β-Ga_2O_3 contains two inequivalent Ga positions, one with tetrahedral geometry Ga (I) and the second with octahedral geometry Ga (II). The oxygen atoms are located three distinct positions labeled as O (I), O (II), and O (III), forming a distorted cubic closed-packed structure (Fig. 1.4). One oxygen atom is coordinated tetrahedrally, and the remaining two oxygen atoms are coordinated in a trigonal manner [33]. A summary of the properties for all polymorphs is presented in Table 1.1.

Table 1.1 Summary of the properties of Ga_2O_3 Polymorphs [8].

Polymorph	Lattice parameter (Å)	Refractive index, n	Optical dielectric constant	Volume expansion at 1200K	Bulk modulus (300,GPa)	Comment	Reference
α	a, b = 4.98-5.504 c = 13.4-13.6	1.74-1.95	3.03-3.80	0.035	~185	Corundum, rhombohedral structure, space group $R\bar{3}c$, bandgap larger than all other polymorphs (~5.2 eV)	Yoshioka et al.[31], Stepanov et al.[27], and He et al. [34]
β	A = 12.12-12.12.34, b = 3.03-3.04, c = 5.80-5.87	1.68-1.89	2.82-3.57	0.024	~150	Monoclinic structure, space group C2/m	Kohn et al.[35], Stepanov et al.[27], He et al. [34], and Geller et al [25].
γ	A = 4 9.4–10.0	/	/	/	/	Defective spinel, cubic structure, space group $Fd\bar{3}m$	Stepanov et al. [27]
δ	A = 9.4-10.0	/	/	0.04	160	Possibly bixbyite. Suggested to be a nanocrystalline form of ε-Ga_2O_3	Roy et al.[22], Playford et al.[23]
ε	A = 5.06-5.12, b = 8.69-8.79, c = 9.3-9.4	1.6	/	0.028	160	Orthorhombic structure, Space group $Pna2_1$	Yoshioka et al.[31] and Kroll et al.[36]

1.4.2 Electrical Properties

Gallium oxide is known to be an ultra-wide bandgap semiconductor, with an energy gap of about 4.7-4.9 eV [39, 40]. A semiconductor with a ultra-wide energy bandgap has a higher electric breakdown field, therefore Ga_2O_3 (8 MV/cm) has an electric field value higher than that of other commonly used semiconductors, such as Si (0.3 MV/cm), 4H-SiC (2.2 MV/cm) and GaN (2.0 MV/cm) as shown in Fig. 1.5 [2].

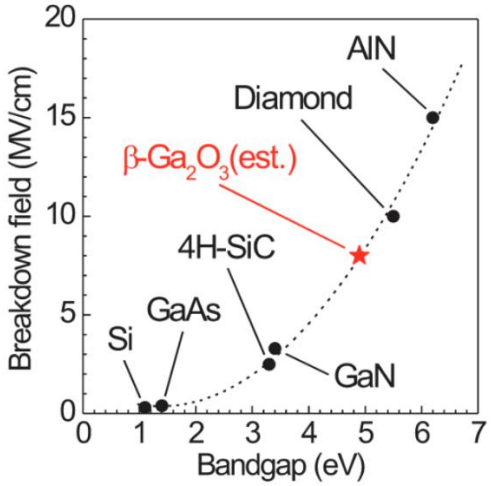

Figure 1.5 Electric field vs Bandgap [39].

The critical electric field breakdown (V/cm) relates to many crucial parameters for the operation of devices using semiconductor materials. For instance, the critical electric field breakdown varies with the bandgap energy as shown in the following equation:

$$E_{br} = a(E_g)^n \quad (1.1)$$

where E_{br} is the critical electric field breakdown in V/cm,

E_g is the bandgap energy in eV, a is a constant whose value is ~10^5 and

n varies from 2.0 to 2.5 [40]

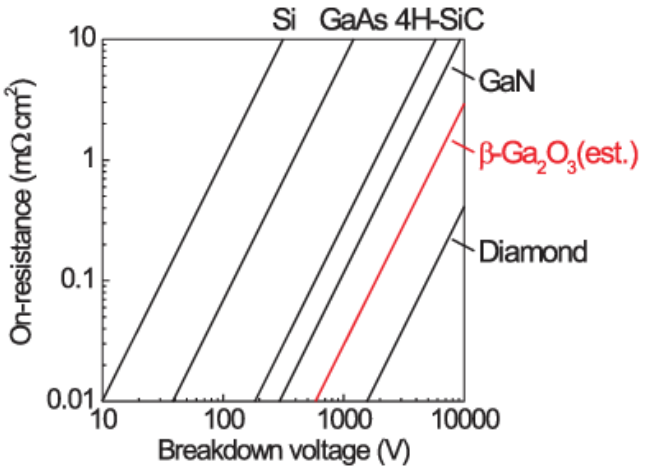

Figure 1.6 Theoretical limits of on-resistances as a function of breakdown voltage for major semiconductors and β-Ga_2O_3 [39].

Another important parameter is the breakdown voltage, and for a diode it is related to the breakdown critical electric field as follows:

$$V_{Br} \approx \frac{\varepsilon_r E_{br}^2}{2qN_d} \tag{1.2}$$

where q is the charge of the electron and

N_d is the doping density

Figure 1.6 shows the on-resistance as a function of the breakdown voltage for various semiconductor materials. The calculation is done with parameters found in Table 1.2. The ability of these materials to withstand higher electric fields with reduced energy loss also results in the capability to operate at higher ambient temperatures, making the use of wide bandgap semiconductors suitable for applications in power devices. In addition, Ga_2O_3 semiconductor with a bandgap larger than 3.4 eV are commercially available with a large-area native substrate up to 1 inch in diameter, with controlled doping concentration and a wide range of conductivities [7]. This would not only translate to ease of mass production and lower cost, but also facilitate fabrication

of vertical electronic devices to better handle operations requiring high power. Its n-type conductivity can be adjusted by doping using Si and Sn, and its resistivity spans over a wide range of 10^{-3} to 10^{12} Ω-cm [41].

Table 1.2 Properties of semiconductors materials [8].

Materials Parameters	Si	GaAs	4H-SiC	GaN	Diamond	β-Ga_2O_3	Comments
Bandgap, E_g (eV)	1.1	1.43	3.25	3.4	5.5	4.85	Bandgap of Ga_2O_3 reported in range 4.7–4.9 eV
Dielectric constant, ε	11.8	12.9	9.7	9	5.5	10	
Breakdown field, E_c (MV/cm)	0.3	0.4	2.5	3.3	10	8	Experimental values for Ga_2O_3 have reached ~0.5 times the theoretical maximum
Electron mobility, μ (cm^2/Vs)	1480	8400	1000	1250	2000	300	
Saturation velocity, v_s (10^7 cm/s)	1	1.2	2	2.5	1	1.8-2	1.8 ⟨001⟩ and ⟨010⟩, 2.0 ⟨010⟩
Thermal conductivity λ (W/cm K)	1.5	0.5	4.9	2.3	20	0.1-0.3	0.13 ⟨100⟩,0.23 ⟨010⟩

1.4.3 Optical Properties

Due to its wide band gap, pure stoichiometric β-Ga_2O_3 is colorless and transparent over a wide optical range, covering visible down to the UV-C (250 nm) region. These optical and electrical characteristics place β-Ga_2O_3 into the realm of transparent conductive oxides (TCOs). In addition, a strong correlation between electrical conductivity and absorption of the films have been reported [42]. The electrical conductivity of the films is not only affected by the doping concentration, but also by the atmosphere in which the film is grown. Films grown in an oxidizing atmosphere are highly insulating and show a transparent or yellowish coloration, which is

indicative of absorption in the blue range of visible light. In the other hand, films grown in reducing atmosphere are conductive and show more of a blueish coloration. This can be explained by the high density of dopants making the material absorb in the red and NIR regions of the spectrum [27].

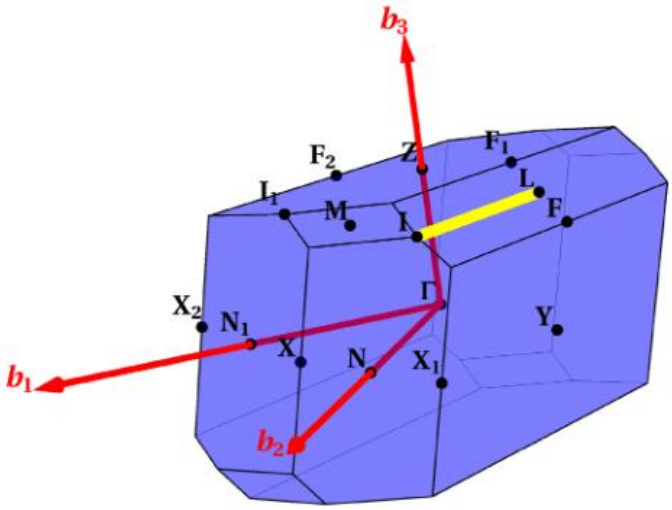

Figure 1.7 The Brillouin zone of β-Ga_2O_3. Labels indicate high-symmetry points. The axes of the reciprocal unit cell are also shown. The yellow line represents the I-L line where the conduction band maximum lies [43].

Numerous theoretical studies using density functional theory have confirmed the direct bandgap of β-Ga_2O_3. However, as depicted in Fig. 1.8, the direct bandgap only exhibits a faint resemblance, lacking a prominent direct bandgap signature. Most studies use density functional theory approach to model the electronic structure of the semiconductor [31]. Peelers et al showed DFT calculations for the lattice parameters and band gap of β-Ga_2O_3 resulted in a fundamental indirect band gap of 4.84 eV and a slightly larger direct band gap of 4.88 eV [43]. Figure 1.7 shows the Brilliouin zone and primitive unit cell belonging to monoclinic β-Ga_2O_3, which was used to calculate the band structure shown in Fig. 1.8. The minimum of the conduction band is located at

Γ, as reported by Peelers et al. The valence-band maximum is located on the I-L line, and is depicted by a yellow line on the face of the Brilliouin zone as shown in Fig 1.7. This surface is used to set the zero of the energy. The direct band gap of β-Ga_2O_3 makes it suitable for a host of photonic device applications, including transparent conductors and deep UV sensors.

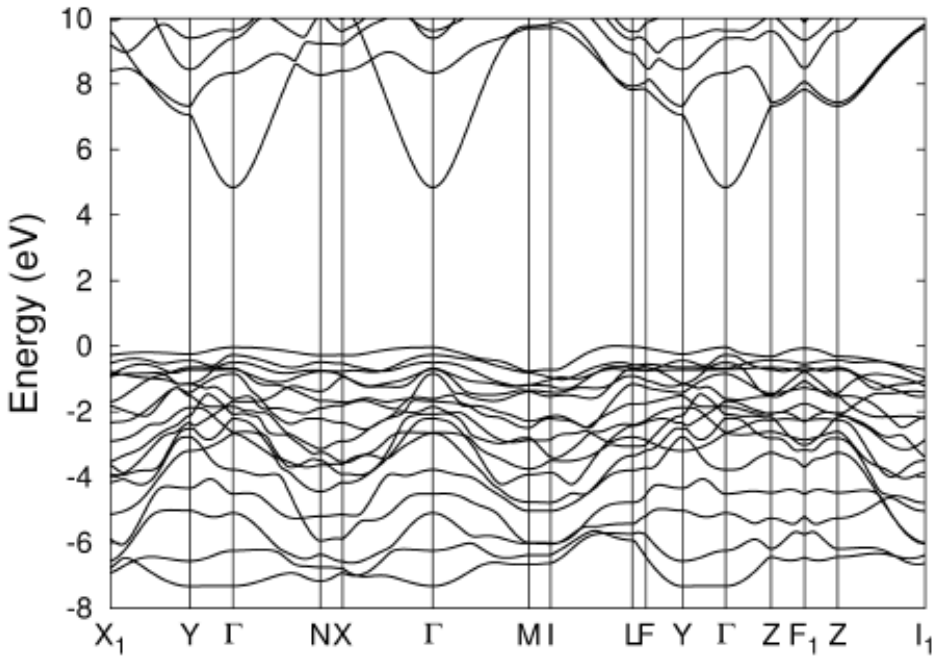

Figure 1.8 Band structure of β-Ga_2O_3 along a continuous path in the Brillouin zone [43].

1.4.4 Power Applications and Figures of Merit

Figures of merit (FOM) are data-based metrics generally used to evaluate power devices performance under certain operating conditions. A FOM can provide guidance while designing a device specification to meet the market expectations. Johnson FOM ($E_c \cdot V_s^2/4\pi^2 T$) indicates the power-frequency capability for low-voltage transistors. Baliga FOM ($\varepsilon \cdot \mu \cdot E_c^3$) identifies material parameters that minimize switching losses in low frequency unipolar transistors. For β-Ga_2O_3, this figure has a value of 3214, much greater than its counterparts GaN (846) and SiC (317) [6]. In

contrast, Baliga high-frequency FOM identifies the device parameters to reduce power loss in high frequency applications. Another FOM is Keyes ($\lambda \cdot \left[\frac{c \cdot V_s}{4\pi \cdot \varepsilon}\right]^{\frac{1}{2}}$), and it establishes the thermal limits of transistors switching properties. Lastly, a set of FOM introduced by Huang includes: Huang's material figure of merit (HMFOM), which estimates the dynamic switching losses as a function E_c, Huang's chip area manufacturing figure of merit (HCAFOM), which indicates the optimal chip area to minimize power loss as a function of E_c^2, and Huang's high temperature figure of merit (HTFOM), which describes the material's temperature rise for the optimum chip area condition delivering minimal power loss[44,45]. β-Ga_2O_3 shows good metrics for almost all FOM when compared to other semiconductor materials, however, the material has the lowest metric for HTFOM, due to its inability to properly conduct thermal energy and its high field strength. Table 1.3 compares various materials FOM with emphasis on β-Ga_2O_3 for power device applications.

Table 1.3 Figure of merit of β-Ga_2O_3 relative to other commonly used semiconductors [8,44].

Figures of merit relative to Si	Si	GaAs	4H-SiC	GaN	Diamond	β-Ga_2O_3	Comments
Johnson = $E_c \cdot V_s^2/4\pi^2$	1	1.8	278	1089	1110	2844	Power-frequency capability
Baliga = $\varepsilon \cdot \mu \cdot E_c^3$	1	14.7	317	846	24660	3214	Specific on-resistance in (vertical) drift region
Combined = $\lambda \cdot \varepsilon \cdot \mu \cdot V_s^2 \cdot E_c^2$	1	3.7	248.6	353.8	9331	37	Combined power/frequency/voltage
Baliga high-frequency = $\mu \cdot E_c^2$	1	10.1	46.3	100.8	1501	142.2	Measure of switching losses
Keyes = $\lambda \cdot \left[\frac{c \cdot V_s}{4\pi \cdot \varepsilon}\right]^{\frac{1}{2}}$	1	0.3	3.6	1.8	41.5	0.2	Thermal capability for power density/speed
Huang HMFOM, $\mu^{0.5} \cdot E_c$	1	3	9	10	40	12	Huang material FOM
Huang HCAFOM, $\varepsilon \cdot \mu^{0.5} \cdot E_c^2$	1	5	78	85	614	277	Huang chip area FOM
Huang HTFOM, $\sigma_{th}/\varepsilon \cdot E_c$	1	0.2882	0.6193	0.1017	0.9986	0.0045	Huang thermal FOM

1.5 Metal-Semiconductor Interface and Mechanism

1.5.1 Bandgap

Materials are often categorized in three main groups, i.e., conductors, semiconductors, and insulators. Resistivity is an intrinsic property used to describe the resistance of electrical current through the materials, and for small wafers is expressed in ohm-cm or Ωcm. For example, most conductors have a resistivity that falls within 10^{-8} to 10^{-4} Ωcm. On the other end, insulators have a resistivity that ranges from 10^{8} to 10^{18} Ωcm. Semiconductor have a resistivity that falls between that of a conductor and that of an insulator, with values that range from 10^{-4} to 10^{8} Ωcm. Another way to explain the differences in conduction of the materials mentioned above is with the introduction of band theory. Electrons in solid materials can have values of energy only within certain specific ranges. The behavior of the electrons in a solid is strongly affected by the properties of all other particles around it. The band energies permitted in a solid is related to the discrete allowed energy levels of single atoms. When a lattice with N atoms is assembled, the energy levels will split into N levels in the solid.

The splitting of sharp and tightly packed energy levels give rise to the so-called energy bands. Energy levels are reorganized into two bands: the valence band and the conduction band. The valence band is the highest occupied energy band and is made from energy levels of the valence electrons as the name suggests. The conduction band is the lowest unoccupied. This band is usually empty since it is a high energy level. The energy gap between the conduction band and the valence band is referred as the band gap, the forbidden zone to electrons in a perfect semiconductor or insulator. For the material to conduct, the system must be given enough energy to excite an electron across this gap. This process can occur thermally, as the temperature increases the likelihood to find an electron in the conduction band increases. This is explained by Fermi-Dirac distribution, which gives the probability to find an electron in any given energy state (E) at a given temperature (T). The fermi function has the following form:

$$f(E) = \frac{1}{e^{\frac{(E-E_F)}{k_B T}} + 1} \tag{1.3}$$

where E_F is the Fermi energy, the energy of the highest state filled at absolute zero,

T is the temperature of the semiconductor and k_B is the Boltzmann constant.

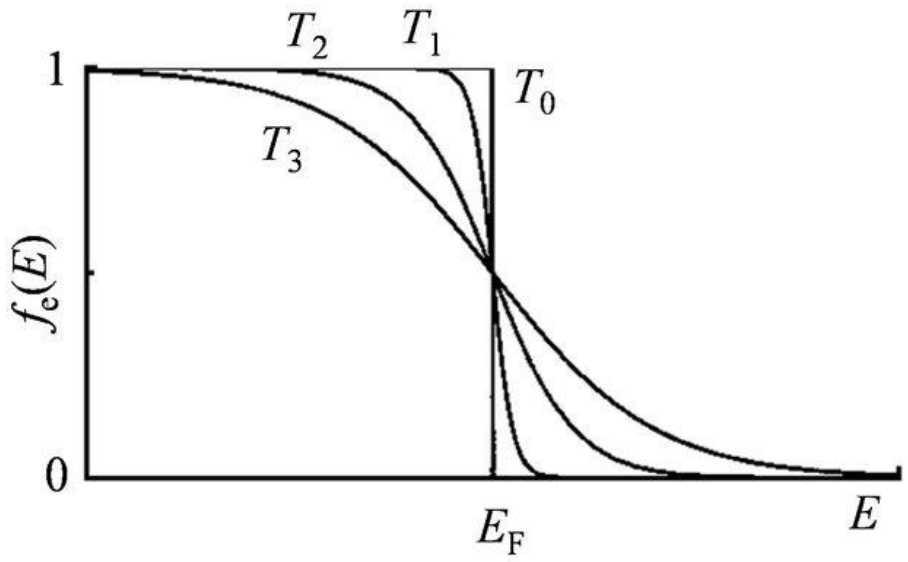

Figure 1.9 Fermi-Dirac distribution at different temperatures, $T_0 = 0$ K [46].

Figure 1.9 shows that at absolute zero ($T_0 = 0$ K), the probability of finding an electron with an energy higher than E_F is zero, and the probability to find the electron below E_F is 1. This allows us to further classify materials according to their band gap energy. Insulators have wide forbidden energy gaps or band gaps (Eg ~9 eV), while the valence and conduction band are overlapped in conductors. In the case of conventional semiconductors like silicon, the energy gap is present, but small (Eg ~1 to 1.5 eV). Figure 1.10 illustrate the differences on the energy bandgap of conductors, semiconductors, and insulators.

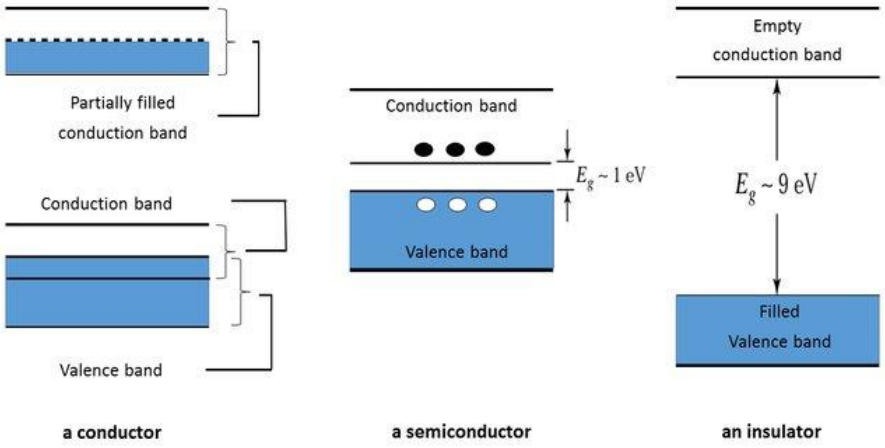

Figure 1.10 Energy Band Diagram of Conductor, Semiconductor, and Insulator [47].

In section 1.4.2 it is mentioned that β-Ga_2O_3 has a direct bandgap of 4.9 eV. Two basic types of band gaps can be found in semiconductor materials, a direct band gap and an indirect band gap. The way used to describe them is by looking at the minimal-energy state of the conduction band and maximal-energy state of the valence band and see where they are located with respect to each other in the Brillouin zone. A direct band gap will have both, the minimum of the conduction band and maximum of the valence band, coinciding at a certain crystal momentum vector (k-vector) as shown in Fig. 1.11 (a). An indirect band gap material will have different k-vectors as shown in Fig 1.11 (b). This means that a direct band gap material will allow direct electron transitions via photonic emission. This property makes the material suitable for optoelectronic applications [48]. An indirect band gap material, the electrons required intermediate steps in the form of phonon assisted transitions.

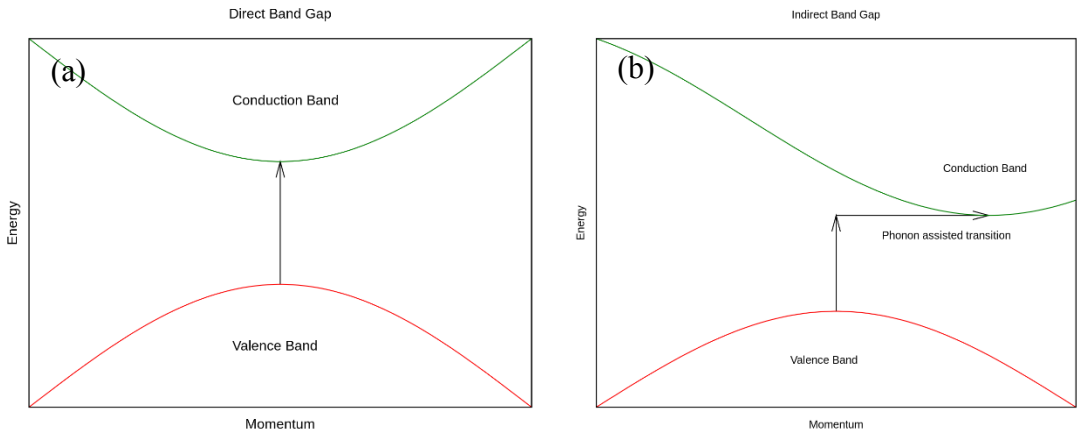

Figure 1.11 Energy vs crystal momentum for a semiconductor. (a) In a direct band gap the electronic transition can occur without a change in the crystal momentum via photo emission, (b) in an indirect band gap the electronic transition can occur with a change in crystal momentum via both photon and phono momentum transfer [49].

1.5.2 Metal-Semiconductor Contact

When a metal and a semiconductor come into intimate contact with each other, thermodynamic equilibrium is reached, and a metal-semiconductor (M-S) junction is created. M-S junction can manifest as either rectifying Schottky ($\Phi_m > \Phi_s$) or non-rectifying Ohmic ($\Phi_m < \Phi_s$) junction, where Φ_s is the work function of the semiconductor and Φ_m is the work function of the metal. The work function is simply the necessary work needed to remove an electron from the fermi level of the metal or semiconductor to vacuum. As the fermi levels of the metal and semiconductor come into alignment, the rectifying properties depend on the Schottky barrier height formed.

Schottky-Mott theory predicts that the Schottky barrier is given by the difference between the metal work function and the electron affinity of the semiconductor in vacuum:

$$\Phi_B^{(n)} = \Phi_m - \chi_s \quad (1.4)$$

where Φ_B is the Schottky barrier height, Φ_m is the metal work function in vacuum,

and χ_s is the electron affinity of the semiconductor in vacuum

Figure 1.12 illustrates the formation of a metal-semiconductor junction in the case of an n-type semiconductor where the metal has a larger work function than that of the semiconductor material. The metal and semiconductor are shown before being placed in close contact. The metal has a work function (Φ_m). The metal conduction band (E_c) and Fermi level (E_F) overlap. Meanwhile, in the semiconductor, the conduction band (E_c) and the valence band (E_v) are separated by the band gap which contains the Fermi level (E_{FS}). The Fermi level of the semiconductor is higher than that of the metal before the junction is created. The electrons flow from the semiconductor into the lower energy states available in the metal until the equilibrium is reached and the Fermi levels of the semiconductor and the metal align.

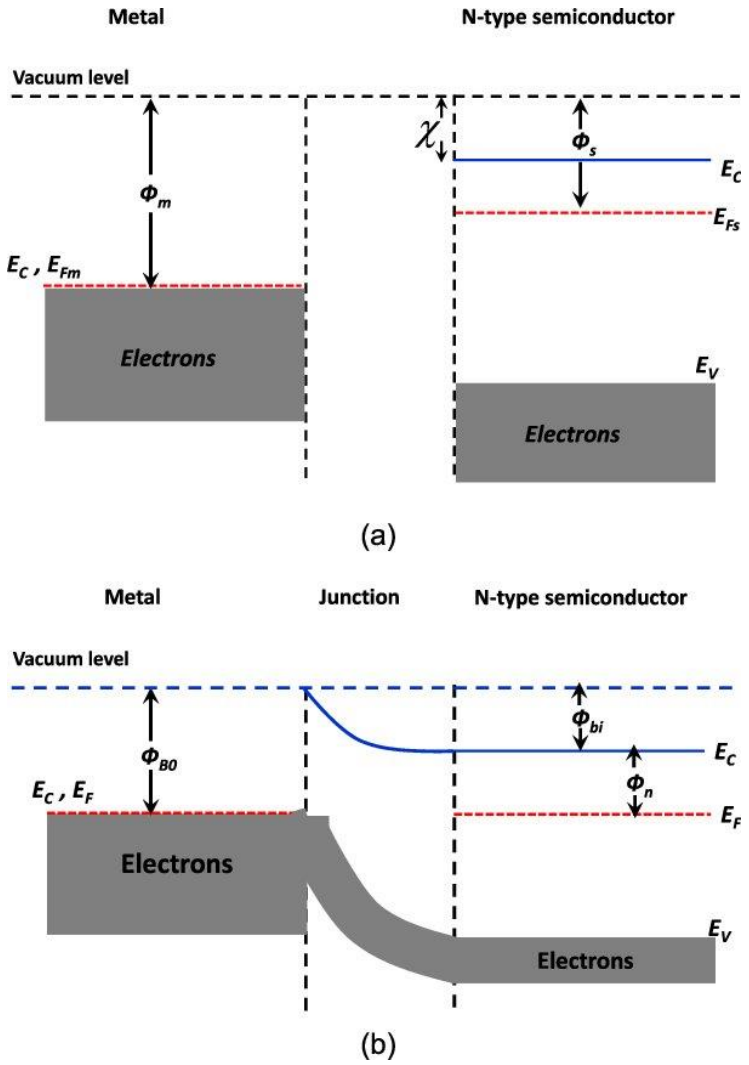

Figure 1.12 Energy-band diagram for the metal–semiconductor junction of an n-type semiconductor. (a) before, (b) after being placed in contact with semiconductor [50].

1.5.3 Conduction Mechanisms in Metal-Semiconductor Contacts

At least three types of conduction mechanisms have been proposed:

i. Thermionic Emission

ii. Thermionic-Field Emission

iii. Field Emission

1.5.3.1 Thermionic Emission

Thermionic emission refers to the excitation of the charge carries directly over the Schottky barrier exclusively due to thermal energy as depicted in Fig 1.13. The barrier width depends on the doping concentration of the semiconductor. In the case, the doping concentrations are kept low ($N_D < 10^{17}$ cm^{-3}), hence the barrier is wide. This mechanism provides rectifying Schottky contacts in the forward bias [51].

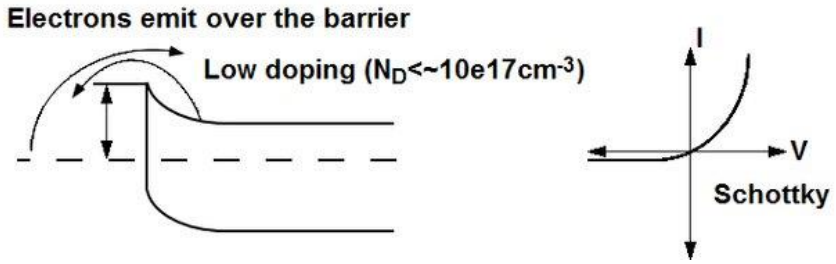

Figure 1.13 Thermionic Emission [52].

1.5.3.2 Thermionic-Field Emission

With moderate doping concentration (10^{17} cm^{-3} < N_D < 10^{18} cm^{-3}), a combination of thermionic and field emission mechanism can occur. In this case, the electrons use thermal energy to be excited over the barrier and tunnel through the thin upper section of the barrier as shown in Fig. 1.14 [51].

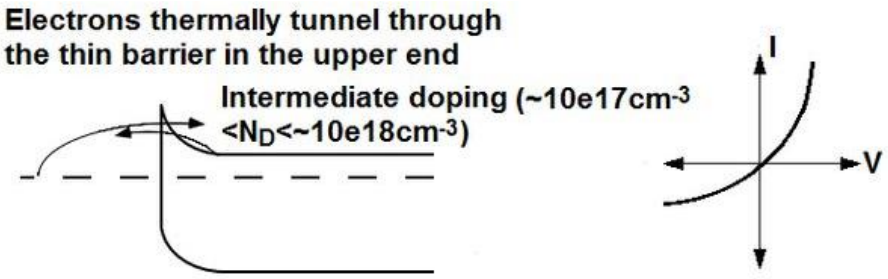

Figure 1.14 Thermionic-Field Emission [52].

1.5.3.3 Field emission

In the field emission conduction mechanism, the electron tunnel through the barrier directly. This is a quantum mechanical phenomenon, known as tunneling. The width of the barrier is significantly thin due to high doping concentrations ($N_D < 10^{18}$ cm^{-3}), so that the electron can easily flow through the barrier as illustrated in Fig. 1.15. This is the preferred mechanism in Ohmic contacts [51].

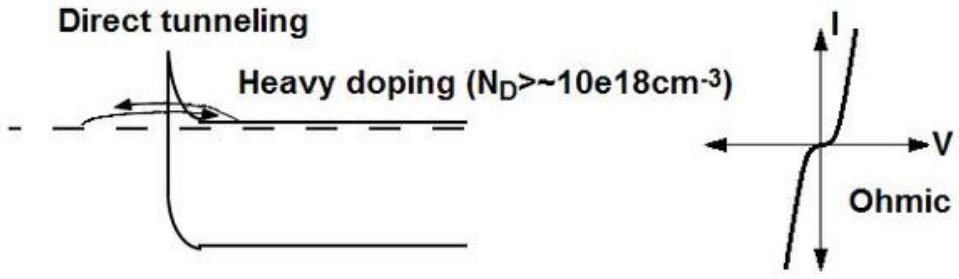

Figure 1.15 Field emission mechanism [52].

2. Literature Search

2.1 Ga_2O_3 Thin Film by Magnetron Sputtering

Focusing on rf-sputtered β-Ga_2O_3 thin films, several groups have been able to successfully grow β-Ga_2O_3 on native Ga_2O_3 substrates, and non-native Si (100), GaN, Al_2O_3 (0001), GaN, MgO (100), $MgAl_2O_4$ (100) and SiC (6H), and even Dimond substrates [53–57] . The characteristics of the films are influenced by factors like deposition pressure, temperature, gas composition, rf power, and annealing conditions. A comprehensive understanding of the impact of each growth parameter is crucial for achieving precise control over film growth.

Deposition Pressure. During the sputtering process, a plasma is typically generated using Ar gas. More information on the sputtering process is provided in section 3.3.2.1. The stability of the generated plasma relies on the deposition pressure, which controls the Ar ion density in the plasma. The target material is sputtered by the impact of the Ar ions. Thus, the ion density can significantly impact the quality of the sputtered film. Ogita et al. first studied the effects of three different deposition pressures (15, 30, 60 mTorr, corresponding to 2, 4, and 8 Pa) for depositing β-Ga_2O_3 thin films [58]. Films of 1 um were deposited at room temperature using Ar as the sputtering gas, followed by annealing at 1000 °C for 1 hr. in air. XRD analysis showed that all films possessed distinct peaks at (400) and (002), corresponding to monoclinic β-Ga_2O_3. However, peak intensity was strongest for the films deposited at 15 mTorr. This indicated that a lower sputtering pressure of 15 mTorr (2 Pa) is best for obtaining good crystallinity. Figure 2.1 shows the XRD pattern for the deposited films by Ogita et al.

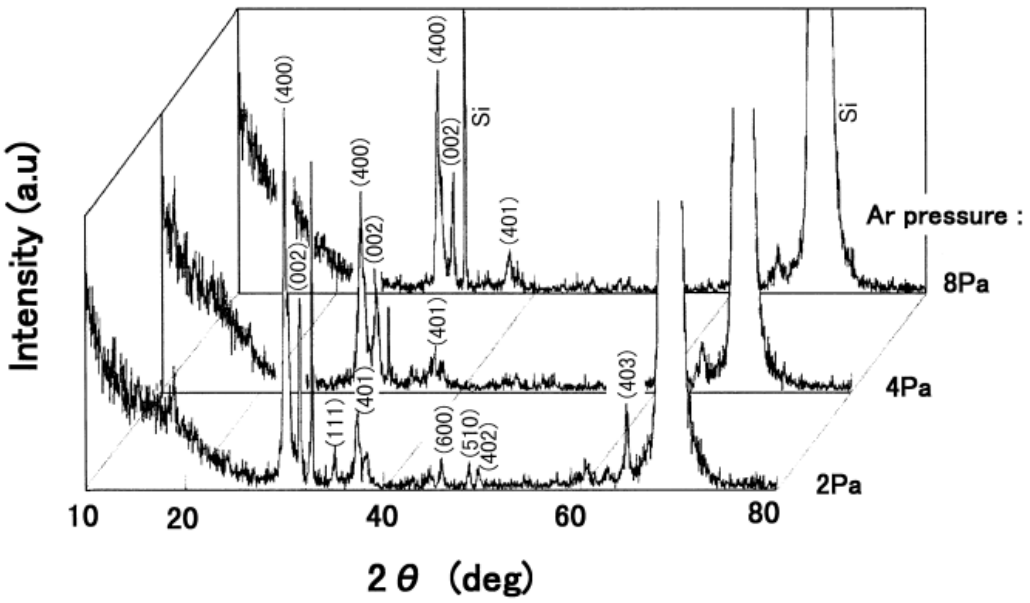

Figure 2.1 X-ray diffraction pattern of Ga_2O_3 thin films produced at the Ar pressure of 15, 30, and 60 mTorr (2, 4 and 8 Pa). The peak value of XRD appears at 15 mTorr (2 Pa) [58].

Mobtakeri et al. studied the effects of deposition pressure and rf power on β-Ga_2O_3 thin films grown on sapphire [59]. For the variation in pressure, growth pressures of 7.5, 9.2,10.4 and 12.2 mTorr were evaluated, with a constant temperature and rf power of 300 °C and 120 W, respectively. For the effects of rf power, 80 W, 100 W, and 120 W were used. XRD, SEM, and UV-Vis data is presented as a function of the increasing pressure and rf power. A summary of the samples prepared is shown in the following Table 2.1.

Table 2.1 Experimental deposition parameters by Mobtakeri et al [59].

Name	Growth Pressure (mTorr)	Ar (sccm)	Temperature (°C)	rf power (Watt)
G3	7.5	15	300	100
G4	7.5	15	300	80
G6	7.5	15	300	120
G7	9.2	45	300	120
G8	10.4	75	300	120
G9	12.2	105	300	120

XRD data shown in Fig. 2.2 displayed that the as deposited films were amorphous, except the film grown at 7.5 mTorr and 120 W. Nevertheless, the peaks observed at 29.2, 36.8, and 56.8 for the film deposited at 7.5 mTorr were very small and broad. The maximum grain size of 18.7 nm was also observed for the film grown at 7.6 mTorr after annealing at 900 °C for 1 hr in air.

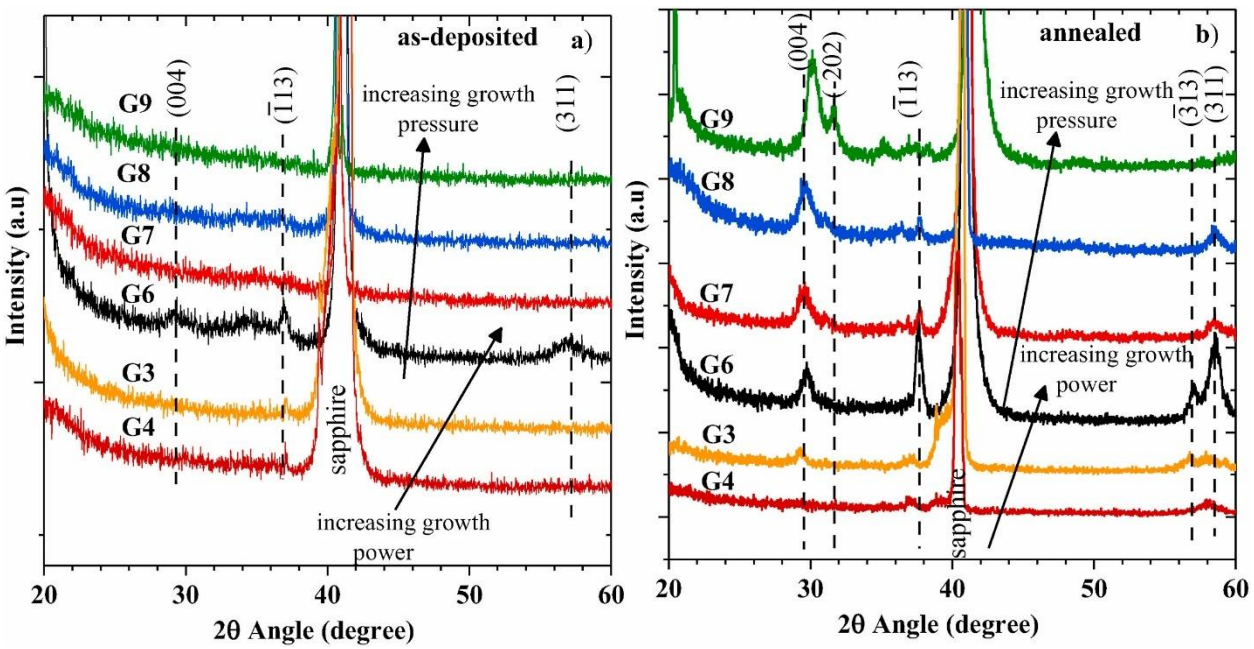

Figure 2.2 XRD patterns of Ga_2O_3 thin films, as-deposited and annealed for 1 h at various deposition pressures and rf powers on sapphire substrate [59].

On the surface morphology of the films, SEM images of the as-deposited samples shown in Fig. 2.3 indicate that grain size increases with increasing pressure. After annealing, the grain size gets bigger, due to crystallization of the Ga_2O_3 films. Furthermore, the increasing growth pressure results in columnar growth with large feature sizes. This means that 3-dimensional (3D) growth is possible at higher pressures, while 2-dimensional (2D) is observed at lower pressures. The difference between these two growth modes is that in the 2D mode the material grows layer by layer, and in the 3D columnar mode, the material agglomerates forming islands.

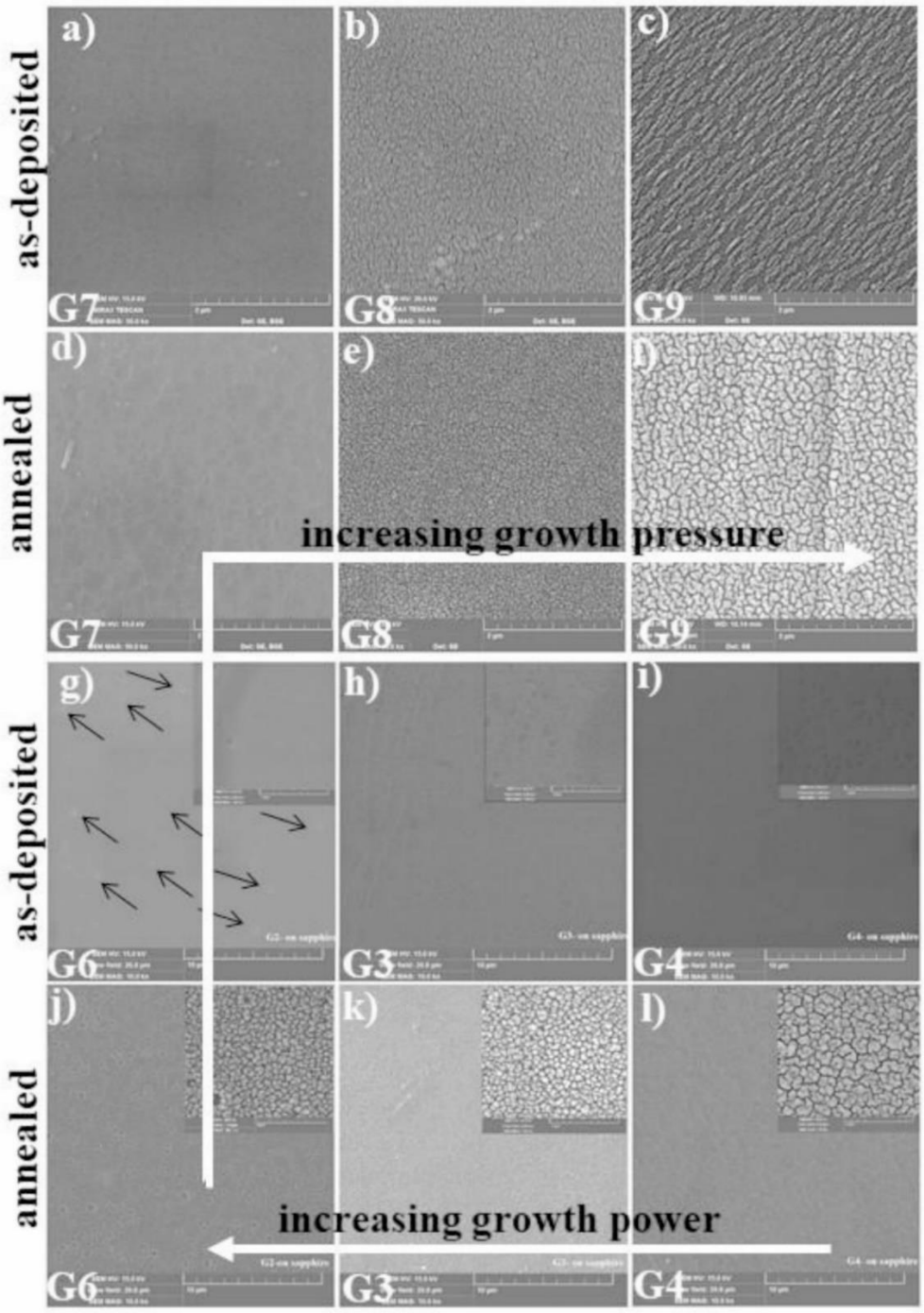

Figure 2.3 SEM images of Ga_2O_3 thin films as-deposited and annealed for 1 h by rf magnetron sputtering at various sputtering pressures and power on sapphire substrate (a,b,c) as-deposited G7, G8, G9, (d,e,f) annealed G7, G8, G9 (g,h,i) as-deposited G6, G3, G4 (j,k,l) annealed G6, G3, G4 [59].

On the effects of the optical properties, UV-Vis spectroscopy shows that the transmittance of the films decreases significantly with increasing pressure (Fig. 2.4). The films presented a change in color from transparent to grayish with increasing pressure. EDS analysis confirmed that an increase in the amount of Ga in the films occurs with increasing pressure. As the growth pressure and sputtering power increased, there was a corresponding decrease in the band gap of the films. Overall, this study showed that lower growth pressure and high rf power was ideal for obtaining films with good structural and optical quality.

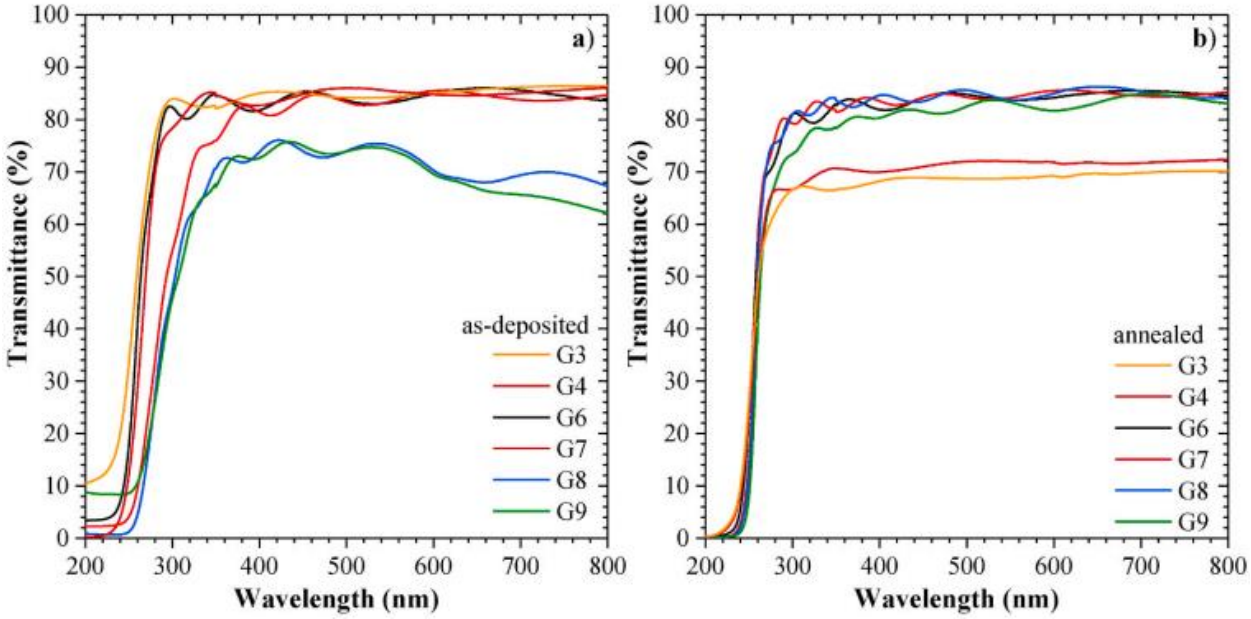

Figure 2.4 Transmittance spectra of Ga_2O_3 thin films for as-deposited and annealed samples deposited at various sputtering pressures and rf power on sapphire substrate (a) as-deposited and (b) annealed films [59].

Deposition Temperature. Kumar et al. deposited Ga_2O_3 films at different temperature ranging from 25 - 800 °C to study the effects of the deposition temperature in the structural and optical properties of Ga_2O_3 films [60]. XRD patterns of Ga_2O_3 revealed that films grown at 400 °C were amorphous, and that films become nanocrystalline at temperatures ≥ 500 °C, indicating film crystallization starting at this temperature (Fig. 2.5).

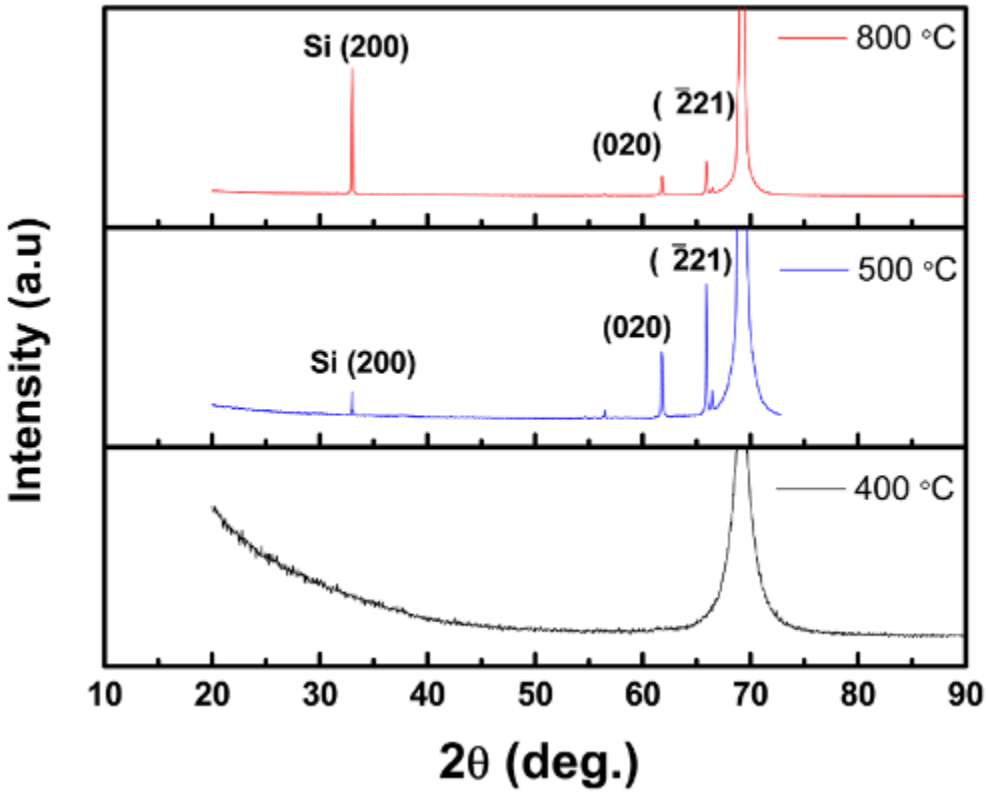

Figure 2.5 XRD patterns of Ga_2O_3 films. It is evident from the curves that the films grown at RT-400 °C are amorphous, whereas films grown at Ts ≥ 500 °C are nanocrystalline. Ga_2O_3 films grown at T_s=800 °C exhibit the presence of an additional small peak, which could be due to the Si-Ga_2O_3 reaction at the interface [60].

The surface morphology was investigated by high-resolution SEM, and it was clear that the grain size increases with increasing in the deposition temperature, as shown in Fig. 2.6. The grain size increased from 15 to 35 nm, with increasing temperature from 400 to 600 °C, then dropping to 30 nm at 800 °C. Kumar suggests that the change in morphology is due to an increase in the adatom mobility with increasing temperature. At low temperatures, the adatom mobility is low, therefore the deposited species stay localized forming amorphous films.

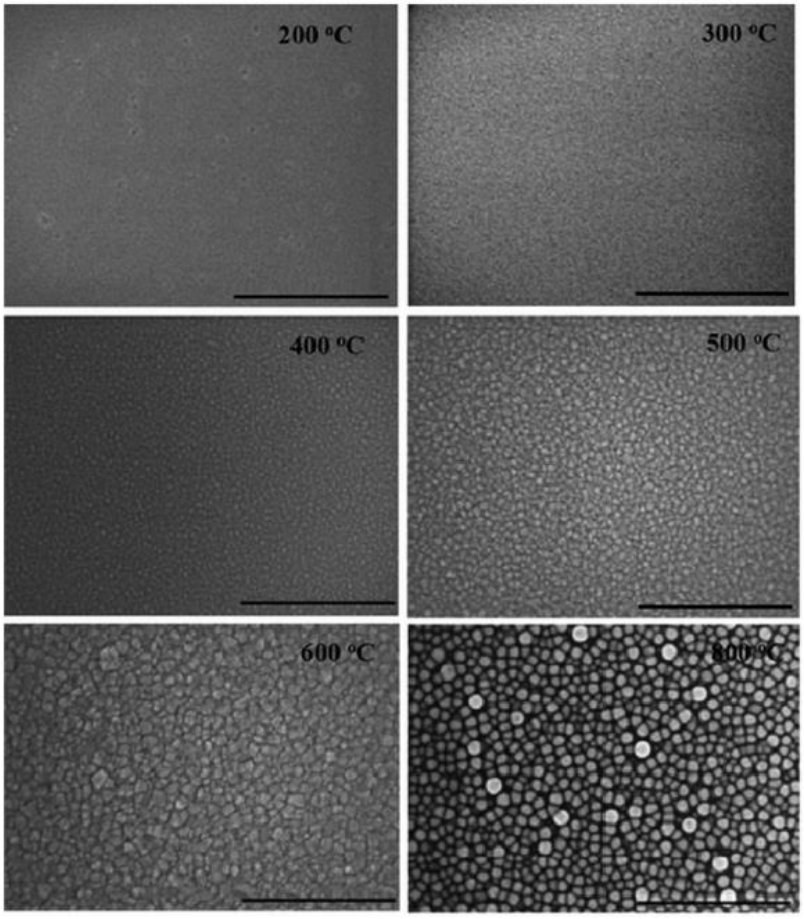

Figure 2.6 High-resolution SEM images of Ga_2O_3 thin films as a function of deposition temperature [60].

Rutherford backscattering spectroscopy (RBS) showed that the deposition temperature notably affected the stoichiometry of the films, and that a temperature of 300 °C or higher was necessary to obtain Ga_2O_3 films with stoichiometric (1.5 O/Ga) concentrations of Ga and O. Figure 2.7 shows the variation of the O/Ga ratio for the films deposited at different temperature. Films deposited at room temperature showed a slightly higher O/Ga of 1.6.

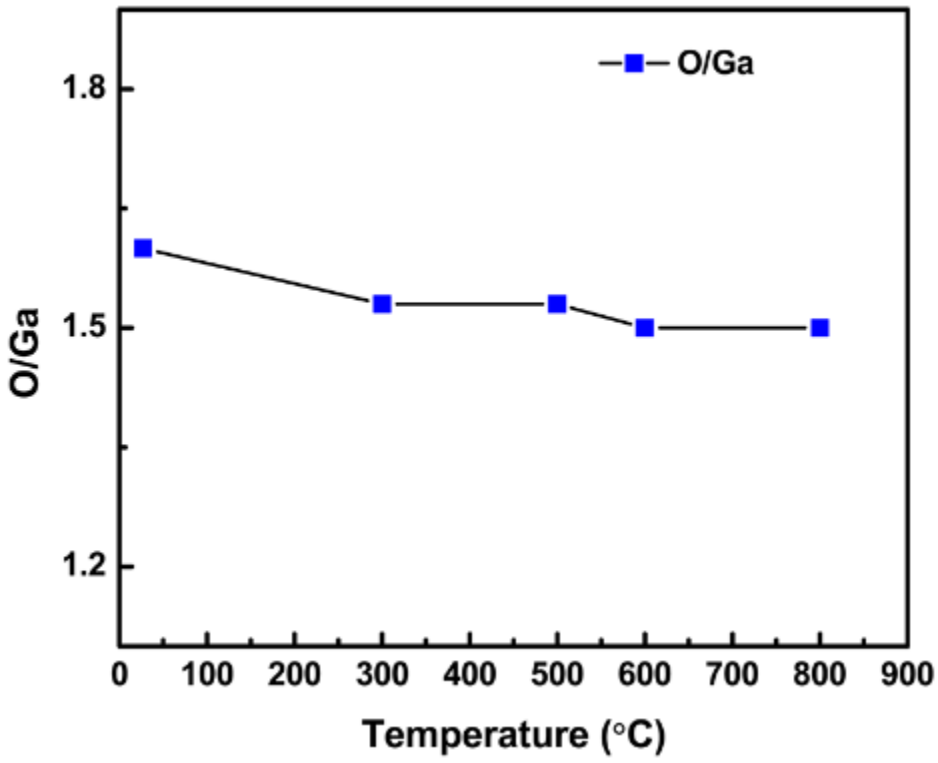

Figure 2.7 Variation of oxygen to gallium ratio in the Ga_2O_3 layers as a function of Ts. The ratio is determined from RBS measurements. Slightly higher values than expected for films grown at RT indicate excess oxygen in the films [60].

Saha et al. deposited n-type Ga_2O_3 films on silicon substrate using rf sputtering, systematically changing the substrate temperature from room temperature up to 800 °C [61]. The study shows that 600 °C is the optimum temperature to achieve high quality Ga_2O_3 films on Si by rf sputtering technique. X-ray photoelectron spectroscopy, energy dispersive x-ray analysis, ellipsometry, Raman spectroscopy, photoluminescence analysis, and atomic force microscopy were employed to examine the structural and optical characteristics, as well as the chemical states, of the deposited films. XRD showed that only the films deposited at room temperature displayed peaks at (400), $(\bar{4}02)$ and (403) planes of monoclinic Ga_2O_3, while films deposited at higher temperature are polycrystalline in nature. The morphology of the films was studied by AFM. Large grain sizes are observed at temperatures of 500 °C and higher, as indicated by the AFM scans in Fig. 2.8. Root-mean-square (RMS) value of the surface roughness of the films are estimated to be 2.6 nm, 5.2 nm, 8.3 nm, and 13 nm for RT, 500 °C, 600 °C and 700 °C deposited films, respectively.

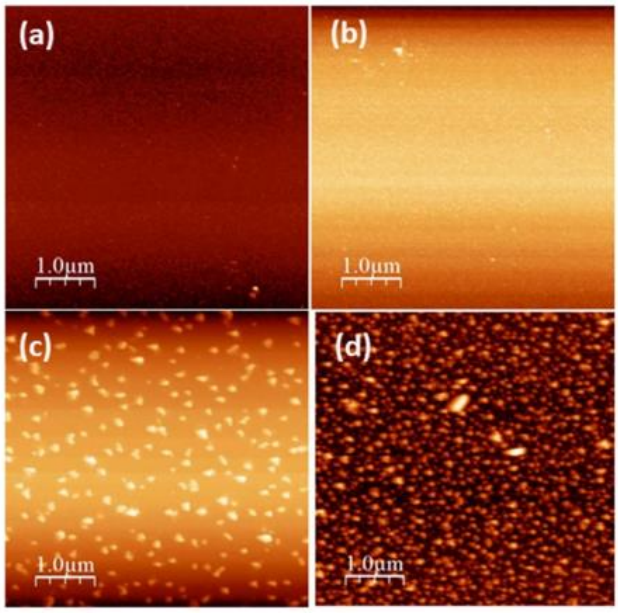

Figure 2.8 AFM images of the grown β-Ga_2O_3 thin films on Si substrate for the substrate temperatures of RT (a), 500 °C (b), 600 °C (c) and 700 °C (d) [61] .

XPS Ga-3d, Ga-2p and O-1s spectra revealed the change in chemical states and composition of Ga_2O_3 with deposition temperature. Particularly, shifting toward higher binding energies of Ga-3d, Ga-2p and O-1s states with increasing temperatures. The transmittance of the film was observed to decrease with increasing temperatures as shown in Fig. 2.9 (a). This reduction in the transmittance of the film can be correlated with an increase of the surface roughness of the films, as shown previously from the SEM data in Fig. 2.6. Saha et al. attribute the reduction in band gap energy to the decrease in lattice strain within the film. The decrease in band gap energy is associated with an increase in film thickness and surface roughness, both of which contribute collectively to the observed changes. The energy bandgap of the films was extracted from the Tauc plot shown in Fig. 2.19 (b). The highest energy values belong to the optical band-gaps, which were obtained to be 5.69, 4.39, 5.01 and 4.31 eV for RT, 500 °C, 600 °C and 700 °C deposited films, respectively.

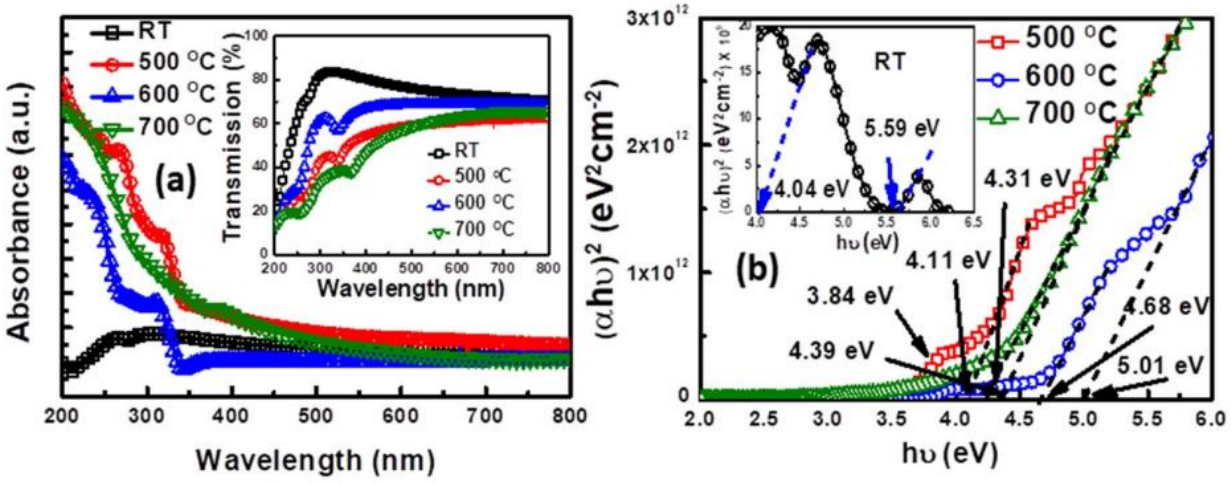

Figure 2.9 (a) Absorbance, transmission of β-Ga_2O_3 film on Si-substrate (RT, 500 °C, 600 °C and 700 °C) within the 200-800 nm wavelength range; and (b) the corresponding Tauc's plots for the deposited films [61].

Deposition Gas. Akazawa et al reported on the formation of various phases of gallium oxide films depending on deposition gas and substrate planes [62]. The films were deposited on c-plane sapphire, a-plane sapphire, and (100) Si substrates by rf magnetron sputtering either in O_2 of H_2O vapor ambient. XRD and GXRD data shown in Fig. 2.10 (a, b) indicates that films grown on sapphire in O_2 ambient at a 300-500 °C temperature range displayed distinct diffraction peaks belonging to $(\bar{2}01)$ β-Ga_2O_3. Crystallization of the films grown in O_2 occurred at temperatures as low as 300 °C. In contrast, the films grown in H_2O ambient, displayed weak diffraction peaks at 300 °C as shown in Fig. 2.11(a, b). Moreover, the films deposited at temperatures of 400 °C or higher grew with a preferred (311)γ-Ga_2O_3.

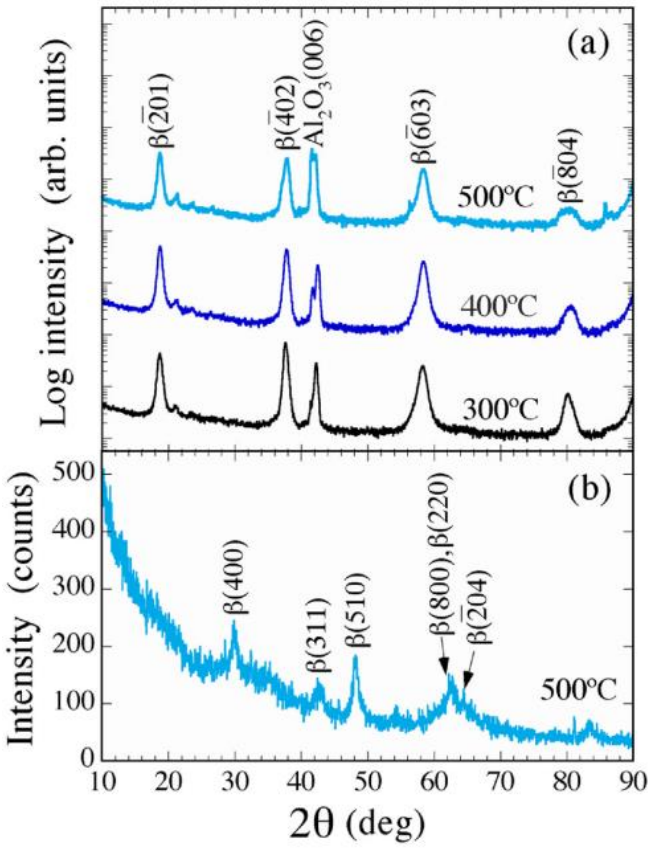

Figure 2.10 (a) XRD and (b) GIXRD patterns of Ga_2O_3 films as-crystallized on sapphire c-planes under O_2 gas flow [62].

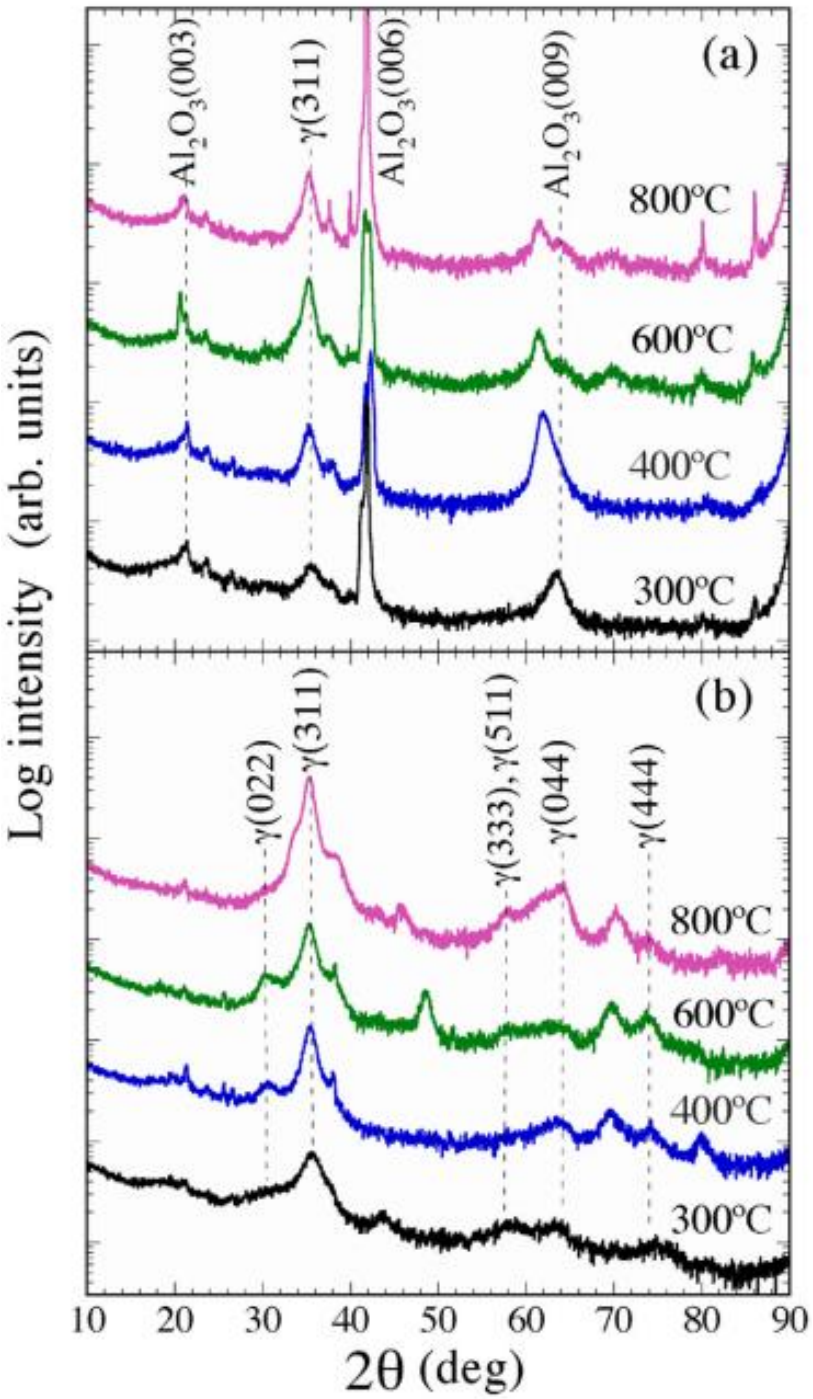

Figure 2.11 (a) XRD and (b) GIXRD patterns of Ga_2O_3 films deposited on sapphire c-planes under H_2O gas flow and solid-phase crystallized [62].

Dong et al. studied the influence of oxygen flow ratio in the growth chamber while depositing Ga_2O_3 films on c-plane sapphire substrates by rf sputtering [63]. The depositions were done at constant pressure and power of 5 mTorr and 60W, respectively. The oxygen percentage was varied, including 0%, 1%, 3%, and 5% with Ar as the main deposition gas. Dong observed that the deposition rate decreased with increasing oxygen flow, from 55.66 nm/hr at 0% to 23.66 nm/hr at 5%. XRD spectra showed distinct peaks belonging to β-Ga_2O_3 for all samples, however the diffraction peak intensity was noted to decrease with increasing oxygen percentage. They concluded that 1 vol. % oxygen during the deposition yielded the best crystallinity. These results align with results published earlier by Ogita et al [58].

A more recent study by Li et al. β-Ga_2O_3 films were deposited on MgO (100) substrate under different oxygen flow to investigate the effects on the structural and optical properties [64]. XRD of the films deposited at oxygen flow ratios of 0% to 5%, showed (400) β-Ga_2O_3 peaks with increased intensity up to 1% oxygen ratio. Then, the diffraction intensity decreased until completely vanished at 8% oxygen ratio where the films became amorphous as shown in Fig 2.12 (a). The group concluded that 1% oxygen ratio is optimal for growing single-crystalline (400) β-Ga_2O_3 films. Figure 2.12(b) shows an enlarge detail of the peak located at 30°, there is an evident shifting of the XRD peak towards higher angle with increasing oxygen growth pressure, suggesting a decrease in the lattice parameter. Although the author fails to address the issue in this study, this shifting of the XRD peaks with the oxygen growth pressure has been previously observed [65]. The results obtained by Li et al, are in agreement with the work performed by Dong et al [63].

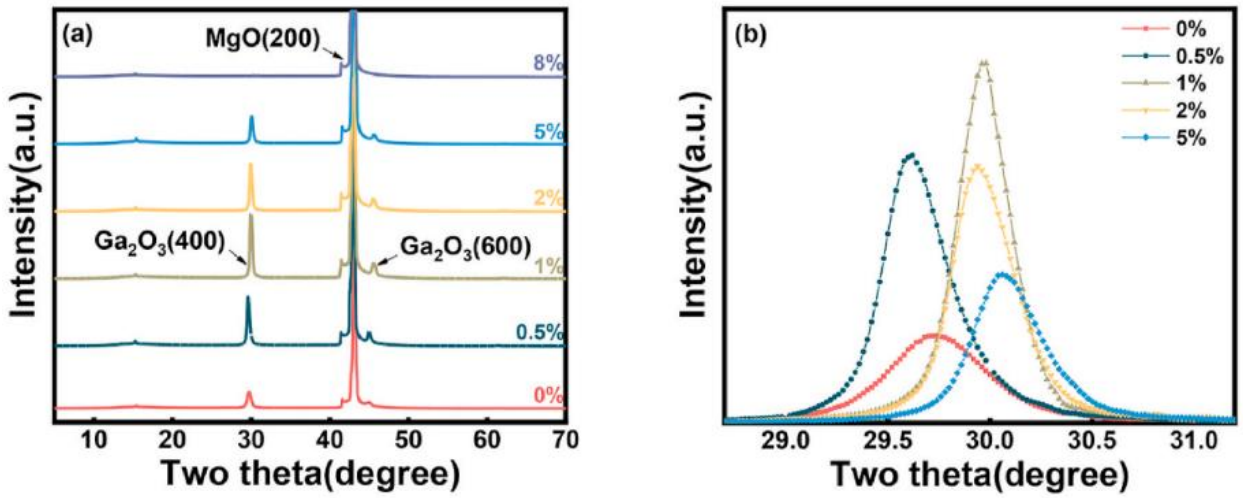

Figure 2.12 (a) XRD diffraction patterns of the deposited β-Ga_2O_3 films under different oxygen flow ratios. (b) Partially enlarged detail of (a) for the samples prepared under the 0%-5% oxygen flow ratio range [64].

Atomic force microscopy images showed that as the oxygen percentage increased, the grain size and roughness parameter of the films also increased indicted in Fig. 2.13. This is attributed to a reduction in the efficiency of the Ar ions bombarding the target, which decreases the ion density near the film surface, causing a reduction in the number of particles reaching the substrate surface necessary for film growth. The roughness of the samples ranged from 11, 3.56, 0.664, 0.581, 0.479, and 1.74 nm with increasing oxygen ratio.

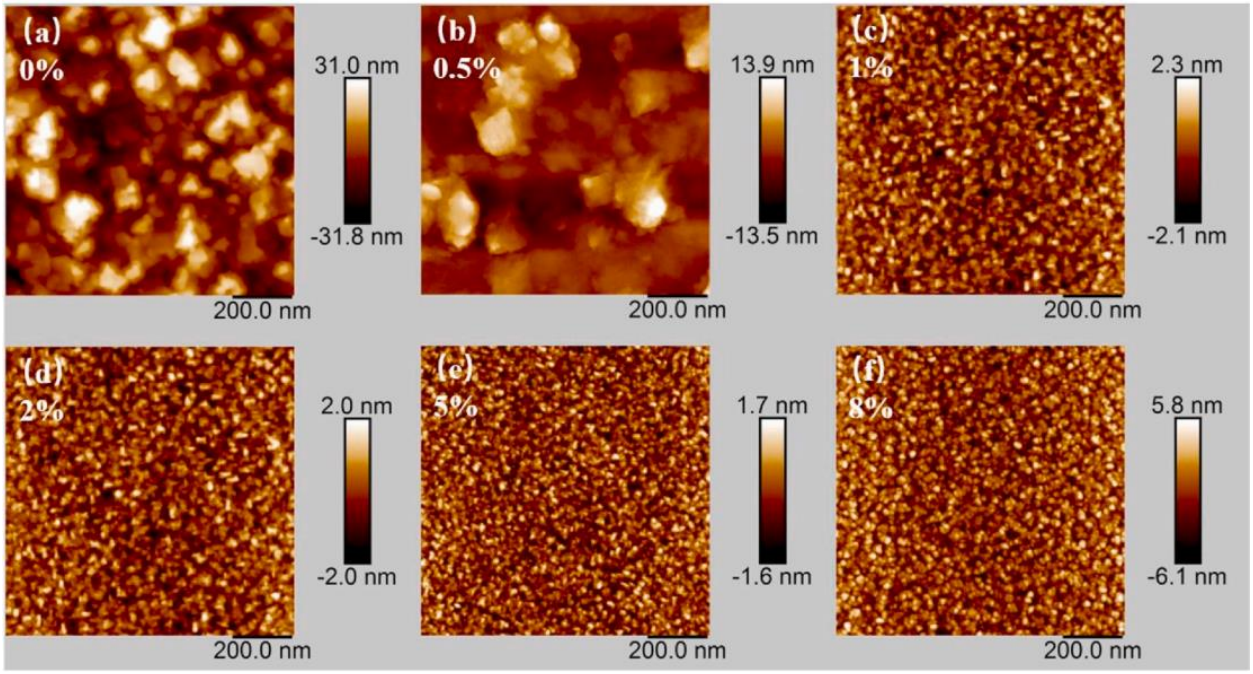

Figure 2.13 AFM images of the β-Ga_2O_3 samples as a function of the oxygen percentage [64].

RF Power. For the examination of sputtering power effects, Li et al deposited Ga_2O_3 thin film on Al_2O_3 (0001) substrate by radio frequency magnetron sputtering [66]. The films were deposited in an Ar/O_2 mixture with flow rates of 40 sccm and 2 sccm respectively. X-ray diffraction results showed that the crystalline quality of $(\bar{2}01)$ β-Ga_2O_3 films improved with increasing power. The three peaks located at 18.95°, 38.40°, and 59.19° corresponding to $(\bar{2}01)$, $(\bar{4}02)$, and $(\bar{6}03)$ plane family of $(\bar{2}01)$ β-Ga_2O_3, respectively. The peak intensity can be seen to increase with increasing rf power, as shown in Fig. 2.14. Further analysis on the normalized intensity and full width at half maximum (FWHM) of the strongest $(\bar{4}02)$ diffraction peak, shows that the intensity of remains constant up to 190 W and then increases abruptly at 200 W. The FWHM of $(\bar{4}02)$ peak starts to decline after rf power of 170 W, the narrowing of the diffraction peak was attributed to an increase in the driving energy of the sputter atoms, which allows them to migrate to more suitable lattice sites resulting in higher crystallinity.

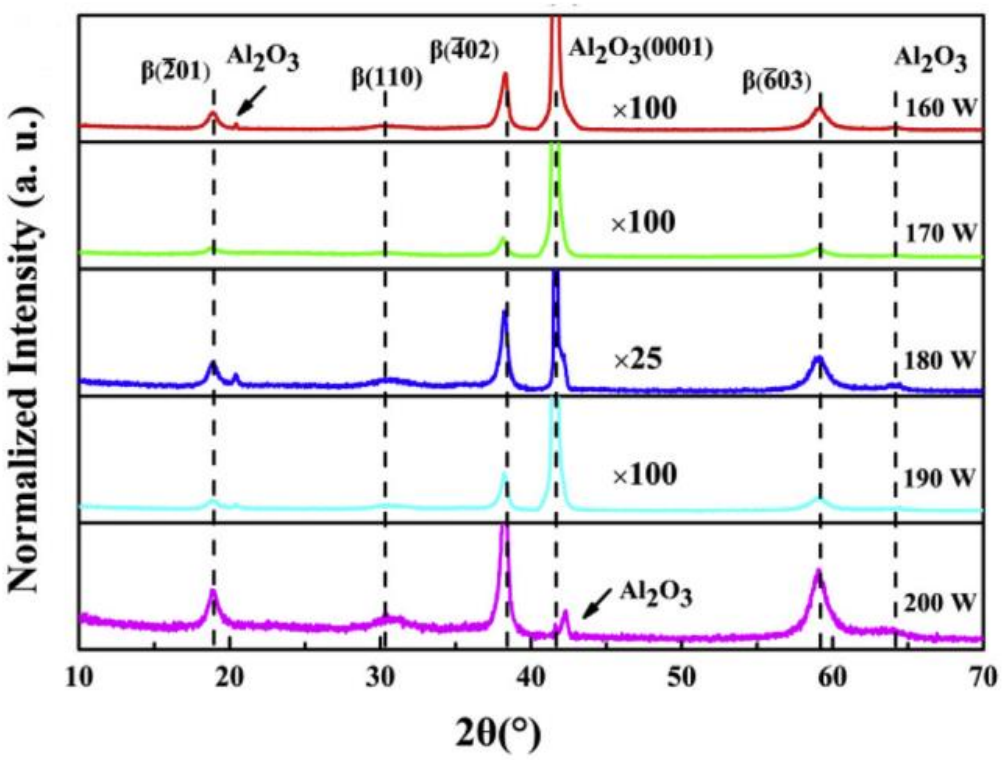

Figure 2.14 Annealed β-Ga_2O_3 films deposited at sputtering power varies between 160 W and 200W [66].

Scanning electron microscopy images and calculation of the grain size from XRD using the well-known Scherer displayed an enlargement of the grain size with increased rf power. Figure 2.15 shows the average grain size using both methods, the size of the grains increases after rf power of 170 W. It is worth mentioning that the small discrepancies in the grain size obtained by both methods is due to variances in the measurement techniques and principles. SEM directly measures particle size by analyzing microscope images, considering particle shape and morphology for a more accurate assessment. Conversely, XRD calculates crystallite size using the Scherrer equation based on diffraction patterns, which may not precisely reflect actual particle dimensions. In their study, Li et al. elucidate that the increase in sputtering power results in more

ionized argon gas particles and greater bombardment on the Ga_2O_3 target. This leads to a higher number of target atoms possessing increased energy for diffusion to appropriate sites, thereby facilitating optimal bonding with adjacent atoms. Elevated bombardment energy leads to a higher substrate temperature during deposition. This dual effect aids target atoms in nucleating and growing. Consequently, as sputtering power increases, the grains gradually enlarge.

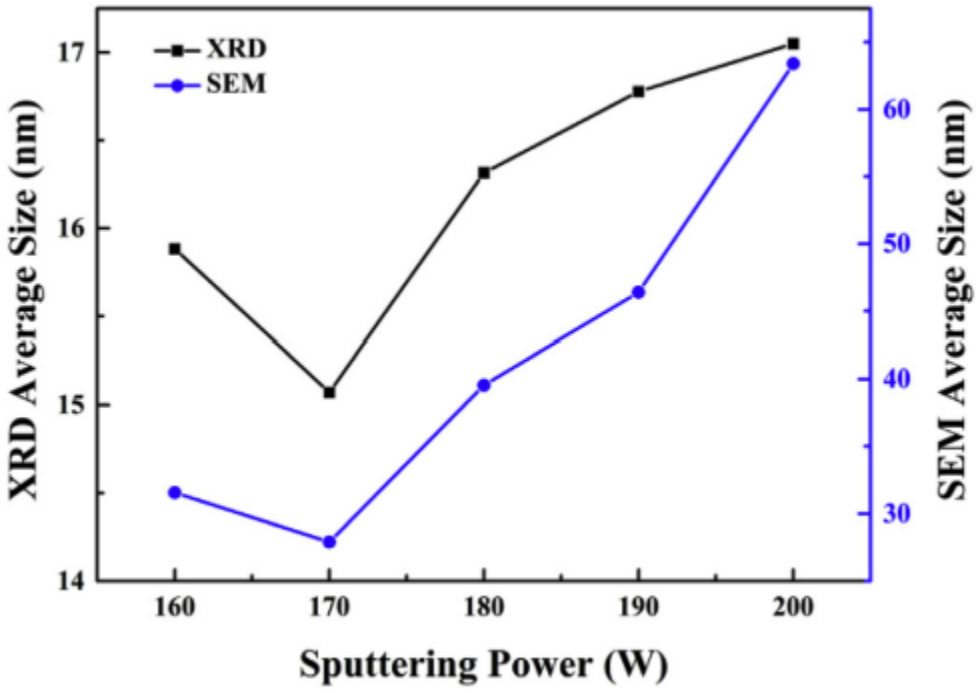

Figure 2.15 β-Ga_2O_3 peak intensity and FWHM as a function of sputtering power [66].

Annealing Parameters. Annealing parameters include temperature, time, and ambient. rf-sputtered Ga_2O_3 thin films are amorphous when deposited at room temperature. Therefore, heat treatment between is a necessary step to achieve crystalline Ga_2O_3 films. Several other groups have reported on the effects of the annealing gas, including nitrogen [67–70], oxygen [71,72], argon [70,73], and vacuum [68] ambient at specific temperatures and processing times.

One of the earliest reports on the effects of annealing temperature on the properties of rf sputtered Ga_2O_3 films was published by Marie et al [74]. Post-annealing treatment was performed at 900 °C and 1000 °C for 1 hr in pure nitrogen ambient. β-Ga_2O_3 diffraction peaks appeared for both samples, showing higher intensity in the sample annealed at 1000 °C indicating a better formation of the β-Ga_2O_3 phase. The sheet resistance was noted to decrease with increasing annealing temperature, denoting an increase in the electrical conductivity of the films.

Dong et al. used annealing temperatures of 800 °C, 900 °C, and 1000 °C post deposition of Ga_2O_3 sputtered films in nitrogen [63]. The diffraction peaks showed higher intensity with increasing temperature as reported by Marie et al [74]. The band gap energy was noted to increase with increasing annealing temperature. Band gap energy of the as deposited films was 4.7 eV, after annealing at 1000 °C the band gap energy increased to 4.8 eV.

Li et al. performed annealing of Ga_2O_3 films at temperatures ranging from 700 °C to 1100 °C [56]. The gas used for these experiments was oxygen. Comparison of the XPS data of the as deposited samples and the samples annealed at 800 °C in O_2 showed a change in the O/Ga ratio. After annealing in O_2 the films showed an increased O/Ga atomic ratio of 1.455, which indicated that annealing in such ambient can effectively reduce the oxygen vacancies in the film. The resistivity of the films firstly decreased and then increased with annealing temperature. It was found that the resistivity of the films is related to the film crystallinity. The lowest resistivity was found for the films annealed at 800 °C, which yielded the best crystallinity.

Haslinda et al investigated the effects of annealing temperature in Ar ambient on the structural, optical, and electrical properties of rf-sputtered Ga_2O_3 films [75]. The annealing temperatures included 400, 600, 800, 1000 °C. XRD data shown in Fig. 2.16. indicate that cubic

γ- Ga_2O_3 with (311) and (-440) orientations at 400 °C. As the annealing temperature was increased to 600 °C, monoclinic phases of β-Ga_2O_3 oriented in (400), ($\bar{2}$02), and ($\bar{7}$12) planes, along with (311) γ-Ga_2O_3 planes were detected. Further increase in the annealing temperature to 800 °C showed dominant β-Ga_2O_3 with additional ($\bar{1}$10) and (401) oriented planes. Coexistence of both β-Ga_2O_3 and γ-Ga_2O_3 phases at 600-800 °C annealing temperatures suggest the formation of polycrystalline Ga_2O_3 comprising the two phases.

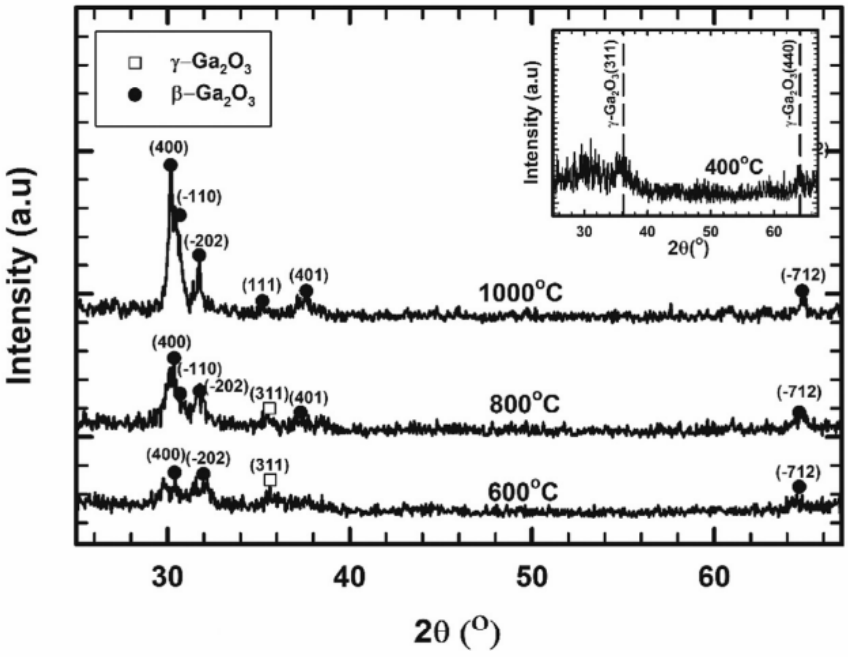

Figure 2.16 HRXRD spectra for Ga_2O_3 films subjected to post-deposition annealing temperature at 400 (inset), 600, 800, and 1000 °C in argon ambient [75].

The annealing temperature also influenced the direct band gap energies. As the annealing temperature increased from 400 °C to 800 °C, an increase direct band gap value was observed from 1.52 eV to 4.71 eV this was attributed to the decreased number of oxygen vacancies. Higher temperatures decreased the band gap energy, due to the formation of an interfacial layer between Ga_2O_3 film and Si substrate and increased oxygen vacancies.

2.2 Homoepitaxial Growth

Compared to heteroepitaxial growth, homoepitaxy is supposed to yield films with improved quality, minimal dislocations, and rotational domains, since the layers share the same crystal structure with the substrate [76]. These defects deteriorate the electrical properties of the grown layers, since they compensate the n-type doping, reduce the carrier mobility, and eventually lead to mobility collapse below a critical doping density [77]. Hence, achieving epitaxial growth, even in instances of zero misfit, remains a challenging endeavor. A more thorough understanding of the growth process is crucially needed to address these challenges effectively. Homoepitaxial growth of β-Ga_2O_3 thin films have been achieved by HVPE [78], MBE [79], MOCVD [80], MOVPE [81], mist-CVD [82], and plasma-assisted MBE [83]. No successful homoepitaxial growth has been reported using rf magnetron sputtering. Studies on three distinct substrate orientations, namely (100)-, (010)-, and $(\bar{2}01)$-oriented β-Ga_2O_3 substrates, are presented next.

(100) β-Ga2O3. Homoepitaxial layers grown on (100) β-Ga_2O_3 substrates were achieved by Oshima et al. using MBE and by Wagner et al. using MOVPE [83,84]. Oshima et al. reported a step-flow growth for the layers grown on (100)-oriented substrates. The surface morphology was strongly influenced by the cleavableness of the (100) and (001), planes. For smooth surfaces, an off-axis direction along the [001] or [00 $\bar{1}$] is required during the surface pretreatment process, i.e., the polishing stage. The layers grown on (100)-oriented substrates by MOVPE resulted in stacking faults in the form of twin lamella as the result of the growth and coalescence of 2D islands. The solution to the stacking faults in the (100) plane is to prepare the surface with a miscut angle of 6° along [00 $\bar{1}$] direction [85].

Cheng et al. used a complementary in and ex situ analytical approach to study the formation of structural defects in homoepitaxial (100)-oriented β-Ga_2O_3 layers and growth mode by molecular beam epitaxy [76]. The layers were grown on a substrate kept at 700 °C, and the gallium cell kept at the same temperature. The plasma cavity was adjusted to 400 W with a constant O_2 flux of 0.6 sccm resulting in a chamber pressure of 6 x 10^{-6} mbar. The crystal structure and morphological properties were analyzed with (i) in situ reflection high energy electron diffraction (RHEED), (ii) synchrotron-based high resolution x-ray diffraction (HRXRD), and (iii) ex situ transmission electron microscopy (TEM) and atomic force microscopy (AFM). RHEED patterns Fig. 2.17 before (a), (b) and after (c), (d) the growth. After the growth vertical streaks were observed indicating atomically flat surface. During the growth the intensity of the specular beam spot was monitored and showed to be periodic in time, this oscillating behavior proved sequential and distinguishable nucleation steps, suggesting a two-dimensional (2D) growth mode of the layers.

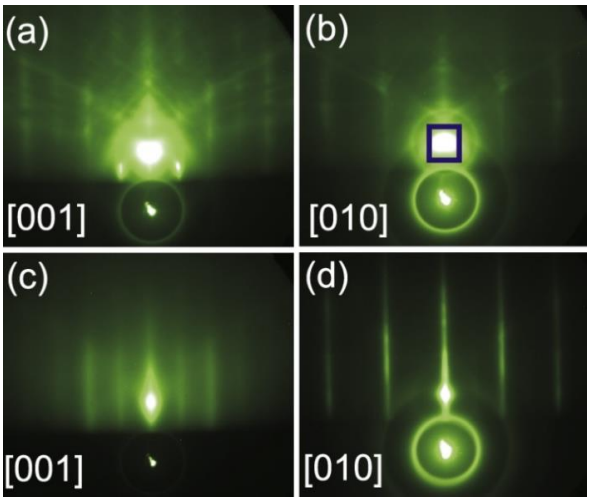

Figure 2.17 The RHEED patterns before growth are shown in (a) and (b) for the (001) and (010) directions, respectively. After growth, the RHEED patterns for the (001) and (010) directions are depicted in (c) and (d), respectively.

The HRTEM image in Fig. 2.18 (a) displays the (010) cross-section of the (100)-oriented homoepitaxial thin film, with the electron beam oriented along the b-axis. Bright dots in the image represent half a unit cell or one monolayer. Notably, the image reveals a significant density of stacking faults marked in blue, along with the presence of twin boundaries marked in green. The twin boundaries were describe earlier as a c/2 glide reflection of the monoclinic lattice on the a-plane [85]. Cheng et al. interpretated the formation of these domains by double positioning [76]. The diffusion length of the species on the substrate is limited by the growth temperature, therefore monolayer islands are formed and some of them are twinned orientation. These islands proceed to grow and eventually merge forming twin domains. To understand the effects of the twin domains on the diffraction pattern, Cheng et al. used JEMS software to compare the electron diffraction pattern of an ideal β-Ga_2O_3 structure and a film containing twin domains. Figure 2.18 (b) and d show the diffraction pattern of grown layer with twin domains and without twin domains, respectively. Figure 2.18 (c) and (e) are from a simulated pattern. The extra diffraction dots are circled in red in the grown layer, and they also appear in the simulated layer containing twin domains. This shows that the extra diffraction spots are due the presence of twin domains in the layer. Figure 2.18 (f) shows the surface morphology of the grown sample probed by AFM. Nuclei with an average height of about 6 Å were observed with preferential elongation along the b-direction. This height agrees with the thickness of one monolayer and is accordant with the 2D growth mode as described by RHEED and HRTEM. The preferential direction of the elongation suggests that the reactive molecules have higher mobility along the b-axis compared to other in-plane directions. The width of a single island is about 6 nm and corresponds well with the average size of the nano-twins observed in the HRTEM.

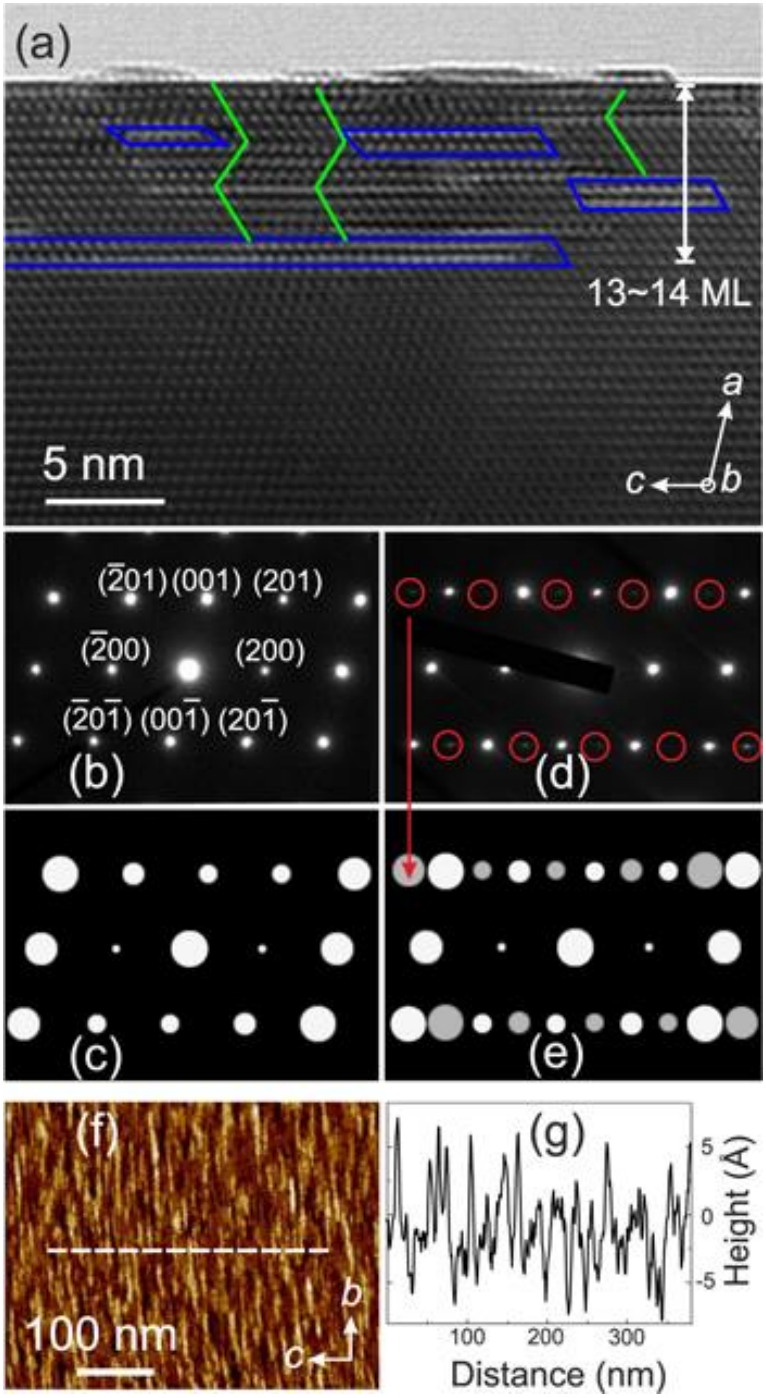

Figure 2.18 (a) The film thickness was estimated to be 14 monolayers thick, with presence of stacking faults as observed by HRTEM. (b)-(d) shows electron diffraction of the deposited films, (c)-(d) are simulations confirming the presence of twin boundary domains. (f)-(g) depicts AFM data of the (001) layers [76].

Figure 2.19 (a) shows the in situ out-of-plane HRXRD curves of the substrate and homoepitaxial film. No additional Bragg peaks were observed, indicating that the crystal does not have any other phases but only the (100)-oriented β-Ga_2O_3. HRXRD also shows that there is a rather broad diffuse scattering under the (200) reflection with a FWHM of 0.39 $Å^{-1}$. This characteristic could stem from a slight distortion of the crystal structure caused by stacking faults and twins, as observed in HRTEM images.

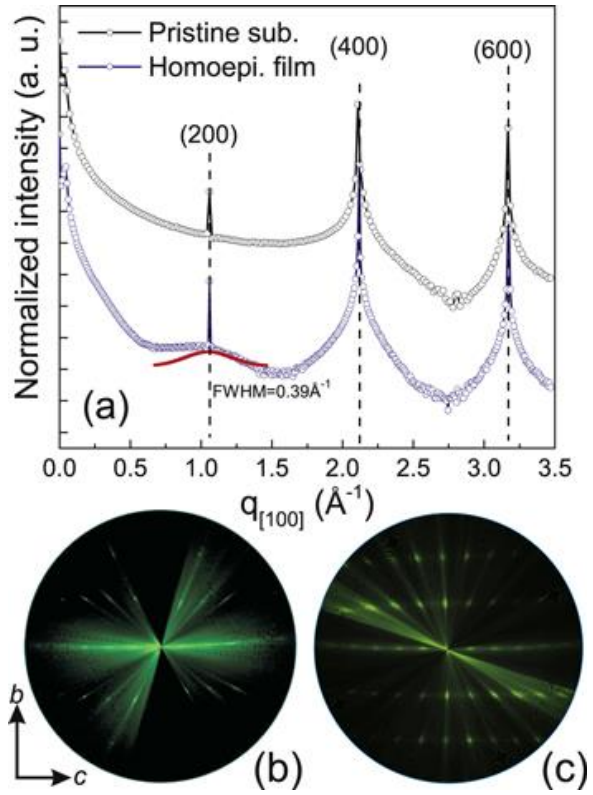

Figure 2.19 (a) X-ray diffraction data collected perpendicular to the surface from both the initial β-Ga_2O_3 substrate, and homoepitaxial films. The homoepitaxial layers displayed diffuse scattering around the (200) diffraction peak, exhibiting a full width at half maximum (FWHM) of about 0.39 $Å^{-1}$. In-plane azimuthal patterns from RHEED before and after the growth process [76].

(010) β-Ga_2O_3. Leedy et al. simultaneously fabricated Si-doped Ga_2O_3 films on semi-insulating (010) β-Ga_2O_3 and (0001) Al_2O_3 [86]. The films grown on native β-Ga_2O_3 showed single crystal homoepitaxial growth as determined by HRTEM and XRD. Figure 2.20 shows XRD scans done on the films fabricated at 590 C on Al_2O_3 and (010) β-Ga_2O_3. Leedy et al. mention that the thickest film grown of 400 nm presented additional reflections at: 44.43° [601], 57.65° [313], 30.32° [110] and 59.91° [113] planes of β-Ga_2O_3 which reduced the film quality, but attribute it to the increasing O_2 partial pressure used during the growth [87].

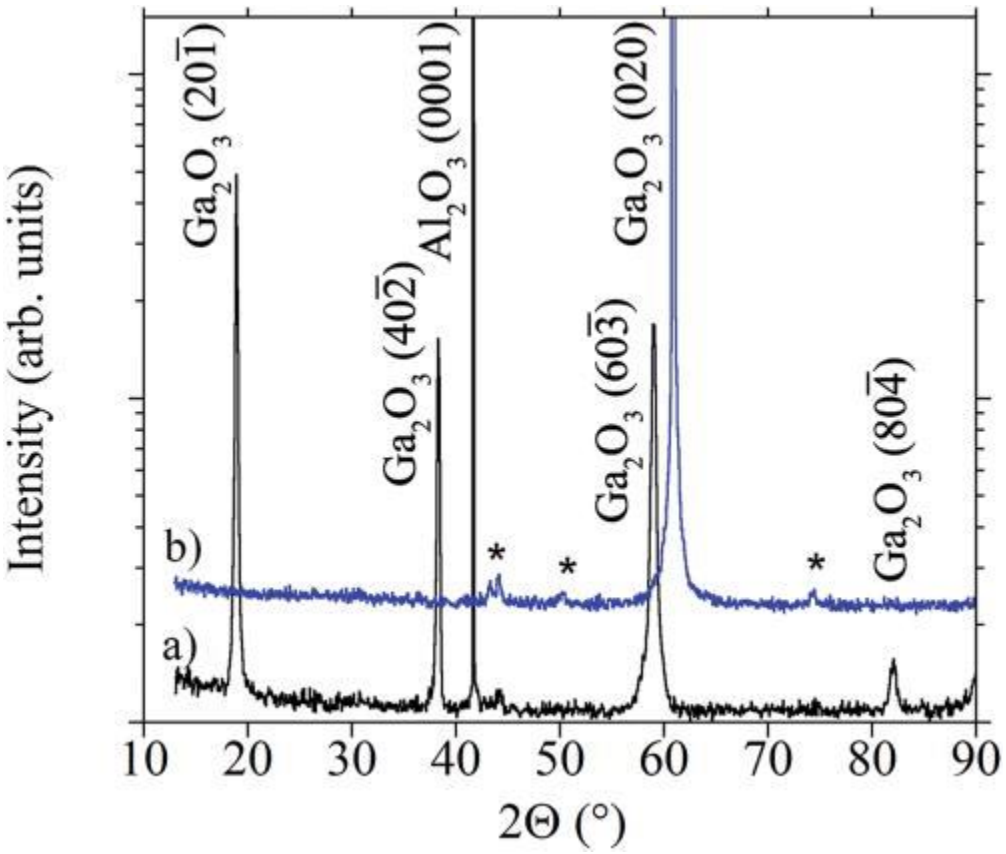

Figure 2.20 XRD patterns of Ga_2O_3:Si films deposited at 590 °C on (a) (0001) Al_2O_3 and (b) (010) β-Ga_2O_3 substrates. [86].

($\bar{2}$ 0 1) β-Ga_2O_3. Most studies have focused on the (010) orientation, however it is not trivial to grow large substrates due to the need to slice the substrates perpendicular to both the (100) and (001) cleavage planes. In contrast, ($\bar{2}$ 0 1)-oriented substrates are significantly easier to prepare at large scale industrial production. Islam et al. grew homoepitaxial ($\bar{2}$01) β-Ga_2O_3 films by atmospheric pressure plasma-enhanced chemical vapor deposition technique [88]. They realized temperature dependent studies between 350 and 600 °C in the search of a low-temperature growth. XRD data shown in Fig 2.21. shows that there were no different diffraction peaks for the films grown at different temperatures, meaning that there were no other secondary phases or different orientations during the growth. However, the peaks presented a shoulder on the left side, indicating that the d-spacing perpendicular to the film surface [$\bar{2}$01] is elongated. This broadening of the Bragg peaks was also observed in homoepitaxial growth on (100)-oriented substrates by Cheng et al [76].

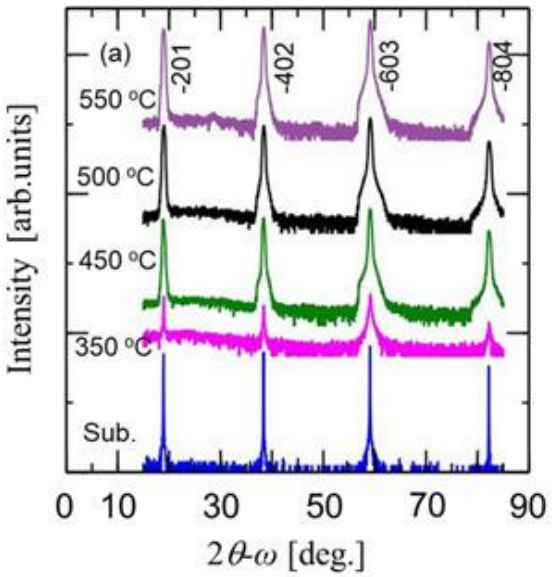

Figure 2.21 XRD profiles of the samples grown at in the deposition temperature range of 350-550 °C [88].

2.3 Doping of Gallium Oxide

The conductivity and absorption of β-Ga_2O_3 films the can be controlled through doping, and it is a necessary step for the semiconductor to have technological significance [41,89]. The β-Ga_2O_3 crystal exhibits an unintentional n-type doping conductivity. This n-type conductivity has been commonly attributed to oxygen vacancies in the crystal, which form donor states. Intentional n-type doping with elements from group IV, such as silicon (Si), germanium (Ge), and tin (Sn) [90–92] have been reported. The carrier concentration can be finely controlled within a broad range of 10^{15}-10^{20} cm^{-3} by incorporating donor dopants [93]. A major drawback is the inability to successfully p-type dope Ga_2O_3 material. Although some potential candidates for p-type doping of Ga_2O_3, including magnesium (Mg), zinc (Zn), beryllium (Be), and nitrogen (N) have been proposed, there are three main factors that makes p-type doping nearly impossible. First, it is generally difficult for single-crystal oxide semiconductors to form shallow acceptor states, since their valence band states are mainly composed of weakly interacting O 2p orbitals. There are instead deep acceptor levels with high activation energy of over 1 eV. Another issue is that Ga_2O_3 has a relatively flat valence band, which translates to a heavy hole effective mass with limited conductivity and diffusion constant. Lastly, it was also theoretically predicted that holes localize in β-Ga_2O_3 as small polarons due to lattice distortion, as opposed to being free holes, i.e., not localized or widespread [93].

2.4 Ohmic Contacts to Ga_2O_3

Ohmic contacts play a vital role in semiconductor manufacturing by establishing a low-resistance connection between semiconductor and external circuitry. Common methods used to create such contacts include the careful selection of metals, specifically choosing metals whose work function matches with the electron affinity of the semiconductor. From Schottky-Mott theory ($\Phi_B{}^{(n)} = \Phi_m - \chi_s$), consequently lowering of the Schottky barrier height. Since ohmic contacts follow the thermionic-field emission or field emission conduction mechanism, another way to create a non-rectifying contact is by introducing localized doping on the surface to minimize the width of the depletion region and promote charge carrier tunneling. Standard metallization for Ohmic contacts to β-Ga_2O_3 include Ti/Au, Ti/Al/Ni/Au, and conductive oxides such as indium tin oxide (ITO). β-Ga_2O_3 electron affinity has been reported to be 4.00 ± 0.05 eV [94,95]. Titanium with a metal work function of ~4.3 eV, would result in barrier height of only ~0.3 eV. ITO work function has been reported in the range of 4.2-5 eV, which will also result in the lowering of the barrier height [96]. The Au layer on all contacts serves to prevent topside oxidation. The mechanism of ohmic contact formation is currently under debate, while it is highly influenced by various processing conditions such as, RIE and Si ion implantation surface treatment, and annealing conditions.

2.4.1 Ti/Au

Higashiwaki et al. demonstrated the first metal-semiconductor field-effect transistor (MESFETs) on β-Ga_2O_3 (010) substrate by molecular beam epitaxy [39]. Ti (20 nm)/Au (230 nm) metallization was utilized, and it was demonstrated that surface treatment with RIE using a gas mixture of BCl_3 and Ar for 1 min was critical for Ohmic contact formation as shown by the red line in Fig. 2.22. Although RIE treatment showed ohmic behavior, the mechanism was unclear,

and it was attributed to the formation of induced surface defects such as oxygen vacancies that function as donors.

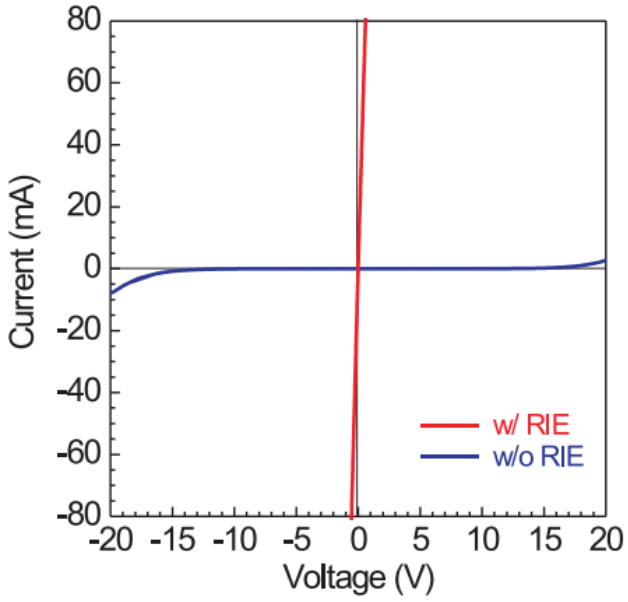

Figure 2.22 I-V curves measured between two contacts (as-deposited Ti/Au) fabricated with and without RIE treatment on n-Ga_2O_3 substrates by Higashiwaki et al [39].

Continuation of this investigation, Higashiwaki demonstrated a depletion mode field-effect device on β-Ga_2O_3 (010) by MBE [97]. Si-ion implantation doping (N_d=5x10^{19} cm^{-3}) was performed on the electrode regions, followed by an activation annealing at 925 °C in N_2 gas for 30 min. The surface was treated again with BCl_3 RIE, and Ti (20 nm)/Au (230 nm) were deposited. The Ti/Au stack was annealed at 470 °C for 1 min in N_2 by rapid thermal processing. The annealed contacts showed ohmic behavior (Fig. 2.23(a)), and the specific contact resistivity was 8.1 x10^{-6} Ωcm^2. Higashiwaki also observed a defective Ga_2O_3 region and a reacted Ti-Ga_2O_3 region at the annealed Ti/Ga_2O_3 interface, shown in a TEM micrograph in Fig. 2.23(b).

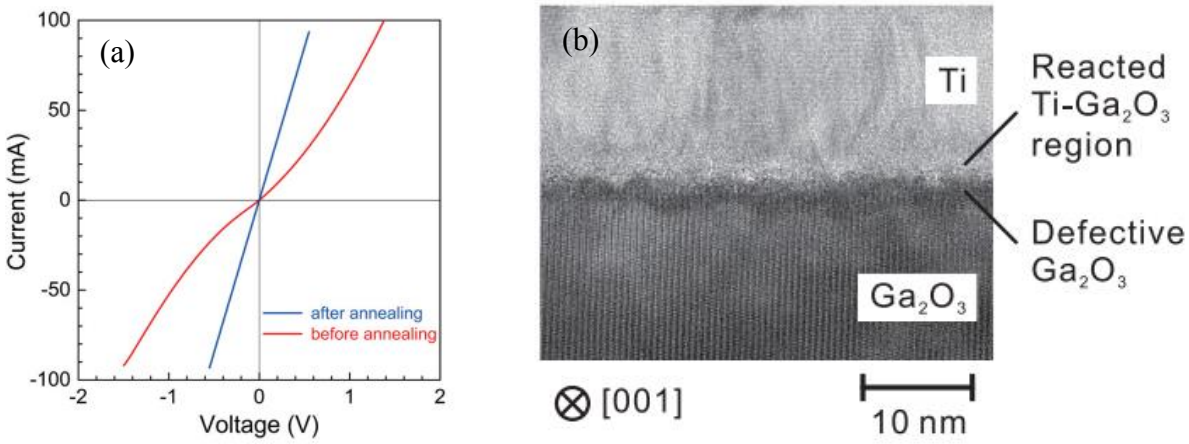

Figure 2.23 (a) I-V characteristics of Ti/Ga_2O_3 interface before and after annealing. (b) Reacted Ti/Ga_2O_3 interface after annealing at 470 °C in N_2 [97].

Lee et al studied the interfacial evolution of Ti/Au metallization on β-Ga_2O_3 (010) substrates under different annealing conditions [98]. Ti (20 nm)/ Au (50 nm) contacts were deposited using E-beam evaporation. TEM samples were prepared via conventional focused ion beam (FIB), then subjected to three different annealing metallization conditions: (a) unannealed (as-deposited), (b) 470 °C for 1 min in N_2, and (c) 470 °C for 15 min in N_2. High-angle annular dark field (HAADF) images of the three conditions were taken. For the as-deposited sample a slight reacted region is observed. The 1 min annealed sample showed the formation of two separate layers at the interface. Energy dispersive X-ray spectroscopy (EDX) confirmed that the additional layer was a Ga-rich layer on top of a Ti-TiO_x layer as shown in Fig 2.24. TEM (HRTEM) images showed that the Ti-TiO_x layer is partially lattice matched with monoclinic β-Ga_2O_3 substrate. A defective Ga_2O_3 was observed, as previously reported by Higashiwaki et al [39]. After 15 min annealing, the interface intermixed, and Ti-rich nanocrystals are observed.

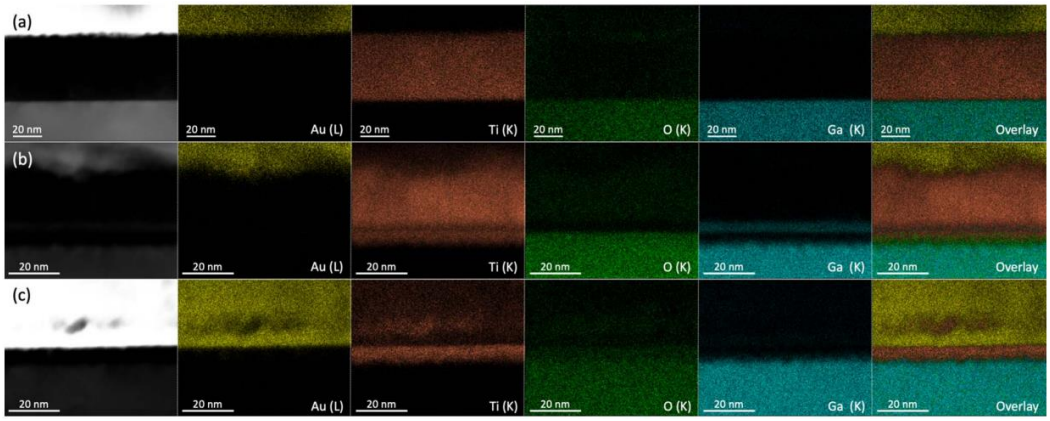

Figure 2.24 EDX mapping of the Au/Ti/ β- Ga_2O_3 interface at distinct stages in the annealing process: (a) as-deposited; (b) after a 470 °C 1-min N_2 anneal; and (c) after a 470 °C 15-min N_2 anneal. The elemental distribution counts are shown; yellow, orange, green, and blue represent Au (L), Ti (K), O (K), and Ga (K), respectively. Note the distinct Ti-TiO_x and Ga-rich layers in (b). Also note that in (c), Ti-rich nanocrystals are observed and the Ti-TiO_x layer remains roughly the same thickness as in (b) [98].

The proposed mechanism by Lee et al. is based on a sequence of interdiffusion and interfacial reactions taking place at the metal-semiconductor interface, shown schematically in Fig. 2.25. During the first minute of the anneal, Ti diffuses downwards where it reacts and steals oxygen from the Ga_2O_3 by substitution of Ga atoms in the substrate forming a Ti-TiO_x layer. The substituted Ga atoms react with Ti to form a thin localized layer of Ga-rich species, $TiGa_x$, observed on top of the Ti-TiO_x layer. Further annealing for 15 min breaks the lattice match between the TiO_x layer and β-Ga_2O_3 suggesting that the interface is not electrically stable [98]. The overall reaction between Ti and Ga_2O_3 can be understood as redox reaction, favoring the formation of TiO_x at the interface, and has been documented in earlier research [99,100]. Chemical analyses conducted by Lee et al in another study, suggest that Ti/β-Ga_2O_3 interface is not thermodynamically stable under annealing either [100].

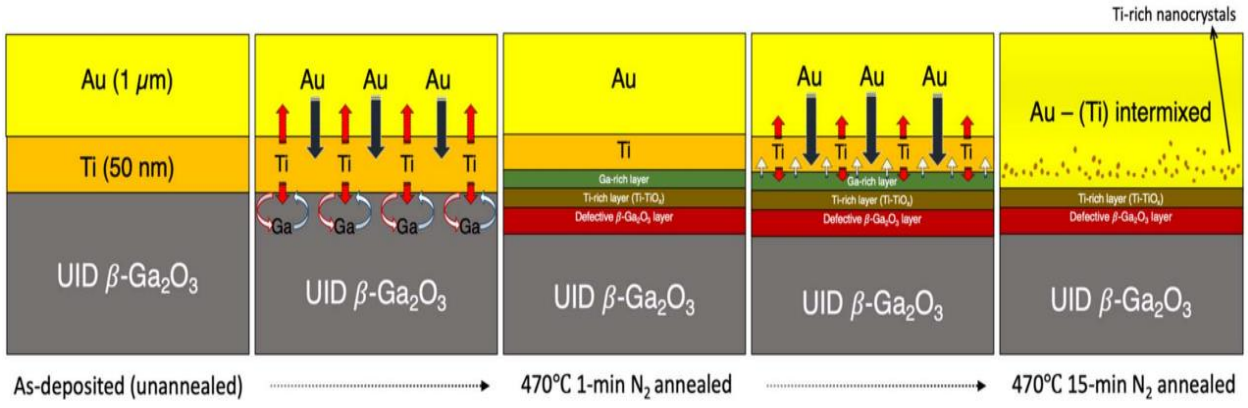

Figure 2.25 A schematic of the proposed evolution of the Au/Ti/ β-Ga_2O_3 interface during 470 °C annealing [98].

Lee and Peterson also correlated the influence of processing parameters on the metallization of Ohmic contacts, including RIE, Si ion implantation, and annealing. They achieved a low specific resistivity of ~10^{-5} Ωcm^{-2} in heavily doped samples by Si-ion implantation, treated with BCl_3 RIE. In addition, thermally accelerated aging of the Ti/Au interfaces was performed for the first time. EDEX measurements in STEM mode of the 1 min 470 °C annealed samples showed that the interface in stable upon accelerated thermal aging at 300 °C for 108 h. HR-TEM showed that a ~1 nm interfacial layer at the Ti-TiO_x/ Ga_2O_3 boundary is present in all samples treated with RIE (Fig 2.26). This layer does not appear in sample without RIE treatment, instead, the layers are partially lattice matched. They observed a direct correlation between the presence of this ~1 nm layer and the improvement of the aging stability of the interface [101].

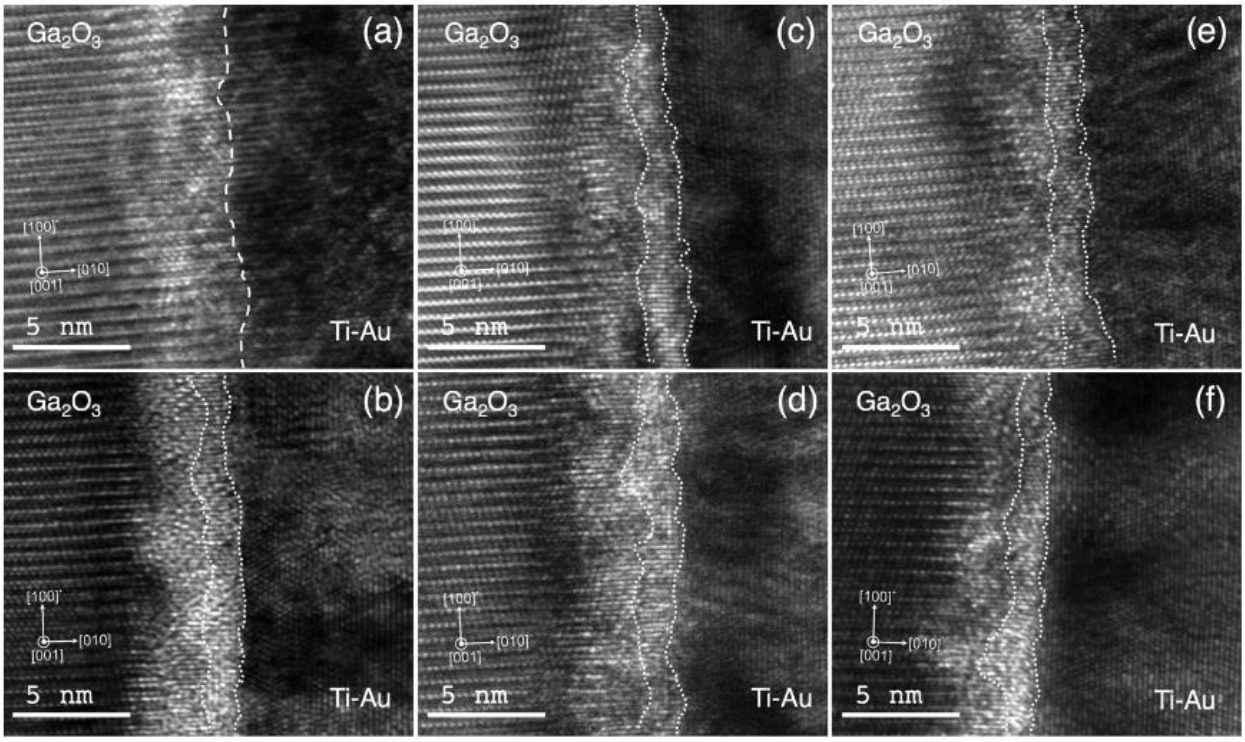

Figure 2.26 Cross-sectional HR-TEM images of (a) aged sample A, (b) unaged sample B, (c) unaged sample C, (d) aged sample C, (e) unaged sample D, and (f) aged sample D. The non-implanted sample A exhibits partial lattice-matching of the Ti-TiOx layer formed at the interface to the substrate, as seen in (a). Samples with Si-ion implant + RIE (samples C and D, in (c-f)) do not have this layer. Instead, the implanted samples have a thin (∼1 nm) interfacial layer [101].

Lyle et al. examined the chemical and electrical properties of Ti/(010) β-Ga_2O_3 and Ti/(001) β-Ga_2O_3 interfaces as a function of the annealing temperature. The contacts made of Ti (5 nm) were deposited using electron beam evaporation, and in situ XPS was performed for contacts under the as-deposited up to 670 °C annealing conditions. From the XPS analysis, Ti oxidation was stronger on the (001) β-Ga_2O_3 surface than the (010) β-Ga_2O_3 substrate surface with increasing annealing temperature. This is shown in (Fig. 2.27), the fits correspond to different Ti 2p oxidations states, which Leyle et al attribute to the formation of Ohmic contact. J-V

characteristics on the as deposited Ti/Au samples was used to correlate the XPS measurements to the Schottky diode properties. Schottky barrier heights of 0.64 eV and 0.49 eV were obtained for the (010) and (001), respectively. The lowest barrier height was obtained after annealing at 350 °C for 10 min, which is close to the temperature range of 400-500 °C commonly employed [102].

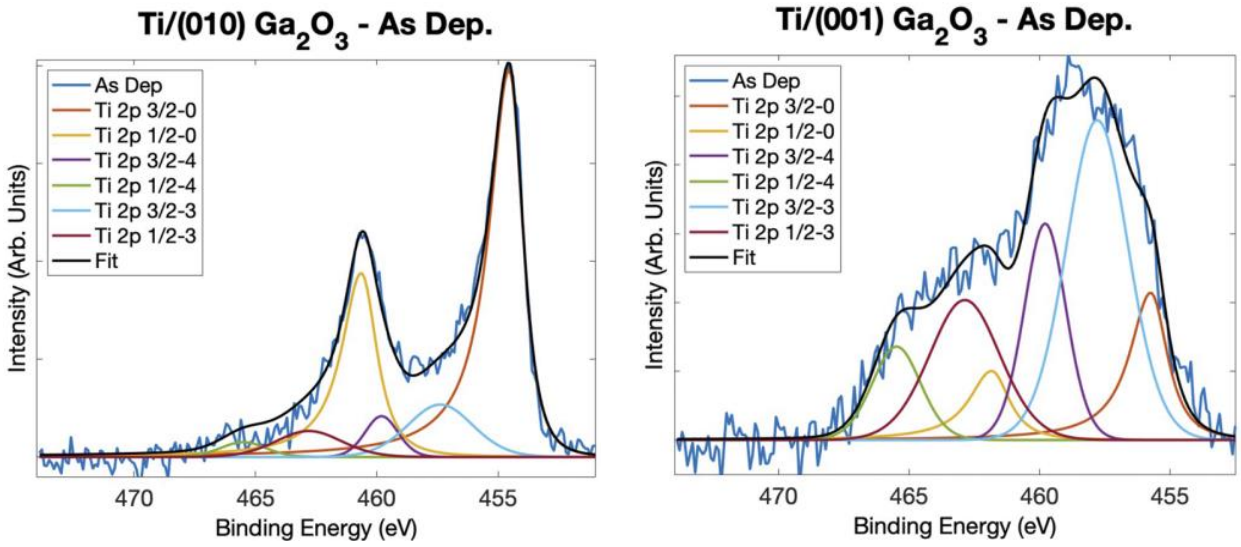

Figure 2.27 (a) XPS high-resolution scans of the Ti 2p peaks demonstrating fundamentally different bonding for (a) Ti/(010) β-Ga_2O_3 and (b) Ti/(001) β-Ga_2O_3 with 5 nm of Ti [102].

So far, the studies presented have only focused on (010) and (001) β-Ga_2O_3 surfaces. Kim et al. conducted a study on Ohmic contact formation as a function of the annealing temperature and three crystallographic orientations, including (001), (010), and ($2\bar{0}1$) Ga_2O_3 planes. The contacts were Ti (20 nm)/Au (80 nm), deposited by e-beam evaporation. Annealing for 1 min at 400 °C in N_2 ambient yield Ohmic contact behavior on the (001) and ($2\bar{0}1$) surfaces, but not on the (010) surface (Fig. 2.28). This was attributed to the discrepancies in the density of the dangling bond (calculated) among the three crystallographic orientations, (001) (2.69×10^{15} cm^{-2}), ($2\bar{0}1$) (2.68×10^{15} cm^{-2}), and (010)(1.70×10^{15} cm^{-2}). The lowest specific resistivity was

observed in (001) β- Ga_2O_3 of ~$5x10^{-4}$ Ωcm^2. All contacts degraded after annealing at 500 °C [103]. These studies suggest that ($2\bar{0}1$) β-Ga_2O_3 orientation is perfect for the investigation ohmic, as it will be shown in future sections.

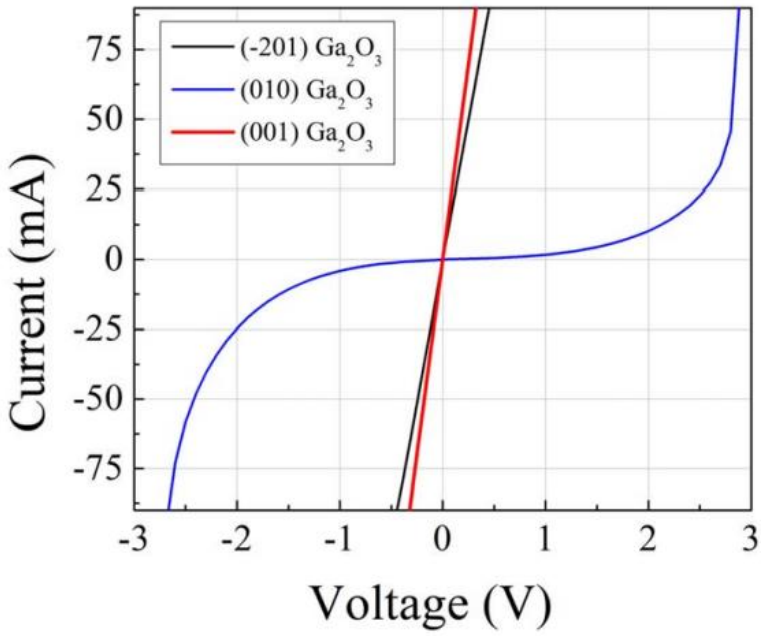

Figure 2.28 I-V curves between metal pads with 2 μm spacing of 400 °C annealed Ti/Au contact on Ga_2O_3 substrates with various crystal orientations [103].

Ion implantation has been explored to achieve highly doped contact regions for low-resistance Ohmic electrodes. Sasaki et al. developed a donor doping technique for (010) β-Ga_2O_3 via Si-ion implantation, to control the electron concentration at contact surface. The contacts were deposited A high electrical activation efficiency above 60% was obtained after annealing in nitrogen gas at temperatures ranging from 900 - 1000 °C. The surfaces with Si^+ concentrations of $5x10^{19}$ cm^{-3} showed the lowest specific contact resistivity of $4.6x10^{-6}$ Ωcm^2.

Bhattacharya et al. demonstrated the first metalorganic vapor deposition phase epitaxy-regrown (MOVPE) ohmic contacts on Fe-doped (010) β-Ga_2O_3 metal semiconductor field effect

transistor (MESFET). A trench of 10-20 nm was etched using SF_6/Ar RIE, followed by a 500 nm thick channel of heavily Si-doped β-Ga_2O_3 (1.7×10^{17} cm^{-3}) on the contact region. The structure of the Ohmic metal stack was Ti/Au/Ni (20 nm/100 nm/30 nm), it was annealed at 470 °C in N_2 ambient for 1.5 min. The specific contact resistivity was $8.3x10^{-7}$ Ωcm^2. This is the lowest specific contact resistivity on β-Ga_2O_3 reported thus far [104].

2.4.2 Conductive oxides

As mentioned above, ITO is also utilized as an alternative to form Ohmic contact to β-Ga_2O_3. Being a transparent conductive oxide, it is expected to be more thermally stable than conventional Ti/Au contacts. This assumption was confirmed by studies performed by Oshima et al. The group studied ITO/Pt contacts in contrast to Ti/Pt contacts deposited on unintentionally (UID) doped (010) β-Ga_2O_3 under different in the annealing conditions. ITO/Pt contacts demonstrate good stability and Ohmic behavior at temperatures up to 1000 °C, while Ti/Pt contacts degraded in temperatures higher than 450 °C [105].

Another study by Carey et al. showed that ITO interlayers between Ga_2O_3 and Ti/Au metallization produces Ohmic contacts after annealing in the range of 500-600 °C. Layer without ITO did not produce Ohmic contacts at similar temperatures. The specific contact resistivity of $6.3x10^{-5}$ Ωcm^2 was obtained after annealing for 30 s at 600 °C in N_2 ambient [106].

2.4.3 Other metals

In addition to the conventionally utilized Ti/Au and ITO Ohmic contact structures, alternative metals have undergone investigation for their application on β-Ga_2O_3 substrates. Mg/Au contacts on β-Ga_2O_3 were examined by Shi et al. The contacts were prepared by e-beam evaporation annealed at 300, 400, 500, and 600 °C. The lowest specific contact resistivity was in the order of 10^{-5} Ωcm^2 after annealing at 600 °C for 2 min in Ar [107].

Yao et al. did a systematic study of a total of nine metals, including Ti, In, Ag, Sn, W, Mo, Sc, Zn, and Zr on n-type single crystal β-Ga_2O_3 substrates as a function of the annealing temperature up to 800C. They studied the electrical behavior and morphology of the contacts at each annealing temperature. From the selected metals only Ti, and In formed Ohmic contacts as observed in earlier studies. Ag, Sn, and Zr showed a pseudo-ohmic behavior and their morphology presented a major issue. SEM imaging showed that the later contacts become rough after annealing at temperatures higher than 400 °C, presenting melted and resolidified phases. The metal work function of the selected metals ranged from 3.5-4.6 eV, however only Ti and In displayed Ohmic behavior. Yao et al concluded that the metal work function is not a dominant factor when forming Ohmic contacts to β-Ga_2O_3, and that limited interfacial reactions play a more significant role. In the case of Ti contacts, the possible intermetallic phases are Ti_3Ga, Ti_2Ga, Ti_5Ga_3, Ti_5Ga_4, TiGa, Ti_2Ga_3, Ti_3Ga_5, $TiGa_2$, and $TiGa_3$. A TEM micrograph is shown in Fig 2.29, the EDX lines after annealing at 400 °C indicate that a diffusion of the layers through the metal-semiconductor interphase occurs [99].

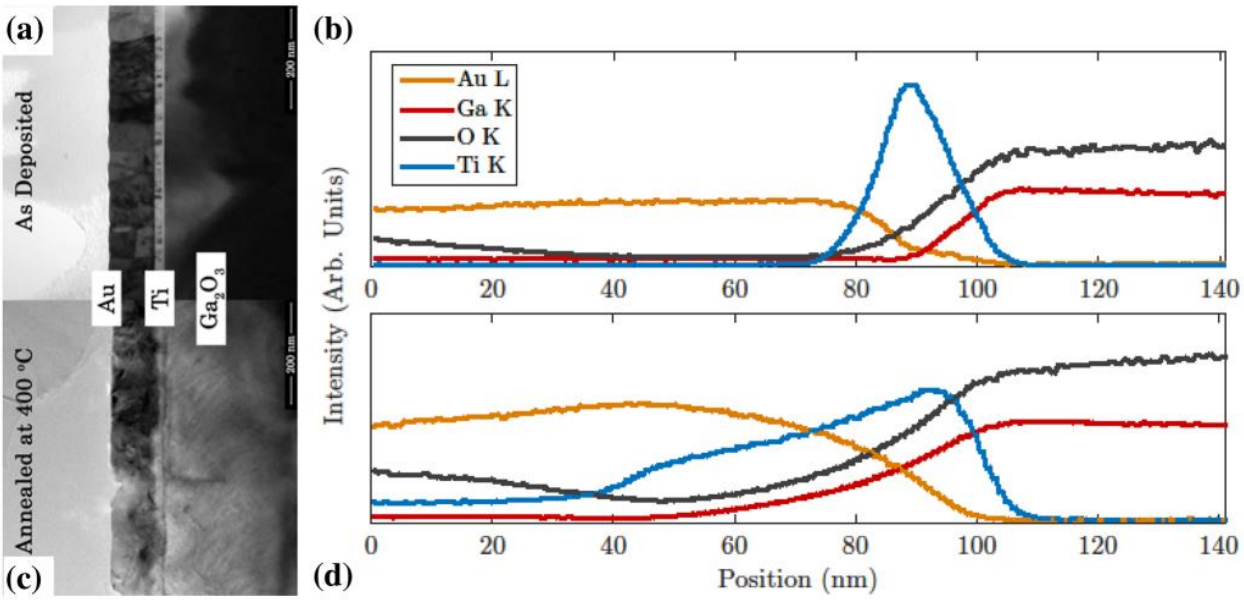

Figure 2.29 (a, c) Cross-section TEM micrographs and (b, d) EDX line profiles of Ti/Au contact on Ga_2O_3 as deposited and after annealing at 400 °C, as indicated [99].

2.5 Schottky Contact to Ga_2O_3

For Schottky contact formation, a large barrier height is required. Therefore, metals with higher work function have been utilized, including Ni [108–111], W [112], Cu [113], Ti (unannealed) [102,108], Pd [108,109,114], Au[94,115], Ag [116], Pt [117,118] , and Mo [108,109]; oxides contacts such as ITO [119,120], PtO_x [116,121,122], RuO_x [116], AuO_x [116,121], AgO_x [116,121] , IrO_x [116,121], PdO_x [116,121], and SnO_x [123]; and nitrides such as TiN [118] and graphite [124]. Figure 2.30 shows the calculated Schottky barrier heights for various metal work functions fabricated on different substrate orientations of β-Ga_2O_3. Research conducted by Li et al. [85] on the inherent reverse mechanism of Ni-based Schottky barrier diodes indicates the potential to approach the intrinsic breakdown electric field (6 MV/cm) in β-Ga_2O_3 SBDs, provided that a sufficiently high barrier height (approximately 2.2 to 3 eV) is attained.

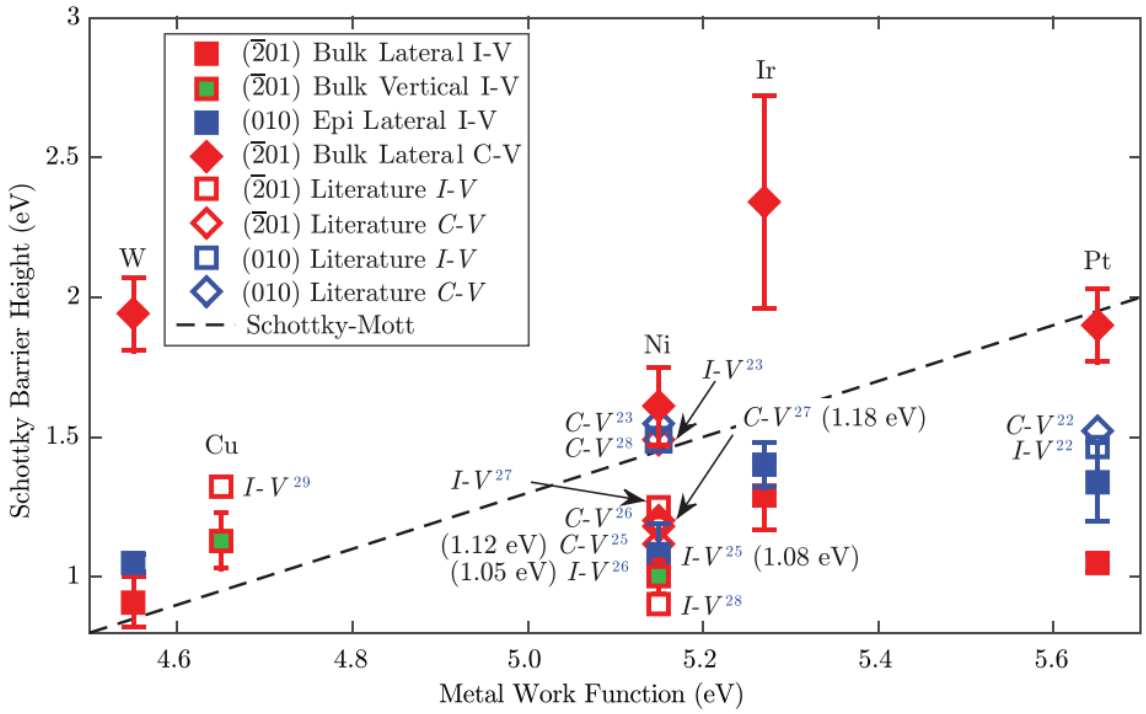

Figure 2.30 Calculated Schottky barrier heights compared to the metal work function for Schottky diodes on (010) bulk and (010) epitaxial β-Ga_2O_3. The Schottky–Mott predicted line is determined based on the Schottky–Mott relation equation (1.4) [125].

2.6 Alloys to Ga_2O_3

Boron oxide (B_2O_3) and lutetium oxide (Lu_2O_3) are two materials of interest due to their potential in alloying with gallium oxide (Ga_2O_3) for various applications, particularly in optoelectronics. This section explores the characterization and properties of Ga_2O_3 films co-sputtered with B_2O_3 and Lu_2O_3, focusing on XRD, EDS, UV-Vis spectroscopy, and optical bandgap measurements.

B_2O_3. Li et al. investigated the properties of high- and low-pressure phases (Fig. 2.31) of crystalline boron oxide (B_2O_3) using first-principle calculations based on a local-density approximation (LDA) [126]**.** Both phases are identified as insulators with wide LDA band gaps: 6.20 eV for B2O3-I (low pressure) and 8.85 eV for B_2O_3-II (high pressure). The investigation extends to the total density of states, which are further broken down into atomic and orbital components. Bond strength and charge transfers in these crystals are explored through overlap populations and Mulliken effective charges, revealing that B_2O_3-II exhibits greater ionic character compared to B_2O_3-I. Additionally, the study concludes that the planar sp^2 bonding in B_2O_3-I is stronger than the tetrahedral sp^3 bonding in B_2O_3-II. Furthermore, optical properties such as conductivities, dielectric functions, and energy-loss functions are analyzed using wave functions across numerous k points in the Brillouin zone. The calculated static dielectric constants for B_2O_3-I and B_2O_3-II are found to be 2.32 and 2.35, respectively, indicating similar optical spectra with one notable difference. B_2O_3-II displays significant optical anisotropy, while B_2O_3-I exhibits greater optical isotropy.

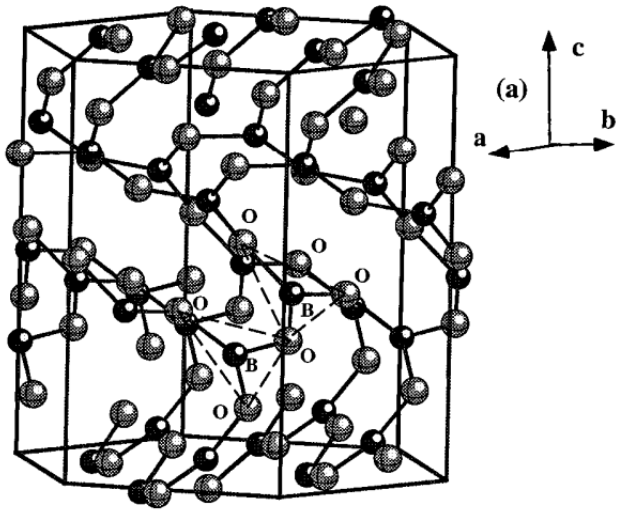

Figure 2.31 Crystal structure of B_2O_3-I (low pressure) shows a hexagonal unit cell [126].

Lu_2O_3. Binary lutetium oxides, Lu_2O_3 stands out as the stable solid phase containing closed-shell trivalent Lu ions. This compound demonstrates a robust insulating behavior due to its wide band gap of approximately 5.5-5.9 eV [126-128]. Kaminaga et al. [131] studied LuO and L_2O_3 epitaxial films deposited by pulse laser deposition method. The films were grown on CaF_2 (001) substrate at a deposition temperature of 300 °C in Ar/O_2 (1%O_2) ambient. The film thickness for Lu_2O_3 layer was estimated to be 40 nm, and was obtained via X-ray reflectivity measurements. In the current study Lu_2O_3 deposited on CaF_2 (001) was used a reference sample, nevertheless, the obtained data serve as background for this dissertation. Figure 2.32 (a) shows XRD results for LuO and Lu_2O_3 films deposited on CaF_2 (001). Lu_2O_3 in this experiment was caused by surface oxidation of LuO layer generating (001) Lu_2O_3 peaks due to the introduction of oxygen vacancies in the film. Absorption spectra of both Lu and Lu_2O_3 films is shown in Fig. 2.32 (b), where Lu_2O_3 shows a sharp absorption edge. Pictures of both films included inset of Fig 2.32 (b). Lu_2O_3 film shows as with a bluish transparent appearance in contrast to LuO which has a dark-brown coloration due to absorption in the visible range.

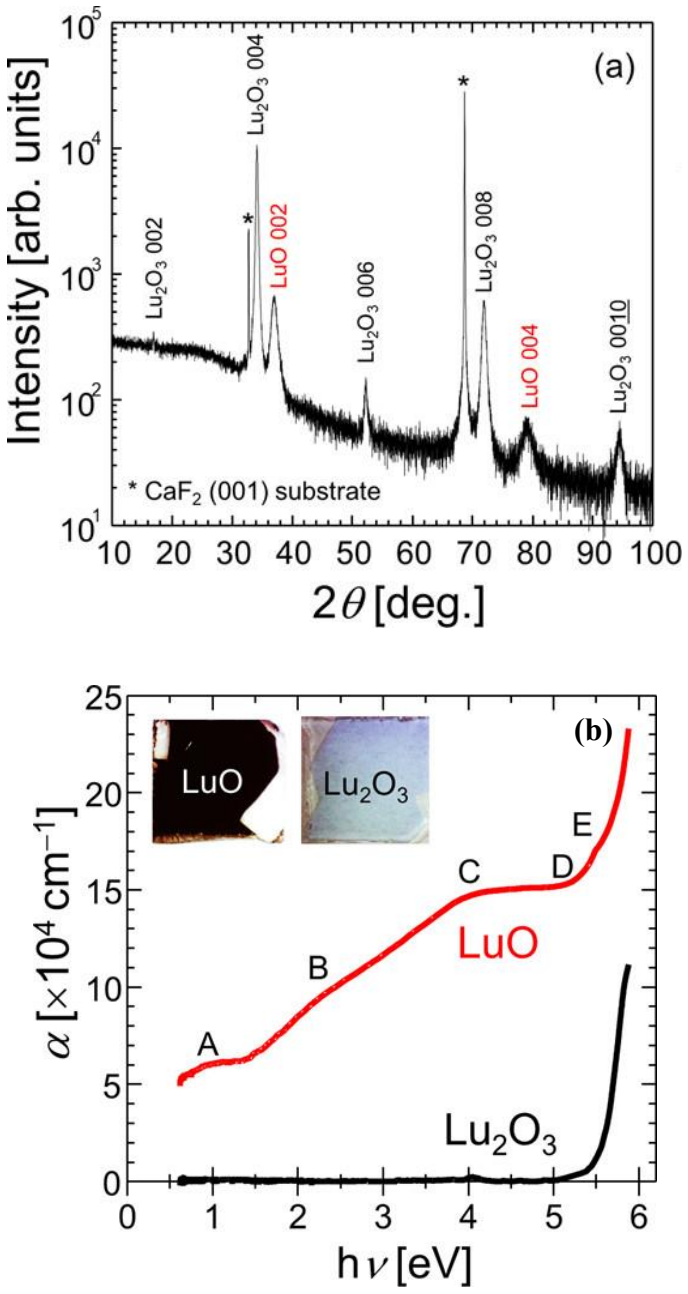

Figure 2.32 (a) XRD and (b) absorbance of Lu and Lu_2O_3 thin films deposited on CaF_2 [131].

Another study by Mandal et al. focuses on Lu_2O_3, Ga_2O_3, and Eu_2O_3 co-sputtering on soda lime glass substrates by rf sputtering deposition [132]. Europium oxide has strong bonding properties, for this reason it was used as a binder to co-sputter Lu_2O_3 and Ga_2O_3.The fabricated films were characterized by XRD, UV-Vis, FESEM, and ED-XRF. The films were deposited in

Ar flow of 35 sccm and base pressure of $7x10^{-6}$ mbar. A film thickness of 433 nm, obtained from ED-XRF, was achieved showing good uniformity, crystal structure and transparency. Figure 2.33 microstructural data collected with FESEM in the form of a micrograph, which indicates the appearance of grains. The average grain size was reported to be 100 nm. The reported transmittance in the visible region was about 83%. The group used Tauc plot method to extract a bandgap of 3.96 eV for the oxide films. Mandal et al reported on the film composition via EDS, identify the three individual elements: 12 at% Lu, 70 at% Eu and 18 at% Ga.

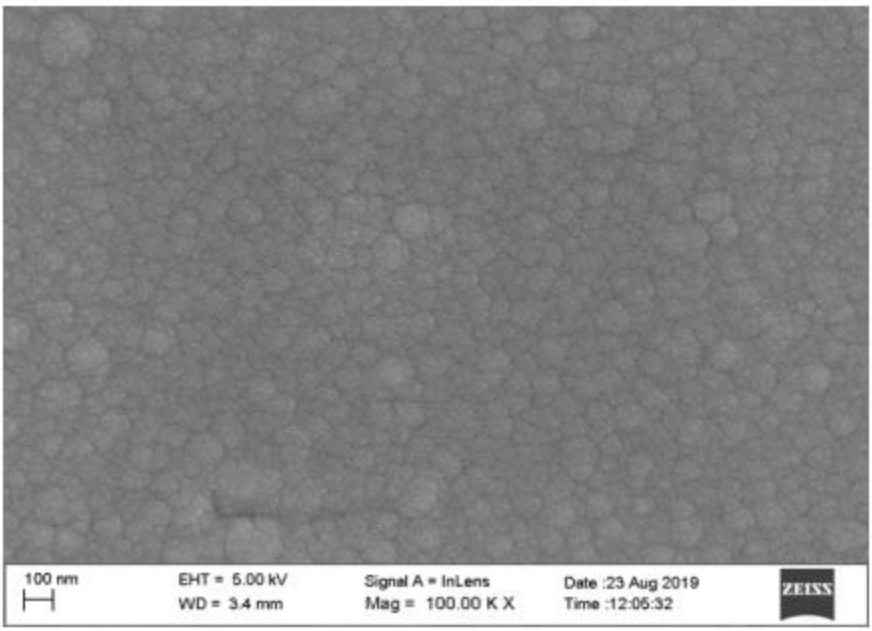

Figure 2.33 FESEM micrograph of $Eu_{1.4}Ga_{.36}Lu_{0.24}O_3$ [132].

2.7 Ga_2O_3-Based Schottky Diodes

The unavailability of p-type doping in Ga_2O_3 have pushed research and development to focus shift on unipolar devices. One of the simplest vertical devices is a Schottky barrier diode (SBD), which consist of two terminals consisting of a Schottky contact directly on the semiconductor substrate, and an ohmic contact deposited on a heavily doped metal-semiconductor interface as illustrated by Fig. 2.34. This is a rectifying device, meaning that in the forward bias the barrier to current flow is reduced and the electrons into the semiconductor via thermionic emission or thermionic field emission. Conversely, in the reverse bias, the barrier to current flow is increased and electron flow is decreased. If the reverse voltage is further increased the device reaches electrical breakdown. Since Ga_2O_3 is an intrinsically n-type material, Schottky diode are easily formed. However, as presented in section 2.4, Ohmic contacts and their mechanism of formation is still under continual extensive research.

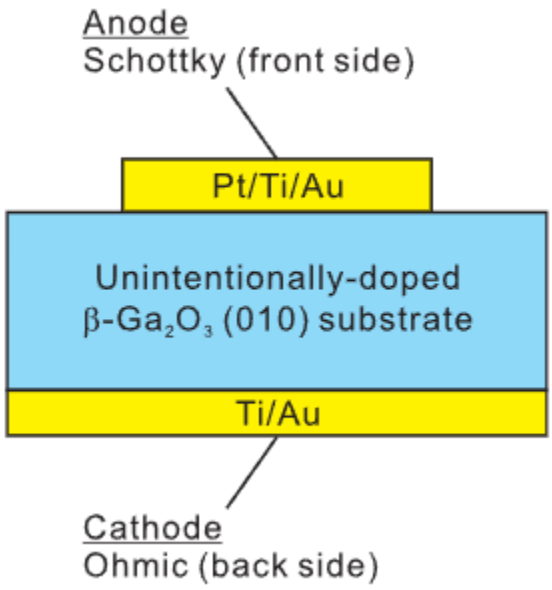

Figure 2.34 Cross-sectional schematic illustration of Ga_2O_3 SBD [133].

Higashiwaki et al. [133] demonstrated a simple SBD on unintentionally n-doped single-crystal Ga_2O_3 shown in Fig. 2.35. The crystal was grown by floating zone (FZ) method, the Schottky and Ohmic contacts structure were made of Pt/Ti/Au and Ti/Au, respectively. The device showed decent characteristics: with ideality factors close to unity of 1.04-1.06, a Schottky barrier height of 1.3-1.5 eV, and on-resistance (R_{on}) of 4.30 and 7.85 $m\Omega cm^2$.

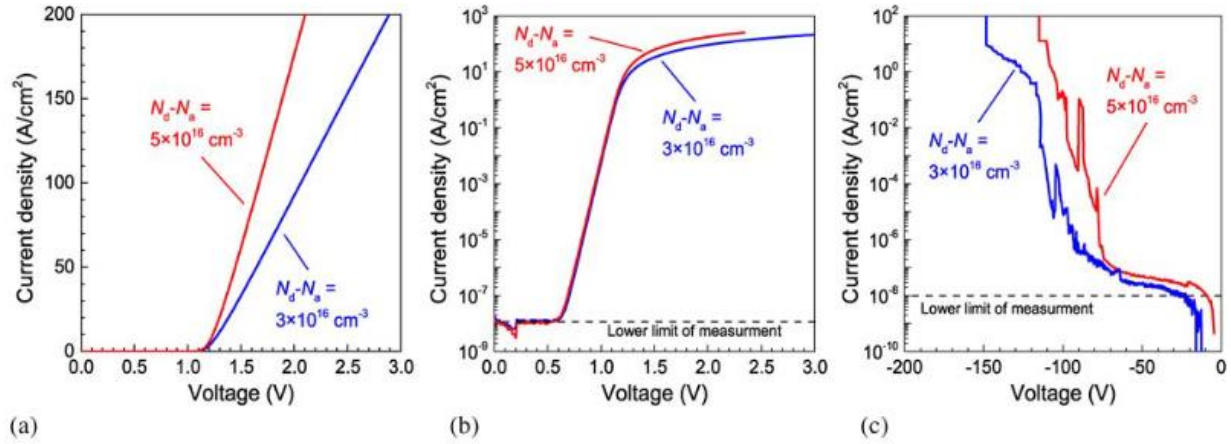

Figure 2.35 (a, b) Forward and (c) reverse J-V characteristics of Ga_2O_3 SBDs [133].

More sophisticated Ga_2O_3 SBD have been fabricated by introducing a field plate, N-implanted guard ring (GR), and more recently a floating metal ring (FMR) terminations to minimize the electric field concentration at the edges of the metal contacts and increase breakdown voltage (V_{br}) [134,135]. A summary of SBD structures and references is presented in Table 2.2.

Table 2.2 Summary of SBDs [136].

SBD Structure	Dopant	Doping Con. $\times 10^{16}$ (cm^{-3})	Thickness (μm)	Ideality factor	R_{on} (mΩ-cm^2)	V_{br} (V)	BFOM (MW-cm^{-2})	E_c (MV-cm^{-2})
Vertical	Sn	4	1.4		2	100		0.71
Vertical	Sn	6	1.2	1.13		125		1.04
Vertical	UID			1.04–1.06	7.85–4.30	115 and 150		
Vertical	Sn	$< 10^3$	12			> 1000		0.83
Vertical	Si		7	1.02	3.0–2.4	500		
Lateral	UID			1.4	7.4			
Vertical	UID			1.03	29.4–2.5	120		> 2.1
Vertical	UID		1.2			24		0.2
Vertical	Si			1.03		> 200		
field-plated, Vertical	Si			1.03	5.1	1076		5.1
Vertical	Si	2	10	1.08 − 1.28	6	920–1016	154.07	
Vertical	UID			1.08		50		
Vertical	UID			1.1	12.5	> 40		
Vertical Trench	Si	6	7	1.1	2.9	240		
Vertical	UID		2	3.38	2.58	210	17.1	
Vertical	Si	0.402	10	1.07,	25–1.6	~1600	102.4	1.6
Field-Plated Lateral	UID	290	0.6–0.65	1.25	24.3	3000	> 370	
edge–terminated, vertical	Si	1.33	10	1.02	0.58	650	26.5	
Edge–terminated, vertical	Si	0.21	20	1.1	250	2300	21.2	1.15
bevel-field-plated, Vertical	UID		2		3.9	190		4.2
Trench	UID	2	10	1.08	15	1230		
Trench	UID	5–6	7		3.09	300		
Vertical edge termination with SiNx	Si	5–2	7	1.27	1.35	> 100		
Vertical	UID				2.9	> 200		
Vertical Trench	Si	0.1–0.2	10	1.07		1500		
Lateral	Sn	30	8		34.2	1700		1.6

Table 2.2 Continuation.

SBD Structure	Dopant	Doping Con. $\times 10^{16}$ (cm^{-3})	Thickness (μm)	Ideality factor	R_{on} (mΩ-cm^2)	V_{br} (V)	BFOM (MW-cm^{-2})	E_c (MV-cm^{-2})
Vertical	Si	2	7	1.03	0.59	466	308	
Filed Plate and Non-Filed Plate, Vertical	Si	1	10	1		1050		
Vertical Trench with FP	UID	1.47	10	1.08	9.1	2330	780	
Vertical	Si		20	1.03	18.2	1711	159	
vertical GR/FP SBD	Si		7.4	1.04	4.7	1430		
vertical SABFP	UID		8	1.2	2	1100	600	3.5
Vertical	UID			1.02				
Vertical FP	Si	0.436	8	1.08	22.2	760	26	
Vertical	UID	3	6		3	940	295	
Vertical	UID	1.5	10	1.05	5.1	1550	470	
Vertical	Si	0.612	8	1.06	240	1900		
Vertical	Si	2.80	10	1.02 ± 0.02	5	730	140	
Vertical ion implanted ET	Sn	1.50	10	1.11	5.4	1500		
Vertical with CF4 Plasma Surface Treatment	Si	3.5	8		4.6	470		
Vertical with BFPT	UID	30	8		2.3	1050		
Vertical Trench with FP	UID	1.25	10	1.3	8.8	2890	950	
Vertical	UID	1.6	7	1.02	8.47	472		

3. Processing Techniques

In semiconductor manufacturing, various processing techniques are utilized to create electronic devices. These include wafer cleaning to remove contaminants, photolithography for pattern transfer, semiconductor growth methods for growing bulk crystals and thin films, doping for altering electrical properties, annealing to enhance crystalline structure, and plasma etching for precise material removal. Each technique plays a vital role in producing high-quality semiconductor components with specific functionalities and performance attributes. This section details some of the most important processing techniques used for semiconductor materials that were employed in this dissertation.

3.1 Cleaning Methods

Two substrates were used in this dissertation, mainly c-plane Al_2O_3 and Ga_2O_3 native substrate. This section summarizes the cleaning methods used for both substrate surfaces:

The surfaces of c-plane double-sided polished sapphire were first prepared by degrease-cleaning in boiling in acetone¸ alcohol, rinsed in deionized (DI) water at 110 °C for 10 min each. The cleaning was followed by dipping the substrate in buffered HF acid for 10 minutes to remove any oxide layer formed, rinsed in DI water, and finally dried with N_2 prior mounting on a heater substrate.

Prior to the deposition of Ohmic contacts, the Ga_2O_3 substrates were degreased by sequential sonication in acetone (10 min), isopropanol (10 min), DI water (10 min).The substrates were then soak in hydrochloric acid (HCl 10%), rinse in DI water, soak in boiling H_2O_2 at 85 °C for 5 min, rinse with DI water, and finally blow dried. This cleaning procedure was found to improve Ohmic contact conductivity [137].

3.2 Photolithography

Photolithography is a technique used in microelectronic technology to selectively pattern a thin film over a substrate, to protect the selected areas during etching, deposition, or implantation procedures. Usually, an ultraviolet (UV) light source is used to transfer the pattern from a photomask to a light-sensitive photoresist. Today, pattern transfer is exclusively done by photolithography in the IC industry. A series of successive patters can lead to complex multilayer structures in a semiconductor device [138]. The following sections detail the process of lithography used for this investigation and the different masks utilized to fabricate metal contacts to β-Ga_2O_3.

3.2.1 Photolithography Process

i. Coating

After proper cleaning of the wafer, with methods discussed in section 3.1, the first step in the photolithography process is the application of a light-sensitive organic material called photoresist. The wafer is placed on a Chemat technology spin coater KW-4A (9036 Winnetka Ave. Northridge, CA 91324 USA). The instrument is display in Fig. 3.1 (a). Here, the substrate is held by a vacuum chuck as illustrated by the diagram shown in Fig. 3.1 (b). The photoresist is dispensed on the wafer and then it is spun at a rate of 1,500 to 6,000 rpm, depending on the desired final thickness. Typical photoresist thickness before soft baking ranges from 1 μm to 6 μm. Spinning times range from 10 s to 60 s. At these speeds, centrifugal force causes the solution to flow to the edges, where it builds up until expelled when surface tension is exceeded. The resulting polymer thickness, T, is a function of spin speed, solution concentration, and molecular weight (measured by intrinsic viscosity) [138]. Each photoresist has thickness to spin speed data in the form a spin curve for the user to select the desired final thickness (Fig. 3.1 (c)).

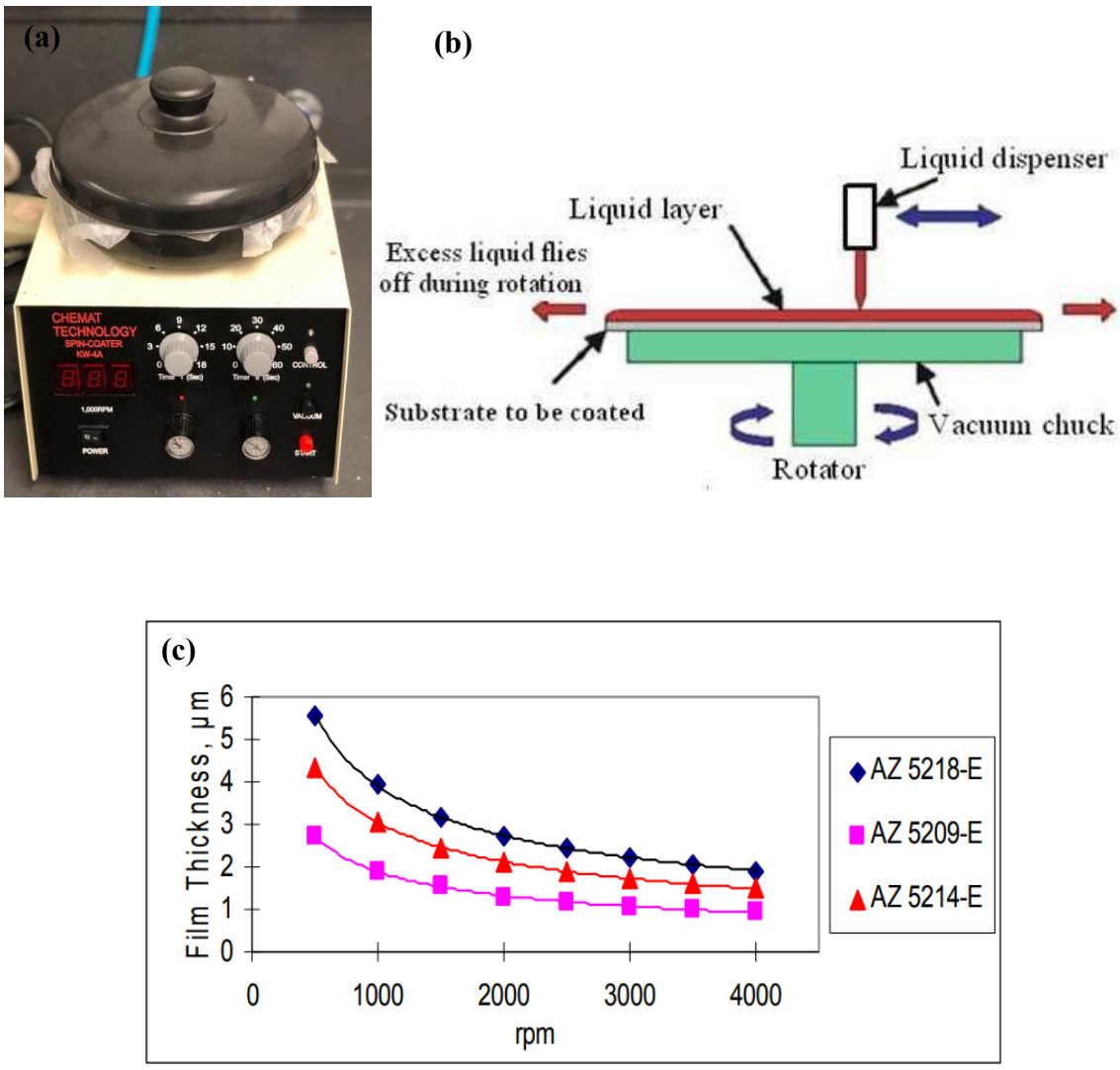

Figure 3.1 (a) Chemat Technology spin coater KW-4A, (b) schematic of spin coating process, (c) AZ 5200-E series photoresist spin speed curves [140-141].

ii. Soft bake process

After coating the wafer, it is necessary to heat the sample before exposure is done. The wafer is placed on a VWR ceramic top hotplate stirrer (Cat. No. 97042-642), as shown in Fig. 3.2, and heated up to temperatures ranging from 95-115 °C for 1-3 min. This procedure guarantees consistent photolithography and adhesion performance, aiding in the removal of excess solvent from the resist to strengthen the remaining film.

Figure 3.2 VWR ceramic top hotplate stirrer.

iii. Film rehydration

Films thicker than 4 μm may require a rehydration hold between soft bake and exposure. Hold times are typically 30 - 60 min at relative humidity of 40 - 45%. This step is required when wet etching or plating.

iv. Exposure

The sample is then exposed with a Karl Suss MJB3 Mask aligner fitted with 200-Watt mercury short-arc lamp (365 nm - 405 nm exposure wavelengths) powered by a Mimir 505C optical energy controller as shown in Fig. 3.3. The Karl Suss MJB3 Contact Aligner system can perform precision mask-to-wafer 1:1 contact printing in hard contact mode, with an exposure resolution of 1.5 μm and an alignment resolution of 0.25 μm. Approximate exposure intensities are: 14.5 mW/cm^2 (141 W) at 365 nm, 25 mW/cm^2 (193 W) at 405 nm. It can accommodate exposure of irregularly shaped substrates and standard wafers from 1 mm to 3 inches wafers. Mask holder can fit masks up to 4 inches in diameter.

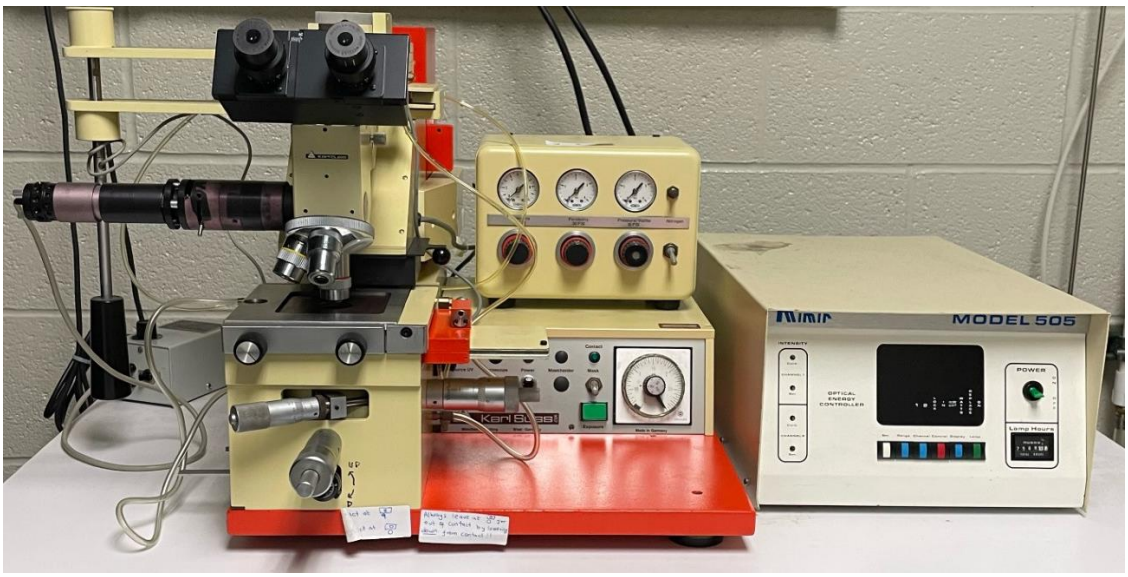

Figure 3.3 Karl Suss MJB3 Mask aligner with Mimir 505C energy controller.

When the photoresist film is exposed to UV radiation (E_0), the radiation-affected areas change its chemical resistance to the developer solution depending on the tone of the photosensitive material. There are two types of photoresists (Fig. 3.4):

Negative Photoresist

Negative resist is rendered un-dissolvable anywhere the deposited energy is > E_0.

Positive Photoresist

Positive resist is rendered dissolvable to developer anywhere the deposited energy is > E_0.

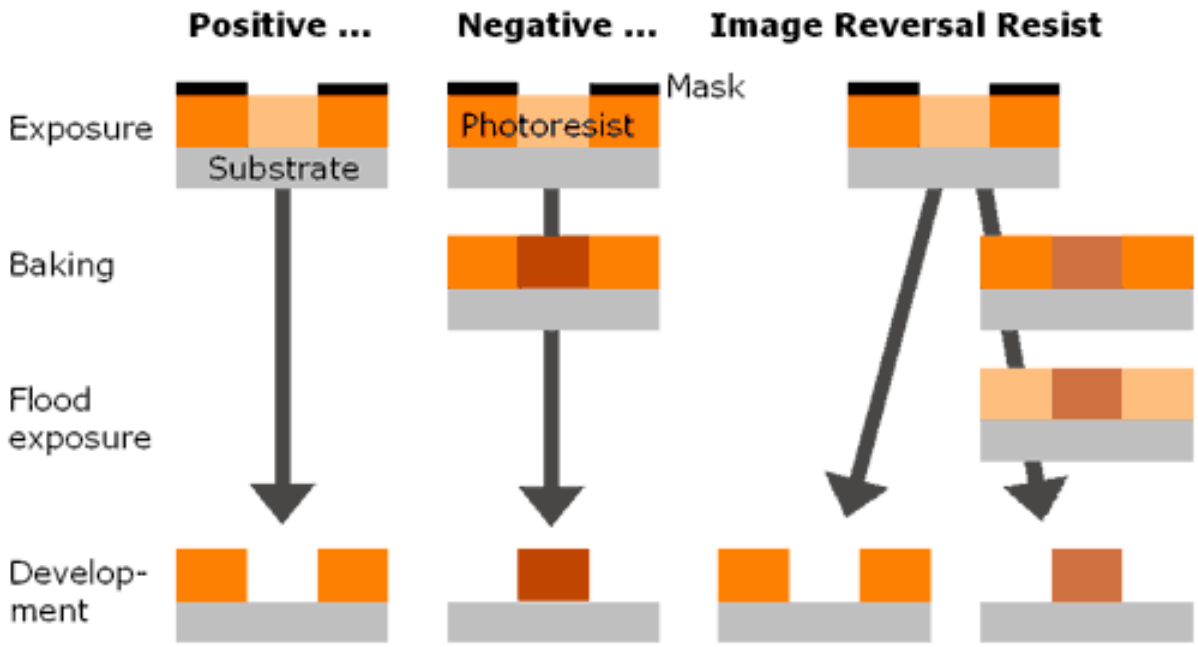

Figure 3.4 Negative photoresist, positive photoresist, and image reversal photoresist *[141]*.

v. Post expose bake

This step maximizes process latitudes and mitigates standing wave effects caused by monochromatic exposure. Temperatures range from 100-115 °C, for 1-3 min. Reversal bake (130 °C, for 1-3 min) can be done in this step to prepare the sample for image reversal.

vi. Image reversal

Another post-exposure treatment is known as flood exposure. This process is done without a mask, and it is used to reverse the effects of radiation on the photoresist films. The image reversal process can make a negative tone photoresist behave as a positive tone and vice versa.

vii. Developing

Development involves dissolving unpolymerized resist material, thereby converting the latent resist image created during exposure into a relief image. This image then serves as a mask for subsequent removal or deposition steps. Table 3.1 shows the photoresists used for this investigation and their appropriate developers.

viii. Hard bake

This step improves adhesion in wet etching processes and patten stability in dry etching processes. Temperatures from 100-110 °C to ensure minimal thermal distortion of the pattern.

Table 3.1 Photoresist and developers.

Photoresist	Tone	Developer	Comments
AZ nLOF 2070	Negative	300 MIF	/
AZ P4620	Positive	AZ 400K 1:4	/
AZ 5214 E	Positive with image reversal capability	AZ 400K 1:4	TLM, Schottky Contacts

3.2.2 Masks

As mentioned in above, a photomask is used to transfer a pattern onto the photoresist-coated wafer. The mask is made of a nearly optical flat glass (transparent to near UV) with an absorber pattern metal (e.g., an ~800 Å chromium layer). Masks referred as contact masks, usually make direct contact with the wafer. There are other masks referred as soft-contact masks, where a small separation (10-20 μm) is left between the mask and the substrate. Contact masks can be further categorized as positive or dark field, where the pattern is clear with the background

containing the absorber metal. Oppositely, a negative or bright field mask is a mask where the pattern is made from the absorber metal with a clear background [138]. Figure 3.5 depicts both types of masks.

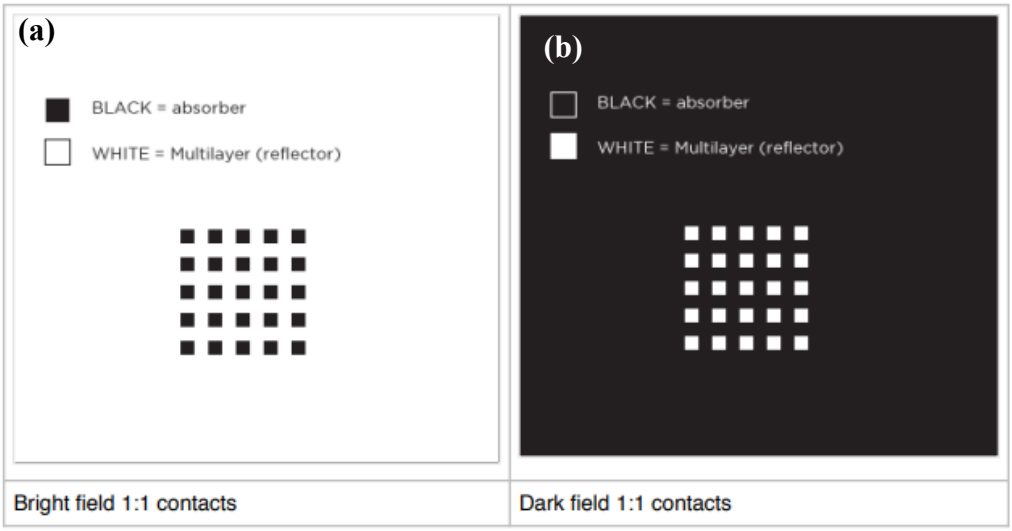

Figure 3.5 Bright field contact mask (a) and dark field contact mask (b). Black is absorber. White is multilayer *[142]*.

3.2.2.1 TLM Mask

The Transmission Line Measurement mask is a dark field mask with an array of 6 lines with 200 x 200 μm^2 squares of the reflective material, as shown in Fig. 3.6. The lines are spaced by increments of 7 μm till 14 μm, and then by increments of 10 μm till 74 μm (7, 14, 24, …,74 μm). A close view of the pattern is shown in Fig. 3.7. The TLM mask was used to fabricate all ohmic contacts and measure their contact resistivity. The TLM method is explained in more detail in section 4.5.1.

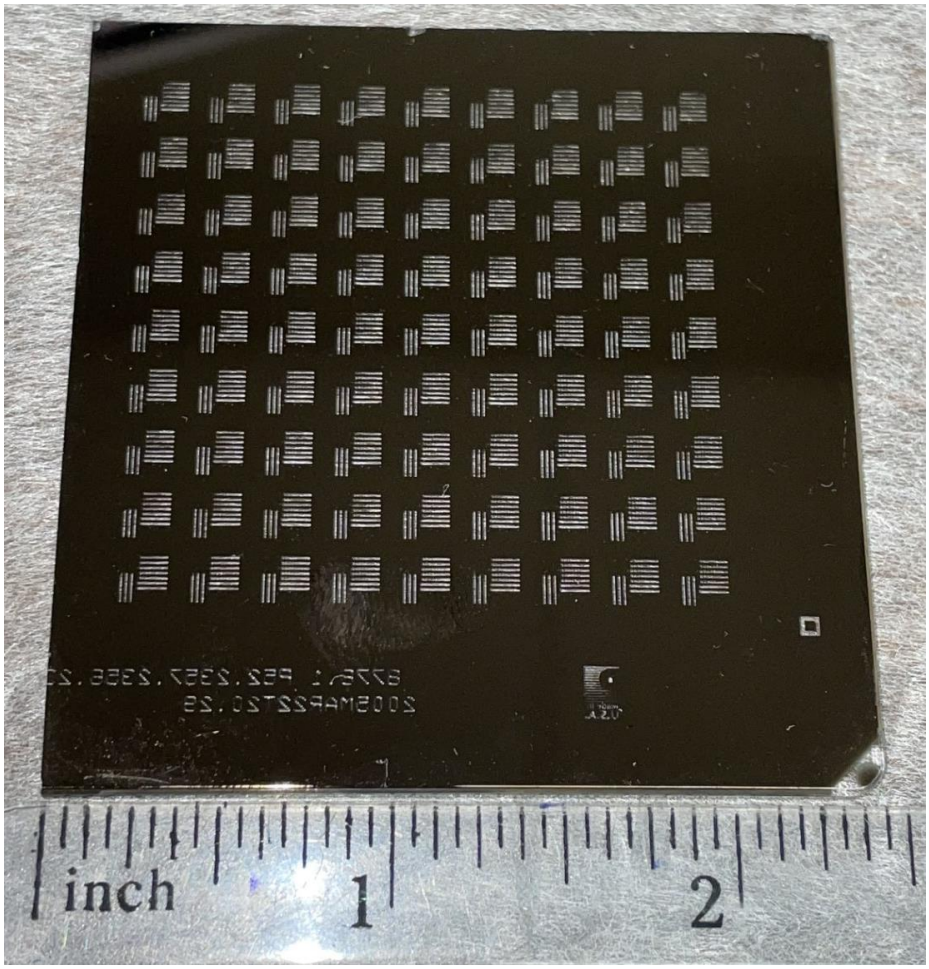

Figure 3.6 TLM 2.5-inch mask.

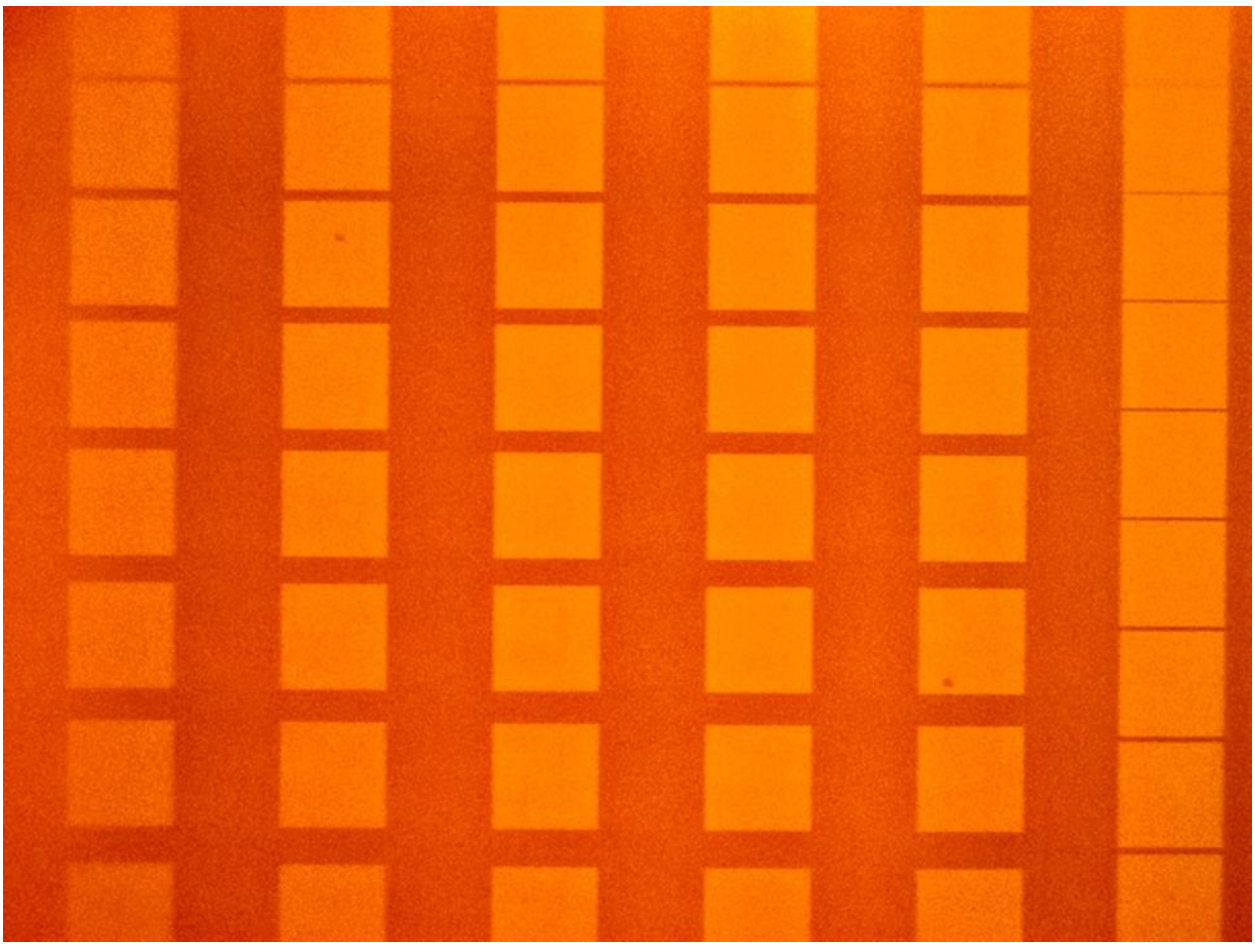

Figure 3.7 Transmission Line Measurement pattern, dimension of the contact is 200 μm^2.

3.2.2.2 Schottky Contact Mask

Schottky diode mask is a bright field mask, with an array of 10 x 10 circular patches with the absorber material, as shown in Fig. 3.8. A close-up of the 200 μm in diameter circles is shown in Fig. 3.6. This mask was mainly use for the fabrication of the Schottky metal contacts. Methods for the barrier height and ideality factor extraction are discussed in section 4.5.2.

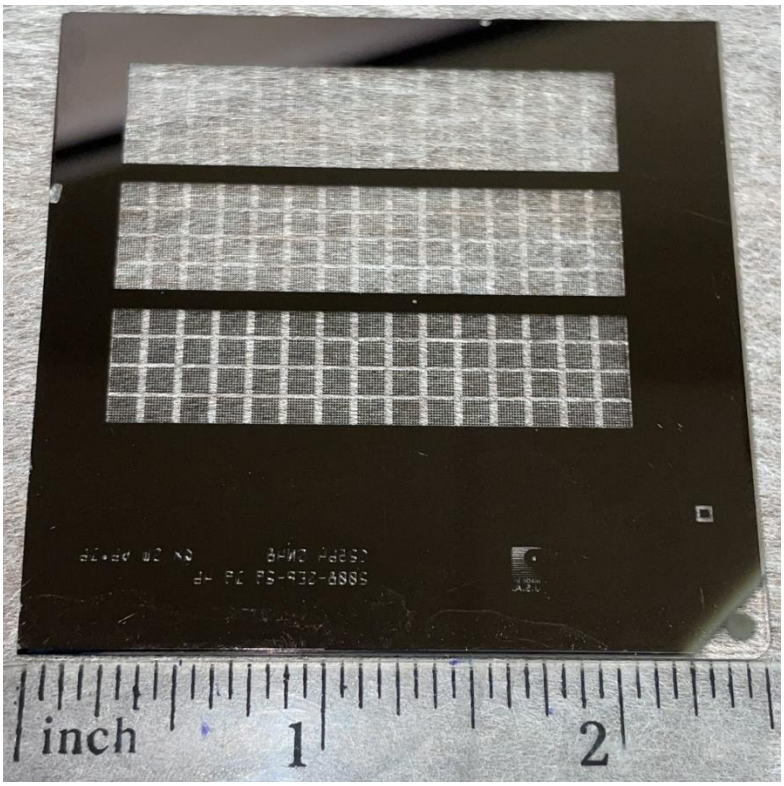

Figure 3.8 2.5-inch Schottky barrier diode contact mask.

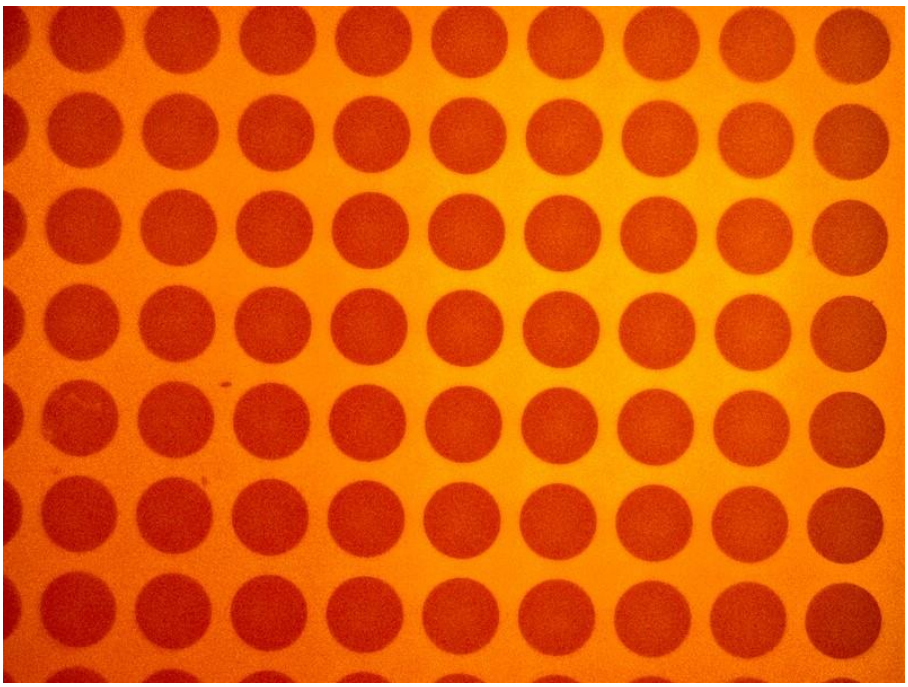

Figure 3.9 Schottky contact pattern, diameter of the circular patches is 200 μm.

3.3 Semiconductor Growth Methods

3.3.1 Bulk Crystal Methods

The process of creating a semiconductor wafer starts with the growth of a large, single crystal of the semiconductor material, known as a boule. Czochralski [143] or float-zone method [144], are methods commonly used, both of which involve the controlled growth of semiconductor crystal from a molten pool of high-purity semiconductor material. Growing β-Ga_2O_3 single crystals from bulk is a difficult and energy demanding task due its high melting point (~1800 °C) and strong tendency to form twining and cleaving [145–147]. Currently, undoped and doped β-Ga_2O_3 wafers of 25.5 mm to 50.8 mm in diameter (2" max) grown by edge-defined film-fed method are commercially available from Tamura Corp. and Namiki Precision Jewel Co. in Japan. The following sections provide details on some of the methods used for the growth of β-Ga_2O_3 from bulk.

3.3.1.1 Verneuil Growth

The Verneuil method was developed by Auguste Verneuil in 1902. The process starts with a fine powder (typically 1-20 μm in size) of the desired material. The powder is pushed with a hammer into an enclosed chamber where it is then carried through a muffle and exposed to an oxyhydrogen flame. The particles fuse and fall on the surface of a molten boule as shown in Fig. 3.10. The rate of crystal growth is dictated by the gas flow, the rate of powder feeding, and the rate at which the boule is lowered. The resulting boules have dimensions of only 3/8 inch in diameter and 1 inch in length, which renders this method unsuitable for meeting the demands of modern large-scale production. The first single crystal of β-Ga_2O_3 using the Verneuil method was grown in 1964 by Chase, measuring 1 cm in diameter and 2.5 cm in length [148].

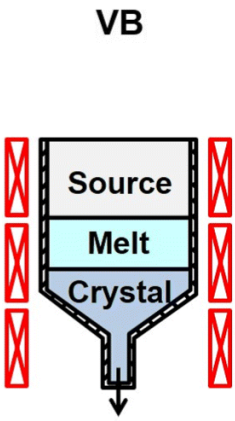

Figure 3.10 Simplified diagram of Verneuil process for synthesizing Ga_2O_3 [93].

3.3.1.2 Float Zone

The floating zone (FZ) method uses a moving a liquid zone between the feed material and a rod containing the seed. As the zone slowly moves along the feed material, a single crystal may be obtained. This method does not require a crucible, with facilitates the growth of congruent and incongruent materials. The melting zone is held by surface tension only, and collapsing of the

liquid is a major issue [149]. Figure 3.11 shows a schematic of floating zone single crystal growth process.

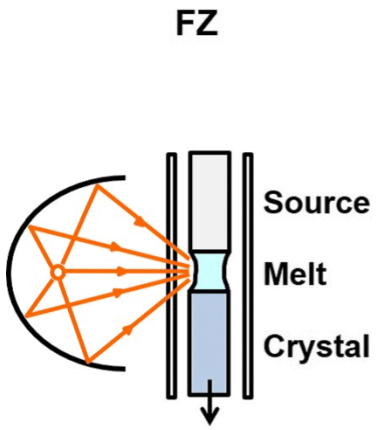

Figure 3.11 Schematic of float zone single crystal growth [93].

Ueda et al. reported the successful growth of β- Ga_2O_3 using the FZ method in 1997 [150]. The feed rods were prepared with Ga_2O_3 powder (4N), grounded with or without SnO_2 powder (4N) in a mortar and pressed at 280 MPa, then sintered in air at 1300 °C for 16 h. The crystal was grown at a rate of 15 mm/h in a mixture of N_2 and O_2 gas. The samples grown had dimensions of (3-5)×(5-10)×(~0.3) mm. Undoped samples grown in an O_2 environment had conductivity $\sigma < 10\text{-}9\ (\Omega\cdot cm)^{-1}$. Introduction of N_2 increased the conductivity σ to as high as 38 $(\Omega\cdot cm)^{-1}$ at a N_2/O_2 ratio of 4/6. Higher concentration of N_2 caused the Ga_2O_3 growth to become unstable. The Sn-doped sample had a conductivity of $\sigma = 0.96\ (\Omega\cdot cm)^{-1}$ [137].

Later in 2004, Víllora et al. [147] grew single crystal of β-Ga_2O_3 with 1 inch in diameter for three different crystallographic directions namely, ⟨100⟩, ⟨010⟩, and ⟨001⟩. The feed rods were prepared with 4N purity powder, cold press and subsequently annealed in air at 1450 °C for 10 h. The pulling rate was varied between 1 and 5 mm/h with a constant gas flow of 250 ml/min of O_2

and the same for N_2 gas. The crystals exhibited high transparency in the visible and near-UV spectra, along with electrical conductivity characterized by resistivity ranging from 0.08 to 0.11 Ωcm.

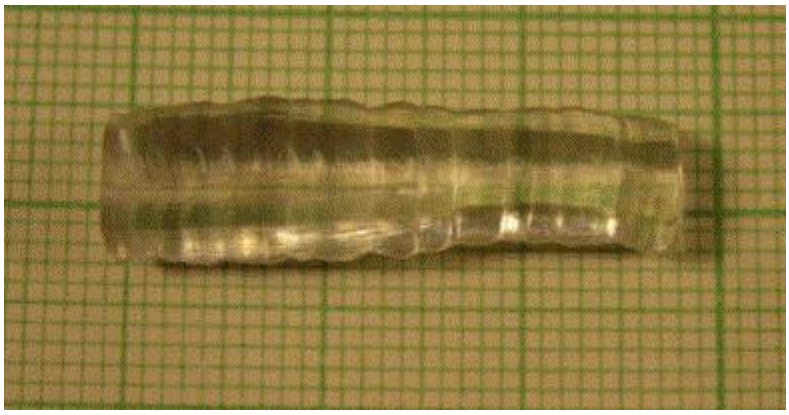

Figure 3.12 As-grown β-Ga_2O_3 single-crystal ingot by Zhang et al [89].

Zhang et al. grew 6 mm diameter and 20 mm length Ga_2O_3 single crystals along (010) by FZ method [89]. The ingot shown in Fig. 3.12 were prepared with (5N) β-Ga_2O_3 powder by cold isostatic press under 70 MPa. Similarly, the rods were sintered at 1500 °C for 10 h. The crystals were grown at a rate of 5 - 10 mm/h under dry air flow.

3.3.1.3 Czochralski Process

Czochralski method is attributed to Jan Czochralski, a Polish scientist who first developed this approach in 1915 while researching the crystallization rates of metals. In the Czochralski method (Cz), the material is put into a non-reactive cylindrical shaped crucible and melted by resistance or radio-frequency heaters, as depicted in Fig. 3.13. A seed crystal, maintained at a temperature lower than its melting point, is inserted from the top into the melt. This process creates a melt meniscus between the seed and the melt, which then solidifies as the seed is gradually lifted

and simultaneously rotated. The crystal growth rate and diameter are controlled by the heating power, pulling rate, and rotation rate of the seed crystal [151].

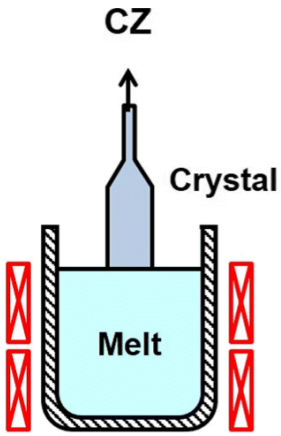

Figure 3.13 Schematic of the principle of the Czochralski method [93].

The first successful growth of single crystal β-Ga_2O_3 by the Czochralski method was reported by Tomm et al. in 2000 [143]. Some of the issues encountered by Tomm et al. were the high melting point of the material (~1800 °C) and the evaporation of Ga_2O_3. The high melting point of Ga_2O_3 requires an Iridium (Ir) crucible, however the crucible easily oxidizes in an oxygen-rich atmosphere forming a volatile IrO_2 product. Consequently, the Ir crucible should be kept in a O_2 deficient atmosphere. Ga_2O_3 is known to decompose into volatile GaO, Ga_2O, and Ga species in O_2 deficient environments and elevated temperatures. The following chemical equations show the decomposition of β-Ga_2O_3 in such environment.

$$Ga_2O_3\,(s) \rightarrow 2\,GaO\,(g) + \tfrac{1}{2}\,O_2\,(g) \qquad (3.1)$$

$$2\,GaO\,(g) \rightarrow Ga_2O\,(g) + \tfrac{1}{2}\,O_2\,(g) \qquad (3.2)$$

$$Ga_2O\,(g) \rightarrow 2\,Ga\,(g) + \tfrac{1}{2}\,O_2\,(g) \qquad (3.3)$$

To address this issue, Tomm et al. used a modified gas mixture consisting of 10% CO_2 and 90% Argon (Ar). With these conditions the evaporation of the material was minimized. The growth rate was 2 mm/h under a rotation of 15 min^{-1} using (5N) Ga_2O_3 as the starting material. Figure 3.14 shows a picture of the crystal grown by Tomm et al., the crystal obtained was transparent to slightly blue, and had dimensions of 20 - 22 mm in diameter and 2 - 3 in in length [143]. Galazka et al. demonstrated theoretically and experimentally that the scale-up of β-Ga_2O_3 crystal size is strongly affected by the formation of metallic gallium in the melt [152]. The obtained crystals were 2 inches in diameter.

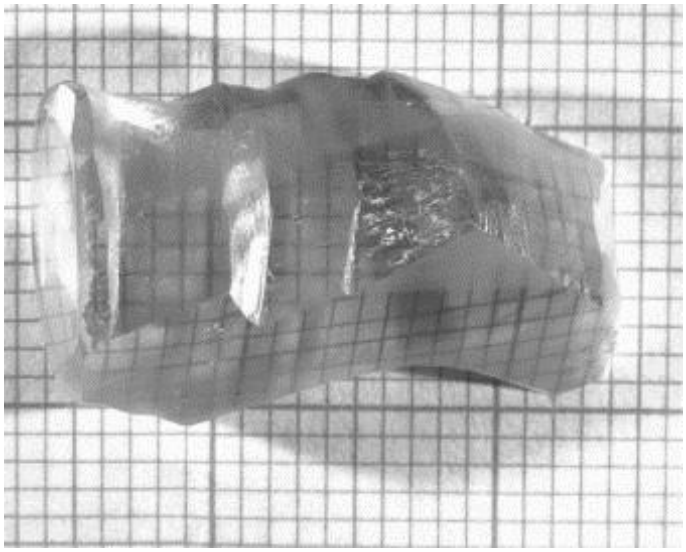

Figure 3.14 Undoped Ga_2O_3 crystal, internal clear, original color is bluish [143].

3.3.1.4 Edge-defined Film-fed Growth

Studies on the growth of sapphire tubes done by La Belle et al. (1971) lead to the discovery of the edge-defined growth (EFG) method [153–155]. The material is melted in a non-reactive crucible by induction or resistance heating in a controlled environment as shown in Fig. 3.15. Then the melt is fed by capillary action into a slit where is then drawn upwards by the seed crystal. The

resulting filament dimension is dictated by shape of the die, and not the melt column. EFG is universally used for large-scale production of sapphire single crystals.

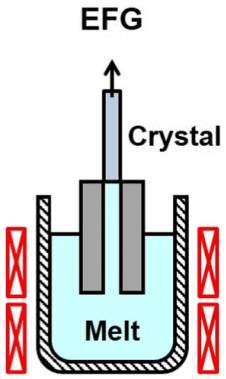

Figure 3.15 EFG method [93].

The first successful demonstration of β-Ga_2O_3 single crystals grown using EFG technique was reported in 2006 by Shimamura et al [144]. The group was able to grow 2 inches β-Ga_2O_3 single crystals bulk crystals. They showed experimental evidence of the feasibility of β-Ga_2O_3 crystals growth by this method, however the crystals obtained exhibited significant cracking and appeared to be polycrystalline. Later, Aida et al. [156] reported the growth of β-Ga_2O_3 single crystals by EFG. The crystals were 50 mm wide, with no polycrystalline inclusions. They started with a iridium crucible heated by rf coils. The size of the die was 3 x 50 mm^2.

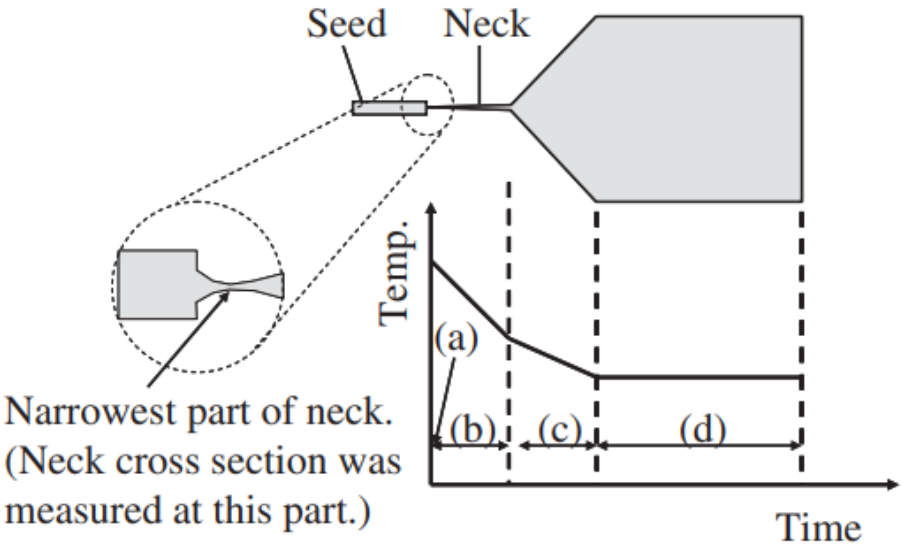

Figure 3.16 Aida et al. Illustration for growth stages and typical temperature profiles: (a) seeding process, (b) necking process, (c) spreading process, and (d) main-part growth process [156].

The process was separated into four distinct stages, namely seeding, necking, spreading, and main growth as depicted in Fig. 3.16. After the seeding process, the pulling speed was controlled during the initial stage of the necking process. Once the neck started to form, the pulling speed was fixed at 10 mm/h, and the temperature was lowered to a certain rate. When the crystal started spreading the temperature reduction rate was set to 18 °C/h until the crystal reached the dimensions of the die. Finally, after the spreading process the temperature was fixed and the pulling rate was 10 mm/h during the main-part growth. The dislocation densities of the crystals were estimated from the FWHM ranging from 75-160 arcsec. The research team also found that dislocations propagate from the seed crystal to the grown crystal, suggesting that narrower necks may hinder the propagation of these dislocations. Figure 3.17 shows examples of single crystalline and polycrystalline grown by Aida et al. Several groups have tried to refined the EFG method to improve crystal quality, size and production rate [157–160].

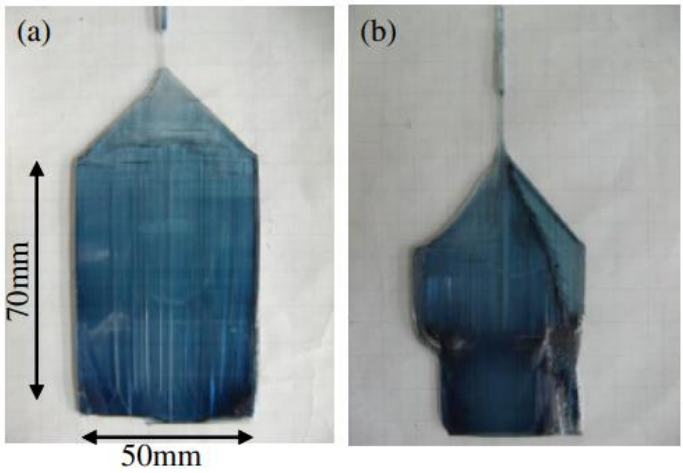

Figure 3.17 As-grown Ga_2O_3 ribbons: (a) single-crystalline, (b) polycrystalline. [156].

3.3.2 Thin Films

In recent years, there have been numerous attempts to obtain single crystalline thin oxide films with good crystallography properties and controlled carrier concentrations to use them as wide band gap transparent semiconducting oxides (TCOs) in microelectronics, optoelectronics, power electronics, short wavelength photonics, and gas sensing applications. Some of the most common growth techniques used to grow homoepitaxial and heteroepitaxial Ga_2O_3 thin films include, atomic layer deposition [69,161], pulsed laser deposition [162,163], rf-sputtering [164–168], molecular beam epitaxy [169–174], and metal-organic chemical vapor deposition [175,176]. Heteroepitaxial films have been grown on substrates such as Al_2O_3, Si, GaAs, TiO_2,ZrO_2:Y, MgO [84]. Although this variety of substrates promote the multifunctional development of Ga_2O_3-based devices, the resulting epilayers have high density of extended defects due to the differences in lattice symmetry, along with large lattice mismatch between the films and the substrates. Homoepitaxial films on β-Ga_2O_3 substrates have also been fabricated [79,177], and shown excellent quality due to minimized lattice mismatch. This section details some of the methods used for thin film deposition, with focus on rf magnetron sputtering deposition.

3.3.2.1 Sputtering

Among the physical vapor deposition (PVD) methods, sputter deposition is the selected method for this investigation, not only because it is an established industrial process but also because it is suitable for large area fabrication roll-to-roll processing, easy control composition, atmospheric processing, and low cost [16]. Magnetron sputtering is a versatile technique that can produce stoichiometric homogenous films with uniform thickness, high density, and strong adhesion. The technique has been successfully employed to achieve high quality epitaxial films for oxides and other materials more cost-effectively than the previously mentioned techniques. Another characteristic is that this technique allows better understanding of the thermodynamics involved during the process of deposition. Sputter deposition requires simple equipment, fewer precursors than are used in other techniques, such as pulsed laser deposition or molecular beam epitaxy, making the technique affordable, easy to operate with a high production rate.

Sputter deposition technique has an interesting story starting from the mid-19th century, where Grove (1852) observed deposits of metal films by "spluttering" or "cathode disintegration", while studying the electro-chemical polarity of gases using a direct current (dc) glow discharge [178]. Wright (1877) developed this technique further by using the cathode as the source for the film forming material [179]. Sputtered deposit films found commercial applications in the 1930s by Fruth (1932), where he describes equipment and methods for applying gold electrode surfaces to microphone diaphragms [180]. Before time, sputter deposition was based on exclusively on cathode sputtering or dc diode sputtering, then the technique was almost completely replaced by thermal evaporation methods until the improvement in vacuum technology in the late 1950s and early 1960s [179]. Sputter deposition regained significant interest with the realization that a wide variety of conductive materials could be deposited using direct current (DC) sputtering (Kay [181],

Thornton and Green [179],Westwood [182]), and the introduction of radio frequency (rf) sputtering for ceramics and other dielectric materials by Anderson et al (1962) [183]. The magnetron sputtering technique was further developed during the 1960s and 1970s, resulting in the first planar magnetron sputtering apparatus by Chapin [184], shown in Fig. 3.18. Since then, magnetron sputtering deposition has been as a prevalent technique for applying metallic and compound thin films, finding utility across various industrial sectors [179].

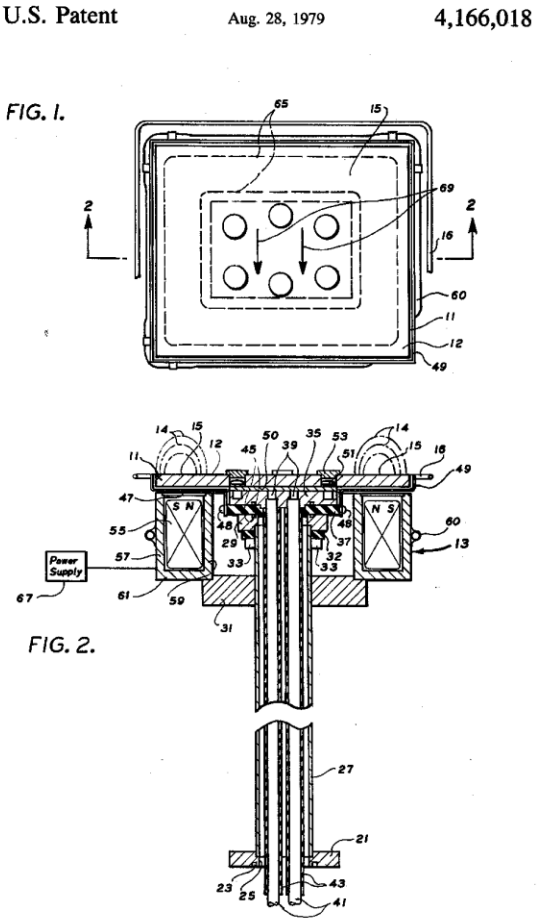

Figure 3.18 Sputtering apparatus is described in which a magnetic field is formed adjacent a planar sputtering surface, the field comprising arching lines of flux over a closed loop erosion region on the sputtering surface (Inventor: John S. Chapin) [184].

In the sputtering method, a solid source containing the material to be sputtered is placed on a negatively charged cup (cathode) and the substrate to receive the material is placed on a positively charged holder (anode). Both cathode and anode are placed inside a chamber where a high vacuum ($\sim 10^{-7}$ Torr) is pulled. The holder containing the substrate can be a heater or a thin film deposition rate monitor depending on the experiment. A working gas or deposition gas (such as Ar, Ne, Kr, and Xe) is introduced, this gas will generate the desire atmosphere during the deposition process, sourcing the energetic particles for the sputtering process.

When an electric field is applied across the anode and the cathode, the deposition gas will be ionized, forming a plasma of high energetic ion species. The positively charged ions sense the generated electric potential and are abruptly accelerated towards the cathode containing the target, where they collide with the atoms within the target material. The cathode also has a magnet to generate a constant magnetic field that traps the electrons in the vicinity, increasing the ionization rate and consequently the sputtering yield [15]. Being a PVD deposition technique, sputtering relies on the physical removal of atoms from the target material through momentum exchange between the energetic species of a plasma and the atoms within the cathode target. The sputtered material is directed toward the substrate using a cylindrical glass cup, where it is deposited in the form of a thin film [185]. The sputtering system is commonly equipped with either a dc source or a radio frequency (rf) source. Conductive materials can be easily sputtered with a dc power source since they do not build charge on the target material. However, if dc power is used with dielectric targets, they will build up a charge over the time of the deposition process. This due to the accumulation of positive ions on the surface of the target material, and can eventually repel the ionized gas (also positively charged) resulting in the complete cessation of the sputtering process. To solve this problem, an alternating electrical potential, i.e., a rf source is applied in the vacuum

environment. Furthermore, on the negative cycle the bombardment of the target takes place, and this is when charge builds up on the surface of the target material. Then, a positive cycle follows to "clean" the surface of any positive charge build-up by attracting the electrons in the chamber to the surface of the target, giving it a negative bias. This alternating process continues at a radio frequency of 13.56 MHz, and allows for the deposition of dielectric materials. Figure 3.19 depicts the process of magnetron sputtering.

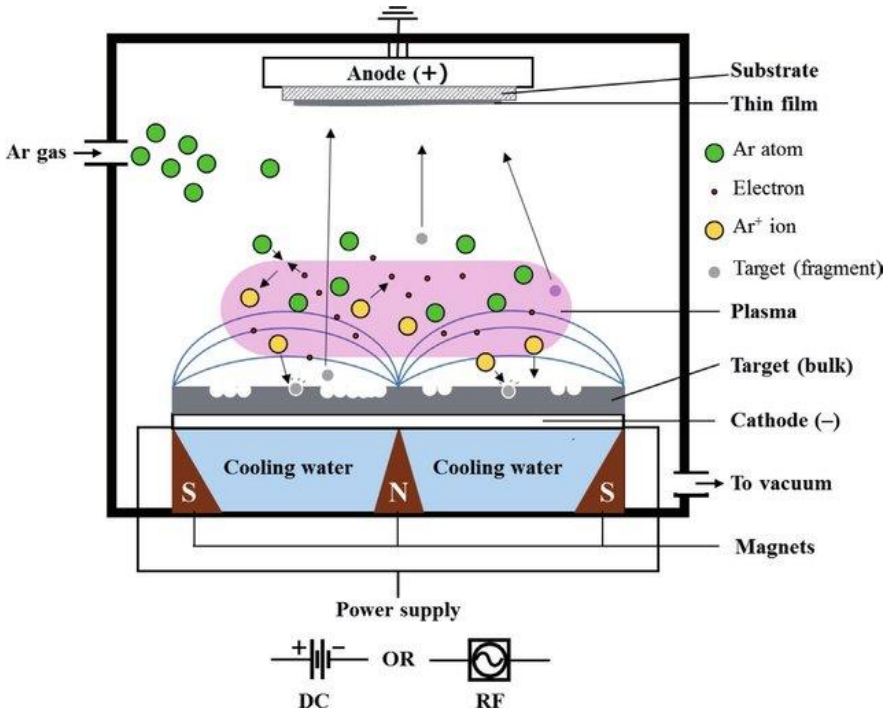

Figure 3.19 Schematic representation of a magnetron sputtering equipment and deposition process [186].

The sputtering deposition system shown in Fig 3.20 (a). was used to deposit Ga_2O_3 films and metal contacts to Ga_2O_3. The system is a CVC model SC-3000 vacuum system which is operated with a mechanical pump and a Pfeiffer Hipace 300 CF-F-turbo-pump equipped with a TC 400 controller (Pfeiffer Vacuum Inc. 24 Trafalgar Square, Nashua, NH 03063), to achieve a base

pressure of 1×10^{-7} Torr within 12 hours. The chamber is made by an 18 inch-diameter bell jar, enclosing three 2-inch diameter sputter cathodes, as shown in Fig. 3.20 (b). As mentioned above, there are two available power sources, namely dc and rf for depositing metals (i.e., Au, Sn, Ti, etc.) and insulating targets (i.e., Ga_2O_3, SiO_2, Al_2O_3, etc.) respectively. The cathodes in our system can be sourced with a MDX 500 W dc power supply (with negative or positive output voltage, and 500 V at 1 A or 1000 V at 0.5 A), one 300 W rf power supply (AJA 100/300 / Seren Industrial. Power Systems R301 @ 13.56 MHz) and a second 300 W rf power supply (RF-3-XIII RF VII, Inc. @ 13.56 MHz). In fact, this is a standardized frequency, recommended by the International Communication Union (ITU) radio regulations for industrial, scientific, and medical instruments (ISM), which is centered around 13.56 MHz with a bandwidth of 14 kHz [187].

Other accessories include an Inficon film thickness monitor (XTM/2 Deposition Monitor) installed on an aluminum holder, along with a Blue Wave BN substrate heater sourced by a BWS-1000 power supply. The substrate heater can provide substrate temperatures up to 800 °C. Two of the cathodes have flexible heads with an electric-pneumatically driven shutter suitable for executing Sn delta and uniform doping of the films. A high purity Ga_2O_3 (99.99%) ceramic target was used for all thin film deposited in this work. Metallic targets such as Au and Ti were used for depositing metal contacts to the grown films.

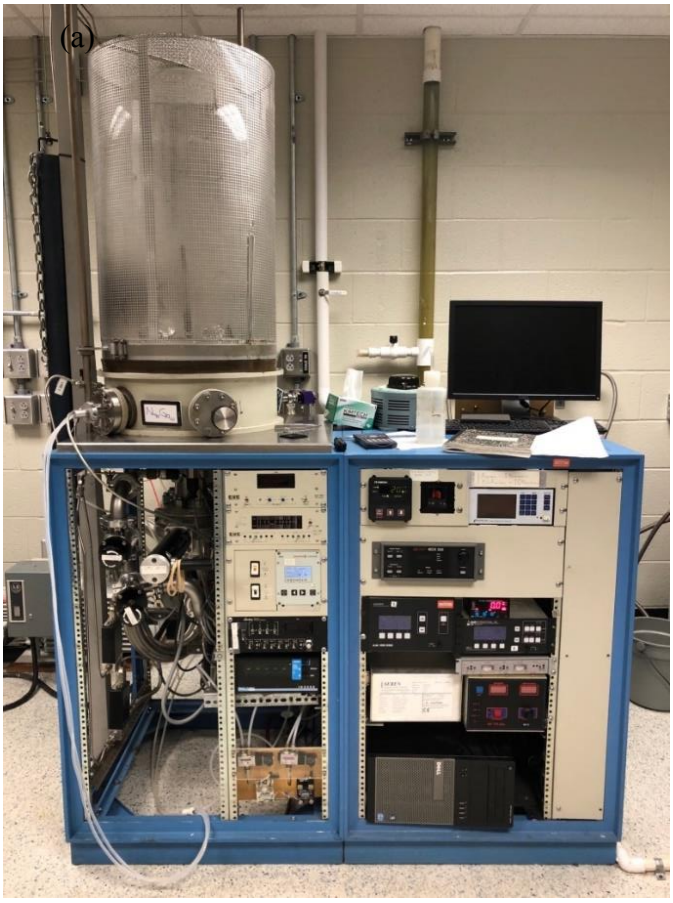

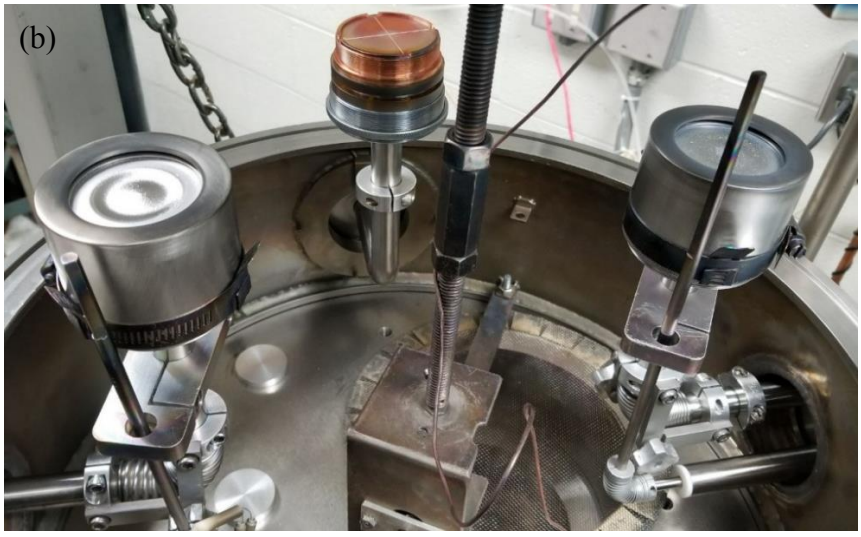

Figure 3.20 (a) CVC model SC-3000 vacuum system, (b) 2-inch diameter sputter cathodes and targets mounted.

3.3.2.2 Molecular Beam Epitaxy (MBE)

Molecular bean epitaxy (MBE) is another epitaxial growth technique, which enables precises growth control of thin film thickness. This is because MBE growth rate is very slow, of about 1 μm/hr which allows a step-flow film growth. The material to be deposited is in the form of a high purity powder inside an effusion cell. The cell is surrounded by a heating element that sublime the powder material, which slowly condense on the substrate surface. This deposition technique requires ultrahigh vacuum. A diagram of the MBE system is shown in Fig. 3.22. Ga_2O_3 growth by MBE is done by oxidation using ozone or oxygen radicals of the sublimated Ga atoms from a metal source [173]. MBE is widely used in the fabrication of Ga_2O_3 thin films [171,188–190].

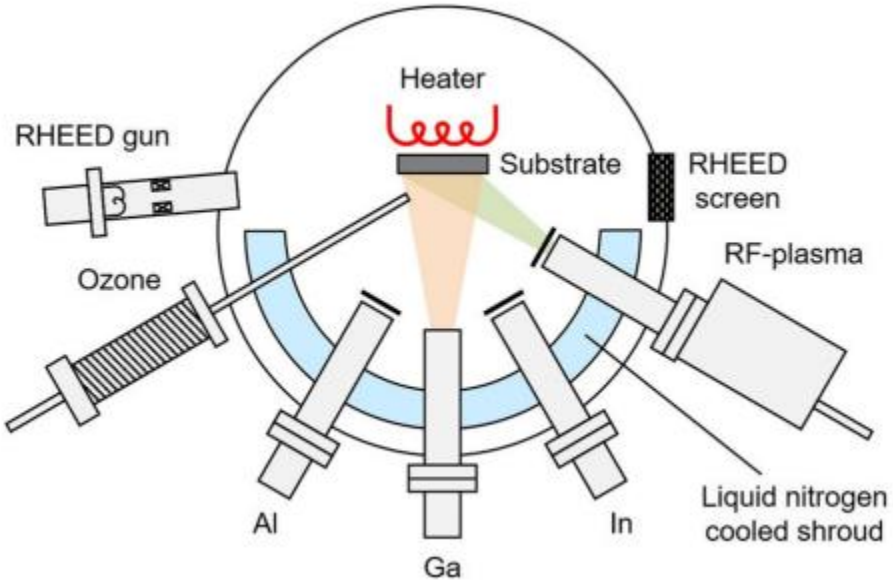

Figure 3.21 Schematic of MBE machine with both O3 inlet and O-plasma cell for β-Ga_2O_3 epitaxial growth [93].

3.3.2.3 Metal-Organic Chemical Vapor Deposition (MOCVD)

As the name suggests, metalorganic chemical vapor deposition is a chemical vapor deposition method. In contrast to rf-sputtering and MBE, the deposition is done by means of a chemical reaction at a moderate pressure (10-760 Torr), rather than in vacuum. The technique is commonly used for compound semiconductors such as Ga_2O_3 [84,191–193] and can create complex semiconductors multilayer structures[194,195]. Figure 3.23 shows a MOCVD reactor set up to grow Ga_2O_3 thin films. The technique uses Ga precursors such as trimethylgallium (TMGa) and triethylgallium (TEGa), and ultrahigh purity O_2 and H_2O during the growth. Growth rates have been optimized and increased to about 4 μm/hr.

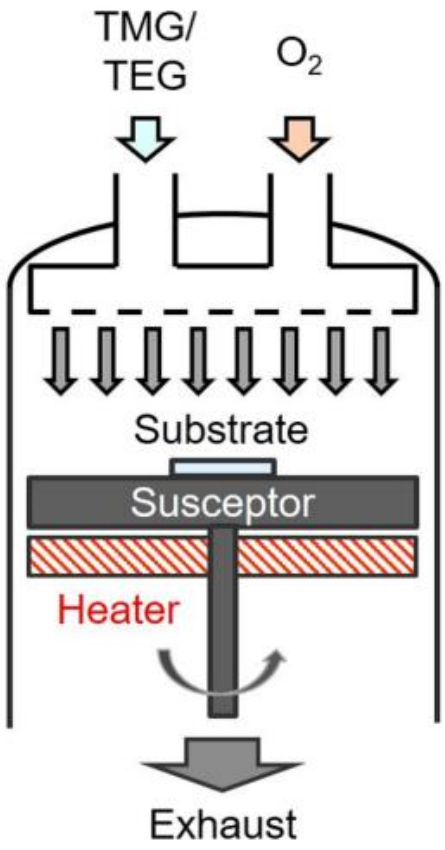

Figure 3.22 Schematic of MOCVD reactor for β-Ga_2O_3 epitaxial growth [93].

3.4 Doping

Doping β-Ga_2O_3 was discussed in section 2.3. In this section the configuration used for the doping of β-Ga_2O_3 films by sputtering is presented. Figure 3.24 shows the sputtering chamber, configured for uniform doping. The cathodes have a goose-neck that can be adjusted to simultaneously deposit Sn doping material and Ga_2O_3 film on a substrate. A dc power corresponding to 2, 3, 4, 5, and 6 mA was used to deposit Sn, with the intention of varying the carrier concentration in the films. The rf power was kept constant at 100 W. All samples were deposited at a substrate temperature of 450 °C in Ar/O_2 (1% O_2).

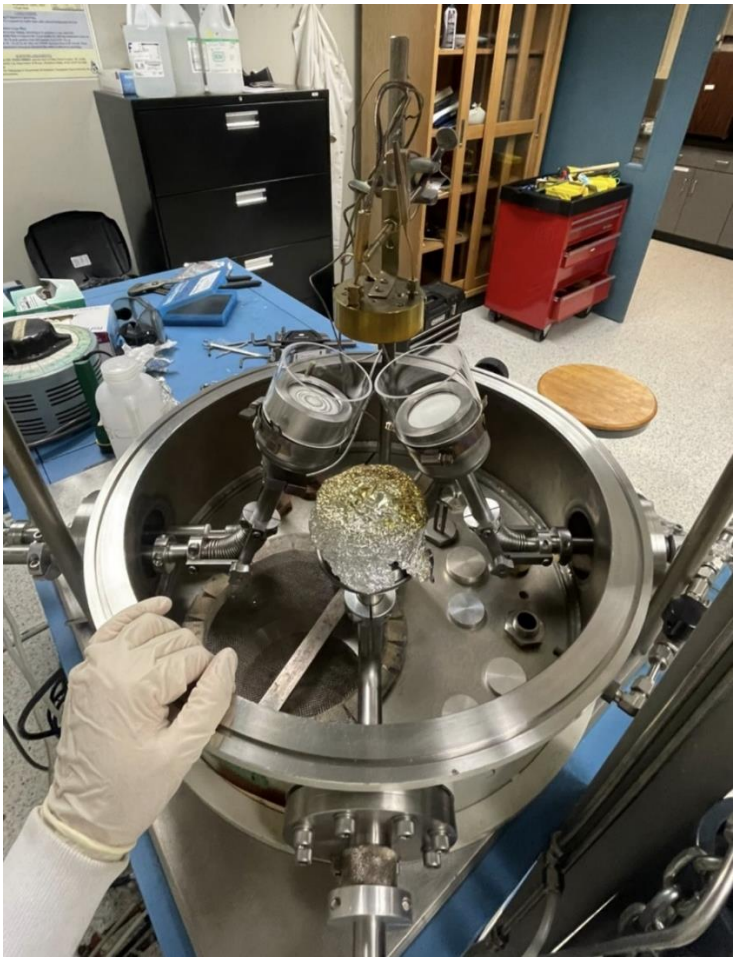

Figure 3.23 Sputtering chamber with Sn-doping configuration.

3.5 Annealing

Samples were annealed using an RTP-300 Rapid thermal Processor (RTP). The RTP can heat the sample from room temperature (RT) to 900 °C in less than 20 s. The apparatus uses high intensity halogen lamps (J120V-1000WB) arranged on the walls of a quartz box. The quartz box is kept in an ambient made of different gases, mainly Ar, O_2, N_2, or Ar:O_2 mix. A gas flow 3LPM was used for every run. The annealing times varied up to 6 min. The sample is placed on a silicon wafer which is fitted with a thermocouple to monitor the temperature (Fig. 3.26). In this dissertation, different gases and gas mixtures were utilized to explore their impacts on the crystal structure and electrical properties of the films and contacts. A picture of the apparatus is shown in Fig. 3.25.

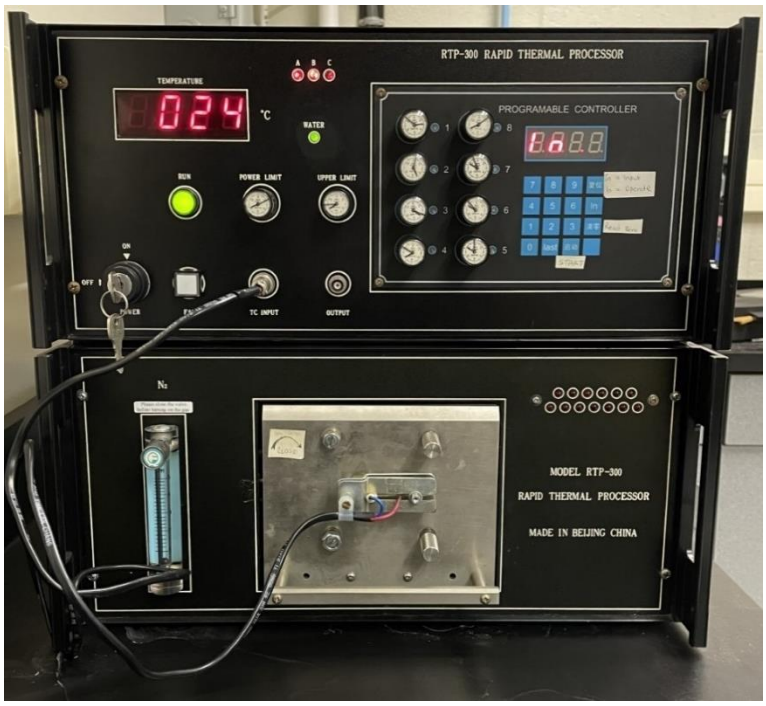

Figure 3.24 RTP-300 Rapid Thermal Processor.

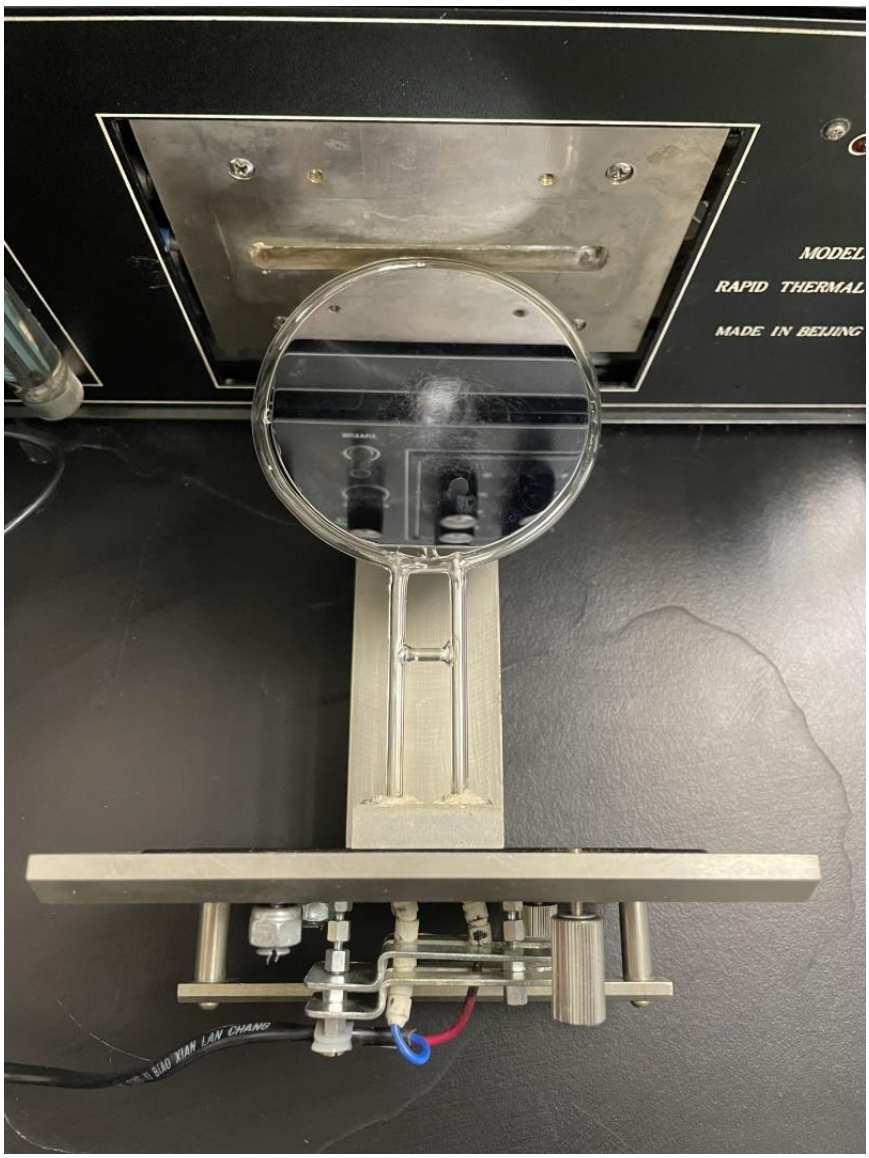

Figure 3.25 RTP-300 sample holder with thermocouple.

3.6 Plasma Etching

Inductively Coupled Plasma (ICP) etching and Reactive Ion Etching (RIE) are two common plasma etching techniques used in semiconductor fabrication and other industries. The principal difference between these two techniques is based on that ICP uses inductive coil to generate a high-density plasma that is separate from the sample. These ions are then directed towards the sample surface with the help of a separate potential placed between the gas and the sample.

On the other hand, RIE etching involves the use of a combination of reactive gases and a rf electric field to generate a plasma. The sample is placed on a powered electrode, and the ions from the plasma bombard the sample surface for etching. ICP etching systems typically feature higher plasma densities and superior uniformity compared to RIE systems, leading to more precise and controlled etching processes. Conversely, RIE systems may feature lower plasma densities and exhibit less uniformity across the sample surface; nonetheless, they remain effective for numerous etching applications.

ICP etching systems offer advanced process control capabilities, allowing for fine-tuning of parameters such as gas flow rates, power levels, and pressure. They are often preferred for high-precision etching applications in semiconductor device fabrication, Micro-Electro-Mechanical Systems (MEMS), and nanotechnology. RIE systems also provide process control options but may have fewer adjustable parameters compared to ICP systems.

Our system is a Minilock-Phantom (ICP-RIE) from Trion Technology uses a combination of both technologies mentioned above. The plasma is generated by a set of magnetic coils surrounding the chamber. A rf power source connected to the cathode generates a DC bias that attracts the generated plasma to the etching surface. This setup allows the user to decouple the ion density, which is controlled by the induction coils, from the ion energy, which is determined by the acceleration of the ions due to the rf source. Figure 3.27 shows a schematic of the RIE-ICP system, emphasizing the ICP power source and a separate rf source connected to the cathode.

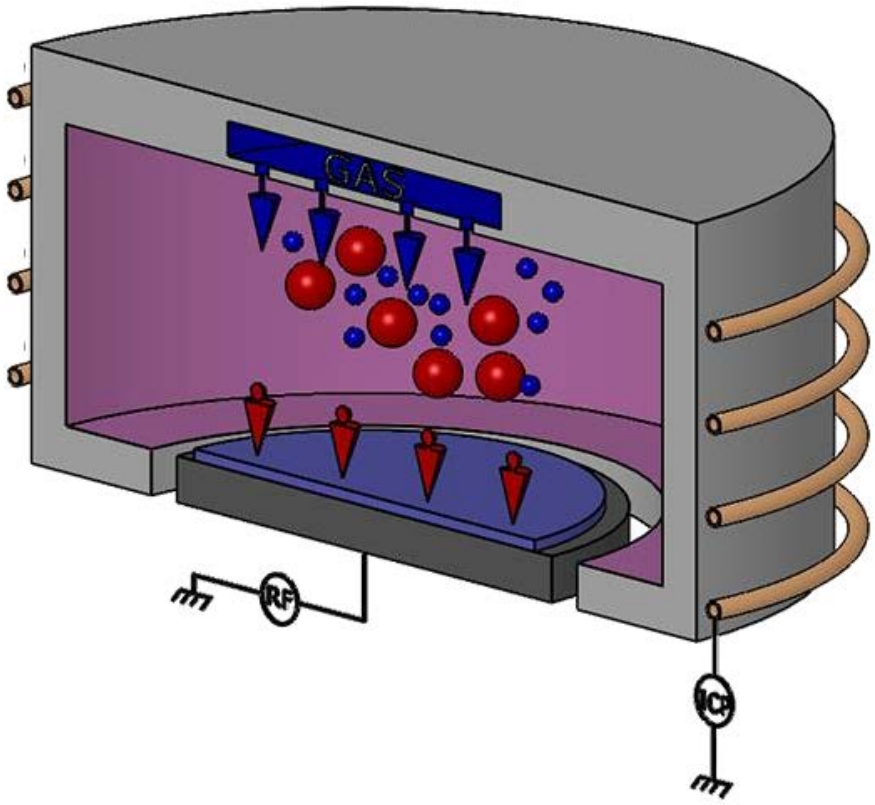

Figure 3.26 ICP-RIE chamber diagram.

The system is equipped with a 600 W, 13.56 MHz solid state rf generator, it has a loadlock that allows the main chamber to continue pumping, while the sample is loaded or unloaded. This configuration is ideal for toxic gas chemistries since it prevents exposure to the atmosphere between runs. The sample holder is a mechanic arm that can hold wafer sized up to 4 inches. Typical gases are: N_2, O_2, Ar, SF_6, SF_3, He-O_2 mixture, CHF_3, CCl_2F_2, Cl_2, CF_4, and $SiCl_4$. The user can load a recipe with parameters such as, etching pressure (mTorr), ICP (W), RIE (W), etching time (s), temperature (°C), and gas flow (sccm). The system is shown in Figure 3.28.

Figure 3.27 Minilock-Phantom ICP-RIE, Trion Technology.

4. Characterizations Methods for β-Ga_2O_3

This chapter provides an in-depth exploration of various materials science techniques employed for the microstructural, compositional, optical, and electrical characterization of the β-Ga_2O_3 samples. These techniques encompass a range of analytical methods aimed at examining the internal structure, chemical makeup, optical properties, and electrical behavior of the β-Ga_2O_3 specimens. The utilization of these techniques facilitates a comprehensive understanding of the material's properties and paves the way for informed analysis and interpretation of experimental results.

4.1 X-ray Diffraction (XRD)

X-ray diffraction was used for structural characterization of the Ga_2O_3 films. The instrument shown in Fig. 4.1, a Bruker AXS X8 Prospector equipped with a high brightness Cu Incoatec micro source, advanced X-ray optics and a highly sensitive Apex II CCD area detector. This is a non-destructive technique which enables identification of crystalline nature, including orientation, phase composition, lattice parameters, and the presence of strain and grain size.

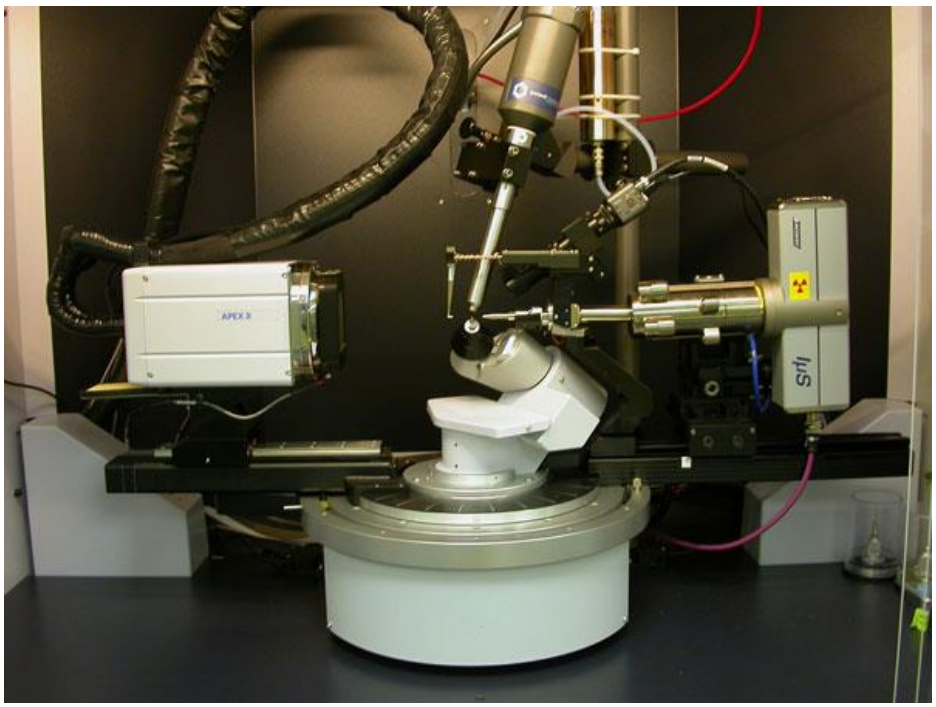

Figure 4.1 Bruker AXS X8 Prospector.

In crystalline materials, the atoms are arranged in a regular manner. This is a necessary condition to implement the XRD technique, as diffraction will only occur if the incident x-rays are diffracted by a periodic array of atoms. An incident x-ray beam is directed towards the sample at a specific angle ranging from $2\theta = 10° - 90°$. The x-rays are scattered by different plane in the material and constructive or destructive interference occurs. Once the diffracted x-rays exit the sample, the detector can only read signals at the angles where constructive interference occurred. The resulting diffracted x-rays have a travel at a different optical path. The magnitude of the length traveled depends on the distance between the crystallographic planes and the incident angle. This can be mathematically summarized in the Bragg equation.

Figure 4.2 shows a schematic representation of the Bragg equation:

$$n\lambda = 2dsin\theta \tag{4.1}$$

where n is an integer, λ is the wavelength of the incident X-ray, d is the lattice spacing, and θ is the scattering angle.

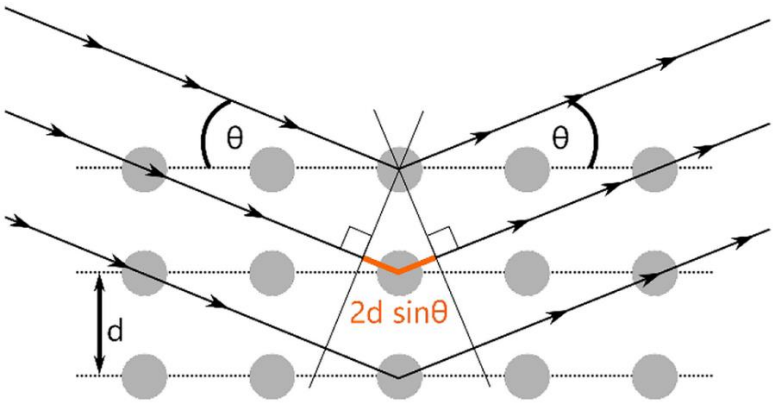

Figure 4.2 Schematic representation of the Bragg Equation [196].

Single crystal β-Ga_2O_3 film grown on c-plane Al_2O_3 substrate, sharp peaks were observed at 2θ = 18.3°, 37.1°, and 57.7° (Fig. 4.3). These peaks can be assigned to $(\bar{2}01)$, $(\bar{4}02)$, and $(\bar{6}03)$ respectively, as reported by Ahman et al [33]. This XRD represent a single crystal structure with same family of planes. There is a small peak at 43° belonging to c-plane Al_2O_3 substrate (006).

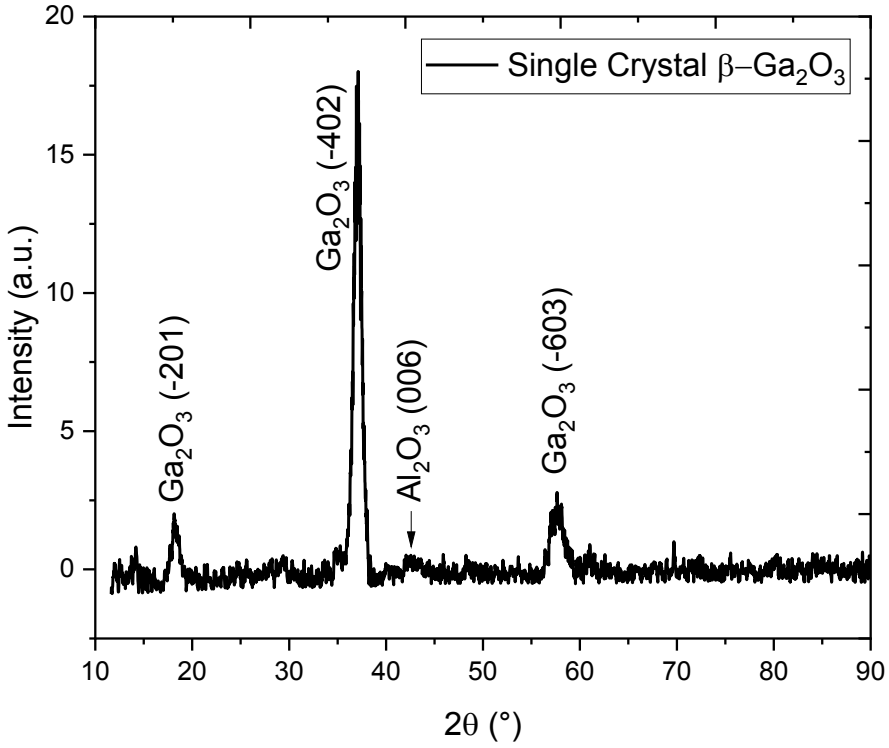

Figure 4.3 θ-2θ XRD scan of single crystal β-Ga_2O_3 ($\bar{2}01$) film on c-plane Al_2O_3 substrate deposited at 400 °C in Ar.

The d-spacing or interplanar spacing in the ($\bar{2}01$) direction can be easily calculated using Bragg's equation (Table 4.1) by solving for d. Initially, X-ray diffraction (XRD) data is utilized, and the positions of the major peaks are identified using the Origin software's multiple peak fit tools. A Gaussian fit is applied to each peak to determine its center, providing a precise measurement of the diffraction angle. Subsequently, Bragg's equation is employed with a wavelength (λ) of 1.5406 Å and considering first-order diffraction (n = 1) to determine the d-spacing for each peak. Table 4.1 shows the results of calculating the d-spacing in in the ($\bar{2}01$) direction with the XRD data from Fig. 4.3:

Table 4.1 Interplanar d-spacing in in the ($\bar{2}$ 0 1) direction.

2Theta (°)	Theta (°)	$d = 1.5406 \frac{\text{Å}}{2sin\theta})$	Error (Å)
18.25177	9.12589	4.82517	±0.01062
37.06611	18.53305	2.41474	±0.00541
57.68992	28.84496	1.59247	±0.0039

Another useful parameter that can be extracted for a particular XRD peak in question is the Full Width at Half Maximum (FWHM), and it is used to calculate crystallite size (Fig. 4.4) using the Scherrer Equation as follows:

$$D = \frac{k\lambda}{\beta cos\theta} \tag{4.2}$$

where D is the average crystallite size in nm

K is a dimensionless shape factor, with a value of 0.9

λ is the X-ray wavelength, CuK_{α} = 1.5406 Å

β is the line broadening at FWHM in radians

θ in the Bragg's angle in degrees

The Crystallite size was obtained using the FWHM from the ($\bar{6}$ 0 3) Bragg peak of β-Ga_2O_3 and substituting into Scherrer equation. Figure 4.4 shows that the average crystallite size remained around 40 nm, except for the film deposited at room temperature. These values strongly depend on the deposition method, deposition temperature, and selected crystal plane, but they are comparable with values found in the literature. Jubu et al, reported crystallite sizes ($\bar{2}$ 0 2) Ga_2O_3 films grown by chemical vapor deposition (CVD) [197]. The reported average crystallite sizes were 37.16, 59.64, and 59.93 nm for deposition temperatures of 850, 950, and 1050 °C, respectively. In terms of the FWHM of the ($\bar{6}$ 0 3) β-Ga_2O_3 Bragg peak, this means that no significant broadening of the peak occurs with increasing deposition temperature and that the crystal quality of the film remains similar to that of the substrate.

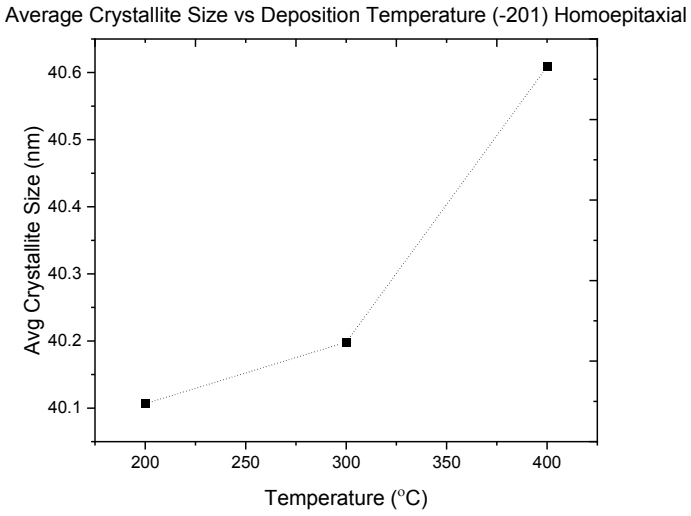

Figure 4.4 Average crystallite size vs deposition temperature of the films deposited homoepitaxially on ($\bar{2}$01) Ga_2O_3.

4.2 Scanning electron Microscopy (SEM)

Scanning electron microscopy was performed on β-Ga_2O_3 sputtered films and alloys for structural and chemical composition analysis. Two SEMs were used in this investigation. This first instrument is a JEOL JIB-4500 multi beam system, fitted with LaB_6 emitter (Fig. 4.5). Some specifications follow: an acceleration voltage ranging from 0.3 to 30 kV, and SEM resolution of 2.5 nm at 30 keV. This SEM runs a EDAX APOLLO XV x-ray energy dispersive spectrometer (EDS), used for chemical composition of the sputtered films, doped films, alloys, and metal contacts. The EDS resolution is 128 eV at Mnk, 100,000 CPS.

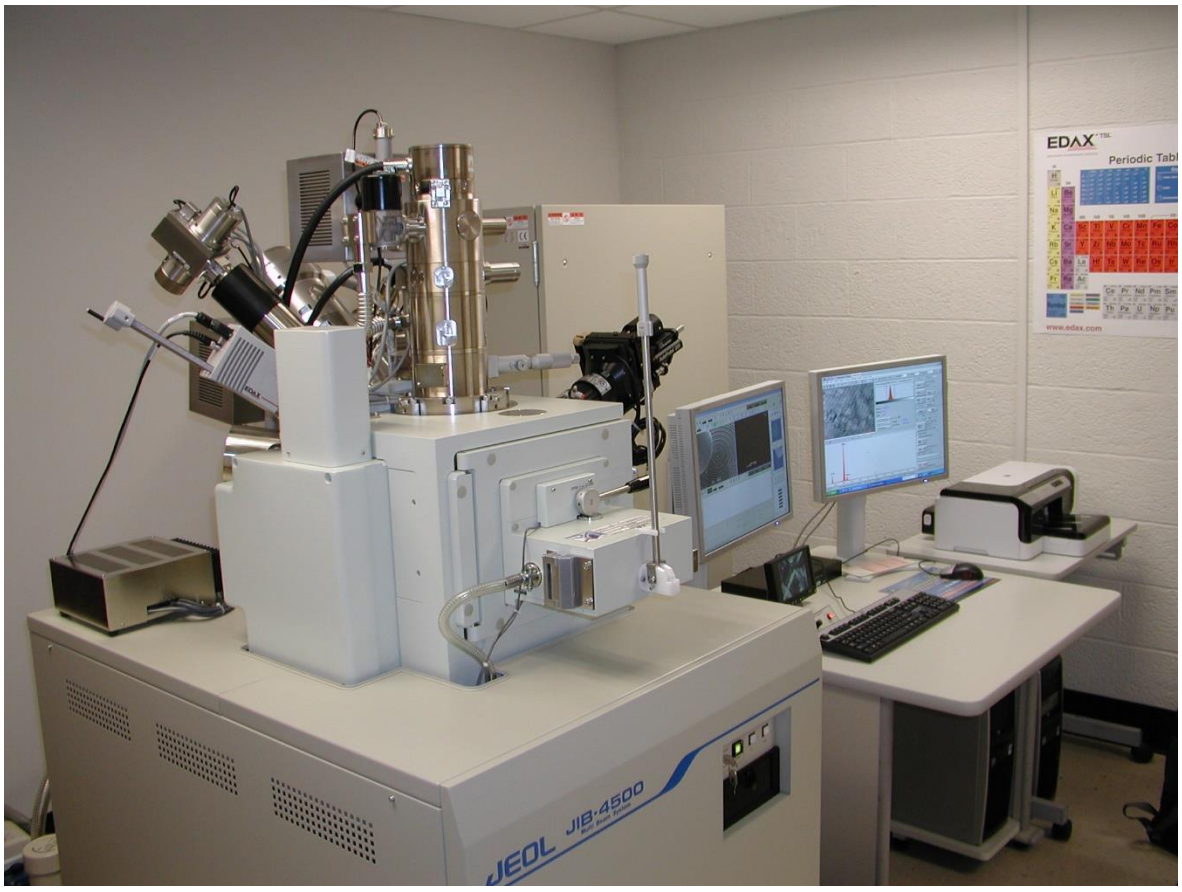

Figure 4.5 JEOL JIB-4500 multi beam system.

The second instrument is a JEOL JSM-7600F scanning electron microscope fitted with a thermal field emission source (Fig. 4.6). The specs are 0.1 to 30 kV acceleration voltage, resolution 1.5 nm at 1kV (GB mode), 1.0 nm at 15 kV. The beam current ranges from 1 pA to 200 nA at 15 kV. The instrument can also operate in scanning transmission electron microcopy (STEM) mode. This instrument was mainly used to measure β-Ga_2O_3 films thickness and elemental analysis while investigating alloys to Ga_2O_3.

Figure 4.6 JEOL JSM-7600F scanning electron microscope.

The SEM operates as follow: An incident beam is produced by an electron gun and directed down a column maintained in vacuum (10 to 100 Pa). The column contains a sequence of magnetic lenses and apertures that work together to produce a focused electron beam as illustrated in Fig. 4.7. As the electron beam scans the sample, a variety of signals are generated from the interaction between the electrons and the atoms in the material. The signals are collected by three different detectors: a secondary electron detector, a backscatter electron detector, and an x-ray detector. These signals are then transmitted to a computer, where they undergo further processing.

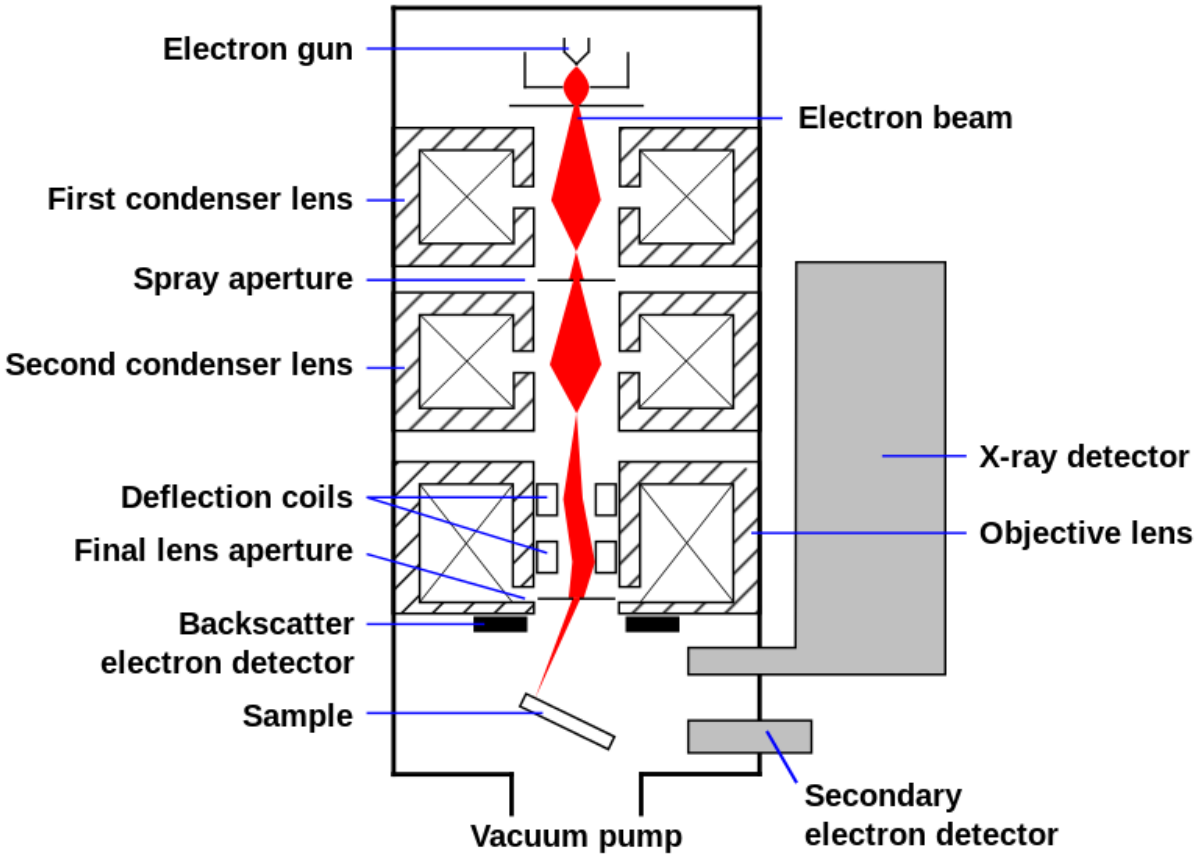

Figure 4.7 Scanning electron microscope column [52].

The main component of the electron gun is the source. There are three main types of electron sources found in SEMs: tungsten (W), solid state hexaboride crystals (LaB_6), and field emission guns (FEG) as shown in Fig. 4.8. Tungsten hairpin has the lowest resolution (4 nm at 30 kV) due its larger emission area. W sources are relatively cheap and designed to be replaced regularly and easily during regular usage of the instrument. Tungsten thermionic sources operate at high temperatures, up to 2800 K, and tend to evaporate over time, increasing the risk of contamination of the SEM column.

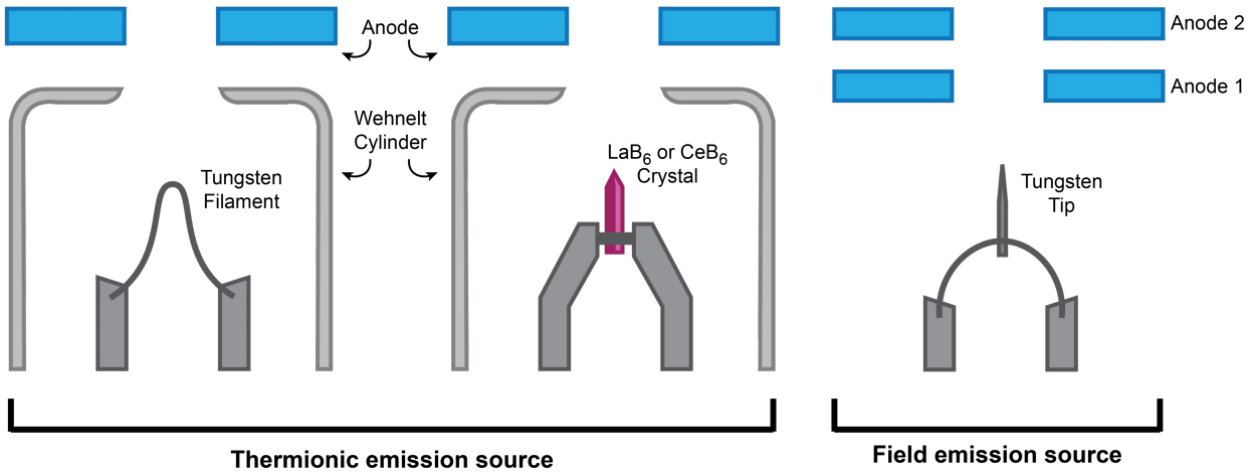

Figure 4.8 Simplified diagram of the electron gun sources for the SEM.

Similarly, LaB_6 sources use thermionic emission to operate. This source has a higher resolution than that of W sources, since hexaboride crystals have a lower work function, which translates to higher electron emission efficiency at comparable acceleration voltages. The brighter beam allows higher signal-to-noise ratios. They have better longevity and resistance to evaporation, making them suitable for most SEM applications.

The third source listed is the FEG. These are usually fabricated from single crystal tungsten sharpened to a tip radius of about 100 nm. The sharp tip drastically lowers the emission area and increases current density. The smaller diameter of the beam produces a coherent and brighter beam up to three orders of magnitude that can be achieved with the previously mentioned. Some limitations are the need for a high vacuum environment for operation, and high price of the source. Nevertheless, FEG sources offer exceptional performance in all SEM applications. A summary of the different characteristic for these three sources is offered in Table 4.2.

Table 4.2 Comparison of electron source characteristics for SEM [198].

	Tungsten hairpin	CeB6 crystal	Schottky FEG
Emission mechanism	Thermionic	Thermionic	Electron Tunnelling
Lifetime	100 h	1500 h	>10,000 h
Tip emitting diameter	100 μm	25 μm	100 nm
Resolution @30 kV	4 nm	3 nm	1 nm
Resolution @1 kV	50 nm	25 nm	5 nm
Low-kV imaging (<5 kV)	Yes	No	Yes
Vacuum	10^{-1} – 10^{-5} mbar	10^{-7} mbar	10^{-9} mbar

The volume where these interactions take place is usually referred as the interaction volume and is depicted in Fig. 4.9. Each depth generates a different signal. The interaction volume increases with increasing electron beam energy and decreases with the composition of the specimen, i.e., the average atomic number. Various types of signals are produced when the electron beam interacts with atoms in the sample:

(i) Secondary electrons (SE): Secondary electrons are produced near to the surface of specimen. This signal helps in images up to a resolution of 1 nm. This signal is collected by the secondary electron detector.

(ii) Back-scattered electrons (BSE): BSE are generated due to reflection of electrons from sample due to elastic scattering. The images from BSE yield statistics about distribution of various elements in the sample. BSE is collected by the backscatter detector located directly on top of the sample at the end of the SEM column.

(iii) Characteristic X-rays: Characteristic x-rays are produced when the beam of electrons removes an electron from inner shell and filling the shell with high energy electron and release the energy (x-ray). The released energy provides information about the composition and measure of the element in the sample. This is the principle behind energy dispersive spectroscopy analysis.

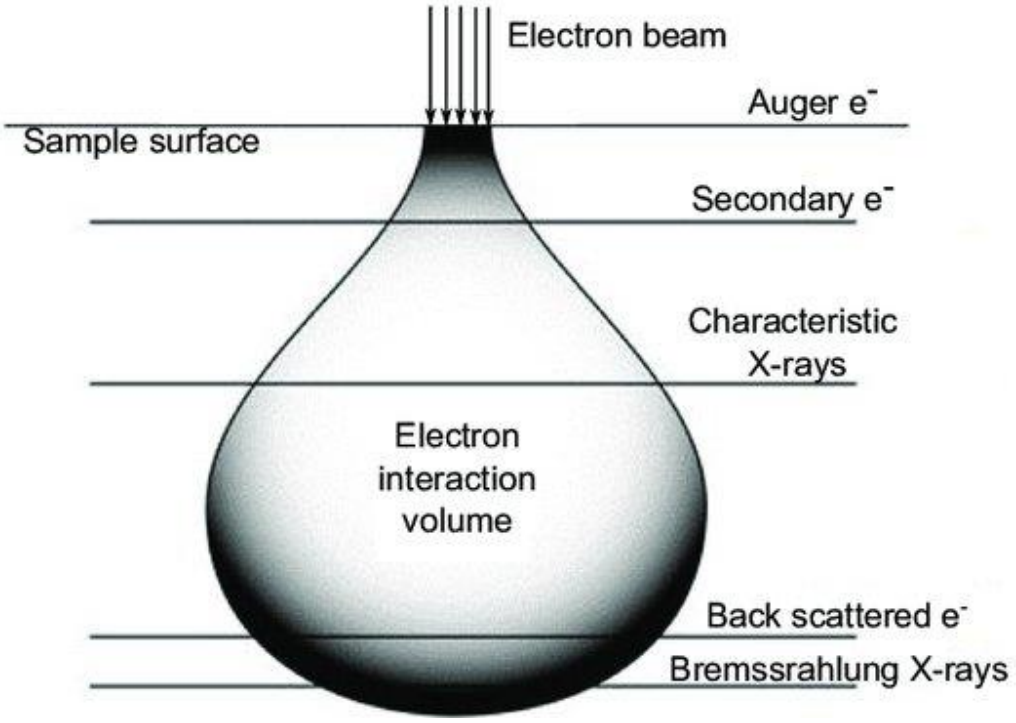

Figure 4.9 Interaction Volume and signal emission [199].

4.3 Atomic Force Microscopy (AFM)

Atomic force microscopy was used to study the surface morphology of the films and substrates used for this dissertation. A 5500 Keysight Scanning Probe Microscope (SPM), shown in Fig. 4.10 is a functional research system for atomic force microscopy (AFM) and scanning tunnelling microscopy (STM). The AFM can be operated in contact and intermittent contact mode, which provides 3-dimensional imaging of the sample allowing visualization of the surface features and roughness analysis. The AFM scan range is 90 μm x 90 μm, the z range is 8 μm with a noise level (RMS) of 0.5 Å. It also has STM capabilities to investigate the electrical conductivity across the specimen. Throughout this dissertation, the primary technique employed was contact atomic force microscopy, and it is discussed in the next paragraphs.

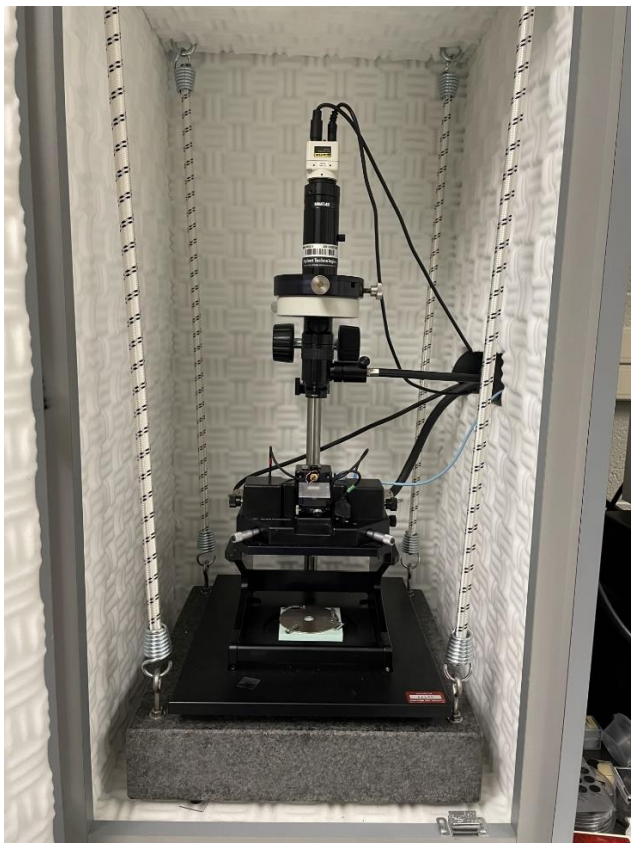

Figure 4.10 5500 Keysight Scanning Probe Microscope.

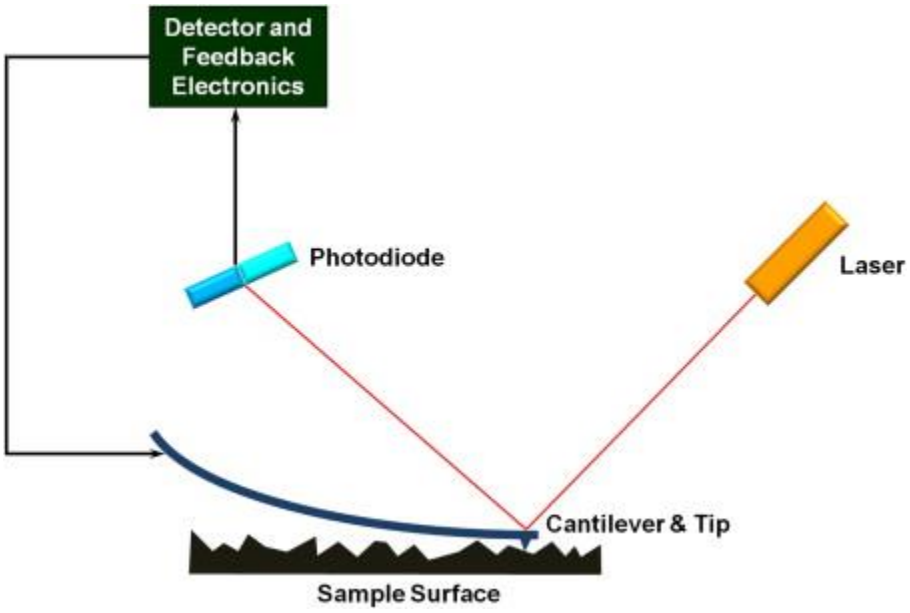

Figure 4.11 Schematic of a typical commercial AFM instrument [200].

The basic set up for contact mode AFM relies in three main components: a laser, a cantilever holding the AFM tip, and a photodiode detector (Fig. 4.11). The laser beam is aligned and reflected from the back of a cantilever coated with a reflective material. As the AFM tip scans the surface, the cantilever will interact with the surface. The deflection of the reflected laser will be read by a 4-quadrant photodiode detector and the surface contour will be measured directly. In this mode, the force between the tip and the surface is kept constant during the scan. By maintaining a constant deflection or height above the sample, small disturbances due to surface features will be displayed as data. This gives topographical images with resolution in the order of fractions of nanometers.

The main parameter obtain with this method is the root mean square (RMS) value which gives information about the surface roughness of the sample. Mathematically, the RMS roughness values is the standard deviation of the z values within a given area (e.g., 10 x 10 μm^2). The substrates of c-plane double-sided polished sapphire used to deposit all heteroepitaxial β-Ga_2O_3 thin films were subjected to thermal desorption by heating at 500 °C for 30 min in UHP O_2. The process produces a smooth surface morphology prior deposition. Figure 4.12. shows the RMS roughness values for the substrates deposited in different atmospheres. Oxygen rich atmosphere results in the smallest RMS (0.2 nm).

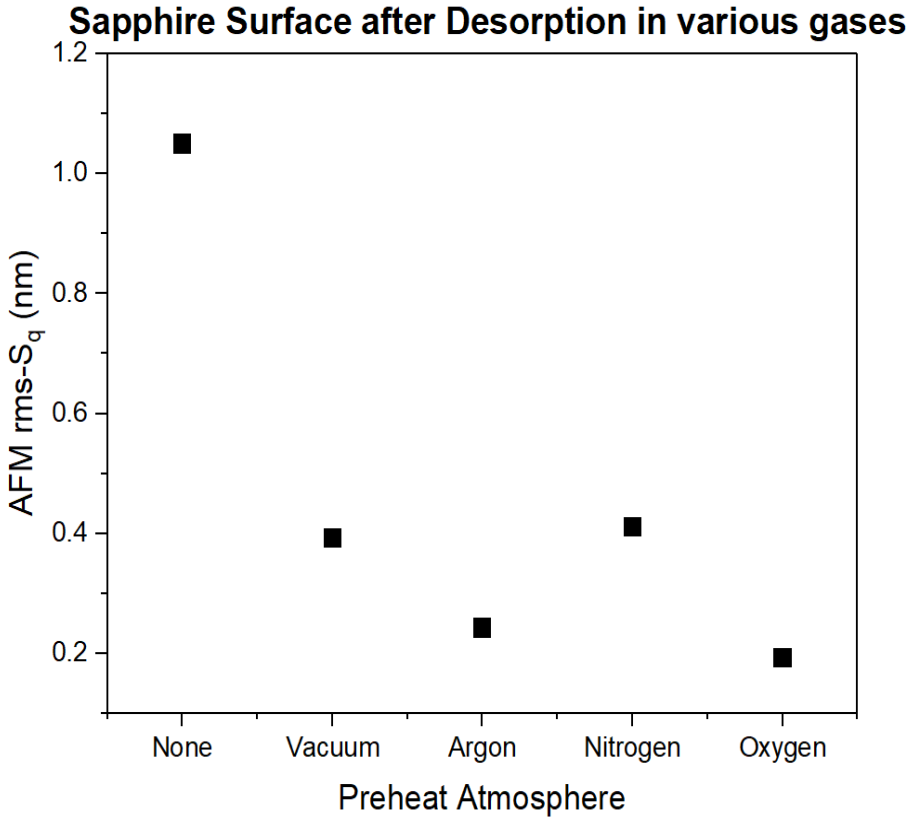

Figure 4.12 Effects of gas composition on the root-mean-square (RMS) surface parameter.

4.4 UV-Visible Spectroscopy (UV-Vis)

UV-Visible spectroscopy was used to examine the optical properties of the films. The spectrometer is an Ocean Optics USB4000-UV-Vis shown in Figure 4.13 (a-b), equipped with a deuterium-tungsten source and Spectra Suite software to analyze the data. The source operates in wavelengths ranging from the UV region (190 nm) to visible region (800 nm). The transmission and absorption spectra of the β-Ga_2O_3 films were acquired through this technique.

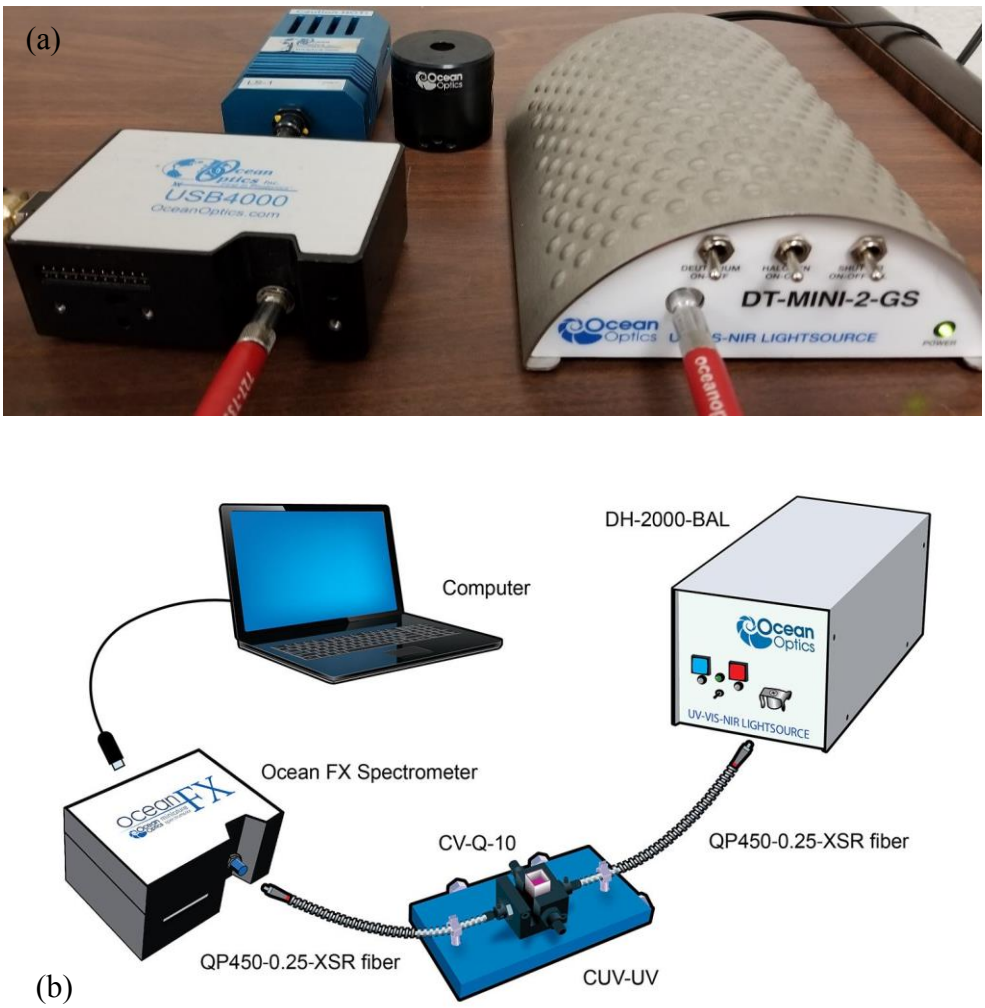

Figure 4.13 (a) Ocean Optics USB 4000-UV-Vis spectrometer, (b) set up by Ocean Optics [201].

A deuterium-tungsten light source is connected via an optical-fiber cable to a sample holder where the substrate is held. A cleaned sapphire or Ga_2O_3 substrate is used as the reference sample before starting the experiment. The light passes through the film and substrate and is collected by the spectrometer through a second optical-fiber cable, where the signal is amplified and sent to a computer for analysis.

The absorption spectrum is used to estimate the optical bandgap of the films by extrapolation of the linear region of a Tauc plot (Fig. 4.14) using the following equation:

$$(\alpha h\nu)^2 = B(h\nu - Eg) \tag{4.3}$$

$$\alpha = \left[\frac{1}{t}\right] \ln(10^A) \tag{4.4}$$

where t is the thickness of the film and

A is the absorbance.

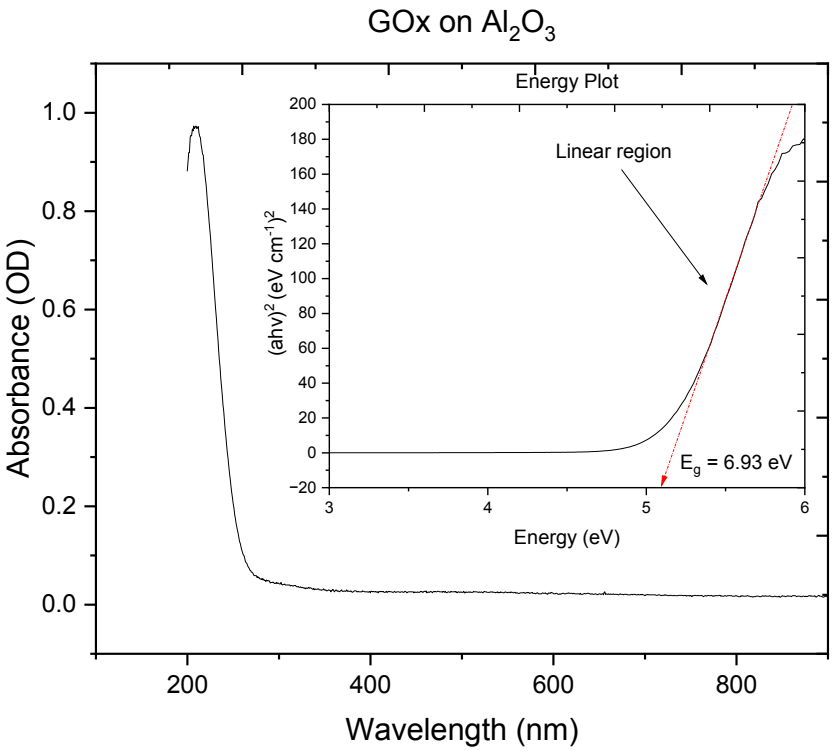

Figure 4.14 Absorption and Tauc plot of GO_x on Al_2O_3.

4.5 Current Voltage (I-V) Measurements

Current-voltage measurements were performed using a 2410 Keithley source meter. The instrument can source a voltage range of 200 mV to 1100 V, a current range of 1 μA to 1A (20 W output power), and a resistance measurement range of 0.2 Ω to 200 MΩ. It can sense 2-point probe and 4-point wire modes. Transmission line measurements on the ohmic contacts were taken using the 4-point wire mode in the multimeter, later discussed in section 4.5.1. Schottky contacts were 2-probed, the samples were mounted on a copper plate with a conductive silver paste. The base of the plate served as the negative terminal were the ohmic contact was connected. A probe on the Schottky contact served as the positive connection in the forward bias (section 4.5.2). Breakdown voltage was obtained using the same setup but reversing the polarization (section 4.5.3). To obtain a sweep scan during the IV measurements a program written in LabVIEW and KickStart software from Keithley was used. At least 300 data point were taken in each measurement in a voltage range of ±10 V. The station is mounted with a Nikon Eclipse ME600 microscope. Fig. 4.15 (a) shows a picture of the station used for electrical characterization and Fig. 4.15 (b) is the 2410 Keithley source meter.

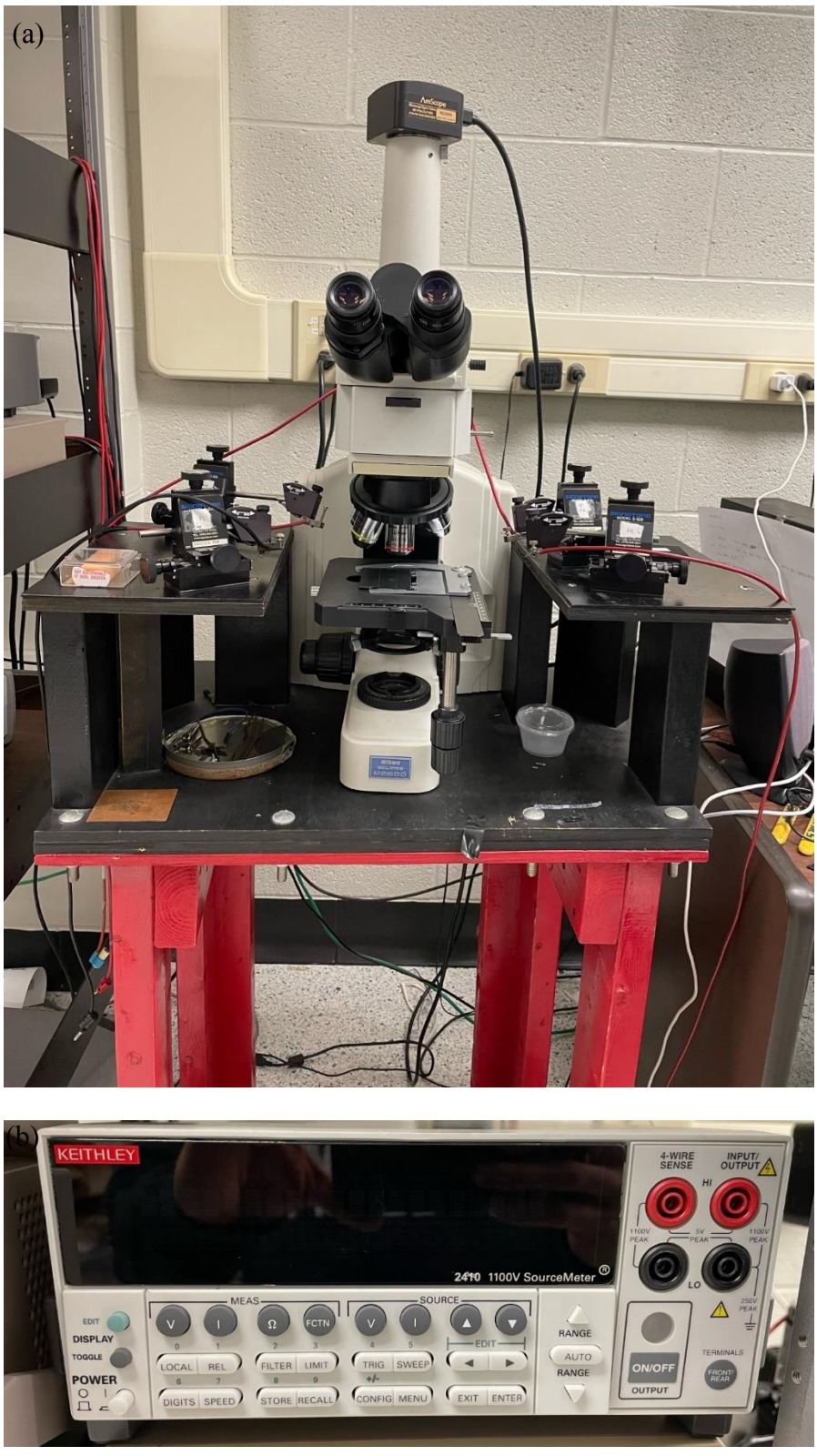

Figure 4.15 Probe station (a), 2410 Keithley source meter (b).

4.5.1 TLM Specific Resistivity Extraction

The transmission line method (TLM) was used for measuring the specific contact resistivity (Fig. 4.16). Several metal contacts were deposited using sputtering and the TLM mask shown in Fig. 3.2. The contacts are spaced apart starting from 7 μm to 74 μm increments of 10 μm. The area of the contact is 200 μm^2.

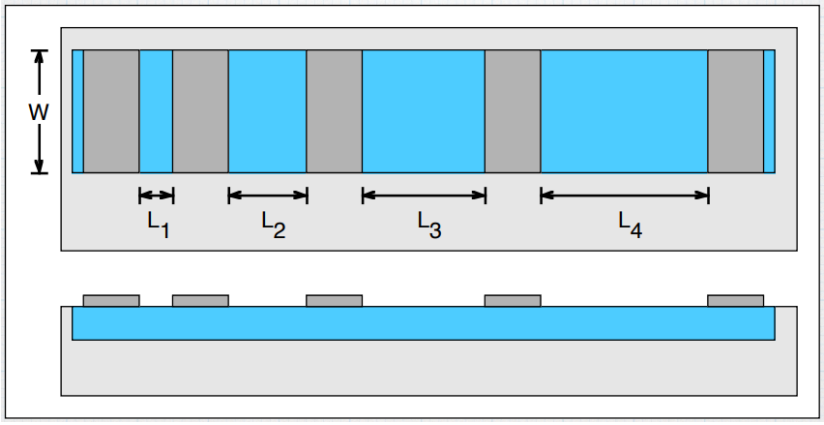

Figure 4.16 Transmission Line Measurement (TLM) [202].

Figure 4.17 shows how the probes are placed in the four-point probe configuration. A dc current is sourced across one of the gaps, and the voltage is measured directly between the current probes. The ratio gives the total resistance across the gap.

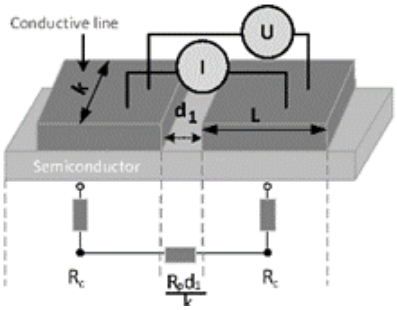

Figure 4.17 Four-point measurement.

Considering only two contacts spaced by a distance L, the measure of the total resistance is made of different components.

$$R_T = 2R_m + 2R_c + R_{semi} \tag{4.5}$$

where R_m is the resistance of the metal contacts, R_c is the resistance associated with the metal/semiconductor interface, and R_{semi} is the resistance of the semiconductor. In most cases the resistivity of the metal is small ($R_m \ll R_c$), and R_m can be ignore. Also, the resistance of the semiconductor is given by:

$$R_{semi} = R_S \frac{L}{W} \tag{4.6}$$

The total resistance becomes:

$$R_T = R_S \frac{L}{W} + 2R_c \tag{4.7}$$

This configuration suggests that a plot of the total resistance can be made, by measuring the resistance at different contact spaces. The measurement is performed using the 4-point probe method. The slope of this plot will yield $\frac{R_S}{W}$, the sheet resistance. The contact resistance, R_c, can be found by extrapolating back to L = 0. The transfer (L_T) length is the average distance that an electron (or hole) travels in the semiconductor beneath the contact before it flows up the metal contact, and it can be found by setting $R_T = 0$. Figure 4.18 shows an example of this plot.

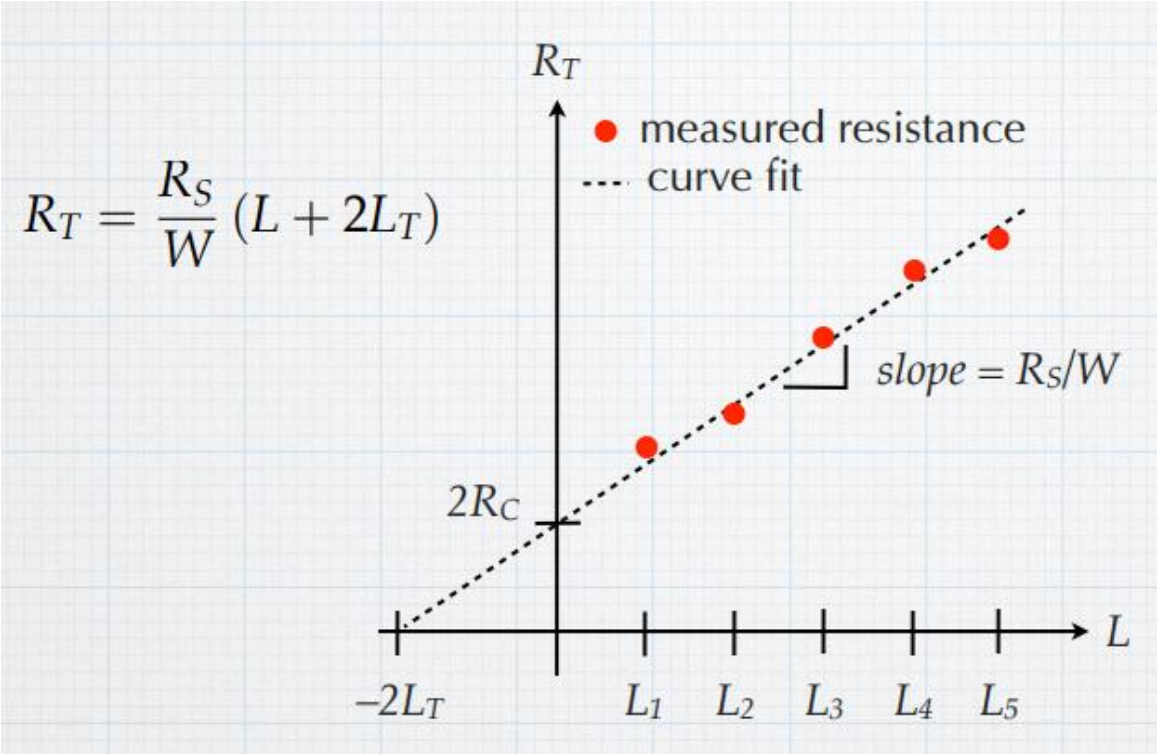

Figure 4.18 TLM plot, the Rs is extracted from the slope [202].

To be able to compare among the fabricated samples with different geometries, a measure that is independent of the contact geometry is the specific contact resistivity:

$$\rho_c = \left[\frac{\partial J}{\partial V}\right]^{-1}_{V=0} = R_c A_c = R_c L_T W \tag{4.8}$$

The specific contact resistivity is the product of the contact resistivity and the effective contact area, and it is expressed in terms of $\Omega \cdot cm^2$.

4.5.2 Schottky Diode Ideality Factor and Barrier Height Extraction

Schottky diodes follows the thermionic emission conduction mechanism. A Schottky diode under a forward bias has the following current-voltage (I-V) characteristics,

$$I_F = I_0 \, e^{\frac{qV_a}{nk_BT}} \tag{4.9}$$

where q is the electronic charge, V_a the voltage applied across the diode, k_B is the Boltzmann constant, T the absolute temperature, and I_F is the forward current. The saturation current (I_0), depends on the barrier height and the charge and it is given by,

$$I_0 = A \, A^{**} \, T^2 \, e^{\frac{-q\phi_B}{k_BT}} \tag{4.10}$$

where A is the effective area of the metal contact, A^{**} is the effective the Richardson's constant which has a value of $146 \; A \; cm^{-2}K^{-2}$ marked with an asterisk to distinguish from the effective area, ϕ_B is the Schottky barrier height potential. Figure 4.19 shows the I-V curve of a Schottky diode with metal contacts of Ti (50 nm)/Au (50 nm) as deposited in room temperature.

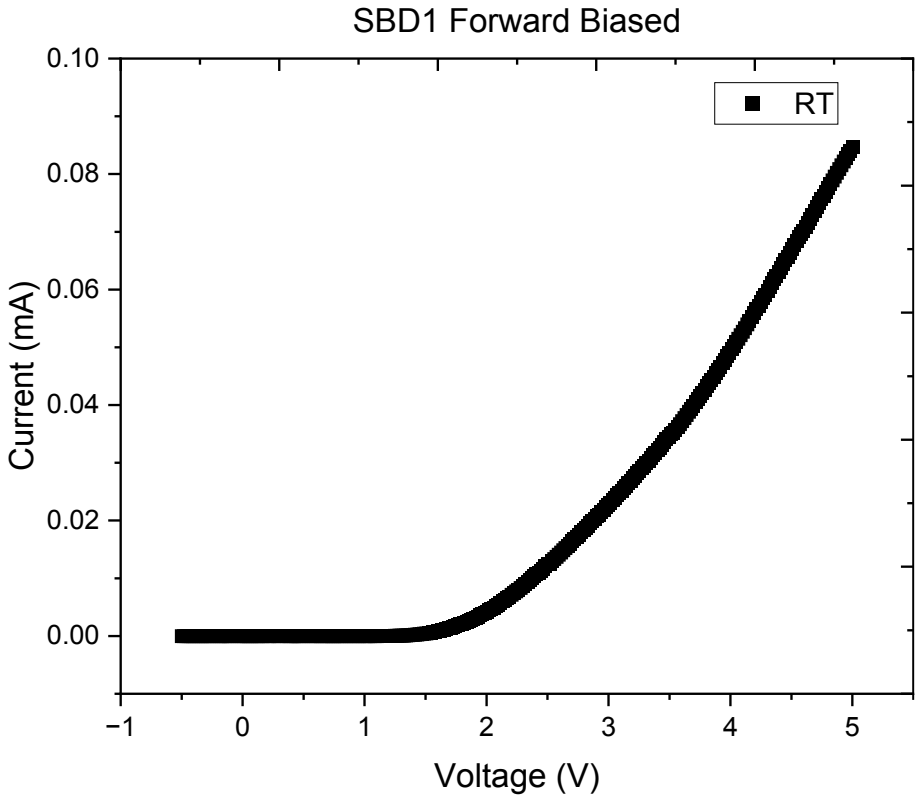

Figure 4.19 I-V curve of SBD3 deposited at room temperature.

By applying the natural logarithm (Fig. 4.20) on both sides of equation a and equation b,

$$\ln(I_F) = \ln(I_0) + \frac{q}{nk_BT}V_a \tag{4.11}$$

and,

$$\ln(I_0) = \ln(A \cdot A^{**} \cdot T^2) - \frac{q}{k_BT}\phi_B \tag{4.12}$$

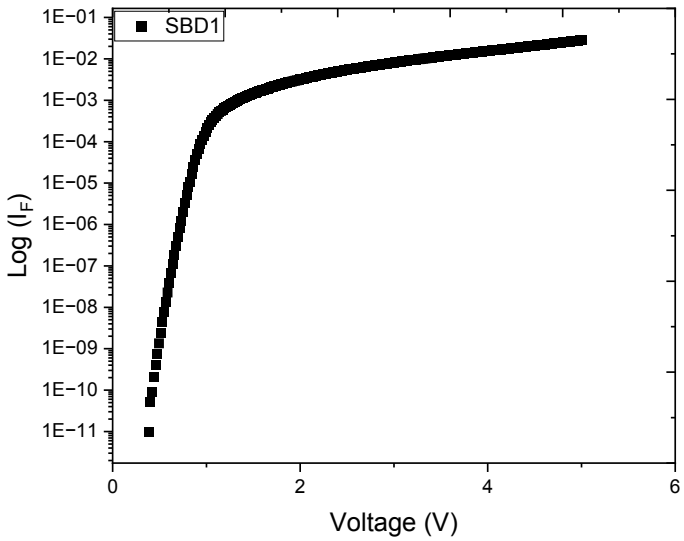

Figure 4.20 Logarithm of the forward current vs the applied voltage of SBD1 deposited at room temperature.

The procedure for extracting the ideality factor is the following, the log plot is trimmed until the only linear region is left. A fitting line with slope $\frac{q}{nk_BT}$ allows us to extract the ideality factor (n). Similarly, equation 4.12 can be used to extract the barrier height (ϕ_B). Figure 4.21 shows this linear fit from which the slope and intercept are extracted for the calculation of the ideality factor and barrier height for the SBD3 in the forward bias.

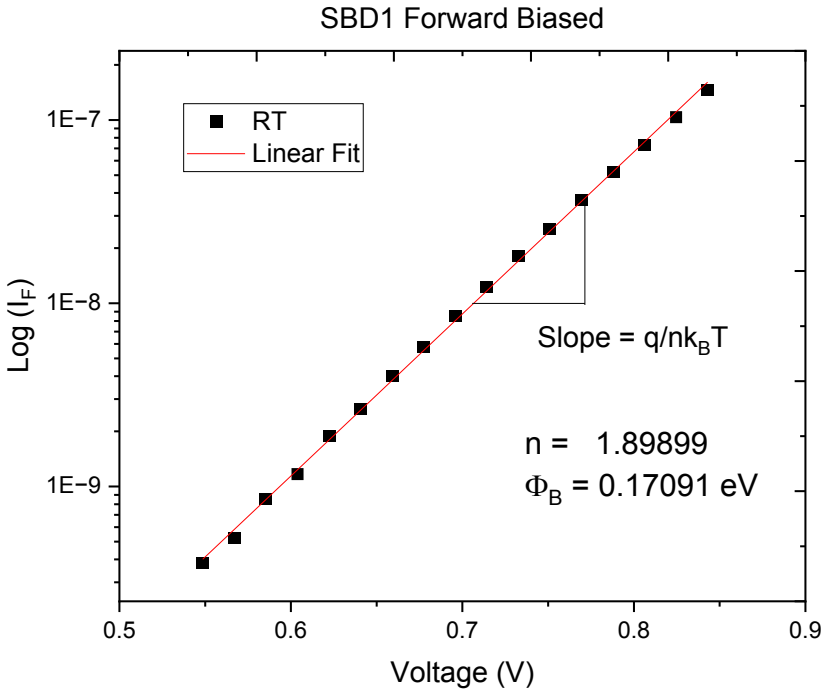

Figure 4.21 Linear fit of SBD3 as deposited and calculated ideality factor and barrier height.

4.5.3 Reverse Voltage Extraction

A nonzero current can be measured in a Schottky diode under a reverse bias. This current is due to a small portion of the electron being thermally excited over the Schottky barrier. The current remains constant under the applied voltage. Then it starts decreasing at higher reverse bias voltages. This is due to a slight lowering of Schottky barrier under the applied reverse voltage. As the bias keeps increasing, the depletion region starts breaking down, this process is known as electrical breakdown. It is destructive to the device as a material breaks down and a surge in the electrical current occurs, and the device becomes fully conductive under reverse bias. The breakdown voltage is the minimum reverse voltage that makes the device conduct significantly under reverse bias.

The breakdown voltage characteristics of an SBD depends on the carrier concentration as,

$$V_{BR} \sim \frac{\varepsilon_0 \varepsilon_m (E_c)^2}{2qN_D} \tag{4.13}$$

where E_c is the breakdown electric field, and N_D is the carrier concentration. Equation 4.12 can be a good estimate when all parameters are known for the specific sample. Instead, a direct measurement was performed on the contact to determine V_{BR}. As mentioned above this measurement is left for the end as it completely breaks down the material. Figure 4.22 shows a measurement of an SBD with a Schottky contact made of Ni (50 nm)/Au (50 nm) under reverse bias, the breakdown voltage is measured to be 45 V.

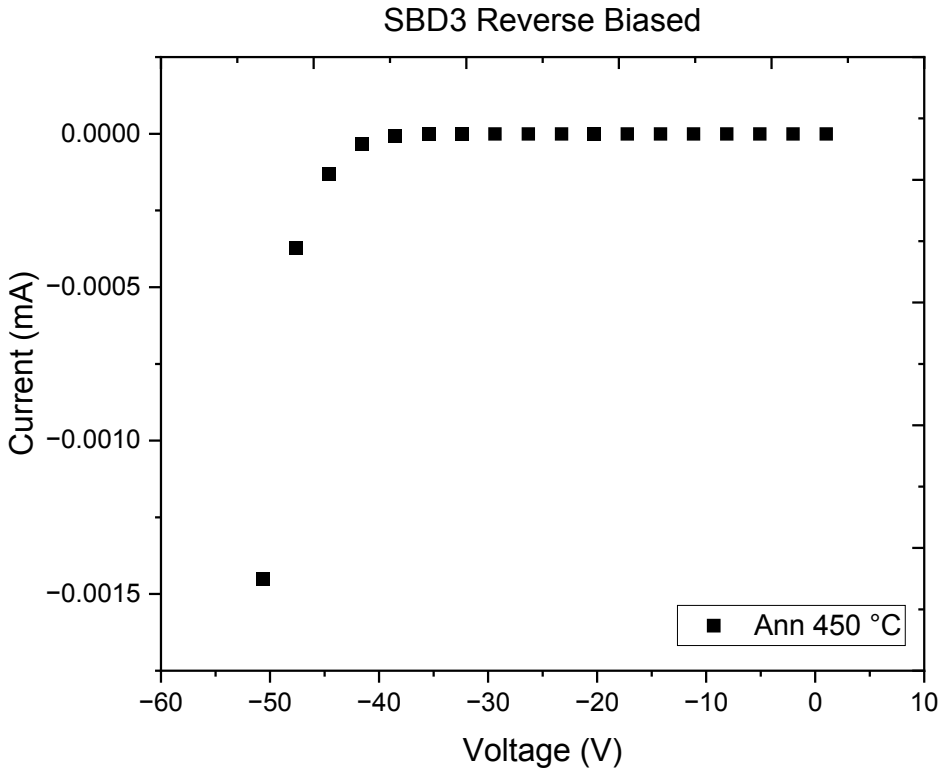

Figure 4.22 SBD3 Reverse Bias, V_{BR} = 45 V.

4.6 Hall Effect

Hall measurements were performed using an ECOPIA HMS-3000 Hall effect measurement system (Fig. 4.24 (a)). The measurements are based on the Van de Pauw method (Fig. 4.23). Square metal contacts of Ti (20 nm)/Au (80 nm) were deposited on the corners of the β-Ga_2O_3 substrates and annealed in Ar ambient up to 600 °C for 6 min to ensure ohmic behavior. This instrument uses the linear region of the IV-curve of the fabricated contacts to estimate the bulk concentration of the carriers in the material, mobility, conductivity, and average Hall coefficient, among other useful parameters.

The principle is as follows, a substrate with he deposited contacts is placed in a spring clip board (SPCB) shown in Fig. 4.24 (c). which facilitates a contact connection without the need of wire boding. The measurements were conducted with a magnetic field of B = 1.05 T or 0.58 T. The SPCB is connected to a headboard to be read by the computer, while the magnet sits around it as shown in Fig. 4.24 (b).

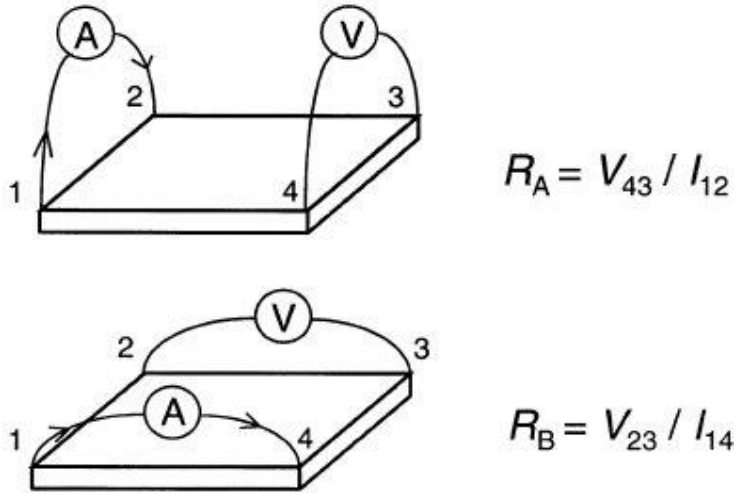

Figure 4.23 Measurement of a square conductivity sample in the Van der Pauw geometry [203].

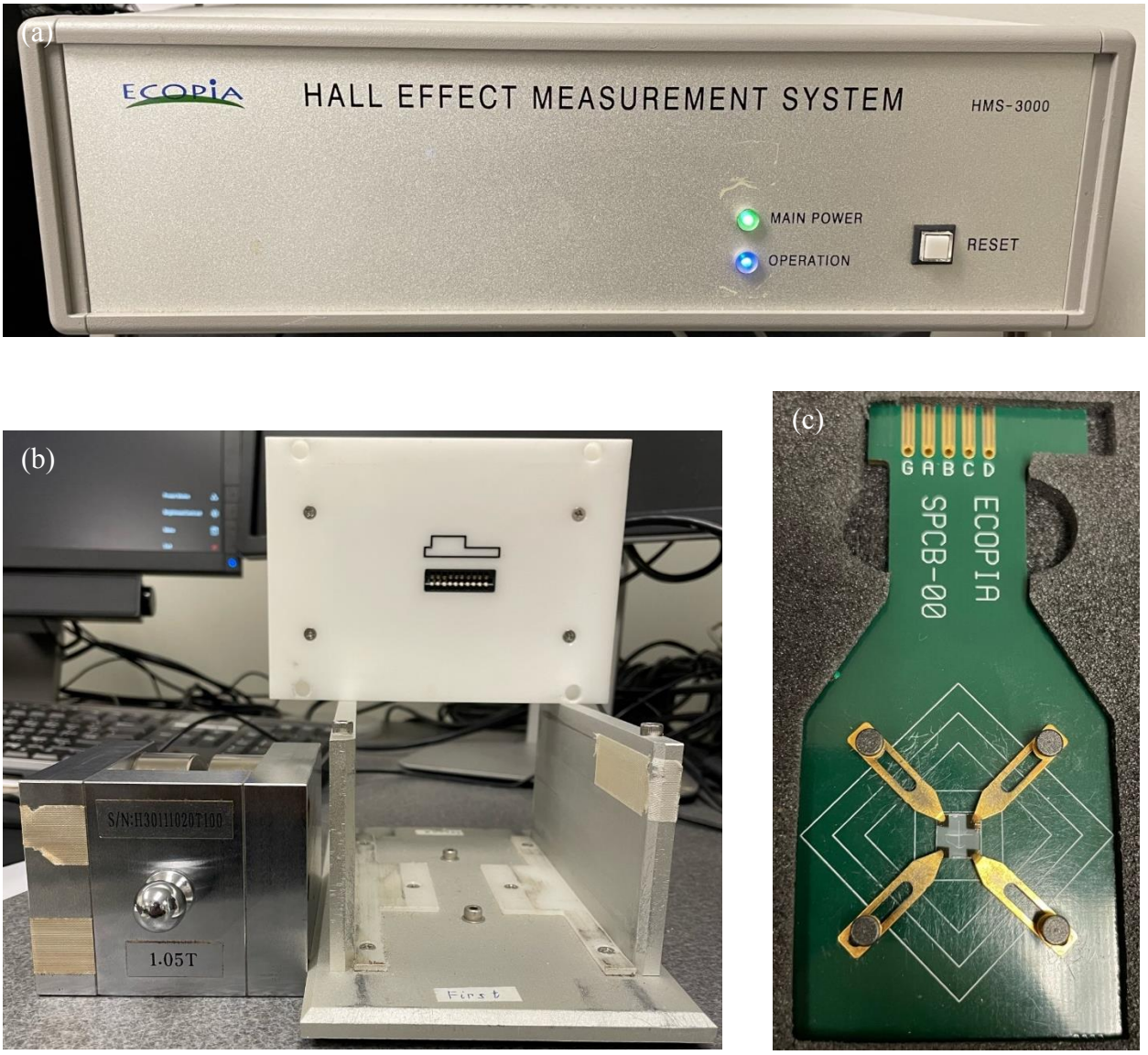

Figure 4.24 (a) ECOPIA HMS-3000 Hall effect measurement system, (b) Magnet and headboard, and (c) SPCB holder.

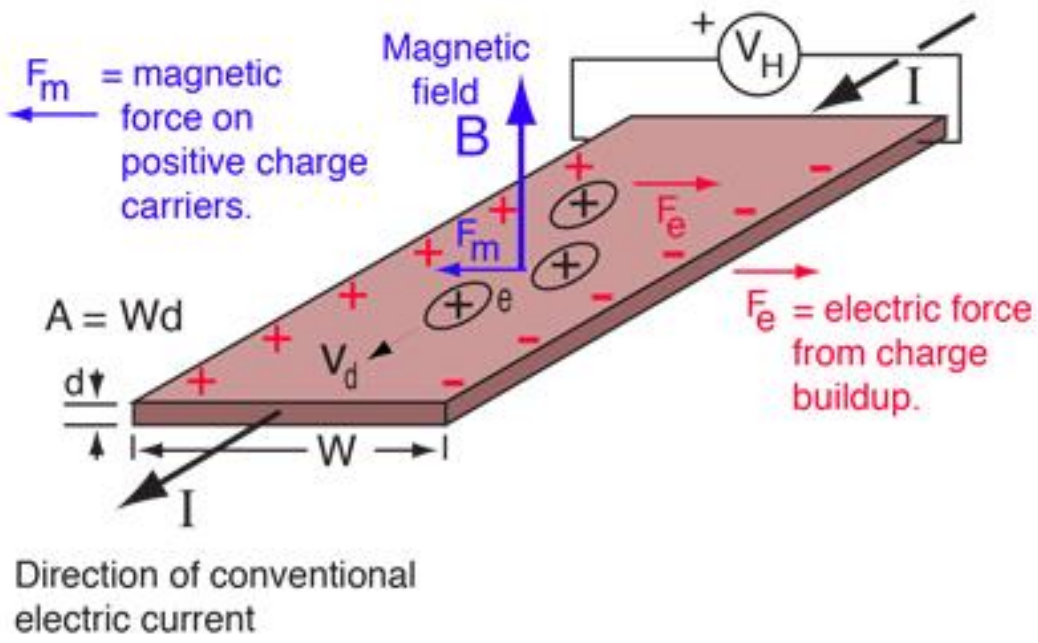

Figure 4.25 Hall effect diagram [204].

The Hall effect measurement uses a small current (~1 mA) applied to the semiconductor through the deposited ohmic contacts. The current in this example is chosen to be conventional. The sample is placed in a magnetic field (a magnet of 1 T), which is perpendicular to the current flow. This exerts a transversal force on the moving charge carriers, which are deflected and pushed to one side of the conductor. Depending on the carrier type (i.e., n-type or p-type), a charge will build up in one side of the semiconductor. In the diagram shown in Figure 4.25, the carriers are positively charged holes, therefore a positive charge will build up on the left of the semiconductor. Once this process reaches equilibrium, a transverse voltage known as the Hall voltage (V_H) is generated. The Hall voltage is related to the current applied, the magnetic field, carrier concentration, the elementary charge, and the thickness of the film:

$$V_H = \frac{IB}{ned} \tag{4.14}$$

The carrier concentration can be expressed in terms of R_H, the Hall coefficient:

$$n = \frac{1}{R_H e} \tag{4.15}$$

The Hall coefficient is characteristic of the material from which the semiconductor is made, particularly, its sign will provide information about the type of carrier within the material being an n-type or p-type material. Notice that R_H depends on parameters controlled by the ECOPIA HMS-3000 system, such as the applied current and the magnetic field. Figure 2.26 displays the control panel of the ECOPIA HMS-3000 Hall effect software, providing users with the interface to input all necessary parameters for conducting a test. The result panel shows all calculated quantities obtained from the test.

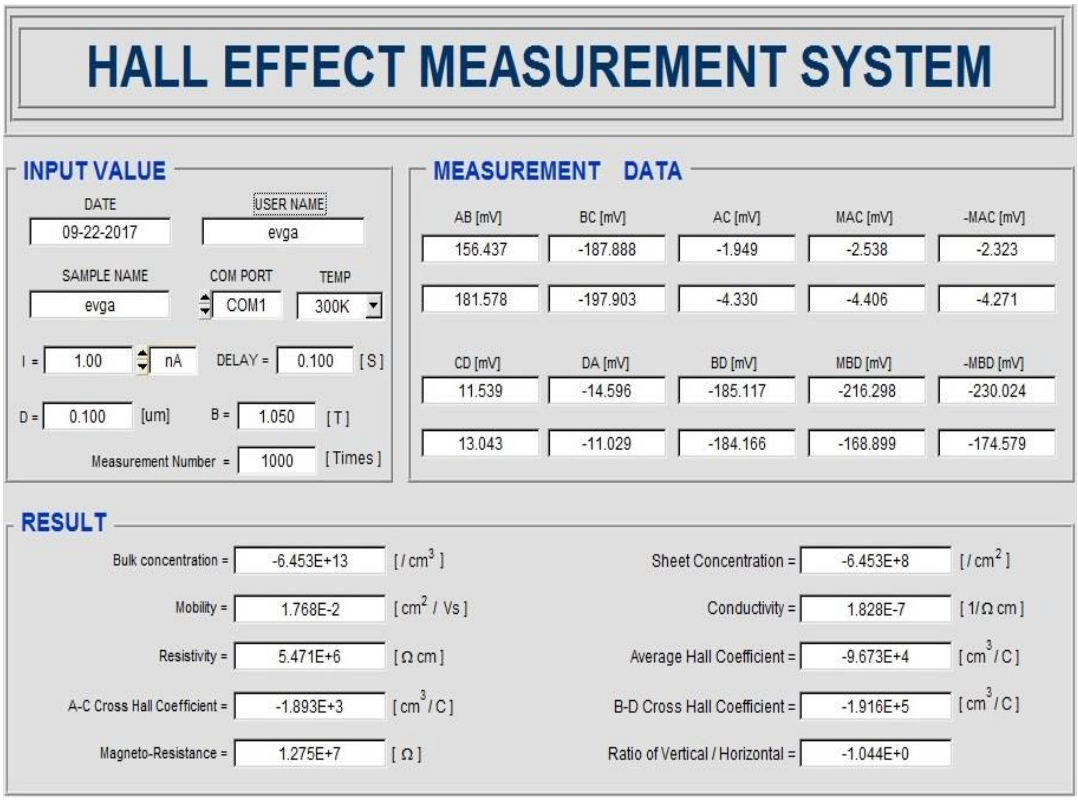

Figure 4.26 Hall effect output panel.

5. Results and Discussion

5.1 Research Design

This chapter presents the results and discussion of results obtained during this dissertation work. The specific aims are outlined as follows: first, to grow β-Ga_2O_3 films on sapphire substrates (section 5.2) and native β-Ga_2O_3 using rf sputtering (section 5.3); second, to produce doped and undoped β-Ga_2O_3 films (Section 5.4); third, to grow Lu_2O_3/Ga_2O_3 and B_2O_3/Ga_2O_3 alloy films on $(\bar{2}\ 0\ 1)$ UID or Sn-doped Ga_2O_3 and Al_2O_3 substrates to manipulate the original bandgap of Ga_2O_3 (section 5.5). The dissertation also aims to gather microstructural, morphological, compositional, and optical data from various characterization methods such as XRD, AFM, SEM, EDS, and UV-Vis for all experiments mentioned above. Subsequently, it intends to correlate the effects of the varying parameters to optimize the films. Furthermore, the developed films will be utilized to fabricate Schottky barrier diodes, and the electrical characterization of these fabricated devices will be carried out (section 5.6).

5.2 Optimization of heteroepitaxial growth of Ga_2O_3 films on sapphire substrates

5.2.1 Introduction

As discussed in the literature review on sputtering, the β-Ga_2O_3 films are highly sensitive to growth conditions such as temperature, deposition gas, and to post annealing treatment. Amorphous or crystalline β-Ga_2O_3 can be grown on c-plane sapphire depending on the oxygen content during the deposition at 400 - 500 °C temperature range. A question that may arise is why sapphire substrate is considered a suitable choice for growing $(\bar{2}01)$ β-Ga_2O_3 films. In contrast to alumina, sapphire is single crystal material that possess trigonal (rhombohedral) crystal structure. Achievement of high quality crystalline β-Ga_2O_3 films deposited on c-plane Al_2O_3 is made possible by their relatively small lattice mismatch of 6.12% and nearly equal thermal expansion coefficients (α_c) of 3.15 x 10^{-6} K^{-1} (for Ga_2O_3) and 4.3 x 10^{-6} K^{-1} (for Al_2O_3) [205,206]. Seiler et al. used pole figure measurements to deduct various epitaxial relationships between Ga_2O_3 phases and Al_2O_3 [207]. Saphire (0001) is a polar plane with either oxygen or aluminum atoms. Consequently, the first plane of gallium oxide would be preferentially a polar plane, with either oxygen or gallium plane depending upon the nature of the surface plane of the sapphire substrate. The $(\bar{2}01)$ plane of β-Ga_2O_3 is a polar plane, therefore the preferential growth of $(\bar{2}01)$ would be favored with respect to other non-polar planes of β-Ga_2O_3. Also, the Ga ions in the $(\bar{2}01)$ are all located in a plane forming an irregular hexagonal configuration similar to that present in $(0001)Al_2O_3$. Moreover, Al_2O_3 substrates are relatively cheap and commercially available with wafers going to 11.8 inches in diameter. In this section, heteroepitaxial growth of β-Ga_2O_3 on (0001) sapphire substrates using radio frequency magnetron sputtering was performed to study the effects of deposition temperature, deposition gas composition, and post annealing treatment on the film properties.

5.2.2 Experimental Procedure

The surfaces of the c-plane double-side polished sapphire substrates were first prepared by degrease-cleaning in boiling acetone, alcohol followed by rinsing in de-ionized (DI) water. The samples were then dipped in buffered HF acid for 10 min and rinsed again in DI-water, dried and mounted on a substrate heater, loaded in a vacuum chamber, and evacuated to 2 x 10^{-7} Torr by a turbo molecular pump. Right before deposition, the sapphire substrates were subjected to thermal desorption by heating at 500 °C for 30 min in UHP O_2, a process previously found essential for sapphire substrate preparation [168]. All the gases used for deposition or for annealing were of UHP grade (> 99.99% pure). The films in this study were deposited from a 2-inch-diameter high purity (99.99%) Ga_2O_3 ceramic target and about 7 cm was maintained between the target and the substrate. A 15-min pre-sputtering was performed to remove any impurities from the target, followed by a deposition of about 120 min for each sample. The gas pressure was set at 10 mTorr, a flow rate of 5.0 standard cubic centimeters per minute at STP and a radio frequency (rf) power of 100 watts and the thicknesses of the resulting films were 90-200 nm.

The first set of samples prepared were of films deposited at different substrate temperatures from 20 °C to 900 °C in pure Ar. The second set of samples was of films deposited at 500 °C, but using different percent mixtures of Ar/O_2 comprising 100/0, 80/20, 50/50, 20/80 and 0/100. To further investigate the effects of deposition temperature in 80/20 and 50/50 Ar/O_2 mixtures, a third and fourth set of samples were deposited in these two mixtures, respectively, while varying the annealing temperature. A 2-inch diameter Blue Wave BN substrate heater was used in which the temperature is determined using a thermocouple placed in direct contact with the substrate. Lastly, further investigation was continued the film deposited in Ar at 400 °C. This sample was diced into several pieces and annealed in N_2 at 400-900 °C for 15 min.

The microstructures of the resulting films were characterized using XRD measurements with a Bruker-Prospector diffractometer (Bruker AXS, Inc., Madison, Wisconsin, USA) fitted with a high brightness Cu Incoatec microsource. The optical properties of the films were investigated using the Ocean Optics QE65000 spectrometer with a deuterium halogen UV-VIS-NIR light source (DT-MINI-2-GS). The compositional property of the films was determined from energy dispersive spectrometry (EDS) measurements using a JEOL JIB-4500 scanning electron microscope fitted with Apollo XV detector (EDAX Inc.). Surface morphology of the films was analyzed using a 5500 Keysight scanning probe microscope (SPM). To determine the thickness of the films, several images of the cross-section of each film were obtained using a backscattering detector in the JEOL JSM 7600F field emission scanning electron microscope.

5.2.3 Effects of Deposition Temperature in Ga_2O_3 Films Deposited in Ar.

Figure 5.1 shows the XRD scans of the β-Ga_2O_3 films deposited on c-plane sapphire substrates at different temperatures from 20 °C to 900 °C using Ar. The thickness of each film is indicated in the corresponding legend. For the films deposited in Ar, the substrate temperature of 400 °C gives the best crystalline quality with appearance of higher intensity diffraction peaks at 18.3°, 37.1°, 57.8° corresponding to ($\bar{2}$ 0 1), ($\bar{4}$ 0 2) and ($\bar{6}$ 0 3) planes of β-Ga_2O_3, respectively. This film has a thickness of 134 nm, less than that of the rest of the films in this group.

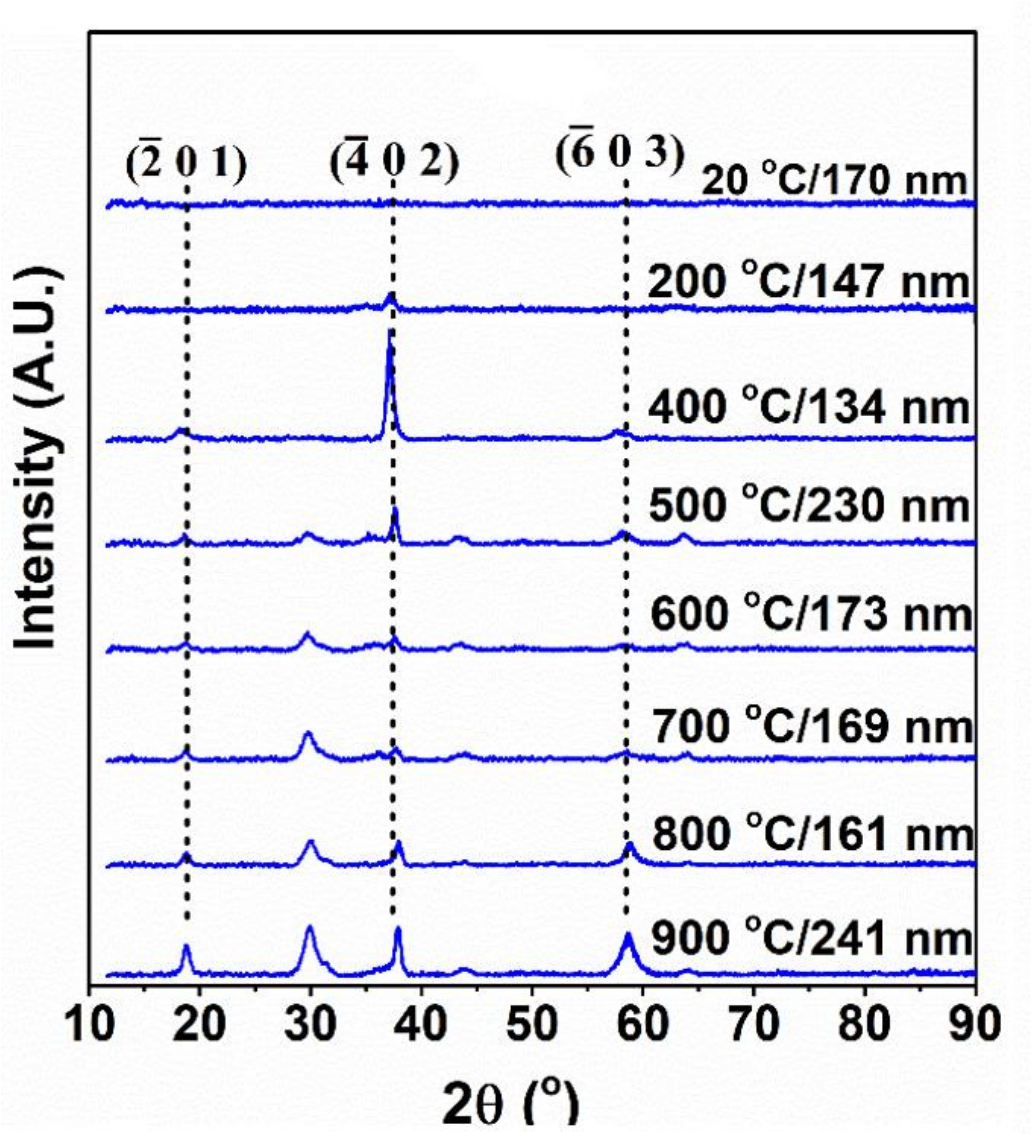

Figure 5.1 XRD scans for films deposited at various temperatures in Ar atmosphere.

Films deposited at temperatures higher than 400 °C were polycrystalline and showed additional peaks at peaks at 30.0° and 63.7° which belong to the (400) and (800) planes of β-Ga_2O_3, respectively [62,208–210]. Additional peak appearing at 43.8° could be associated with a reflection from (311) plane. The film deposited at room temperature (20 °C) showed no diffraction peak, indicating amorphous quality, while appearance of a small ($\bar{4}$ 0 2) peak is observed on the

film deposited at 200 °C. These results indicate that the optimum substrate temperatures for formation of high quality crystalline β-Ga_2O_3 films is 400 °C when using pure Ar. A temperature of 500 °C has been previously found to be the optimum substrate temperature for crystallization with a clear out-of-plane orientation of β-Ga_2O_3 with the sapphire substrate using Ar [60,211].

The deposited samples were carefully cleaved to expose the film cross-section and then measured using SEM backscatter. Figure 5.2 shows SEM backscatter images for films at (a) 20 °C, (b) 400 °C and (c) 900 °C. No direct correlation between film thickness and deposition temperature was observed. In fact, the variation of the thickness of the multiple films could be a result of non-uniformity in the film thickness across each sapphire substrate (1/4 of 2-inch wafer) during the deposition. This thickness non-uniformity is usually reduced by rotation of the sample during deposition, and in our set up this capability is not available. Nevertheless, Zhang, et al and Sun, et al showed that increase in the thickness of Ga_2O_3 films only increases the intensity of XRD peaks [212,213] Therefore, due to the variation in the thickness of our film, no comparison of the XRD peak intensities is made. Several researchers have reported optimum temperatures of 300 °C to 600 °C for sputter-deposited β-Ga_2O_3 films on c-plane sapphire substrate.

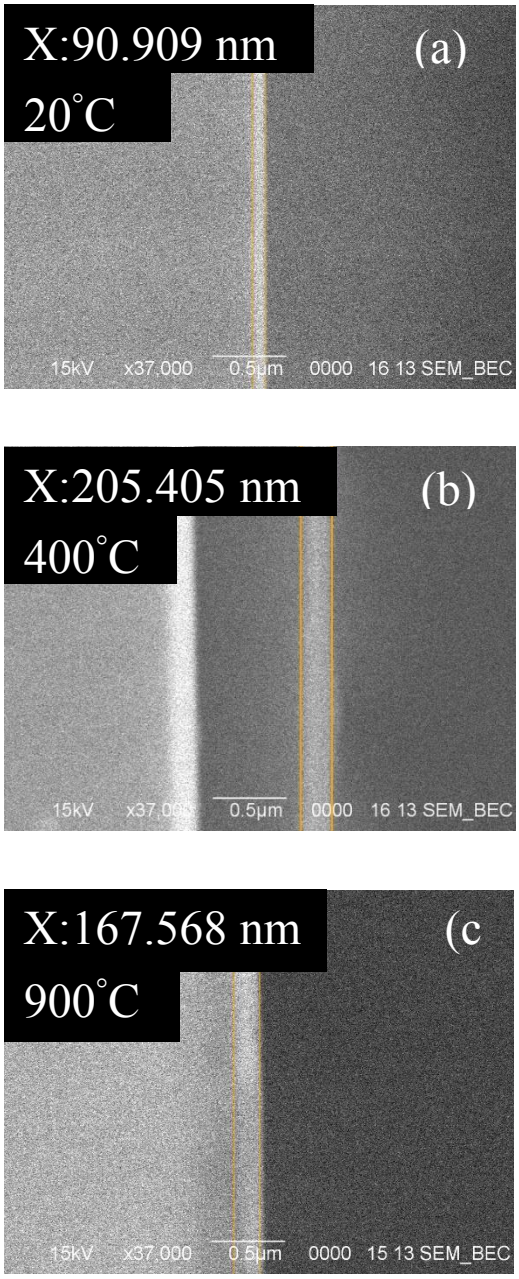

Figure 5.2 SEM backscatter images for films at (a) 20 °C, (b) 400 °C and (c) 900 °C.

AFM 10 x 10 μm scans on the films deposited in Ar at different temperatures were taken to extract the RMS roughness parameter (Fig. 5.3). Two directions were profiled namely, a direction parallel to the scan direction (RMS ∥) and a direction perpendicular to the scan direction (RMS ⊥) . The roughness was extracted from these two profiles using Gwyddion 2.55 software (Released 2019-11-04) and is shown in Fig. 5.4 RMS ∥ value decreases with temperature from 0.184 nm at room temperature to 0.1 nm at 400 °C, and then increases with temperature up to 0.18 nm at 900 °C. This indicates that the film deposited at 400 °C in Ar has an improved surface morphology, which agrees with the results obtained by XRD in Fig. 5.1. Kumar et al. observed an increase in the roughness and grain size of the β-Ga_2O_3 films deposited at temperatures higher than 400 °C via high-resolution SEM and attributed the change in morphology to an increase in the adatom mobility due to increasing thermal energy [60].

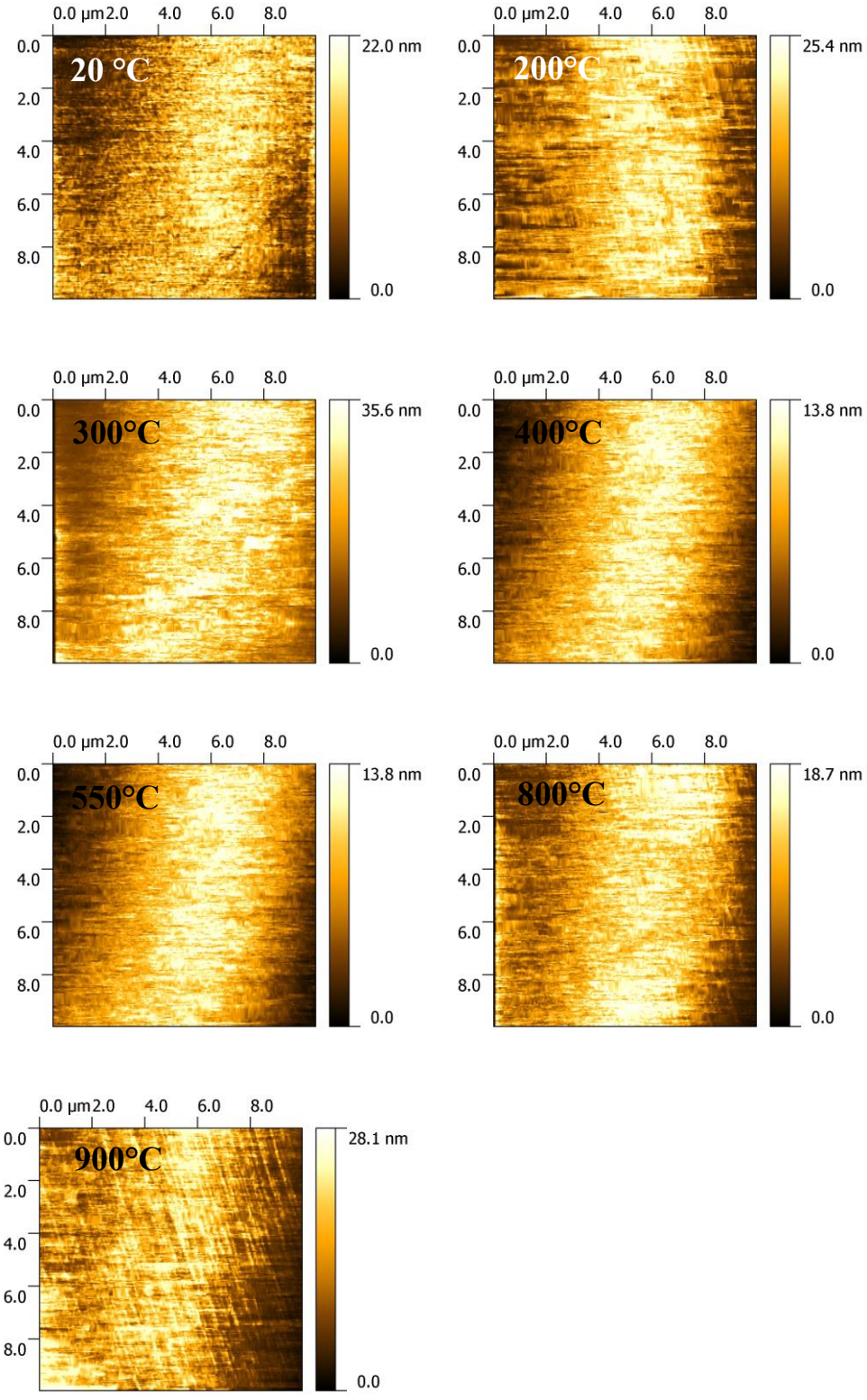

Figure 5.3 AFM 10 x 10 µm scans of GOX films grown on sapphire at different deposition temperatures in Ar atmosphere.

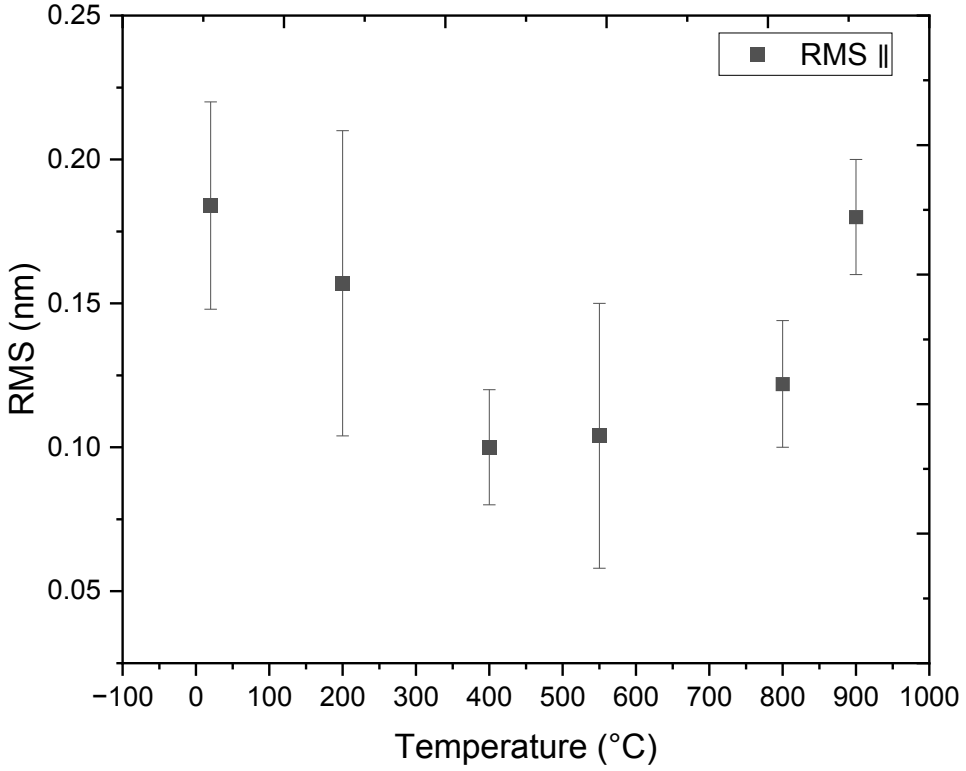

Figure 5.4 RMS values for GOX films grown on sapphire at different deposition temperatures in Ar atmosphere. RMS ‖ is a profile parallel to the scan direction.

The plots shown in Fig. 5.5 (a) - (c) are data from Ga_2O_3 films deposited in Ar at different temperatures. Figure. 5.5 (a) shows the optical transmittance of these films, which falls at 90 - 95%. The transmittance of 100% in this plot is from a sapphire substrate only. To determine the optical bandgap of the films a Tauc plot was constructed as discussed in section 4.4 and is shown in Fig. 5.5 (c). The collected data show that the bandgap decreases from a value of 5.03 eV for the film deposited at 20 °C to 4.96 eV for the film deposited at 600 °C after which the bandgap starts to increase. Each data point represents the average from three runs and the error bars came from the largest deviations from the average values.

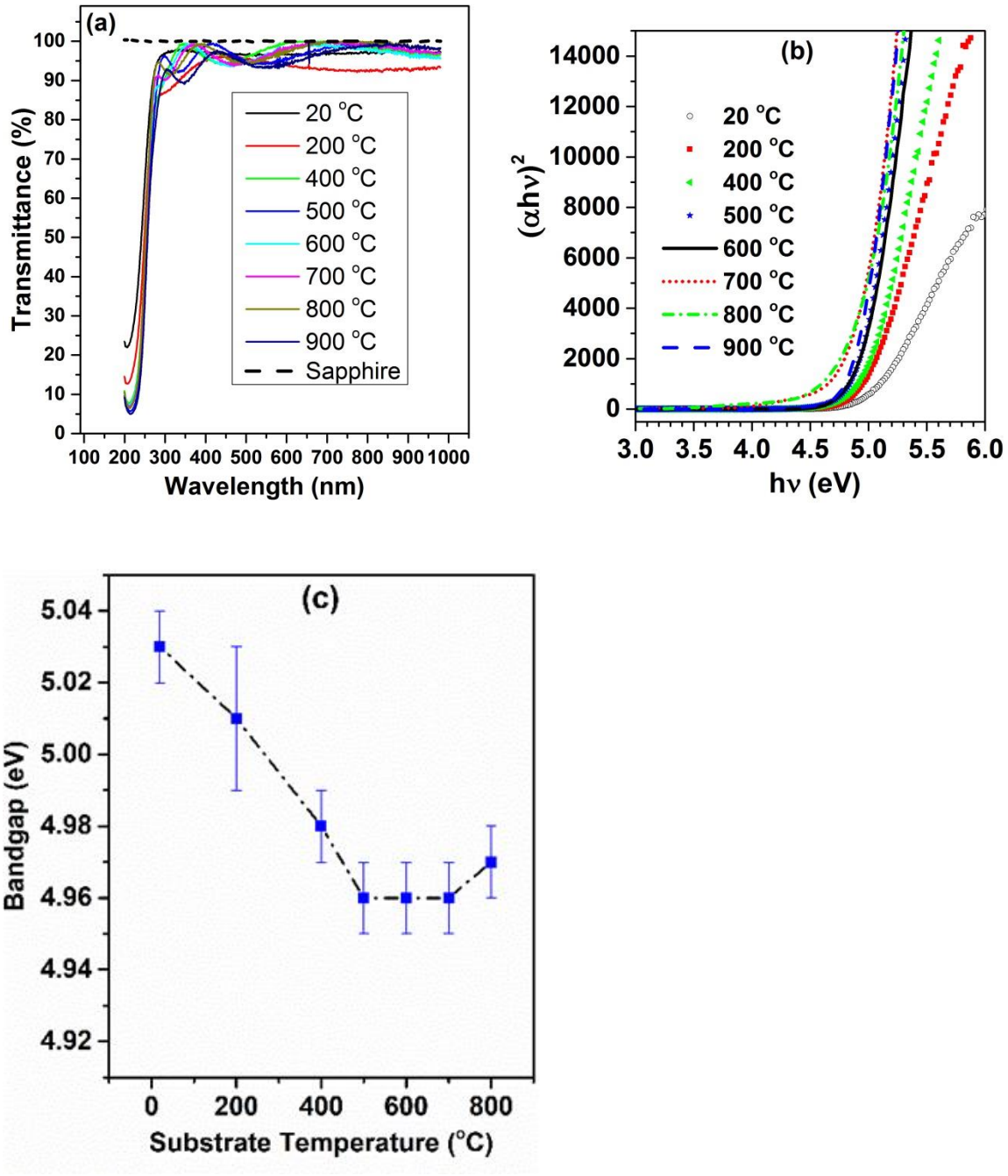

Figure 5.5 Plots of data obtained from Ga_2O_3 films deposited in Ar at different temperatures showing: (a) the optical transmittance of as-deposited films, (b) the variation of $(\alpha h\nu)^2$ versus photon energy ($h\nu$), (c) optical bandgap versus the deposition temperature.

Kumar et al. also observed similar trend in which the optical bandgap of β-Ga_2O_3 deposited using Ar was found to decrease with increase in deposition temperature [60]. The higher values of the bandgap at lower substrate temperatures were attributed to the combined effect of the presence of excess O_2 or amorphous nature of the film, which could explain the case for the films obtained. In the reported study, films deposited above 300 °C were found to be stoichiometric.

5.2.4 Target Poisoning

While depositing the Ga_2O_3 films, the target started to develop a coloration that transferred to the films making it impossible consistent optical data. The issue at hand necessitated the incorporation of O_2 into the gas mixture. This report aims to delve into the impact of gas composition on the composition of Ga_2O_3 films through Energy Dispersive Spectroscopy (EDS) analysis. A qualitative comparison of the target under different gas mixtures is provided to understand the variations in film composition, along with a quantitative analysis of the Ga/O content in the films.

The parameters for the experiments were set as follows: a deposition rate of 2.0 Å/s, a deposition time of 3.0 hours, and varying gas flow ratios of 10:0, 80:20, and 50:50 for Ar:O2. The power used was 100W, the material under study was Ga_2O_3, and the temperature during deposition was maintained at 25 °C. These parameters were carefully selected to investigate the influence of gas composition on the resulting composition of Ga_2O_3 films, shedding light on the importance of oxygen incorporation in the gas mixture for desired film characteristics.

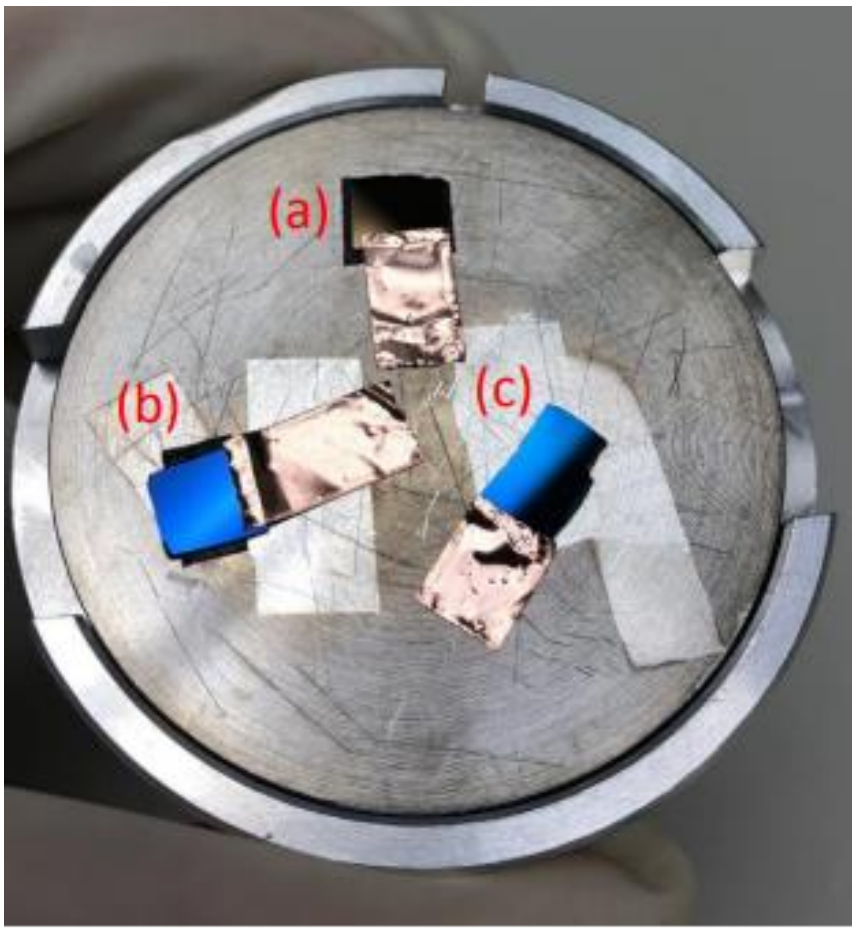

Figure 5.6 EDS Holder containing samples (a) 50:50, (b) 80:20, (c) 100:0 Ar/O_2.

Altering the gas composition has a "poisoning" effect on the target as the oxygen concentration in the mixture decreases. This issue transfers into the deposited films. This effect can be attributed to the depletion of oxygen during the deposition process. In Figure 5.6, the samples are depicted mounted on the Energy Dispersive Spectroscopy (EDS) holder. The sample deposited with 100% Ar (Fig. 5.6 (c)) displays a gradient from pink to blue, indicating variations in thickness. On the other hand, the sample deposited with 50% Ar exhibits a yellow color, indicating a high oxygen content (Fig. 5.6 (a)). Lastly, the sample deposited with 80% Ar shows a blue color (Fig. 5.6 (b)). These color variations provide visual insights into the influence of gas composition on the resulting film characteristics.

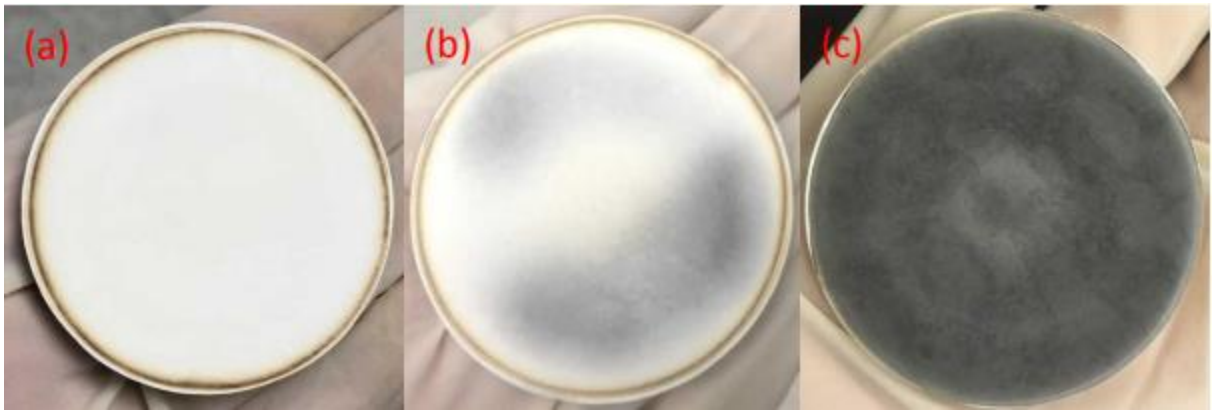

Figure 5.7 Effect of the gas mixture on the appearance of the target: (a) 50:50, (b) 80:20, (c) 100:0 Ar/O_2.

The impact of gas composition is particularly noticeable on the target. Decreasing oxygen content leads to target poisoning due to oxygen depletion as it can be clearly seemed in Fig. 5.7. Electron Dispersive Spectroscopy (EDS) was conducted on three samples using consistent parameters for ZAF method comparison (Fig. 5.8). The sample deposited with 100% Ar displayed a lower oxygen percentage but unexpectedly showed an iron (Fe) peak of unknown origin. The 80% Ar sample exhibited a slight increase in oxygen content and was notably thinner than the 100% Ar sample, as indicated by a silicon substrate (Si) peak.

Conversely, the 50% Ar sample showed the highest oxygen content and the strongest Si peak. This suggests that oxygen levels in the gas mixture affect deposition rates, even with the same deposition time and distance from the target. Table 5.1 summarizes the weight percentages of oxygen in all samples, considering only gallium and oxygen as the elements present in the films. Generally, oxygen content increases with higher percentages of oxygen in the mixture.

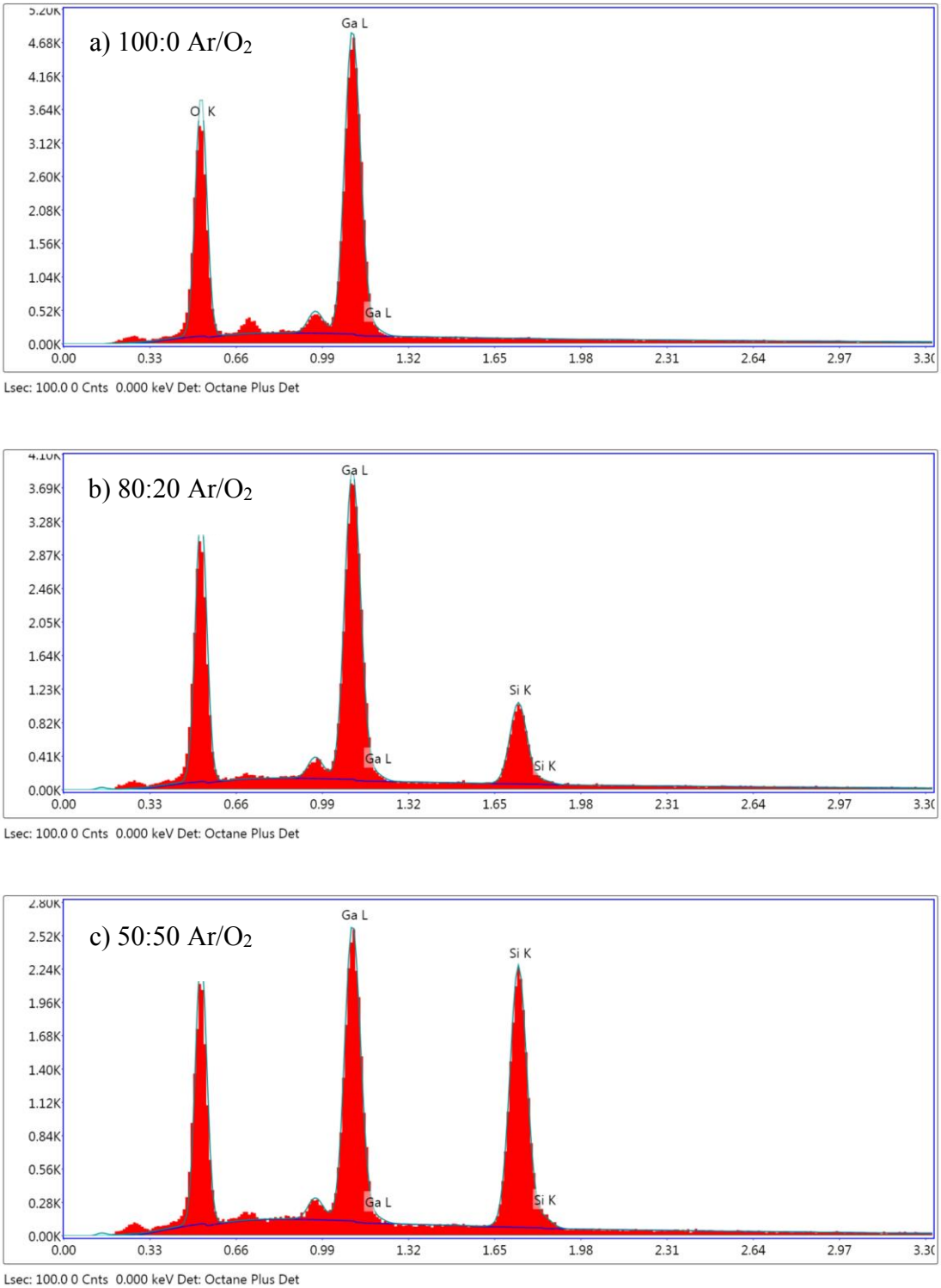

Figure 5.8 EDS of films deposited in a) 100:0 Ar/O_2, b) 80:20 Ar/O_2, and c) 50:50 Ar/O_2.

Ar/O_2 % Ratio	**Atomic %**		**Ga/O**
	Ga(L)	**O**(K)	
100/0	41.28	58.72	0.7036
80/20	39.05	60.96	0.6398
50/50	38.30	61.70	0.6214

Table 5.1 EDS elemental composition of Ga_2O_3 films deposited on Si at 25 °C using different Ar/O_2 mixtures.

5.2.5 Effects of $Ar:O_2$ ratio During Deposition

The film microstructure is established by the mobility of the sputtered atomic species on the surface of the substrate, which in turn is determined by several factors in the sputtering process. Proper optimization of these parameters can therefore be used to tailor the film quality. Explanation for preferential growth directions of sputtered films has been proposed comprising the thermodynamic, kinetic and atomistic models [214]. In the first model, the minimum energy of the substrate-film system (thermodynamic equilibrium) determines the growth direction of the film [215]. In the kinetic model, the eventual orientation of the film is that in which the species have the least mobility, caused by the substrate temperature [216]. In the atomistic model, orientation of the films deposited at high temperatures is determined by the thermodynamics of the growth planes, in which the one with the lower energy is preferred [217]. For these reasons, the change in the deposition gas composition will in turn produce sputtered species with varied

kinetic energies, and the change in substrate temperature will contribute to the kinetics of the species as they condense on the surface of the substrate. In either case, optimum film microcrystalline structures are obtained at different sputtering conditions. Figure 5.9 shows XRD scans of Ga_2O_3 films deposited at distinct Ar/O_2 ratios at 500 °C.

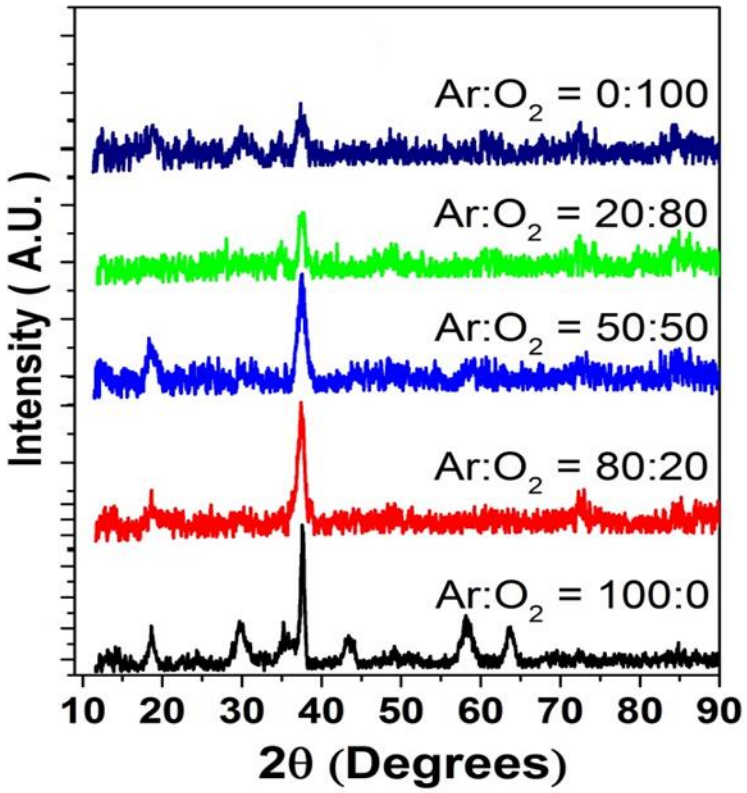

Figure 5.9 XRD scans for films deposited at 500 °C using various $Ar:O_2$ composition ratios. (all samples were deposited at 500 °C).

The XRD scans reveal that good crystallinity can be achieved at 50:50 and 80:20 Ar/O_2 mixture at a deposition temperature of 500 °C. Further increased in the oxygen content makes the films amorphous and the peaks belonging to β-Ga_2O_3 get attenuated. Table 5.2 shows the elemental composition obtained by EDS analysis of Ga_2O_3 films deposited at 500 °C using different Ar/O_2

mixtures. The results show that using higher Ar content in the deposition gas produces correspondingly higher Ga content in the films. This could be due to increased preferential sputtering of Ga arising from increased kinetic energy of the sputtering ionic species when more Ar atoms with larger mass compared to O_2 is present in the gas mixture.

Table 5.2 EDS elemental composition of Ga_2O_3 films deposited on sapphire at 500 °C using different Ar/O_2 mixtures.

Ar/O_2 % Ratio	**Atomic %**			**Ga/O**
	Ga(L)	**O**(K)	**Al**(K)	
100/0	35.98	60.32	3.70	0.60
80/20	19.44	61.64	18.91	0.32
50/50	13.69	65.43	20.88	0.21
20/80	11.30	63.33	25.37	0.18
0/100	4.73	68.85	26.42	0.07

The plot Fig. 5.10 shows the variation of bandgap with the composition of Ar in the Ar/O_2 gas used in the deposition. These films were deposited at 500 °C. It shows that the bandgap reaches a maximum value of 5.06 eV at a percent Ar/O_2 gas composition of 50:50. Takakura et. al., reported a similar trend in β-Ga_2O_3 films deposited on silicon substrates at room temperature using different compositions of Ar/O_2 [218]. The values they obtained were 5.04 eV, 5.08 eV and 5.05

eV for compositions of Ar/O_2 = 0, 0.4 and 0.6, respectively, which peaks at about 50:50 Ar/O_2 as confirmed by our data shown in Table 5.2.

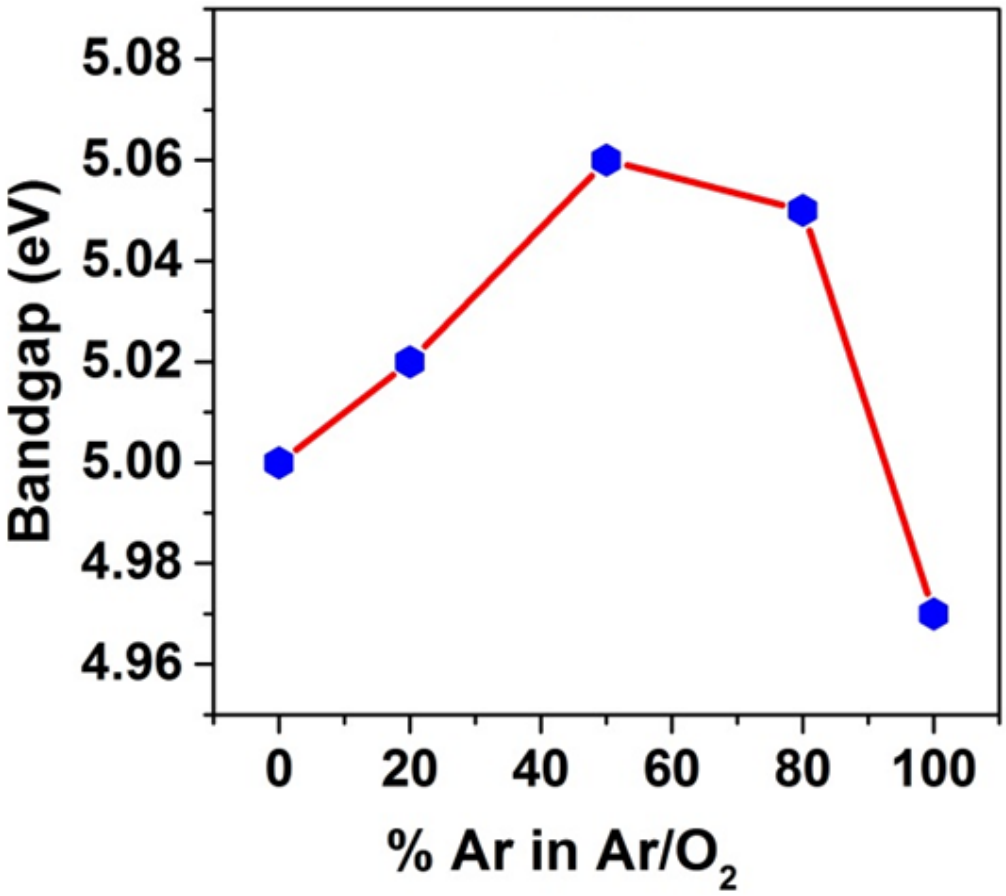

Figure 5.10 Bandgap dependence on deposition gas ratio.

5.2.6 Effects of Deposition Temperature in Ar/O_2 Mixtures.

5.2.6.1 50:50 Ar/O_2 Mixture

The effects of temperature were further studied on the films deposited in 50:50 Ar/O_2 mixture. The films are amorphous at temperatures below 500 °C, where they become crystalline (Fig. 5.11). It seems that films with good crystallinity can be obtain at various gas compositions, but the required temperature for crystallization will vary for each mixture of gases. The sharper XRD peaks belonging to β-Ga_2O_3 were obtained at 700 °C for this set of samples deposited in 50:50 Ar/O_2. AFM 5 x 5 μm scans on the films are shown in Fig. 5.12. A change in the morphology of the film is precisely occurring at 500 °C with the appearance of larger features on the film surface.

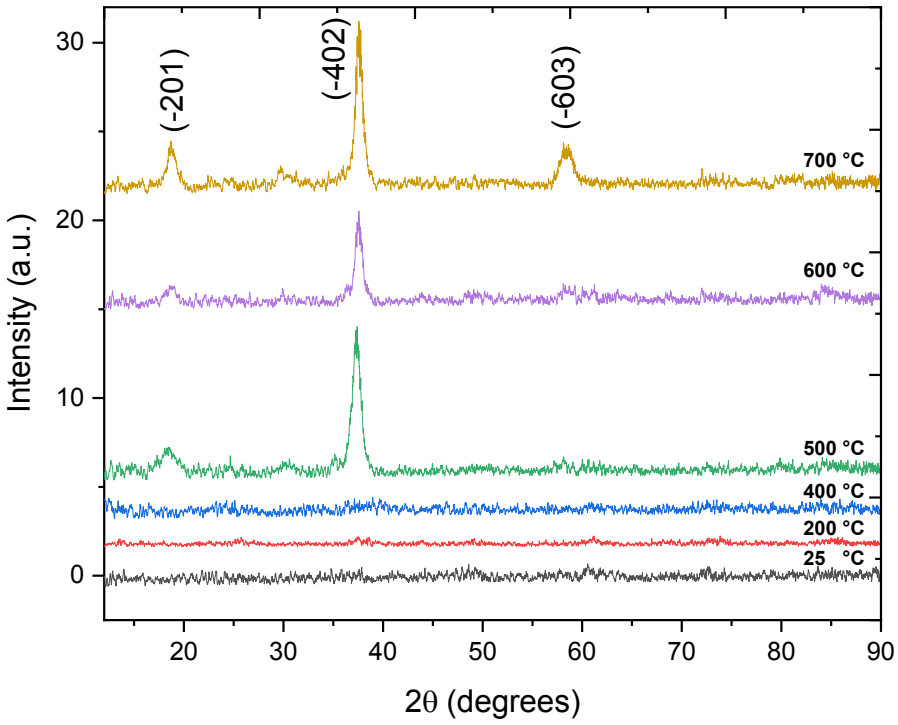

Figure 5.11 XRD scans for samples deposited a various temperature in Ar/O_2 (50:50).

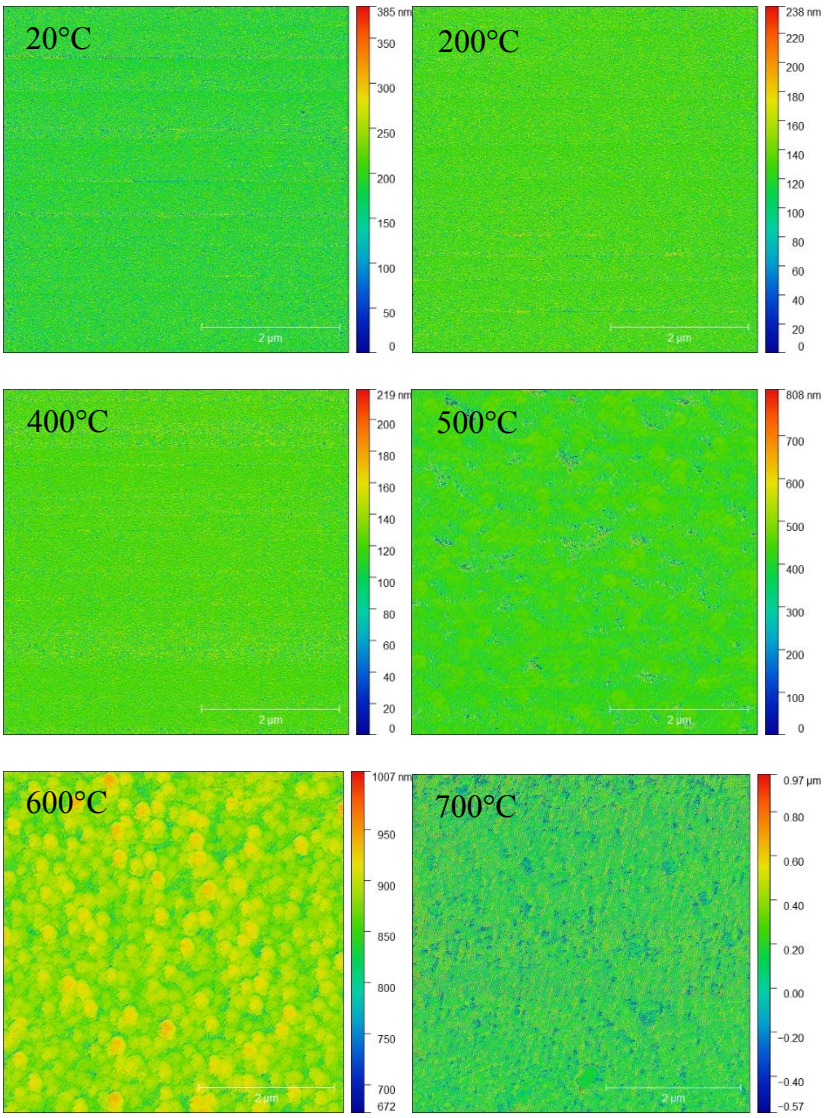

Figure 5.12 AFM 2D 5x5 µm scans of Ga_2O_3 films grown on sapphire at different deposition temperatures in Ar/O_2 (50:50) mixed atmosphere.

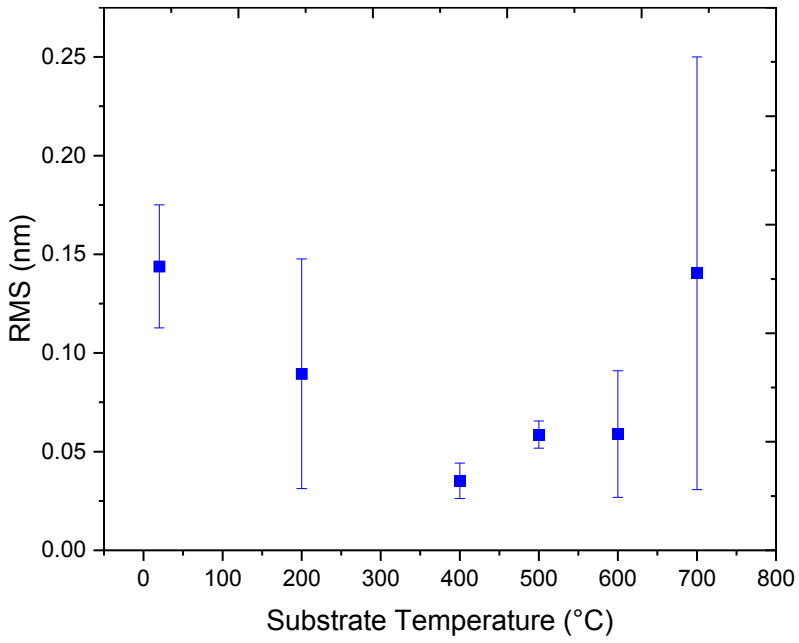

Figure 5.13 RMS GOX films grown on sapphire at different deposition temperatures in 50:50 Ar/O_2 atmosphere.

The RMS roughness parameter is shown in Fig. 5.13, the films roughness initially decreases with increasing temperature and then increases with increasing temperature above 400 °C. Transmittance and absorbance data was obtained for this set of samples deposited in 50:50 Ar/O_2 at a temperature range of 25 – 700 °C. Similarly, a Tauc plot was constructed to obtain the optical bandgap of the films. It is worth mentioning that the bandgaps values shown in Fig. 5.15 (b) for these films, were slightly bigger with a maximum of 5.23 eV at room temperature and followed a similar decreasing trend with increasing temperature.

Above 500 °C, the bandgap values fluctuated around a constant value of 5.03 eV. It is been previously observed that annealing can significantly decrease oxygen vacancies in the crystals [56]. The effect of deposition temperature on the films is similar to that of post deposition annealing. The reduction of oxygen vacancies shifts the Fermi level down, consequently decreasing the optical bandgap at higher temperatures.

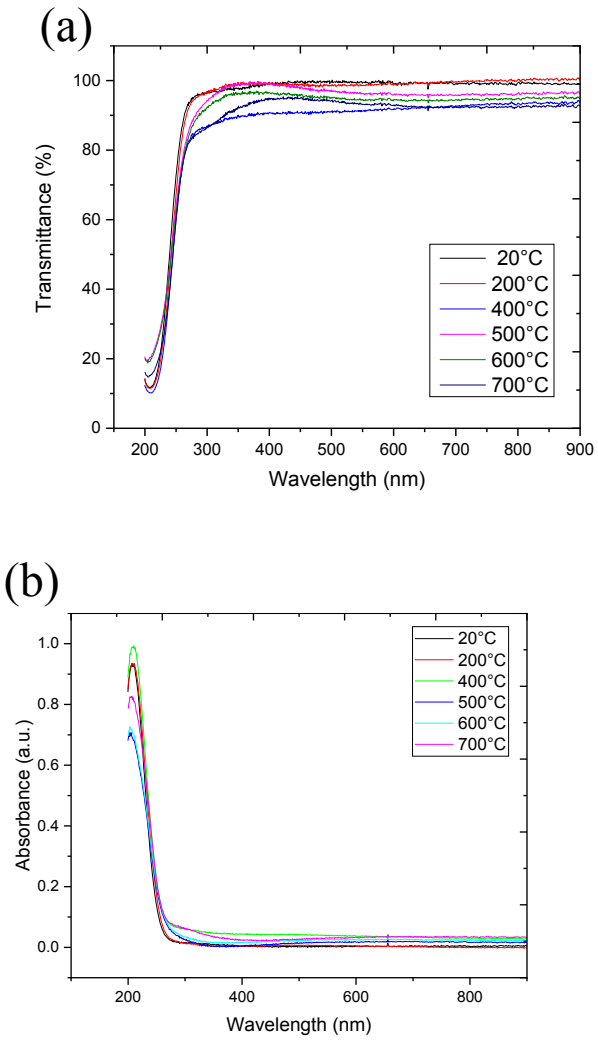

Figure 5.14 Plots showing the optical properties of the films deposited in 50:50 Ar/O_2 at various temperatures: (a) transmittance spectra, and (b) absorbance spectra.

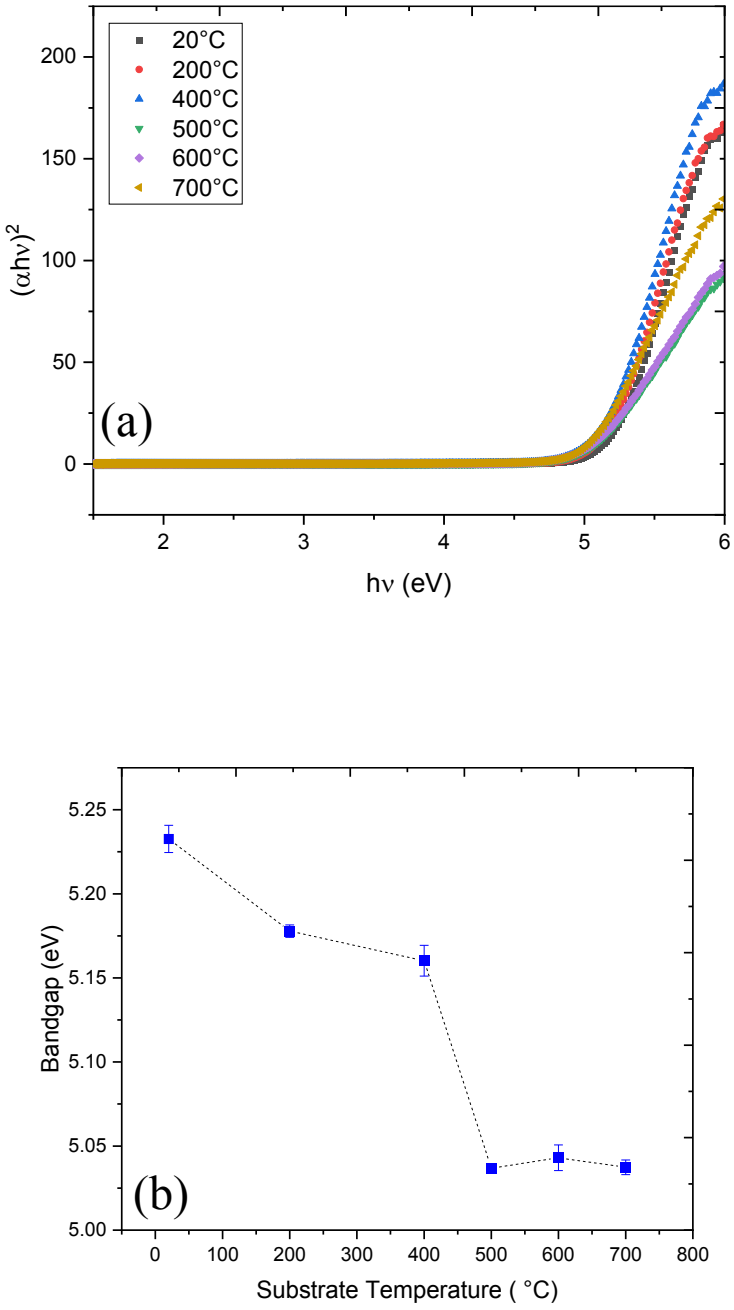

Figure 5.15 Plots of data obtained from Ga_2O_3 films deposited in Ar/O_2 (50:50) at different temperatures showing: (a) the variation of $(\alpha h\nu)^2$ versus photon energy ($h\nu$), and (b) optical bandgap versus the deposition temperature.

5.2.6.2 Ar/O_2 (80:20) Mixture

Temperature effect was also studied in the films deposited in 80:20 Ar/O_2 gas composition. The films this mixture has better crystalline formation at a substrate temperature of 500 °C and 550 °C. The appearance of multiple peaks at 30° from the scans shown in Fig. 5.16 correspond to the (400) plane of β-Ga2O3, which indicate that the films become polycrystalline at temperatures higher than 550 °C. The XRD results indicate that the optimum deposition temperature in this gas mixture is in the range of 500-550 °C. Akazawa found 300 °C to be the optimum temperature when β-Ga_2O_3 was deposited under O_2 gas flow on sapphire c-plane [62].

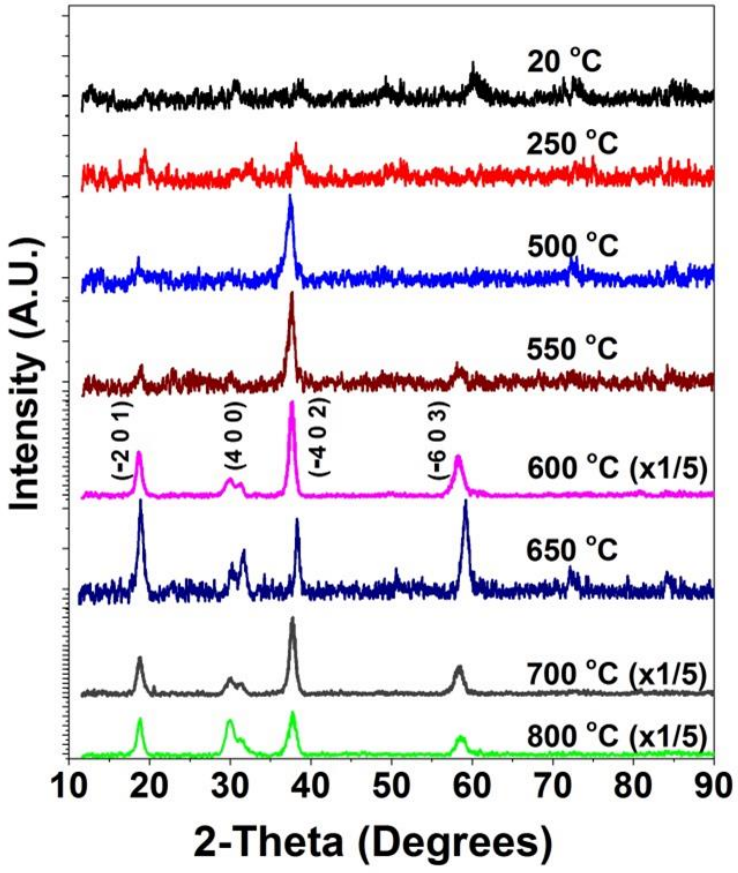

Figure 5.16 XRD scans for films deposited at various temperatures in 80:20 Ar/O_2.

Table 5.3 shows the EDS elemental composition of the films deposited at different temperatures using 80:20 Ar/O_2 mixture.

T_{sub} (°C)	Atomic %			Ga/O
	Ga(L)	**O(K)**	**Al**(K)	
20	4.32	71.79	23.89	0.6
250	13.03	63.96	23.02	0.20
500	17.96	64.49	17.54	0.28
650	12.16	63.10	24.74	0.19
800	10.08	66.24	23.69	0.15

This data indicates that as the substrate temperature is increased, the Ga content in the film reaches a peak value at T_{sub} = 500 °C and then decreases. As explained above, the change in substrate temperature contributes to the kinetics of the sputtered species as they condense on the surface of the substrate. Higher substrate temperatures above 500 °C seems to be unfavorable for condensation of the Ga species onto the substrate, hence the decrease in its content in the film. The aluminum (Al) in the EDS results is due to its presence in sapphire substrate. The contribution of oxygen from both the film and the sapphire substrate as well as lack of a calibration standard limits inference of quantitative compositions of the films using the EDS data.

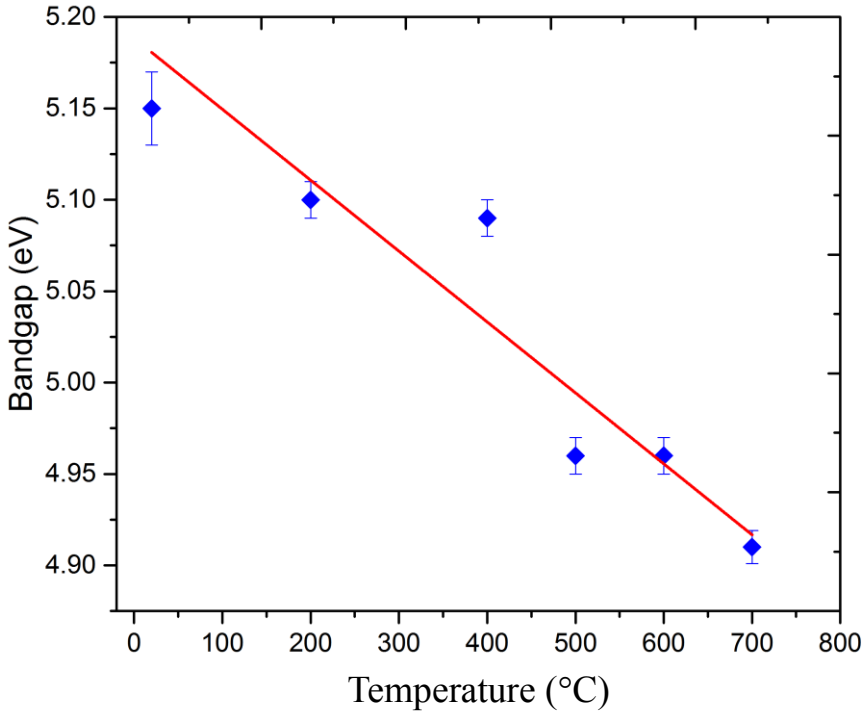

Figure 5.17 Bandgap of films deposited in 80:20 Ar/O_2 mixture.

5.2.7 Effect of the Annealing Temperature on the Ga_2O_3 films deposited on sapphire in Ar atmosphere.

The effect of post-deposition annealing was investigated for a selected set of films deposited at 400 °C in Ar. A sample was diced and annealed at temperatures ranging from its as deposited version, i.e., 400 °C, up to 900 °C. Figure 5.18 shows no further improvement in the quality of the film with post-deposition annealing treatment; this is due to the introduction of addition peaks located at 30.0° and 35.5°, belonging to another set of planes (400) and (111) of β-Ga_2O_3, respectively [219]. The results indicate that there is no further optimization on the microstructure of the deposited films by post-annealing treatment.

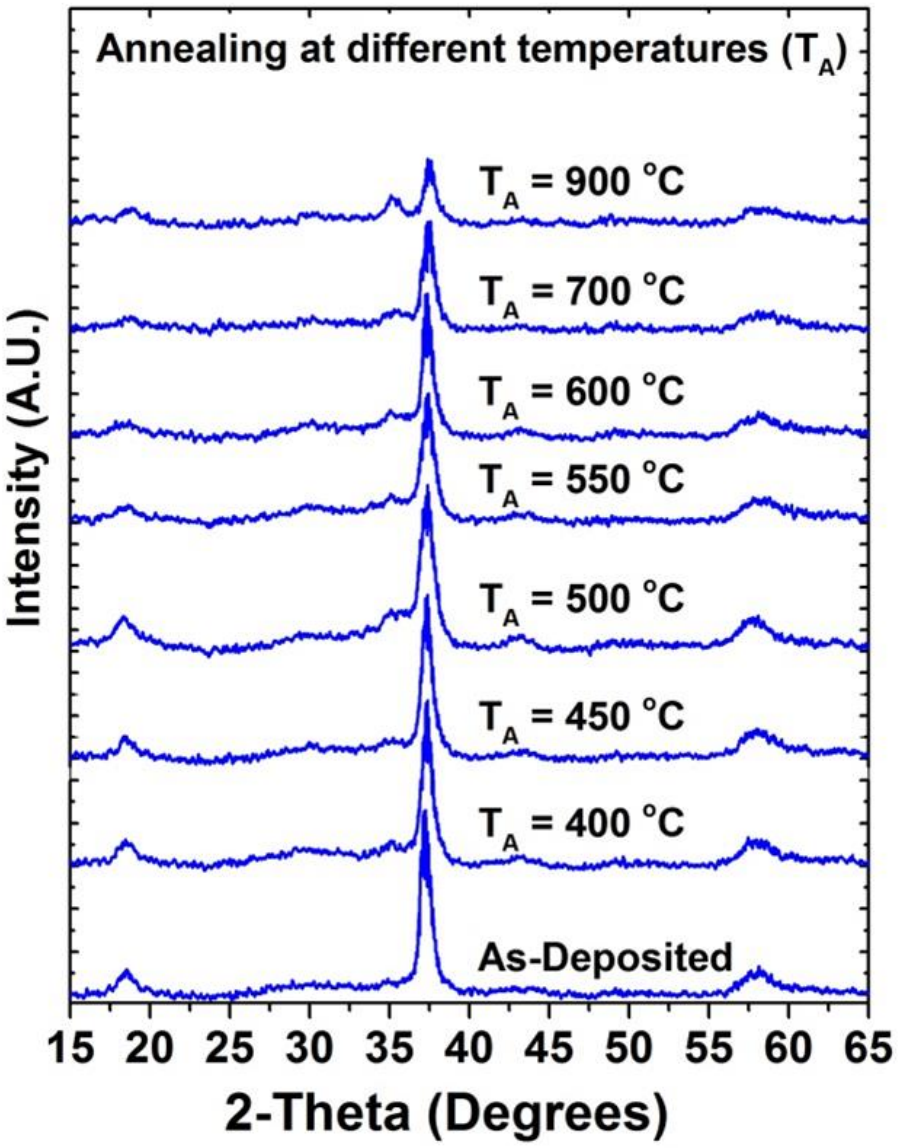

Figure 5.18 XRD scans of Ga_2O_3 films deposited at 400 °C in Ar and annealed in N_2 for 15 min at different temperatures. (b) Variation of the integrated intensity of the ($\bar{4}$ 0 2) peak at 37.2° with annealing temperature.

Figure 5.20 shows the variation of the integrated intensity of the ($\bar{4}$ 0 2) peak at 37.2° with the annealing temperature. The data shows a gentle decrease in the intensity up to annealing temperature of 500 °C, after which, there is a rapid decrease in intensity, indicating a worsening of the crystalline quality of the film. This suggests that improvement of the crystalline quality of the films is achieved with the deposition at 400 °C, and that post-deposition annealing only worsens the crystal quality of the films.

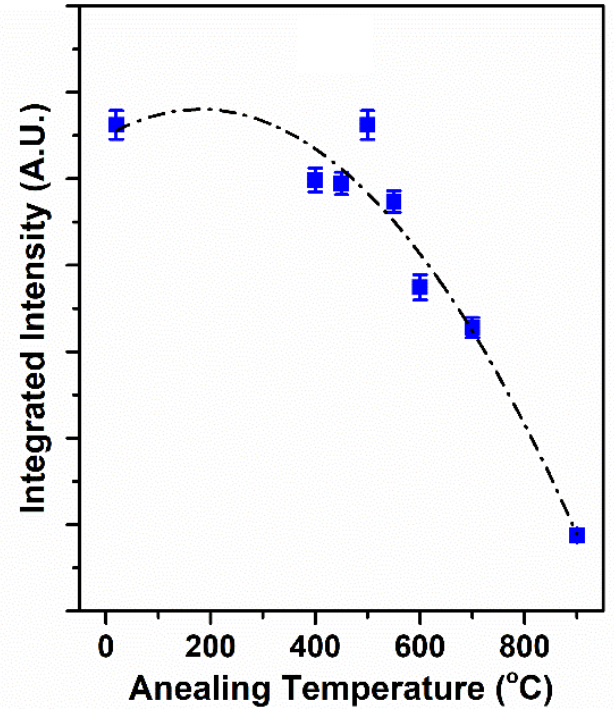

Figure 5.19 Variation of the integrated intensity of the ($\bar{4}02$) peak at 37.2° with annealing temperature.

5.3 Homoepitaxial Growth of Ga_2O_3 films on $(\bar{2}01)$ Ga_2O_3 Substrates

5.3.1 Introduction

In section 2.2 a literature review on homoepitaxial growth was displayed. Even during homoepitaxial growth, the resulted films can present stacking faults, twin boundaries, and rotational domains. These faults can show in HRTEM and electron diffraction, however it is not clear if it has significant effects on the crystal structure since XRD data only shows a small broadening of the characteristic peaks, but no additional peaks appear in any of the studied surface orientations, i.e., (001)-, (0 1 0)-, and $(\bar{2}\ 0\ 1)$-oriented β-Ga_2O_3. In this section XRD data of Ga_2O_3 films grown on the surfaces mentioned above is presented to show the effects of surface treatment before deposition, the effects of deposition temperature on the $(\bar{2}01)$-oriented β-Ga_2O_3 substrate, and Ga_2O_3 films deposited on the three surfaces at a selected temperature of 300 °C.

5.3.2 Experimental Procedure

The $(\bar{2}01)$-Ga_2O_3 substrates grown by EFG were purchased from Sojitz Machinery Corporation, a Japanese based Company. Other substrate Ga_2O_3 substrate orientations were supplied by our collaborator, Dr. Joseph Marret from the Air Force Research Laboratory, Dayton, OH. The substrate dies have dimensions of 5 x 5 mm^2 and are one-sided polished. All substrates were submitted to the cleaning method referenced in section 3.1 which consist sequential sonication in acetone (10 min), isopropanol (10 min), DI water (10 min), 5 min soak in hydrochloric acid (HCl 10%), rinse in DI water, 5 min soak in boiling H_2O_2 at 85 °C, rinse with DI water, and blow dry. A base pressure of ~7.0 E-7 Torr and deposition pressure using Ar of 3.5 mTorr was used for all depositions. The sputtering power was kept at 100 W. Initially the UID $(\bar{2}01)$-oriented substrate was submitted to thermal desorption, but this process created extra peaks

in the XRD, and was omitted for the rest of the samples. For the effects of the deposition temperature, $(\bar{2}01)$-oriented substrates were utilized and subjected to a temperature ranging from room to room to 400 °C in steps of 100 °C, then XRD data was collected. Finally, 300 °C was selected to deposit Ga_2O_3 films on the other two surfaces, i.e., the (001) and (010).

5.3.3 Effect of surface treatment on Films grown on $(\bar{2}01)$ substrate.

Our initial inquiry focused on whether surface treatment was required prior deposition of the homoepitaxial films. To investigate this, the $(\bar{2}01)$ UID substrate underwent annealing at 500 °C in O_2 ambient for 30 min. Subsequent X-ray diffraction (XRD) analysis of the substrate revealed the emergence of additional (100) β-Ga_2O_3 peaks, as illustrated in Fig. 5.20. Therefore, based on these findings, the surface treatment procedure was omitted to streamline the homoepitaxial deposition process. Surface treatment on gallium oxide substrate can lead to the creation of additional peaks in X-ray diffraction (XRD) spectra due to several factors. One plausible reason is the formation of surface defects or impurities during the treatment process, which can introduce new crystalline structures or modify the crystal lattice of the material. Additionally, surface treatments such as annealing or oxidation can induce phase transformations or alter the stoichiometry of the material, resulting in the appearance of new peaks in the XRD pattern. Moreover, literature reviews have demonstrated that gallium oxide samples exposed to oxygen pressure during surface treatment can lead to alterations in the crystal structure and changes in the oxidation state of gallium atoms. These alterations can result in variations in the X-ray diffraction (XRD) pattern, including the emergence of additional peaks or shifts in peak positions, reflecting the structural modifications induced by the surface treatment. Overall, surface treatments can significantly impact the structural properties of gallium oxide, potentially resulting in the emergence of additional peaks in XRD analysis.

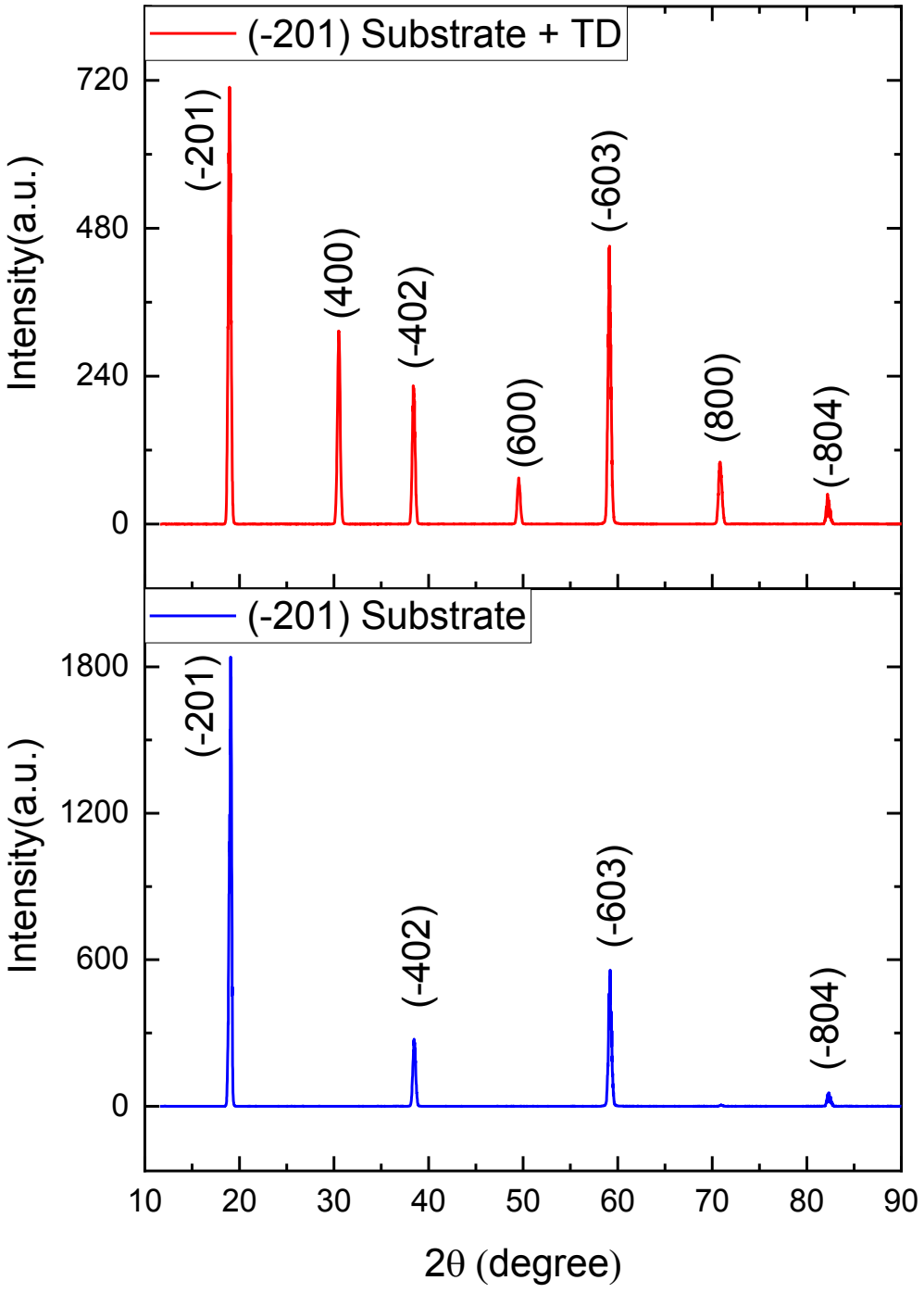

Figure 5.20 Effects of thermal desorption of the pristine $(\bar{2}01)$ UID Ga_2O_3 substrate.

5.3.4 Effect of Deposition Temperature on Films Grown on ($\bar{2}$ 0 1) Substrate.

Figure 5.21 shows the XRD data of the films grown at various temperatures; the substrate is included for comparison. Additional peaks belonging to (100)-oriented planes of β-Ga_2O_3 can be seen in all deposition temperatures above 300 °C. Gallium oxide homoepitaxial films can exhibit extra peaks in X-ray diffraction (XRD) patterns with increasing deposition temperature due to several reasons. Firstly, higher deposition temperatures promote enhanced crystallization, leading to the growth of larger and more well-defined crystallites within the film, which can result in additional diffraction peaks in the XRD pattern. Secondly, elevated deposition temperatures may trigger phase transformations or the formation of new crystallographic phases within the film, manifesting as extra peaks in the XRD spectrum. Additionally, the increased thermal energy facilitates strain relaxation, causing the reorientation of crystal planes or the formation of new crystal domains, contributing to the appearance of extra diffraction peaks.

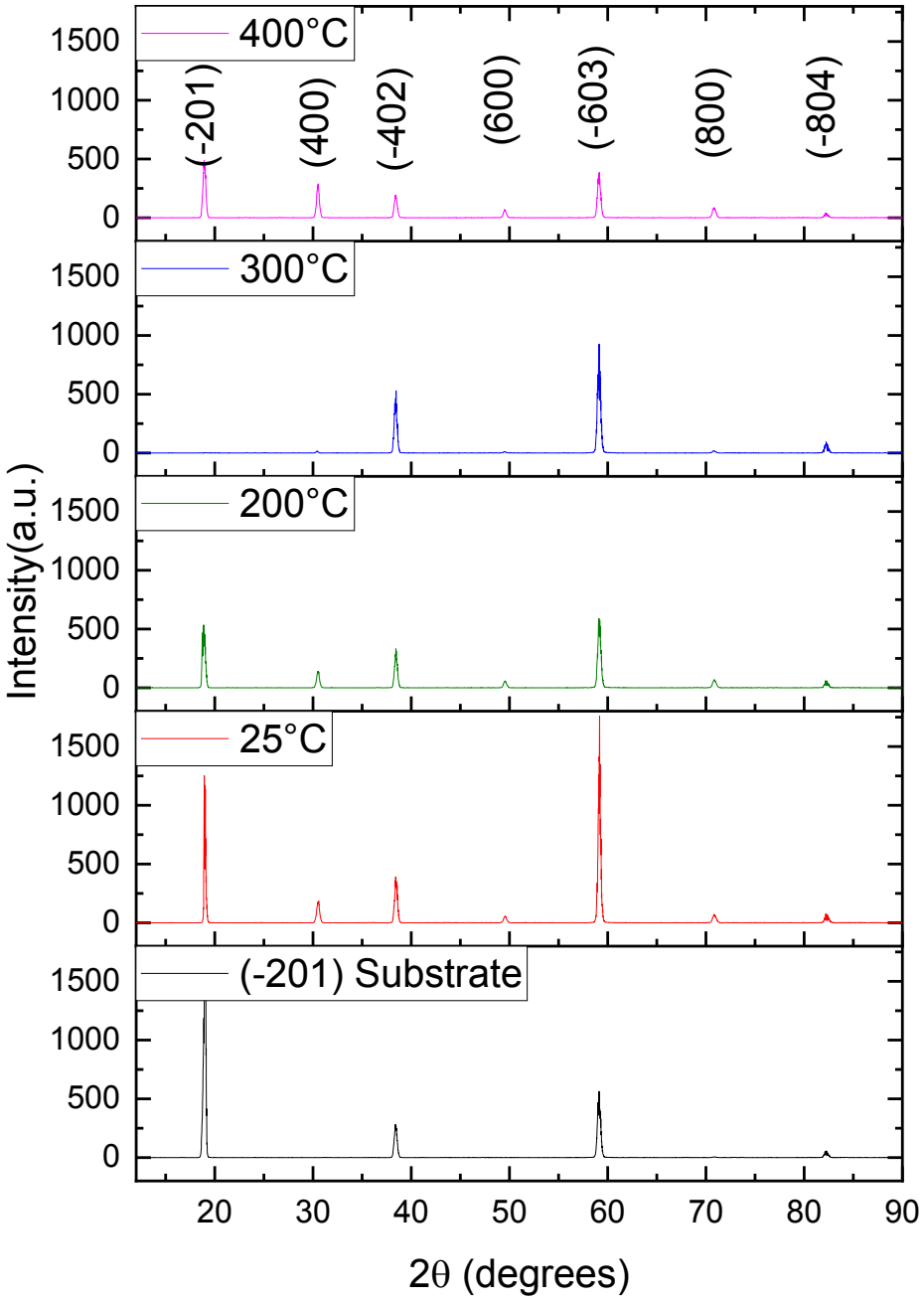

Figure 5.21 XRD of films deposited on UID ($\bar{2}01$) substrate at various temperatures. Substrate is included for comparison.

FWHM was obtained from a gaussian fit the $(\bar{6}03)$ Bragg peak of β-Ga_2O_3, using Origin Pro. Figure 5.22 shows that the average FWHM for $(\bar{6}03)$ Bragg peak of β-Ga_2O_3, there is a sudden increase of the FWHM for the films deposited homoepitaxially on $(\bar{2}01)$ Ga_2O_3 when compared to the pristine substrate. Cheng et al observed a similar broadening of the XRD peaks while studying homoepitaxial (001)-Ga_2O_3 films and was able to correlated this diffused scattering in the XRD with stacking faults observed in HRTEM [76]. This suggests that the films rf sputtered on $(\bar{2}01)$-Ga_2O_3 substrate have stacking faults, however further microstructural characterization in the form of HRTEM needs to be performed to confirm the presence of these fault domains.

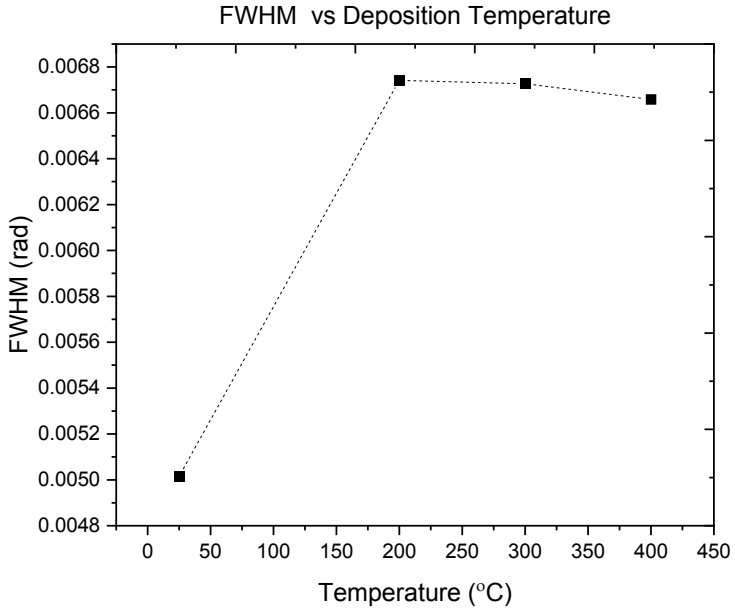

Figure 5.22 Average FWHM for the $(\bar{6}03)$ Bragg peak with increasing deposition temperature of homoepitaxial films grown on $(\bar{2}01)$-oriented substrates.

5.3.5 Homoepitaxial Growth of Ga_2O_3 Films on Various Surface Orientations.

Based on the previous XRD for homoepitaxial growth on $(\bar{2}01)$-oriented substrates, an optimized deposition temperature of 300 °C was selected to further investigate homoepitaxial growth of Ga_2O_3 in other substrate orientation. Three distinct substrate orientations were used, i.e., (001)-, (010)-, and $(\bar{2}01)$-oriented β-Ga_2O_3. This set of homoepitaxial films were all deposited at 300 °C. Figure 5.23 shows the XRD data for the three surfaces which indicates that (100)-, and (010)- films followed the same crystal orientation of each individual substrate, and no foreign peaks are observed for these two samples. XRD data for the $(\bar{2}01)$-Ga_2O_3, films showed Bragg peaks at 18.89°, 38.3°, and 59.01° belonging to $(\bar{2}01)$, $(\bar{4}02)$, and $(\bar{8}04)$ of $(\bar{2}01)$-oriented β-Ga_2O_3, respectively [86]. As observed before, the additional (100)-oriented planes appear on films deposited on the $(\bar{2}01)$ substrate. The second surface is the (010)-oriented β-Ga_2O_3 which a mayor peak at 61° which belong to (020) planes of (010)-oriented β-Ga_2O_3. Lastly, the (100)-oriented surface showed two peaks at 15.6° and 31.9° belonging to (400) planes of β-Ga_2O_3 [220].

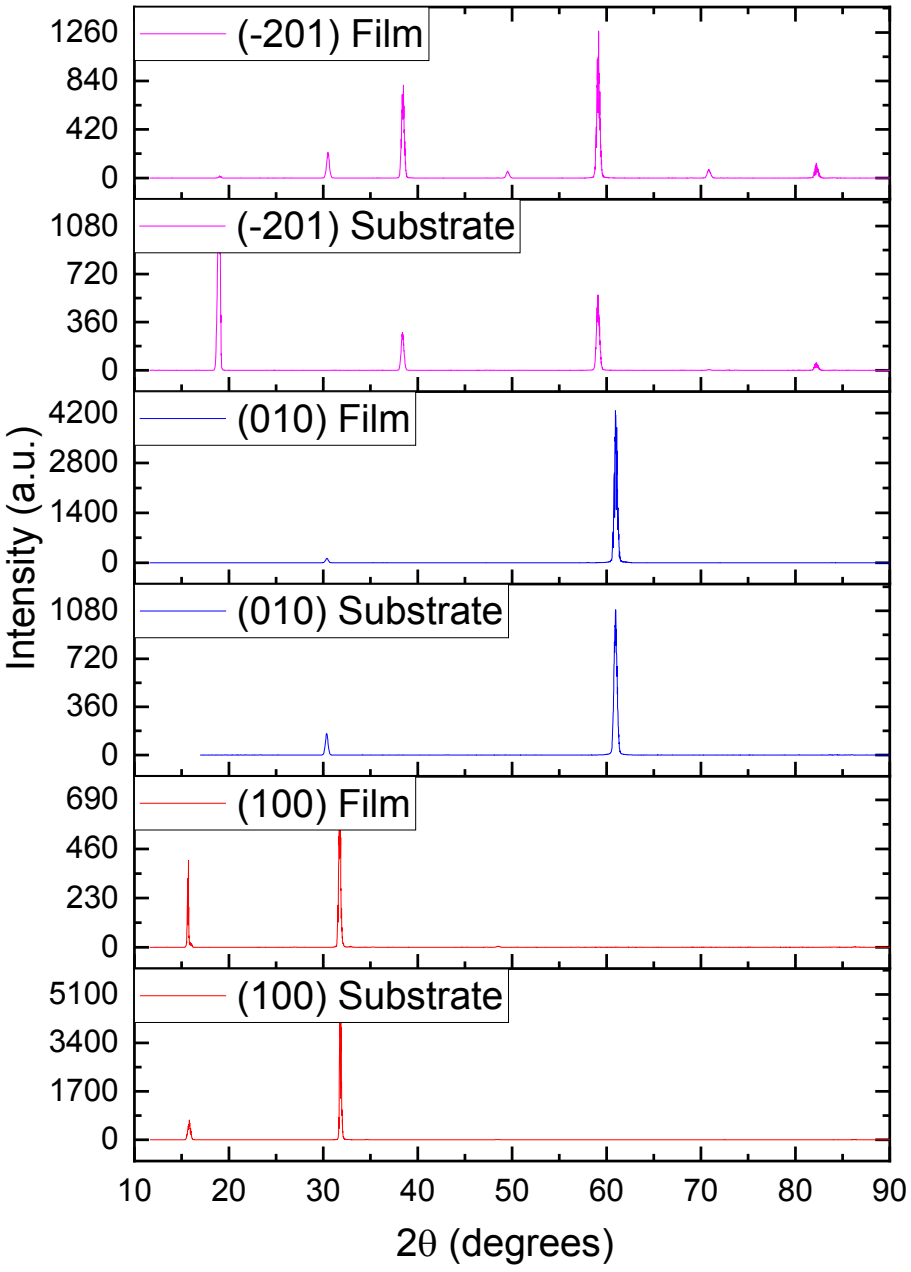

Figure 5.23 Homoepitaxial films deposited on (100)-, (010)-, and ($\bar{2}$01)-oriented β-Ga_2O_3 at 300 °C, and respective pristine substrates.

5.4 Optimization of Doping of Ga_2O_3 Films Grown on $(\bar{2}01)$ Sn-Doped Ga_2O_3 Substrates

5.4.1 Introduction

Undoped stoichiometric Ga_2O_3 should be a transparent insulator due to its large bandgap of 4.87 eV. Nevertheless, Ga_2O_3 exhibits an unintentionally n-type doped (UID) conductivity [221]. The origin of this unintentional doping remains a topic of discussion, with various defects, including oxygen vacancies (VO), hydrogen interstitials (Hi), substitutions (HO), gallium interstitials (Gai), and other impurities being suggested [221]. As introduced in section 2.3 Ga_2O_3 n-type doping has been achieved successfully with elements from group IV such as Si, Sn, Ge, Nb, and Ta with controlled bulk concentration in the range of 10^{16}-10^{19} cm^{-3} for bulk crystals and in the range of 10^{14}-10^{20} cm^{-3} for epitaxial thin films, with corresponding Hall mobility measured to be 140 and 184 cm^2/Vs for bulk crystals and thin films, respectively [221]. Since doping directly affects the conductivity of the film, it is a crucial step for increasing the device's performance. In this section, optimization of the doping concentration was performed by varying the Sn target dc current and post-deposition annealing temperature. The optimized doped films were later used in section 5.6 to fabricate Ohmic contacts to demonstrate a simple Schottky barrier diode device.

5.4.2 Experimental Procedure

Sn-doped $(\bar{2}\ 0\ 1)$ substrates were cleaned using the cleaning method referenced in section 3.2. The setup for doping is shown in Fig. 5.25, where two the targets can be seen aligned towards the substrate holder heater. This configuration allows us to co-sputter Ga_2O_3 and Sn simultaneously to created uniform Sn-doped Ga_2O_3 films. The chamber was evacuated to reach a base pressure of ~7 x 10^{-7} Torr prior to each deposition. During the depositions, a constant mixed gas flux of 9.9:0.1 sccm Ar/O_2 (1% O_2) was inserted. The deposition pressure was kept at 3.5 mTorr and the substrate

holder was kept at 450 °C for all depositions. The power used for the Ga_2O_3 target was 100 W, while Sn was dc sputtered with a current varied from 2 mA to 6 mA in steps of 1 mA. XRD data was collected to verify if the crystal quality of the films remained unaltered after doping with Sn impurities. EDS analysis was done to monitor the Sn concentration with varying target dc current. Finally, Hall effect measurements of the films were taken after annealing for 3 min at temperatures ranging from 200-700 °C in Ar ambient, to obtain crucial parameters such as bulk concentration, mobility, resistivity, sheet resistance of the doped films.

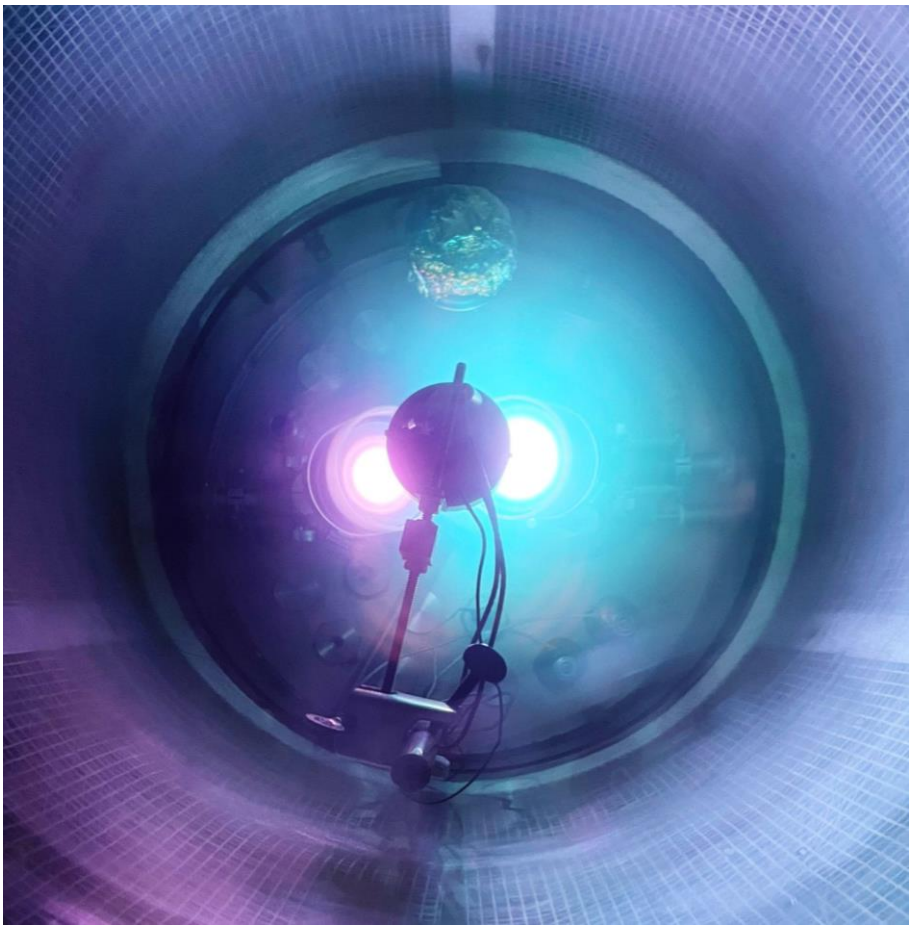

Figure 5.24 Uniform Sn-doping deposition target setup.

5.4.3 XRD of Sn-Doped Ga_2O_3 Films Deposited on $(\bar{2}01)$ Sn-Doped Ga_2O_3 Substrates Using Various Sn Target dc Currents.

Figure 2.25 shows XRD data for the Sn-doped films. The major intensity Bragg peaks located at 38°, 58°, and 82° belong to $(\bar{2}01)$ β-Ga_2O_3 and are present in all films. $(\bar{2}01)$ Ga_2O_3 has a peak at 18°, but this peak was weakly observed only in the film doped at 3 mA. There is an additional peak located at 30°, and was previously observed in our films and substrates, coming from (100)-oriented planes of β-Ga_2O_3. From this data it was concluded that the crystal structure of monoclinic $(\bar{2}01)$ β-Ga_2O_3 is unaltered with the obtained doping concentration.

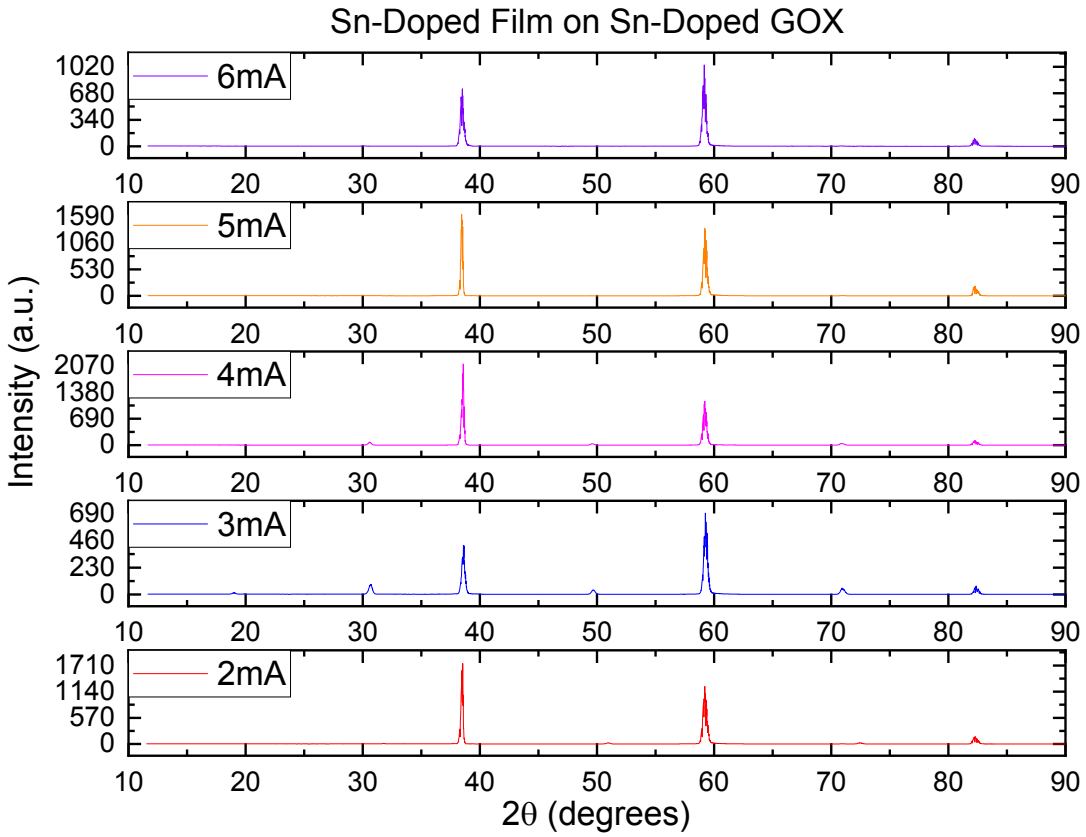

Figure 5.25 XRD of Sn-doped $(\bar{2}01)$ homoepitaxial films with various Sn dc deposition current.

5.4.4 EDS Analysis of Sn-Doped Ga_2O_3 Films Deposited on $(\bar{2}01)$ Sn-Doped Ga_2O_3 Substrates Using Various Sn DC Currents.

To measure the dopants concentration directly, EDS analysis was used to obtain the atomic percentage of Sn in the films. At least 3 scan areas were measured for each sample. Table 5.4 shows EDS data for the films doped at various dc currents, and shows an increase of the average Sn atomic percentage with increasing dc current, as expected. A minimum value of 0.047% Sn was obtained at a dc current of 2 mA, and a maximum value of 0.573% was obtained at the largest dc current of 6 mA. The measurements were consistent across each sample which confirms that uniform doping by co-sputtering Ga_2O_3 and Sn was achieved. Table 5.4 was plotted in Fig. 5.27 for better visualization of the Sn atomic percentage with increasing Sn dc current.

Table 5.4 EDS analysis with increasing Sn DC Current.

Sn dc Current (mA)	Avg Sn (At%)	Avg Ga (At%)	Avg O(At%)
2	0.047	26.033	55.737
3	0.060	26.277	54.860
4	0.103	25.843	54.920
5	0.113	31.393	55.860
6	0.573	31.113	56.293

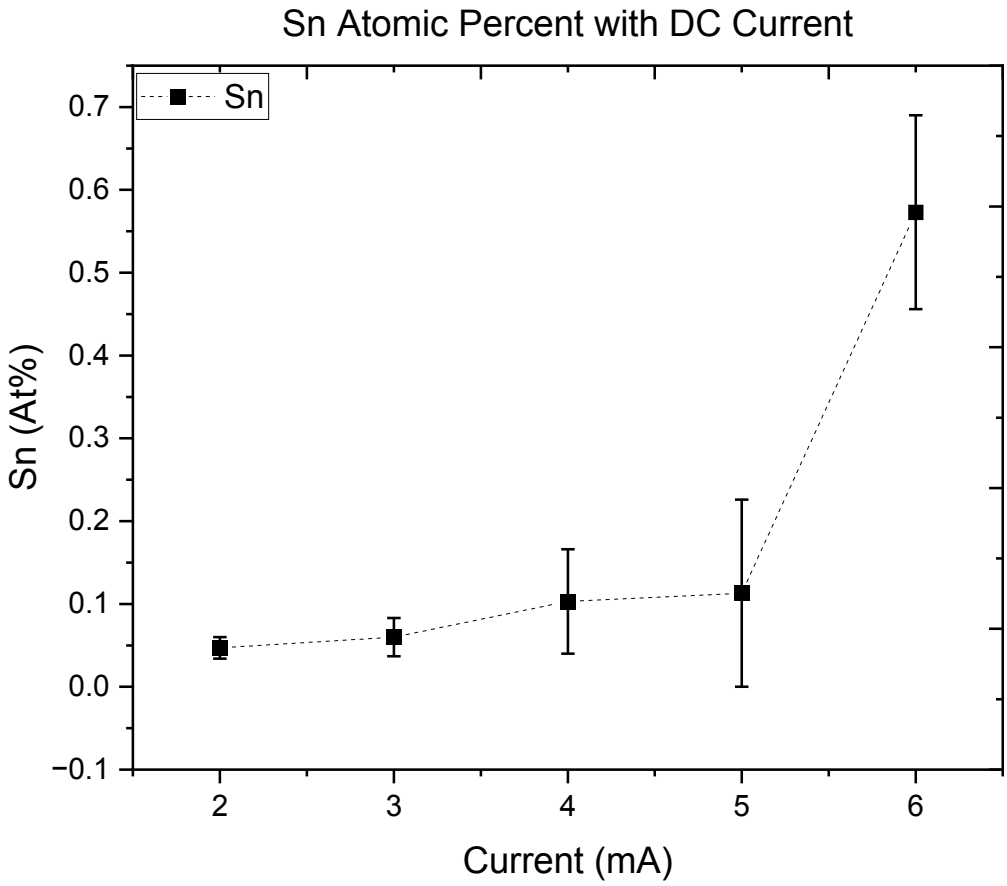

Figure 5.26 Sn atomic percentage with increasing Sn target dc current.

5.4.5 Hall Effect Measurements of Sn-Doped Films on $(\bar{2}01)$ Sn-Doped Ga_2O_3 Substrates

5.4.5.1 Bulk Concentration vs Annealing Temperature

Bulk concentration obtained from Hall measurements on the Sn-doped films deposited on $(\bar{2}01)$ Sn-doped Ga_2O_3 substrates was plotted against the annealing temperature (Fig. 5.27 (a)-(e)) at different Sn target dc currents. The goal was to determine the best annealing temperature which gives the highest bulk concentration in the films. The bulk concentration had lower limit of around 1 $x10^{15}$ cm^{-3} at 200 °C and goes up to 1 $x10^{19}$ cm^{-3} at 600 °C, and then drops after 600 °C. Therefore, the optimized annealing temperature based on the obtained bulk concentration of the films was determined to be at a range between 500 °C and 600 °C, as the bulk concentration tended to drop after 600 °C for most of the samples evaluated. The bulk concentrations obtained in our films fall in the previously obtained bulk concentration range of 10^{14}-10^{20} cm^{-3} for epitaxial films [221]. Annealing temperatures up to 1450 °C for 6 hours in nitrogen ambient has been reported for bulk crystals, to reduce residual stress in the crystal and achieve full activation of donors before the substrate fabrication process [158]. This was not performed on the fabricated films.

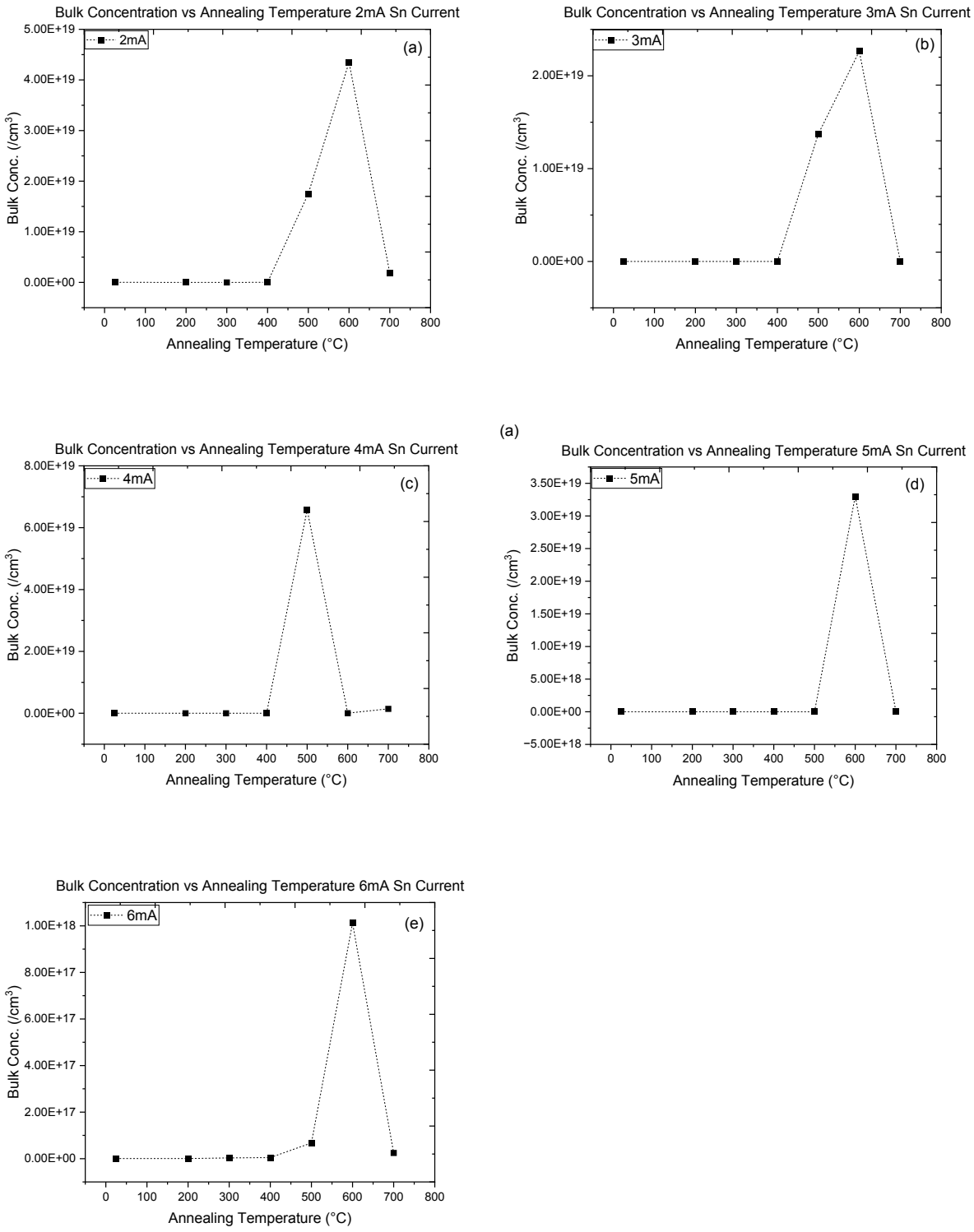

Figure 5.27 Bulk concentration vs annealing temperature for (a) 2mA, (b) 3 mA, (c) 4 mA, (d) 5 mA, and (e) 6 mA Sn target dc current.

5.4.5.2 Mobility vs Annealing Temperature

The Hall mobility was plotted against annealing temperature at different Sn target dc currents to identify the annealing temperature that produces the highest mobility value. Surprisingly, a maximum Hall mobility of 6.8 x 10^3 cm^2/Vs was achieved at 500 °C with a Sn dc current of 3 mA, which significantly contrasts with previous experiments on epitaxial thin films, where the maximum reported mobility ranged from 184 cm^2/Vs and decreased to 140 cm^2/Vs for bulk crystals [221]. However, the high resistivity of our films most likely resulted from a noisy Hall measurement, rendering these results inconclusive and necessitating further investigation.

Additionally, it was noted that the carrier mobility substantially decreased for samples deposited using a Sn dc current of 6 mA at comparable annealing temperatures shown in Fig. 5.28 (e). Excessive doping concentrations within a semiconductor film can have detrimental effects on carrier mobility, impacting the material's electronic properties. One of the primary reasons for decreased carrier mobility is the increased likelihood of carrier scattering events caused by high doping concentrations. When carriers move through a heavily doped region, they experience more frequent interactions with dopant atoms or impurities, leading to increased scattering and reduced mobility. Additionally, excessive doping can disrupt the lattice structure of the material, introducing defects and imperfections that act as scattering centers for carriers, further hindering their mobility. Furthermore, high doping concentrations can cause carriers to become more localized near dopant atoms or clusters, limiting their effective mobility and contributing to decreased overall carrier mobility. These factors highlight the importance of maintaining an optimal doping concentration to ensure high carrier mobility and efficient electronic performance in semiconductor materials.

Based on the bulk concentration data and mobility data, an annealing temperature of 500 °C and a Sn dc current of 5 mA were chosen as the optimal conditions for Ga_2O_3 Sn-doped films on $(\bar{2}01)$ Sn-doped Ga_2O_3 Substrates. Moreover, it is essential to note that the relationship between bulk concentration and carrier mobility is complex and heavily influenced by factors such as annealing temperature and Sn dc current during deposition, indicating that achieving optimal carrier mobility requires careful consideration of multiple parameters during the fabrication process. The observed discrepancy between our results and those reported in literature underscores the complexity of optimizing carrier mobility in Ga_2O_3 Sn-doped films. Future studies should concentrate on refining the optimization process and experimental conditions, including enhancing film uniformity, and reducing defects, to attain more reliable and consistent Hall mobility measurements. Additionally, exploring alternative characterization techniques or doping methods may offer insights into improving carrier mobility and enhancing the overall performance of Ga_2O_3-based electronic devices.

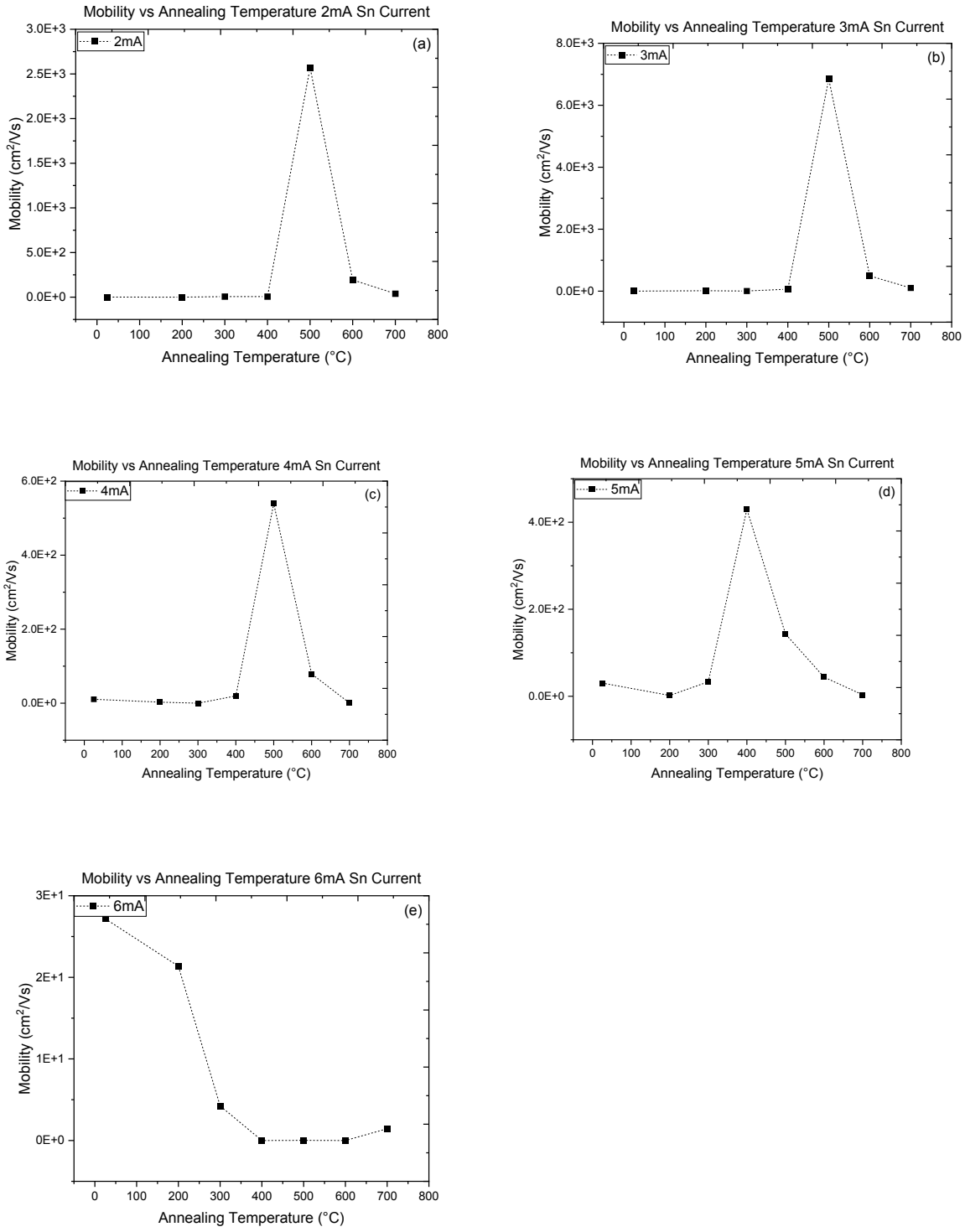

Figure 5.28 Mobility vs annealing temperature for (a) 2mA, (b) 3 mA, (c) 4 mA, (d) 5mA, and (e) 6mA Sn target dc current.

5.5 Optical Band Gap Tunning with Metal Alloys to Ga_2O_3

5.5.1 Introduction

This section explores the modification of the optical bandgap by co-sputtering films containing an alloy or admixture of gallium oxide (Ga_2O_3) and two additional oxides, lutetium oxide (Lu_2O_3) and boron oxide (B_2O_3). Among various band-structure-engineering methods used in modern semiconductor devices, alloying stands out as a crucial technique alongside heterostructures, superlattices, strain, and other effects. For instance, alloying Ga_2O_3 with Al_2O_3 or In_2O_3 has been effectively employed to adjust the bandgap of Ga_2O_3 [194,222]. Alloying Ga_2O_3 with other oxides can significantly impact the optical bandgap of the deposited films. This alteration occurs due to the introduction of additional energy levels within the band structure of the material. When Ga_2O_3 is alloyed with oxides like Ga_2O_3 and boron oxide B2O3, the energy levels associated with these additional elements interact with the energy levels of Ga_2O_3, leading to changes in the electronic configuration and bandgap of the alloyed material. However, the complexity of alloys often leads to composition variations and phase separation, which can impact the original crystal structure, presenting challenges for precise and consistent bandgap engineering [223]. Overall, alloying Ga_2O_3 with other oxides introduces new energy states into the material's band structure, leading to alterations in the optical bandgap of the deposited films. This phenomenon is of great interest in materials science and semiconductor device fabrication, as it allows for tailored control over the optical properties of Ga_2O_3-based materials for various technological applications Characterization techniques like XRD, EDS, and UV-Vis can help understand these changes and optimize alloy compositions for specific optical characteristics.

5.5.2 Experimental Procedure

Ga_2O_3. Two distinct sets of samples were prepared by sputtering deposition to investigate the effects of co-sputtering Lu_2O_3 with Ga_2O_3 in one set, and B_2O_3 with Ga_2O_3 in the second set. Co-sputtering is possible with the use of goose-neck cathodes that can be adjusted below the substrate heated as depicted in Fig. 5.29. Lu_2O_3 was co-sputtered using powers of 20, 30, and 80 W while B_2O_3 was co-sputtered with rf powers of 40, 50, 80 W. The power Ga_2O_3 was kept at 100 W for all samples. The depositions lasted for 2 hours at a temperature of 500 °C in an $Ar:O_2$ (1% O_2) atmosphere. Furthermore, two different substrates were simultaneously used for each selected rf power. A pair of $(\bar{2}01)$ unintentionally doped (UID) and Sn-doped Ga_2O_3 substrates was loaded for each rf power.

Both substrates were one-side polished upon purchase. However, to accurately determine the optical bandgap, substrates with optically transparent surfaces were required, prompting the need to polish the backside of the purchased substrates. Mechanical polishing was performed on all substrates down 1 μm grading using a diamond pad and rotating table. Atomic force microscopy scans on the surface were done to evaluate the roughness of the polished surface and to compare with the default polished performed by the company before purchasing. Table 5.5 shows the roughness parameters obtained for the polished samples, indicating that although an improvement was achieved, the new mechanically polished surfaces were worse in quality than the surface polished by the industry with a difference of 2 orders of magnitude in the RMS parameter.

Al_2O_3. To mitigate the issue of not having a perfectly optical transparent surfaces, the experiment was repeated on c-plane double-side polished Al_2O_3. All samples were deposited on c-plane Al_2O_3 substrates. Prior to deposition the substrates cleaned by general solvent clean

method in acetone, IPA, and DI water. Then, the substrates were submitted to thermal annealing process in O_2 atmosphere at 500 °C for 30 minutes before co-sputtering of the alloy mix. At least 4 different rf powers were used, 0 W, 9 W, 12W, 50 W, 80W.

Table 5.5 RMS values of different surfaces. The selected area in the image to extract these values was 10 x 10 px.

Surface	Run	RMS (nm)	Average (nm)	Error (nm)
Industry Polished	1	0.230	0.263	±0.056
	2	0.319		
	3	0.240		
Un-Polished	1	28.0	37.1	±19.76
	2	56.7		
	3	26.7		
Mechanical Polished (At YSU)	1	1.2	1.5	±0.4
	2	1.9		
	3	1.4		

Figure 5.29 Alloys deposition setup.

5.5.3 Effects of B_2O_3 Sputtering Power Variation on Ga_2O_3

XRD. X-ray diffraction of the B_2O_3/Ga_2O_3 alloy films deposited on UID Ga_2O_3 substrate revealed that additional peaks appear for the samples co-sputtered at a rf power above 50 W. These peaks previously appeared in the homoepitaxial films grown on Ga_2O_3 substrate at a deposition temperature of 400 °C. The films in this set of were deposited at a higher temperature of 500 °C, therefore the additional peaks are to be expected. Nevertheless, for lower a lower rf power of 40 W, the additional peaks are not present. These additional peaks are from the {100} Ga_2O_3 family of planes, and result from the deposition temperature and the distortion of the crystal as boron is introduced to the matrix.

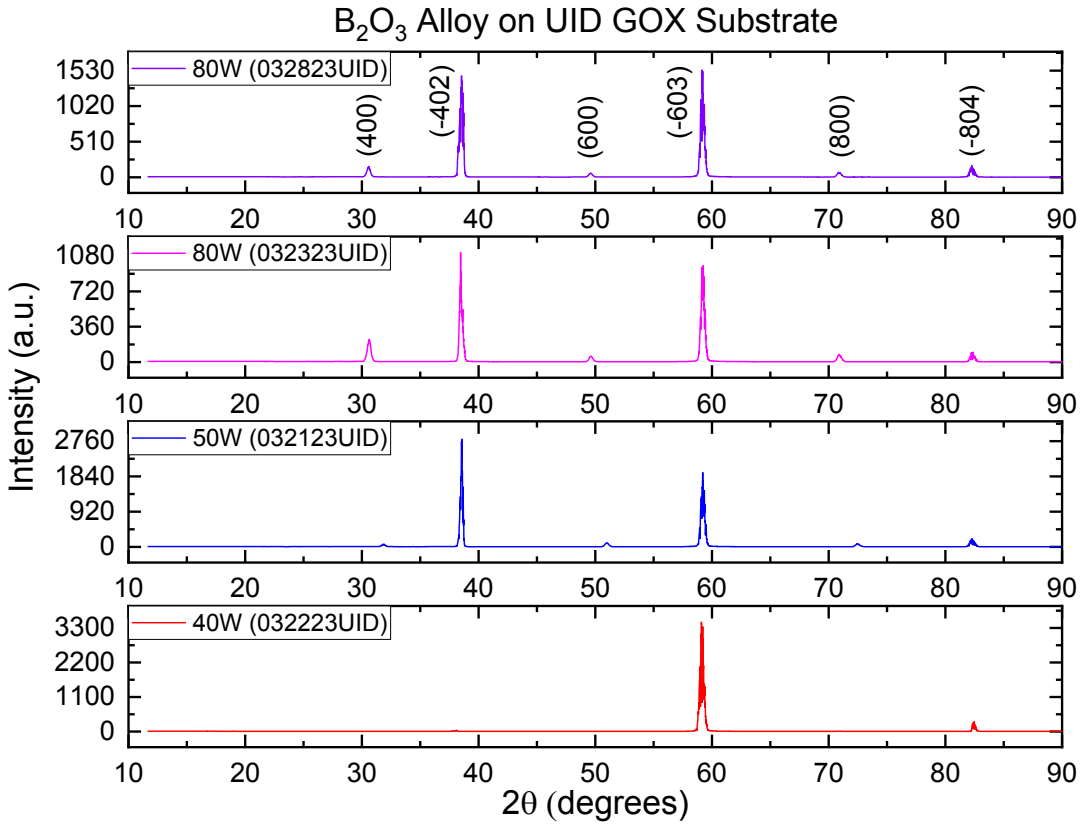

Figure 5.30 B_2O_3 alloy on UID Ga_2O_3 substrate XRD.

EDS. Energy dispersive spectroscopy (EDS) analysis of the B_2O_3/Ga_2O_3 alloy films deposited on the UID Ga_2O_3 substrate confirmed the successful deposition of boron oxide within the films (Fig. 5.31-5.33). The EDS results indicated a noticeable increase in the atomic percent of boron with increasing B_2O_3 rf power during deposition. The average atomic percent of boron obtained from EDS was 47%, 48%, and 52% for rf powers of 40, 50, and 80 W respectively, as depicted by Figure 5.34 where the atomic percent of boron, gallium and oxygen is plotted against the rf power of B_2O_3. This observed increment in boron concentration aligns with expectations, highlighting the direct correlation between the rf power applied during deposition and the concentration of boron oxide incorporated into the alloy films.

EDAX APEX

Eduardo-Alloys

Author: User Apex

Creation: 4/13/2023 2:58:56 PM

Sample Name: 032223_UID

032223_UID

eZAF Quant Result

Element	Weight %	MDL	Atomic %	Error %
Eduardo-Alloys | 032223_UID | Area 1 | Full Area 1				
B K	21.67	1.37	45.90	13.40
O K	25.71	0.04	36.81	8.87
Ga L	52.62	0.20	17.29	6.42
Eduardo-Alloys | 032223_UID | Area 1 | Selected Area 1				
B K	23.99	1.15	48.95	13.14
O K	25.42	0.03	35.04	8.90
Ga L	50.59	0.19	16.01	6.38
Eduardo-Alloys | 032223_UID | Area 1 | Selected Area 2				
B K	23.01	1.23	47.76	13.23
O K	25.42	0.03	35.65	8.89
Ga L	51.56	0.19	16.59	6.39
Eduardo-Alloys | 032223_UID | Area 1 | Selected Area 3				
B K	28.32	1.01	54.28	12.90
O K	24.46	0.03	31.68	8.96
Ga L	47.22	0.19	14.03	6.32

Spectrum Overlay

kV: 15 Mag: 55 Takeoff: 35.4 Live Time(s): 200 Amp Time(µs): 3.84 Resolution:(eV) 129.8

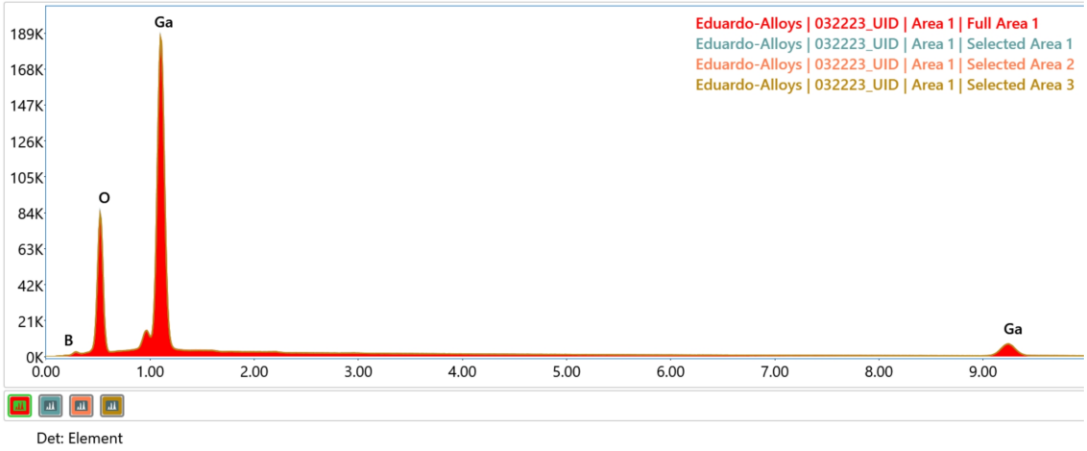

Figure 5.31 EDS report B_2O_3 on UID Ga_2O_3 rf power: 40 W.

EDAX APEX

Eduardo-Alloys

Author: User Apex

Creation: 4/13/2023 2:30:08 PM

Sample Name: 032123_UID

032123_UID

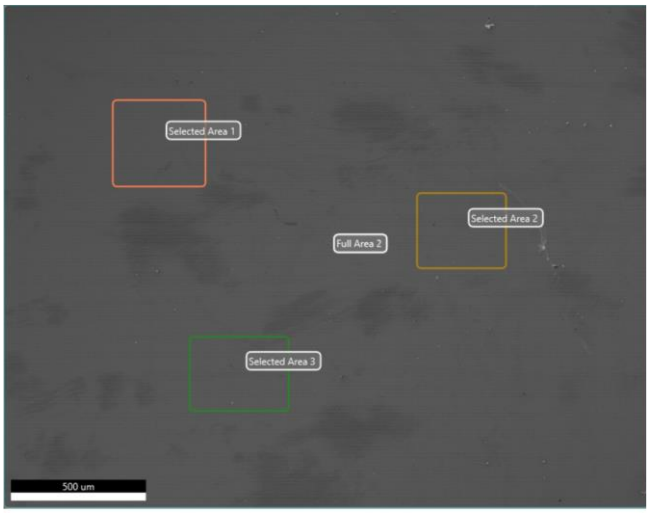

eZAF Quant Result

Element	Weight %	MDL	Atomic %	Error %
Eduardo-Alloys | 032123_UID | Area 1 | Full Area 1				
B K	22.60	5.38	47.11	23.14
O K	25.69	0.16	36.18	9.36
Ga L	51.72	0.83	16.72	6.69
Eduardo-Alloys | 032123_UID | Area 1 | Full Area 2				
B K	26.14	1.06	51.61	12.96
O K	25.08	0.03	33.46	8.92
Ga L	48.78	0.17	14.93	6.35
Eduardo-Alloys | 032123_UID | Area 1 | Selected Area 1				
B K	23.74	1.19	48.53	13.09
O K	25.66	0.03	35.44	8.91
Ga L	50.60	0.18	16.04	6.42
Eduardo-Alloys | 032123_UID | Area 1 | Selected Area 2				
B K	21.35	1.28	45.37	13.30
O K	25.97	0.03	37.27	8.88
Ga L	52.68	0.18	17.36	6.45
Eduardo-Alloys | 032123_UID | Area 1 | Selected Area 3				
B K	25.48	1.12	50.80	13.02
O K	25.20	0.03	33.95	8.94
Ga L	49.32	0.18	15.25	6.39

Spectrum Overlay

kV: 15 Mag: 50 Takeoff: 35.4 Live Time(s): 10 Amp Time(µs): 3.84 Resolution:(eV) 129.8

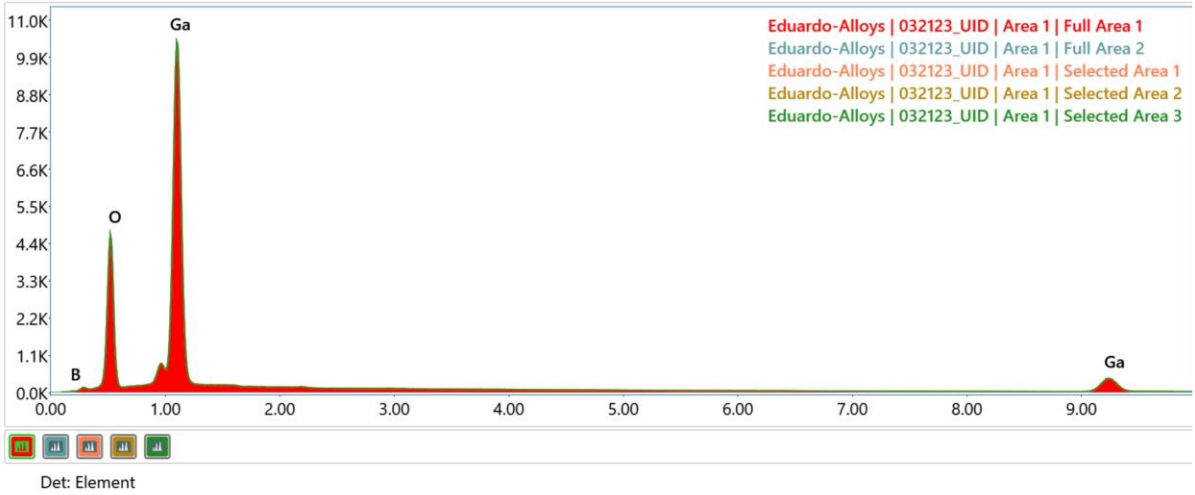

Figure 5.32 EDS report B_2O_3 on UID Ga_2O_3 rf power: 50 W.

EDAX APEX

Eduardo-Alloys

Author: User Apex

Creation: 4/14/2023 1:58:52 PM

Sample Name: 032823_UID_B2O3

032823_UID_B2O3

eZAF Quant Result

Element	Weight %	MDL	Atomic %	Error %
Eduardo-Alloys | 032823_UID_B2O3 | Area 1 | Full Area 1				
B K	26.27	1.20	50.91	13.01
O K	26.70	0.03	34.96	8.93
Ga L	47.03	0.18	14.13	6.43
Eduardo-Alloys | 032823_UID_B2O3 | Area 1 | Selected Area 1				
B K	27.39	1.01	52.27	12.82
O K	26.42	0.03	34.06	8.94
Ga L	46.19	0.16	13.67	6.41
Eduardo-Alloys | 032823_UID_B2O3 | Area 1 | Selected Area 2				
B K	27.32	1.12	52.18	12.89
O K	26.45	0.03	34.13	8.94
Ga L	46.22	0.17	13.69	6.41
Eduardo-Alloys | 032823_UID_B2O3 | Area 1 | Selected Area 3				
B K	28.96	1.08	54.12	12.80
O K	26.01	0.03	32.84	8.97
Ga L	45.02	0.17	13.04	6.38

Spectrum Overlay

kV: 15 Mag: 50 Takeoff: 34.8 Live Time(s): 200 Amp Time(µs): 3.84 Resolution:(eV) 129.8

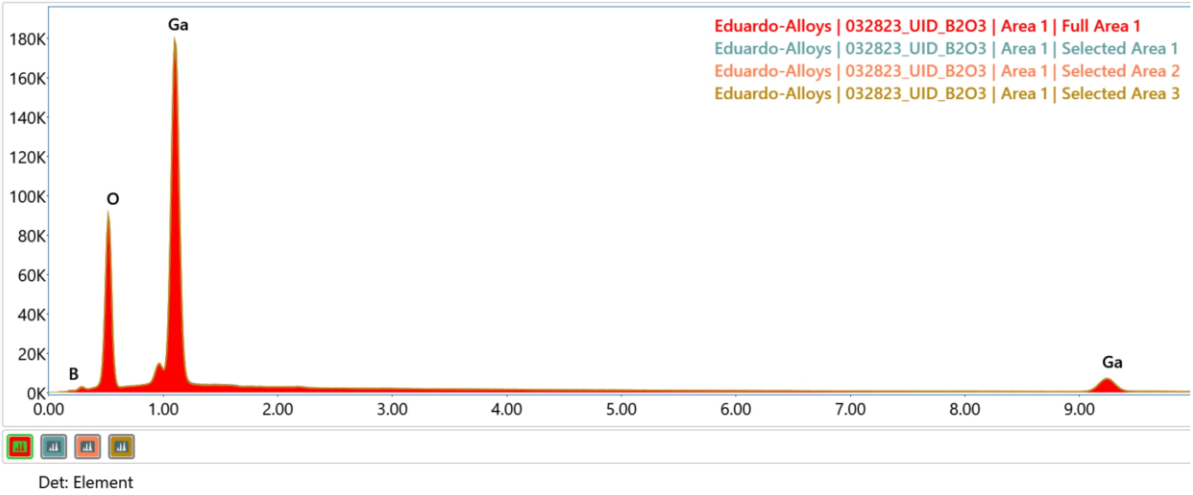

Figure 5.33 EDS report B_2O_3 on UID Ga_2O_3 rf power: 80 W.

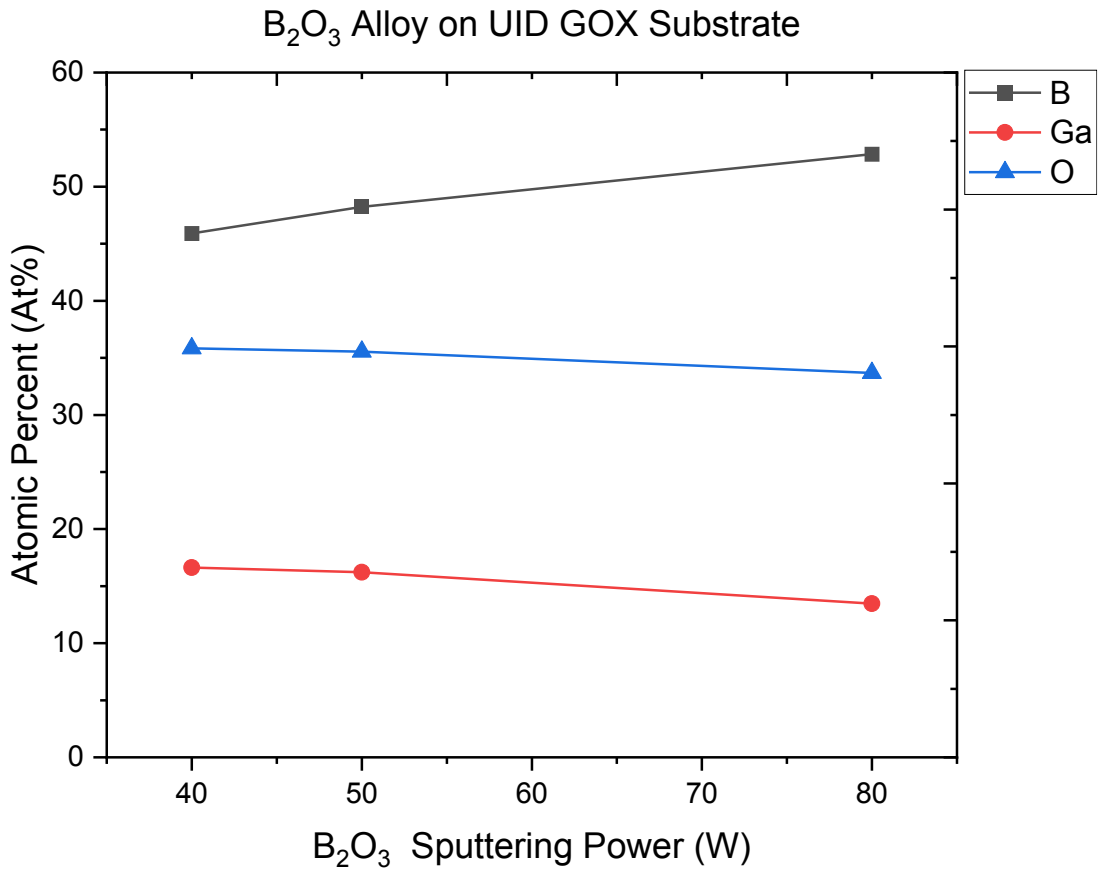

Figure 5.34 Atomic percent of B, Ga, and O of films deposited on UID Ga_2O_3 as a function of the B_2O_3 rf power.

UV-Vis Spectroscopy. UV-Vis spectroscopy was used to analyze the optical properties of the B_2O_3/Ga_2O_3 alloy films deposited on the UID Ga_2O_3 substrate. The results revealed that these films demonstrated high transparency across the entire spectrum. As shown in Fig. 5.35 there was no direct correlation observed between transmittance and rf power. Typically, Ga_2O_3 films absorb light in the ultraviolet (UV) region of the spectrum; however, this behavior was not clearly observed in the transmittance plot presented in Fig. 5.36. Instead, the measurements were noisy in this region, which was attributed to the inability to achieve an optically transparent surface during the polishing process of the purchased substrates. This issue persisted across all mechanically polished samples, impacting the clarity of the UV-Vis spectroscopy results.

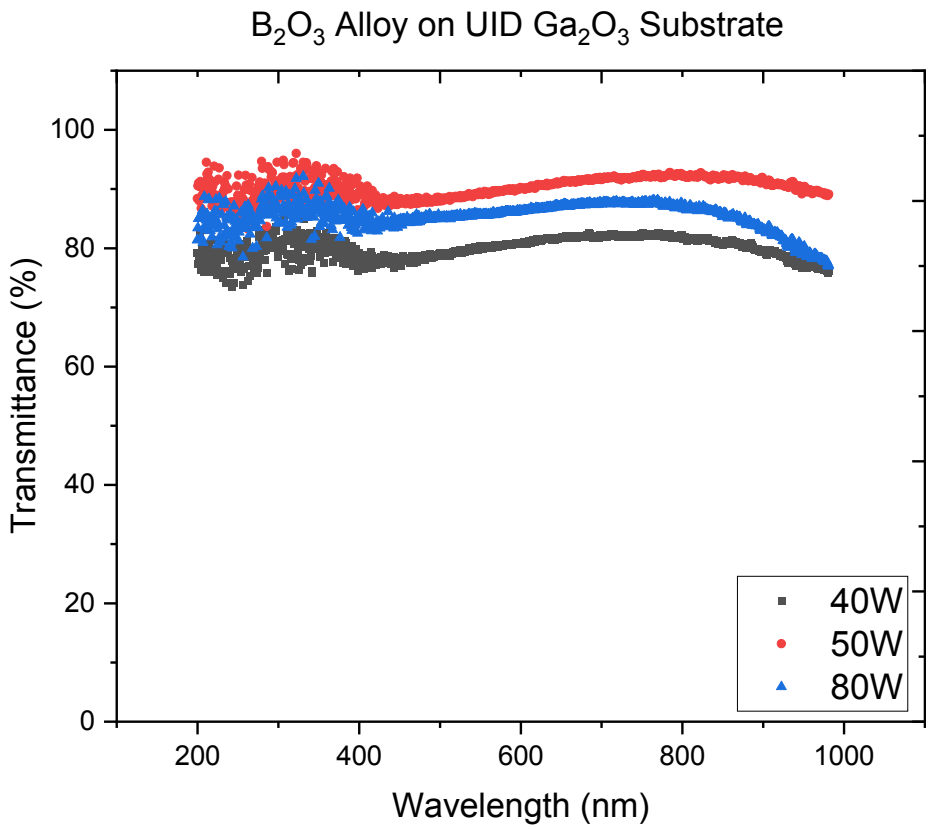

Figure 5.35 Transmittance of B_2O_3/Ga_2O_3 alloy films deposited on the UID Ga_2O_3 substrate.

Absorbance measurements yielded a clearer result. Figure 5.37 (a) demonstrates that the films indeed absorb in the UV region as expected for films co-sputtered with gallium oxide. However, no visible pattern of absorbance is observed with increasing B_2O_3 rf power. Following the absorbance plot, energy plots were constructed to extract the optical bandgap of the deposited alloy films, as depicted in Fig. 5.37 (b). These energy plots allowed for a quantitative assessment of the bandgap characteristics of the B_2O_3/Ga_2O_3 alloy films.

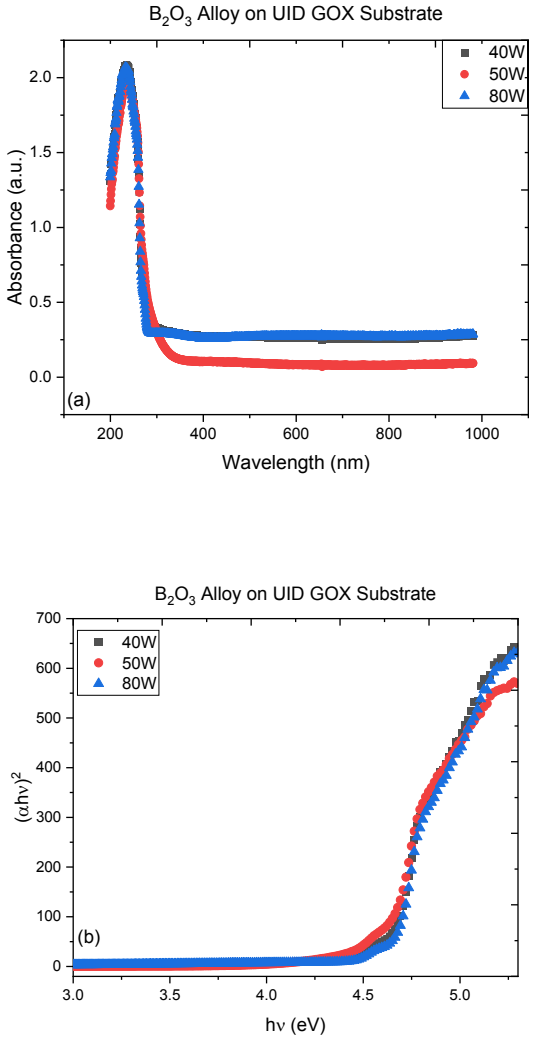

Figure 5.36 Absorbance (a) and energy plot (b) of B_2O_3/Ga_2O_3 alloy films deposited on the UID Ga_2O_3 substrate.

The optical bandgap was plotted as a function of the B_2O_3 rf power (Fig. 5.37). The bandgap is observed to decrease slightly with B_2O_3 rf power from 4.64 eV at 0W to 4.62 at 50 W, then increase again to 4.65 eV at 80 W. Compared to the bandgap of pure Ga_2O_3 which is found to be in the range of 4.7-4.9 eV [39, 40] alloying with B_2O_3 results in the narrowing of the film's optical bandgap. Moreover, variations in surface roughness of the polished substrate can result in scattering or absorption of light, affecting the measured transmittance and absorption spectra.

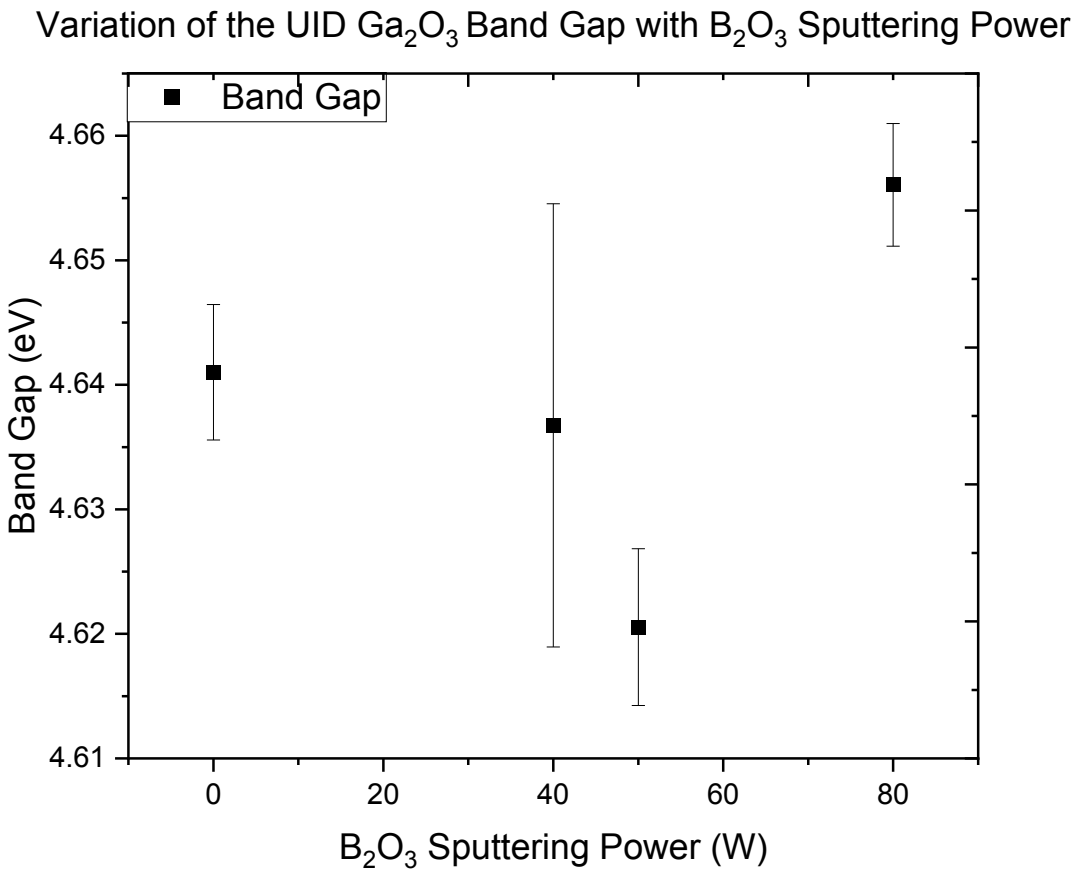

Figure 5.37 Bandgap energy vs B_2O_3 rf power for B_2O_3/Ga_2O_3 alloy films deposited on the UID Ga_2O_3 substrate.

XRD. Similarly, the films deposited on the of $(\bar{2}01)$ Sn-doped Ga_2O_3 substrates showed additional (100) Ga_2O_3 planes at B_2O_3 rf power above 50 W and then their intensity is reduced at B_2O_3 rf of 80 W (Fig. 5.38).

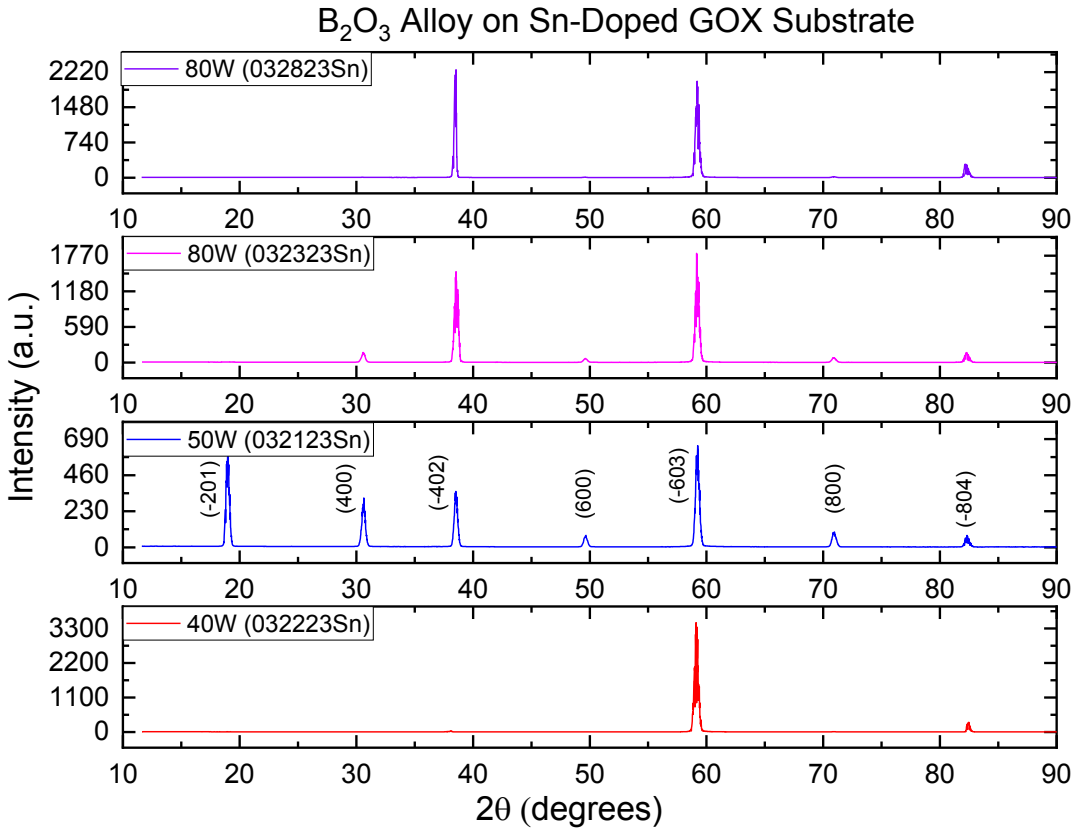

Figure 5.38 B_2O_3 alloy o Sn-doped Ga_2O_3 substrate XRD.

EDS. EDS reports showed a direct correlation between the B_2O_3 rf power and the boron atomic percent in the film, with average values of 48%, 53% and 55% at 40W, 50W, and 80 W, respectively (Fig. 5.39-5.41). EDS results are better illustrated in Figure 5.42 where the atomic percentage of B, Ga, and O is plotted against the rf sputtering power of B_2O_3.

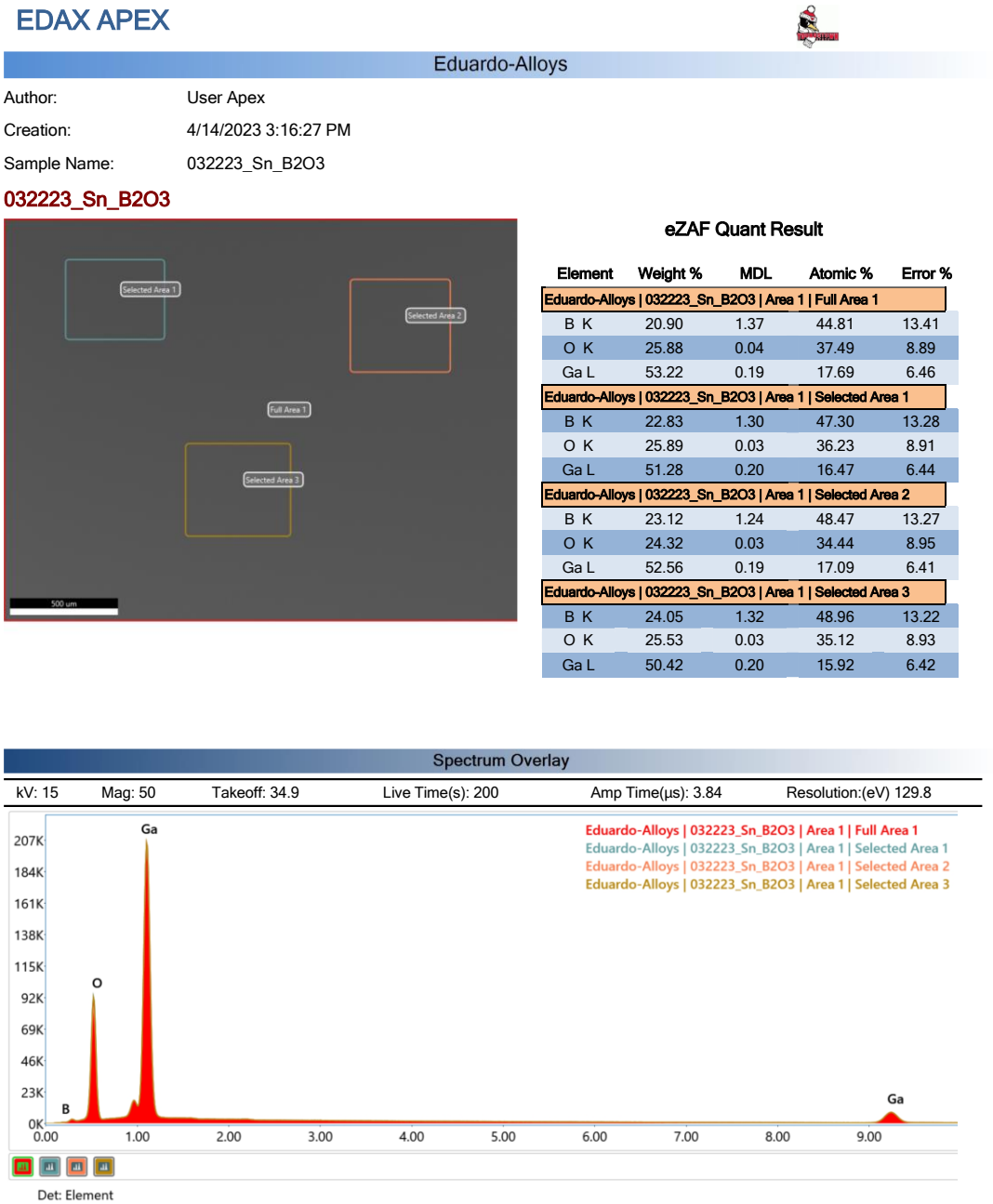

Figure 5.39 EDS report B_2O_3 on Sn-doped Ga_2O_3 rf power: 40 W.

EDAX APEX

Eduardo-Alloys

Author: User Apex

Creation: 4/14/2023 2:55:53 PM

Sample Name: 032123_Sn_B2O3

032123_Sn_B2O3

eZAF Quant Result

Element	Weight %	MDL	Atomic %	Error %
Eduardo-Alloys | 032123_Sn_B2O3 | Area 1 | Full Area 1				
B K	27.44	0.94	52.99	12.48
O K	25.14	0.03	32.81	8.96
Ga L	47.42	0.17	14.20	6.37
Eduardo-Alloys | 032123_Sn_B2O3 | Area 1 | Selected Area 1				
B K	27.69	1.01	53.28	12.88
O K	25.12	0.03	32.65	8.97
Ga L	47.19	0.18	14.07	6.37
Eduardo-Alloys | 032123_Sn_B2O3 | Area 1 | Selected Area 2				
B K	27.35	0.98	52.90	12.87
O K	25.14	0.03	32.85	8.96
Ga L	47.51	0.17	14.25	6.38
Eduardo-Alloys | 032123_Sn_B2O3 | Area 1 | Selected Area 3				
B K	29.54	0.95	55.39	12.44
O K	24.72	0.03	31.31	8.99
Ga L	45.74	0.18	13.30	6.34

Spectrum Overlay

kV: 15 Mag: 50 Takeoff: 34.9 Live Time(s): 200 Amp Time(µs): 3.84 Resolution:(eV) 129.8

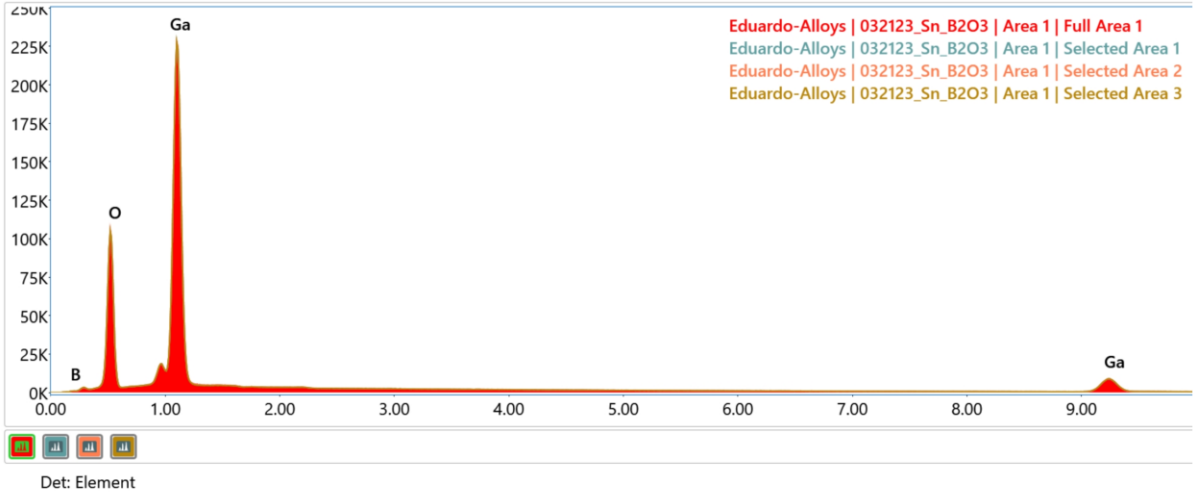

Figure 5.40 EDS report B_2O_3 on Sn-doped Ga_2O_3 rf power: 50 W.

EDAX APEX

Eduardo-Alloys

Author: User Apex

Creation: 4/14/2023 3:54:51 PM

Sample Name: 032823_Sn_B2O3

032823_Sn_B2O3

eZAF Quant Result

Element	Weight %	MDL	Atomic %	Error %
Eduardo-Alloys | 032823_Sn_B2O3 | Area 1 | Full Area 1				
B K	30.44	0.90	55.44	12.34
O K	26.27	0.03	32.33	8.96
Ga L	43.29	0.16	12.22	6.36
Eduardo-Alloys | 032823_Sn_B2O3 | Area 1 | Selected Area 1				
B K	31.47	0.87	56.49	12.29
O K	26.14	0.03	31.71	8.98
Ga L	42.39	0.16	11.80	6.35
Eduardo-Alloys | 032823_Sn_B2O3 | Area 1 | Selected Area 2				
B K	30.66	0.91	55.73	12.38
O K	26.15	0.03	32.10	8.97
Ga L	43.19	0.17	12.17	6.36

Spectrum Overlay

kV: 15 Mag: 50 Takeoff: 34.9 Live Time(s): 200 Amp Time(µs): 3.84 Resolution:(eV) 129.8

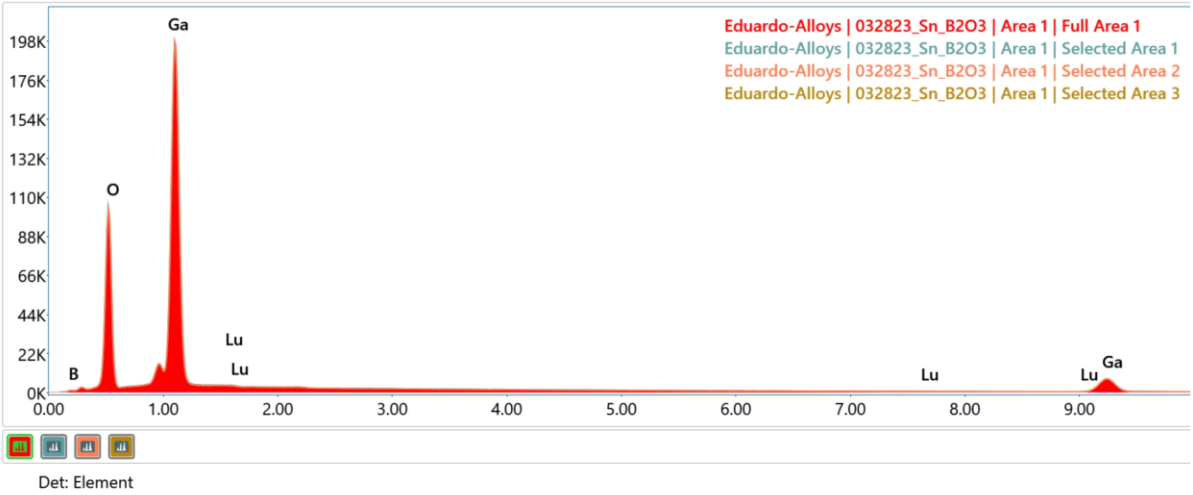

Figure 5.41 EDS report B_2O_3 on Sn-doped Ga_2O_3 rf power: 80 W.

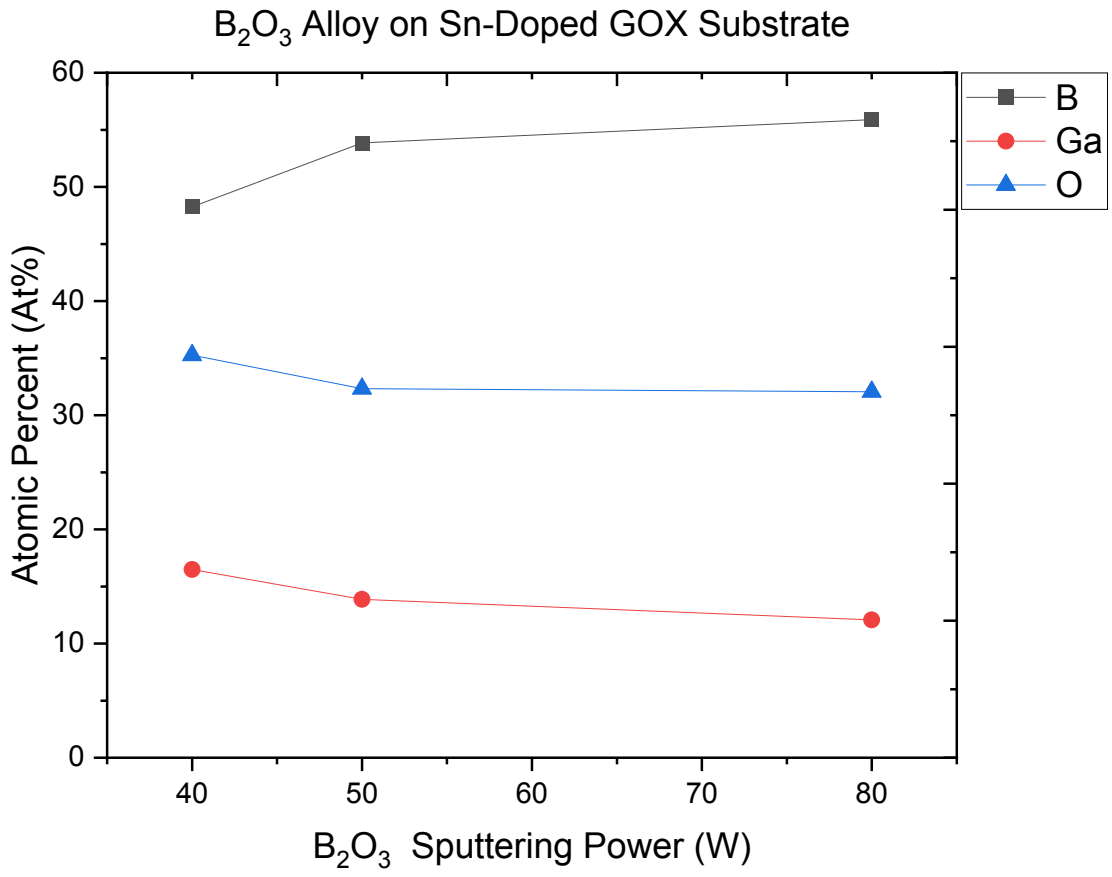

Figure 5.42 Atomic percent of B, Ga, and O of films deposited on Sn-doped Ga_2O_3 as a function of the B_2O_3 rf power.

UV-Vis Spectroscopy. UV-Vis spectroscopy was also used to analyze the optical properties of the B_2O_3/Ga_2O_3 alloy films deposited on the Sn-doped Ga_2O_3 substrate. Similarly, the films showed high transparency across the entire spectrum, but no direct correlation was observed between transmittance and increasing rf power, as depicted in Fig. 5.43.

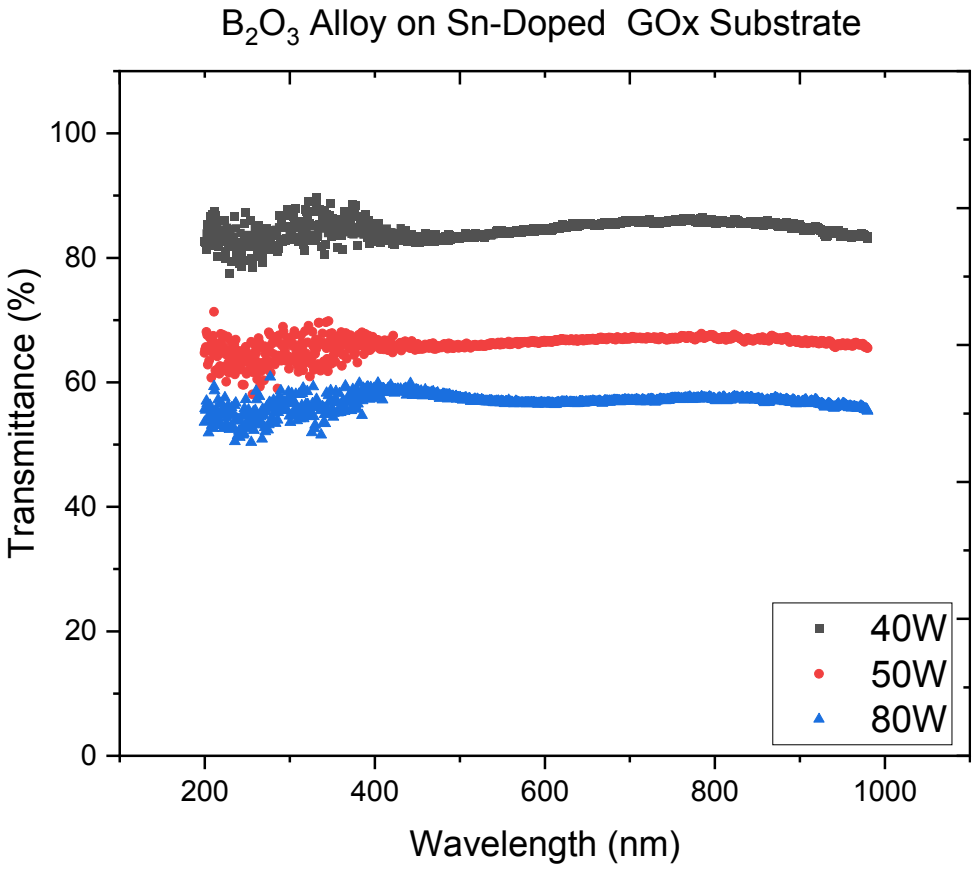

Figure 5.43 Transmittance of B_2O_3/Ga_2O_3 alloy films deposited on the Sn-doped Ga_2O_3 substrate.

Figure 5.44 (a) shows that the films also absorb in the UV region as expected for films co-sputtered with gallium oxide. Figure 5.44 (b) shows the energy plot used to extract the optical bandgap via a Tauc plot.

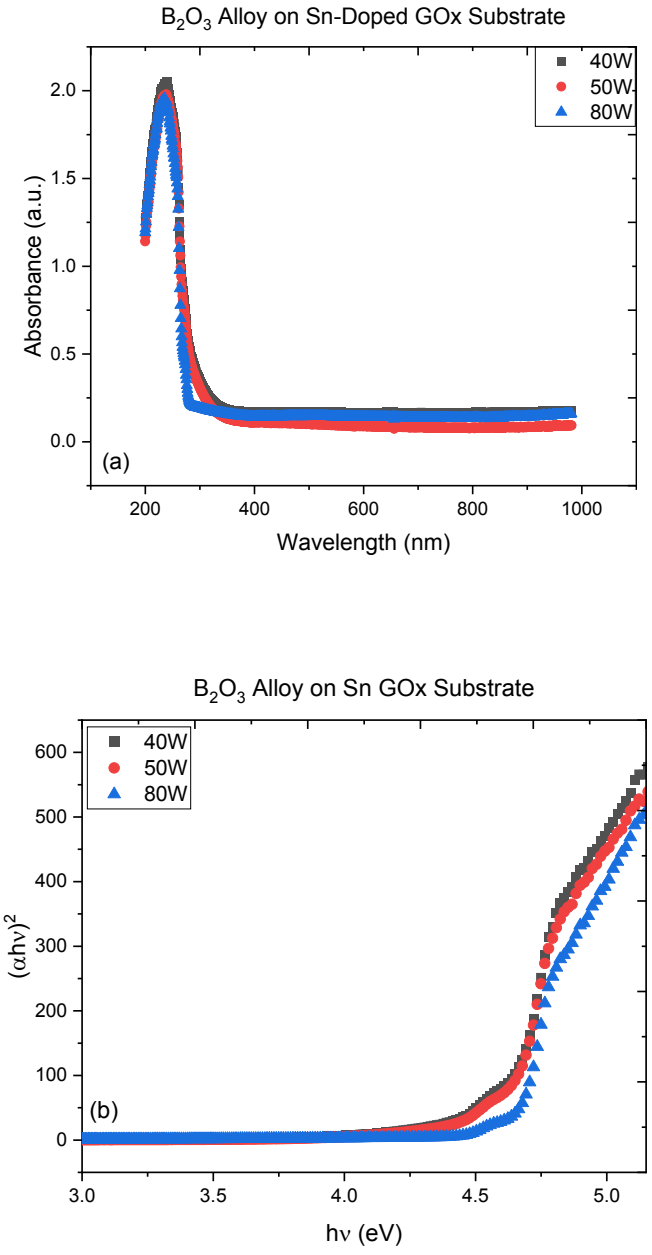

Figure 5.44 Absorbance (a) and energy plot (b) of B_2O_3/Ga_2O_3 alloy films deposited on the Sn-doped Ga_2O_3 substrate.

The optical bandgap for this set is plotted as a function of the B_2O_3 rf power (Fig. 5.46). A similar pattern to the samples deposited in UID Ga_2O_3 was observed. The bandgap energy decreases slightly with B_2O_3 rf power from 4.64 eV at 0W to 4.62 at 40 W, then increase again to 4.66 eV at 80 W.

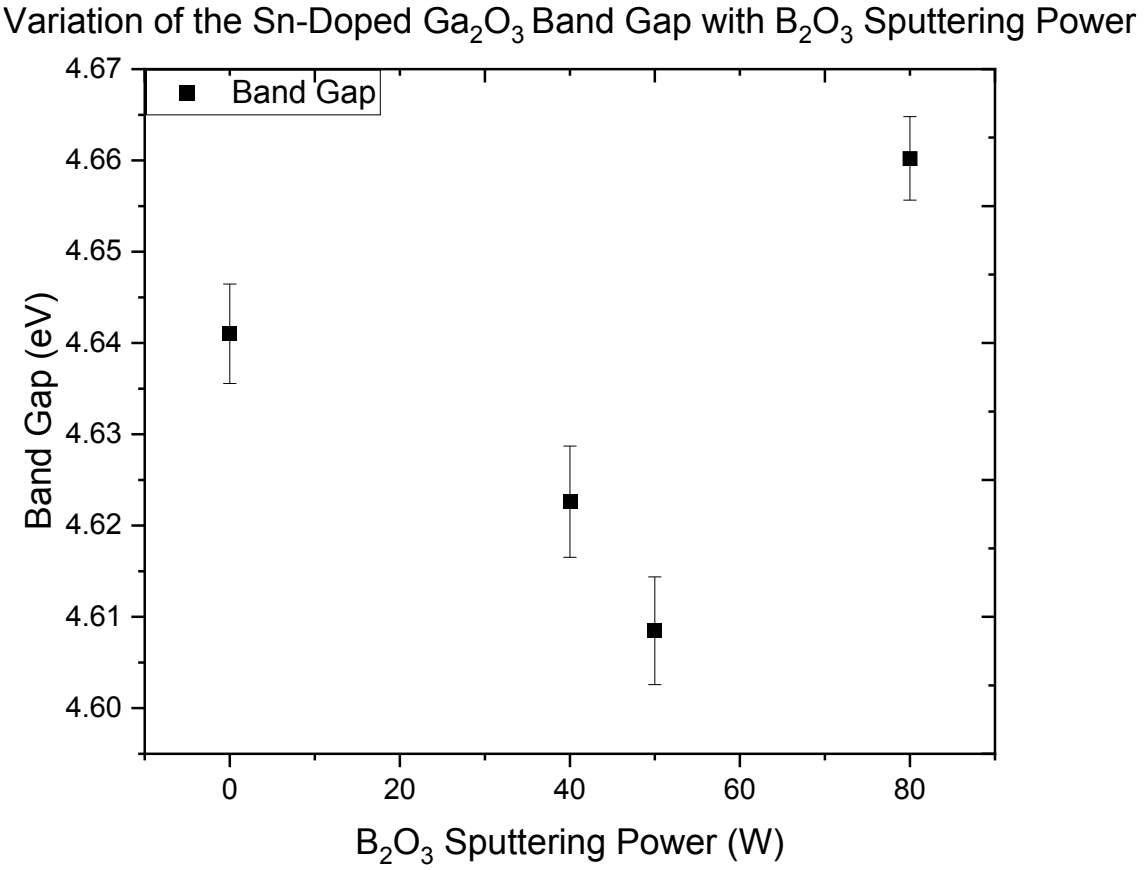

Figure 5.45 Bandgap energy vs B_2O_3 rf power for B_2O_3/Ga_2O_3 alloy films deposited on the Sn-doped Ga_2O_3 substrate.

5.5.4 Effects of Lu_2O_3 Sputtering Power Variation on Ga_2O_3

XRD. Figure 5.46 illustrates the X-ray diffraction pattern of Lu_2O_3/Ga_2O_3 alloy films deposited on the UID Ga_2O_3 substrate. Notably, additional (100) peaks are observed at a lower Lu_2O_3 rf power of 20 W, but these peaks disappear when the rf power is increased to 80 W. Interestingly, no distinct peaks corresponding to Lu_2O_3 are detected in the XRD data, indicating that this phase remains non-crystalline under the deposition conditions used.

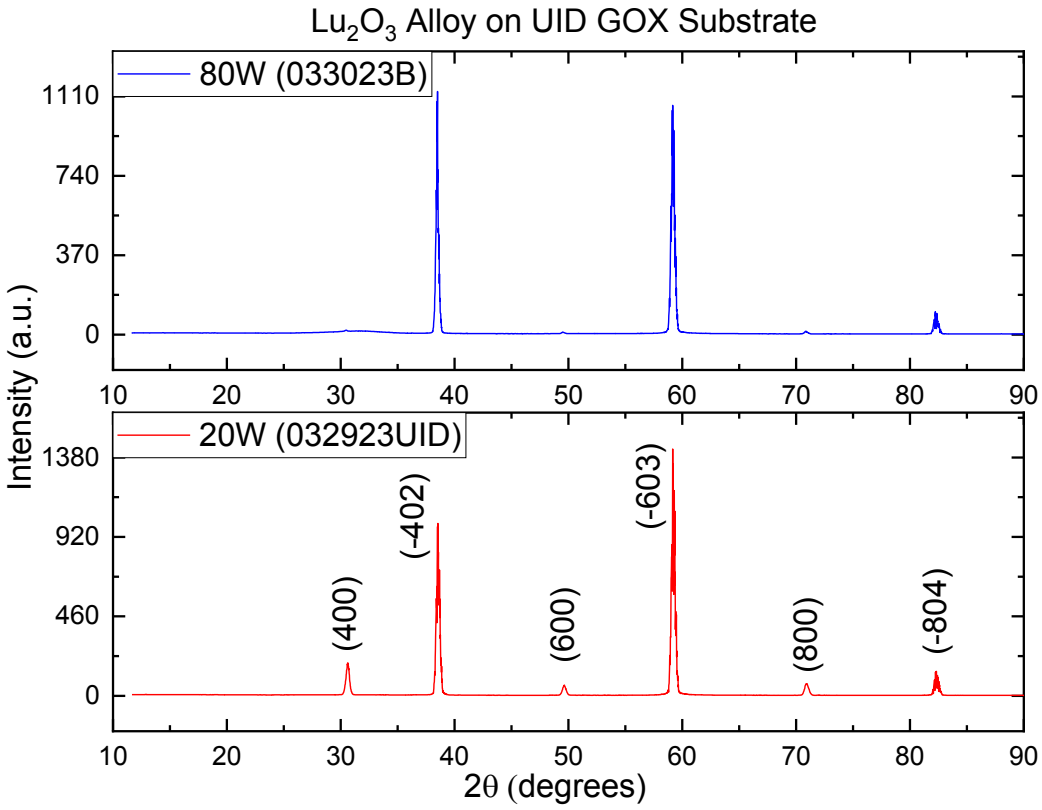

Figure 5.46 Lu_2O_3 alloy on UID Ga_2O_3 substrate XRD.

EDS. The EDS reports indicate a rise in the atomic percentage of Lu_2O_3 within the film as the rf power increases (Fig. 5.47-5.48). The average values obtained from three selected areas were 1.4% at 20 W and 15% at 80 W. At a rf power of 100 W, the estimated deposition rate of Lu_2O_3 was 1.1 Å/s, whereas Ga_2O_3 had a deposition rate of 0.2 Å/s under the same rf power. Despite using 20% of the Lu_2O_3 rf power, the expected concentrations of Lu and Ga should have been similar. However, the difficulty in sputtering Lu_2O_3 under these conditions resulted in a small concentration at an rf power of 20 W. EDS reports are plotted against the rf power in Fig. 5.49.

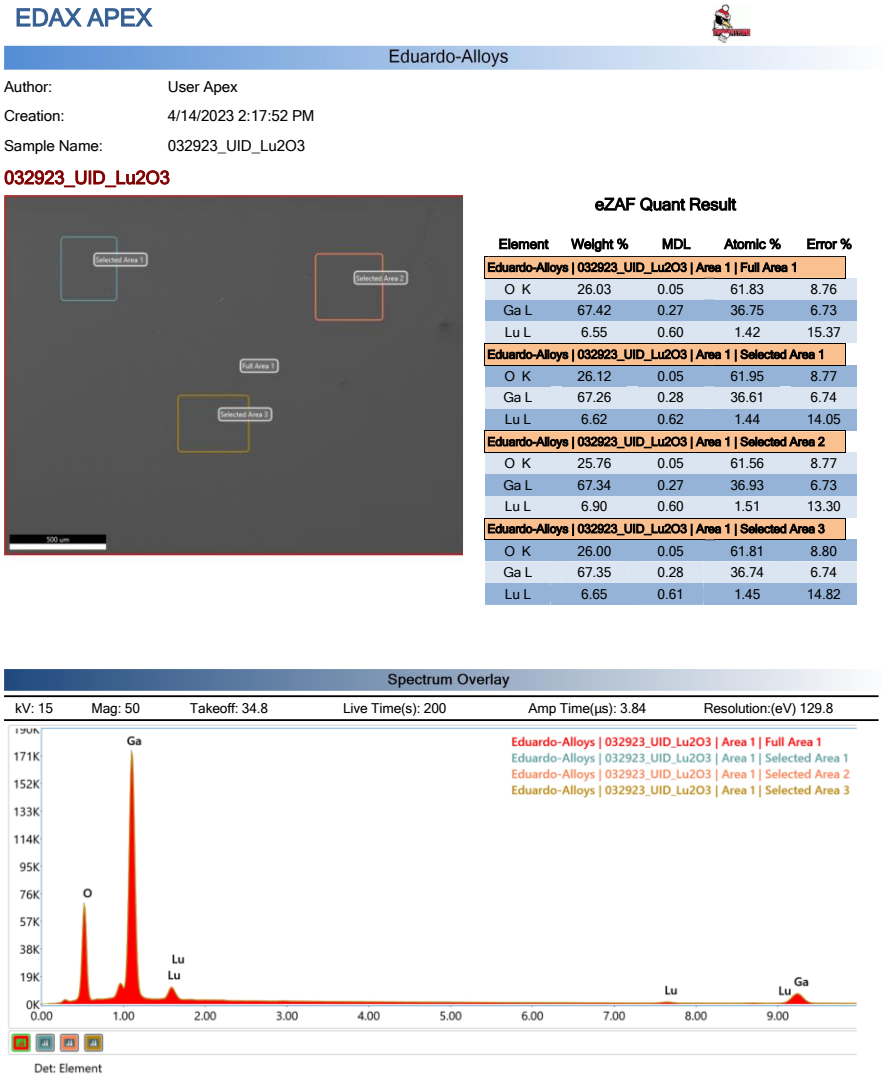

Figure 5.47 EDS report Lu_2O_3 on UID Ga_2O_3 rf power: 20 W.

EDAX APEX

Eduardo-Alloys

Author: User Apex

Creation: 4/14/2023 2:35:32 PM

Sample Name: 033023B_UID_Lu2O3

033023B_UID_Lu2O3

eZAF Quant Result

Element	Weight %	MDL	Atomic %	Error %
Eduardo-Alloys | 033023B_UID_Lu2O3 | Area 1 | Full Area 1				
O K	18.66	0.06	61.71	9.24
Ga L	30.00	0.19	22.76	6.93
Lu L	51.34	0.74	15.52	4.83
Eduardo-Alloys | 033023B_UID_Lu2O3 | Area 1 | Selected Area 1				
O K	18.73	0.06	61.75	9.25
Ga L	30.21	0.21	22.86	6.93
Lu L	51.06	0.78	15.39	4.90
Eduardo-Alloys | 033023B_UID_Lu2O3 | Area 1 | Selected Area 2				
O K	18.29	0.06	61.50	9.27
Ga L	28.86	0.21	22.26	6.94
Lu L	52.84	0.78	16.24	4.77

Spectrum Overlay

kV: 15 Mag: 50 Takeoff: 34.8 Live Time(s): 200 Amp Time(µs): 3.84 Resolution:(eV) 129.8

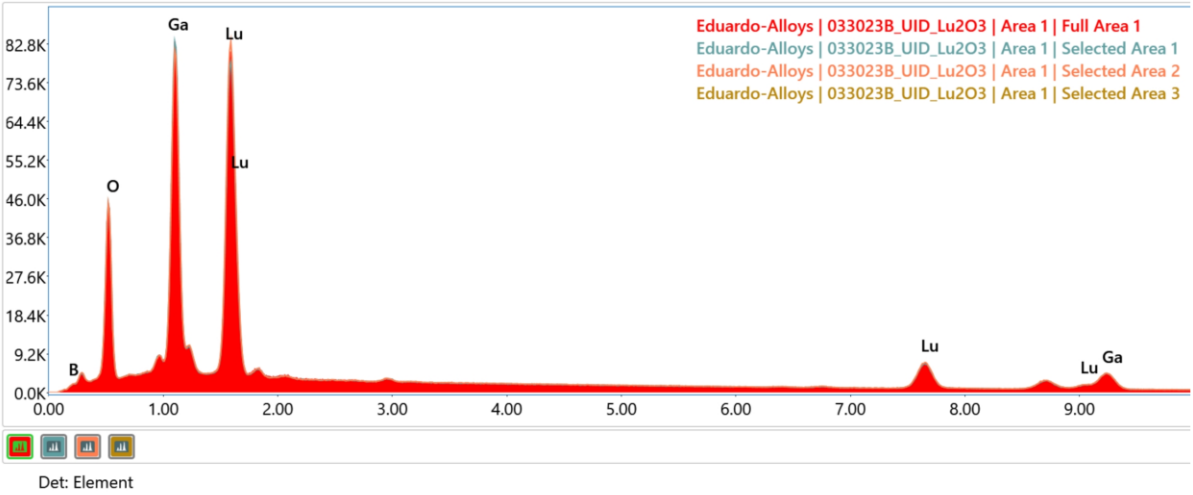

Figure 5.48 EDS report Lu_2O_3 on UID Ga_2O_3 rf power: 80 W.

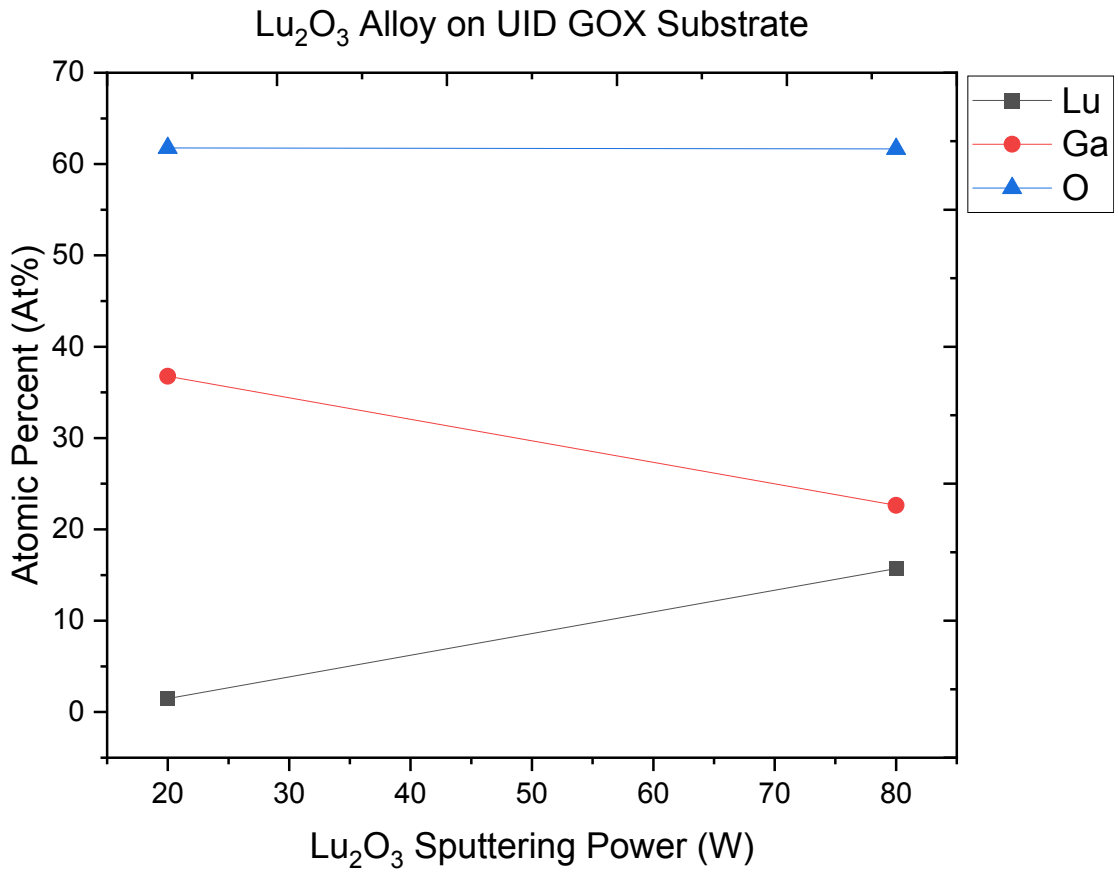

Figure 5.49 Atomic percent of Lu, Ga, and O of films deposited on UID Ga_2O_3 as a function of the Lu_2O_3 rf power.

UV-Vis Spectroscopy. UV-Vis spectroscopy was utilized to examine the optical characteristics of the Lu_2O_3/Ga_2O_3 alloy films deposited on the UID Ga_2O_3 substrate. These samples exhibited a transparency level of 70% across the spectrum. However, there was no clear relationship observed between transmittance and increasing rf power, as illustrated in Fig. 5.50.

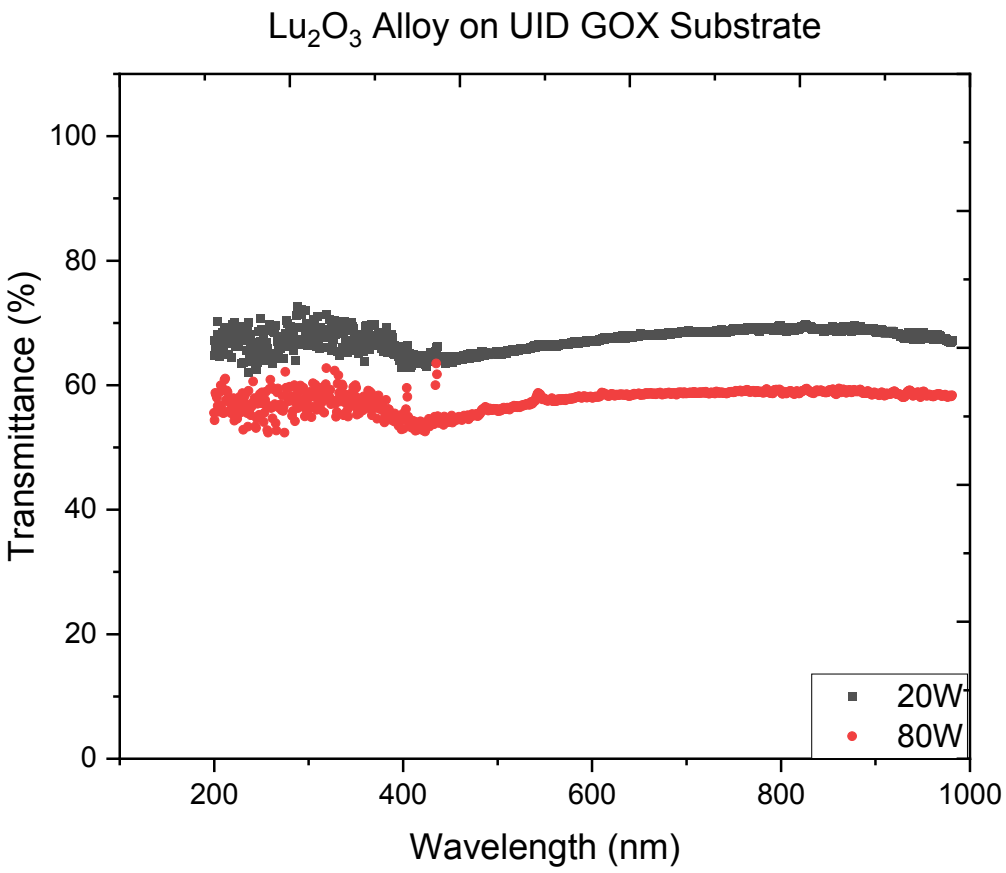

Figure 5.50 Transmittance of Lu_2O_3/Ga_2O_3 alloy films deposited on the UID Ga_2O_3 substrate.

Figure 5.51 (a) shows that the films also absorb in the UV region as expected for films co-sputtered with gallium oxide. Figure 2.51 (b) shows the energy plot used to extract the optical bandgap via a Tauc plot for Lu_2O_3/Ga_2O_3 films.

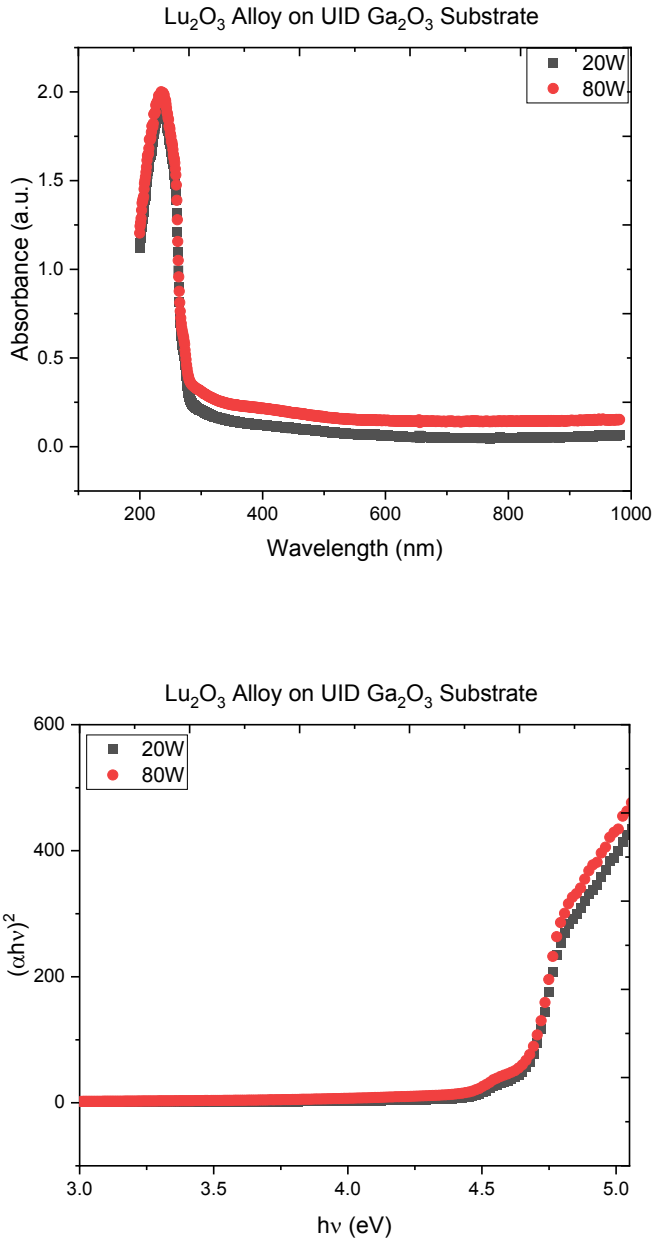

Figure 5.51 Absorbance (a) and energy plot (b) of Lu_2O_3/Ga_2O_3 alloy films deposited on the UID Ga_2O_3 substrate.

The optical bandgap for this set is plotted as a function of the Lu_2O_3 rf power (Figure 5.52). The bandgap energy in the case of co-sputtering with Lu_2O_3 results in a slight increase with Lu_2O_3 rf power from 4.641 eV at 0W to 4.646 eV at 40 W, then increase again to 4.648 eV at 80 W.

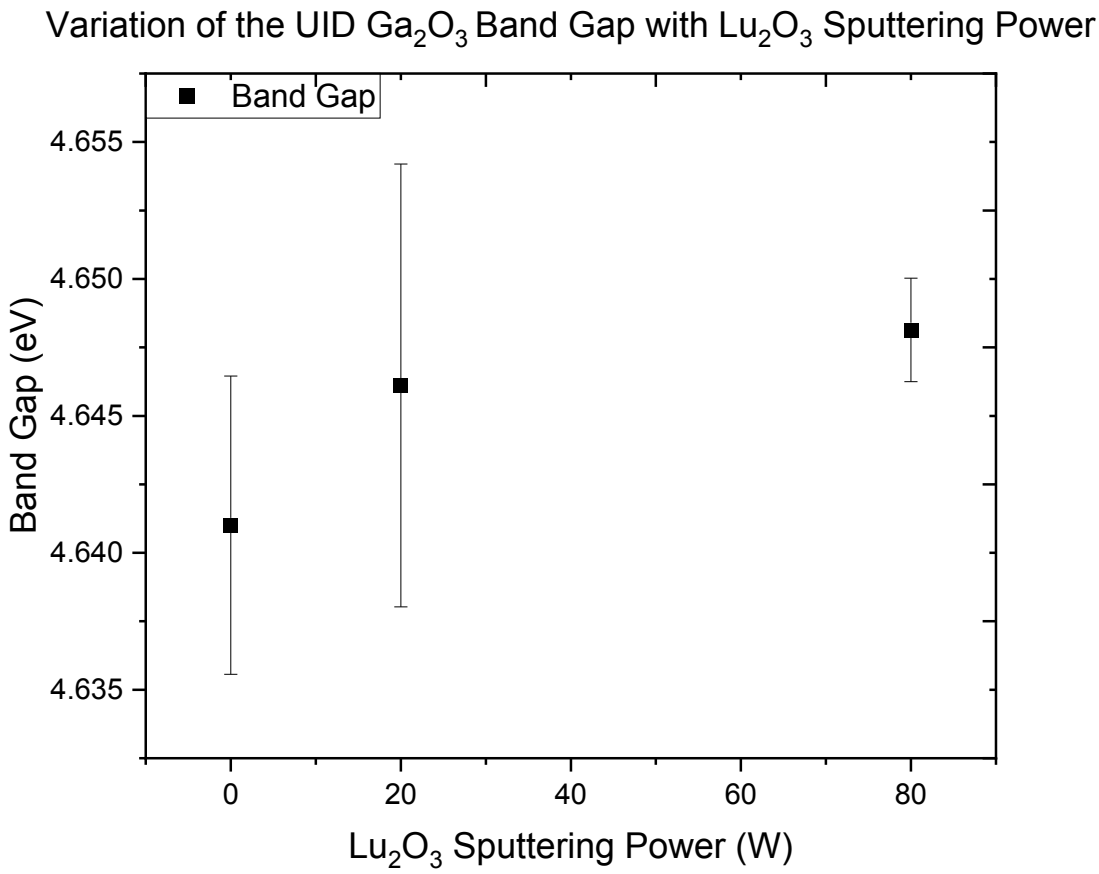

Figure 5.52 Bandgap energy vs Lu_2O_3 rf power for Lu_2O_3/Ga_2O_3 alloy films deposited on the Sn-doped Ga_2O_3 substrate.

XRD. The investigation extended to the analysis of Lu_2O_3/Ga_2O_3 alloy films deposited on the Sn-doped Ga_2O_3 substrate. Consistent with the XRD results shown in Fig. 5.53, two prominent peaks originating from the $(\bar{2}01)$ crystallographic plane of Ga_2O_3 were observed across all samples are present in all samples. The additional peaks were also detected, emanating from the {100} of Ga_2O_3 at rf power of 20 W. However, it is noteworthy that the intensity of these (100) planes was relatively weak at higher rf power of 80 W, indicative reduced orderliness of the corresponding crystallographic planes or lattice spacing within the alloy films.

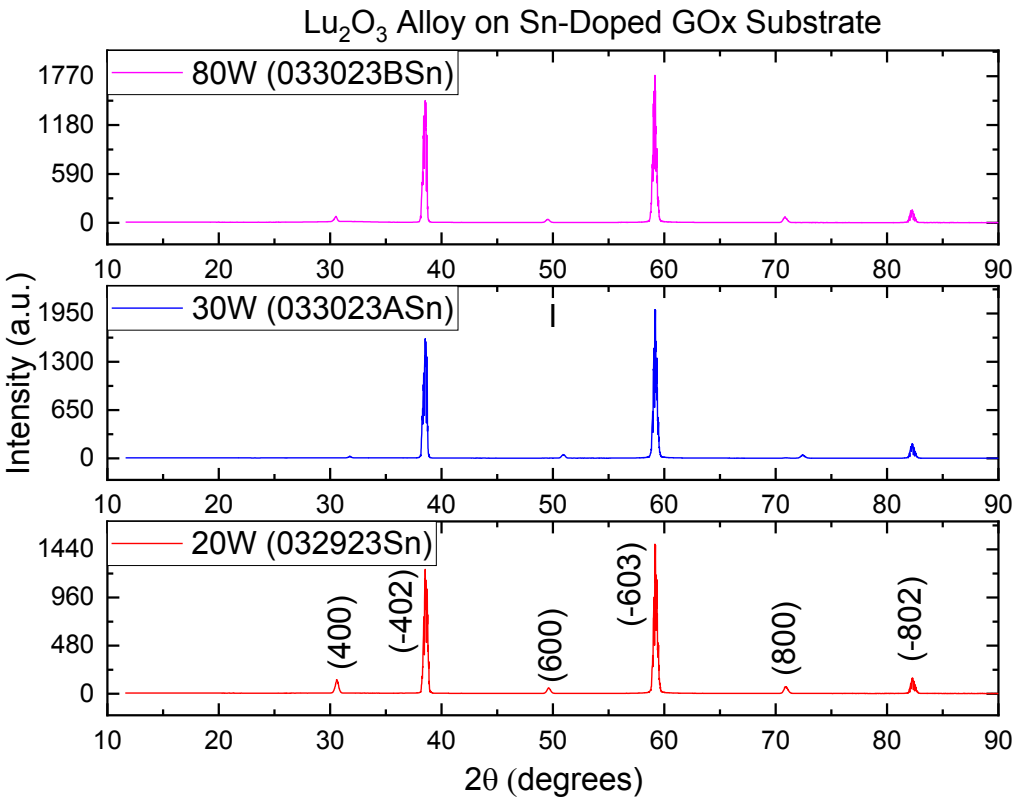

Figure 5.53 Lu_2O_3 alloy on Sn-dope Ga_2O_3 substrate XRD.

EDS. The EDS reports shows an increase in the atomic percentage of Lu_2O_3 within the film as the rf power increases (Fig. 5.54-5.56). Average values obtained are 1.0 %, 2.6%, and 14.6% at 20, 30, and 80 W (Fig. 5.57). Interestingly, there appears to be a decrease in the oxygen atomic percent with increasing rf power. This phenomenon could be attributed to the higher sputtering rates associated with the Lu_2O_3 target, leading to the evaporation of oxygen, resulting in oxygen deficient films.

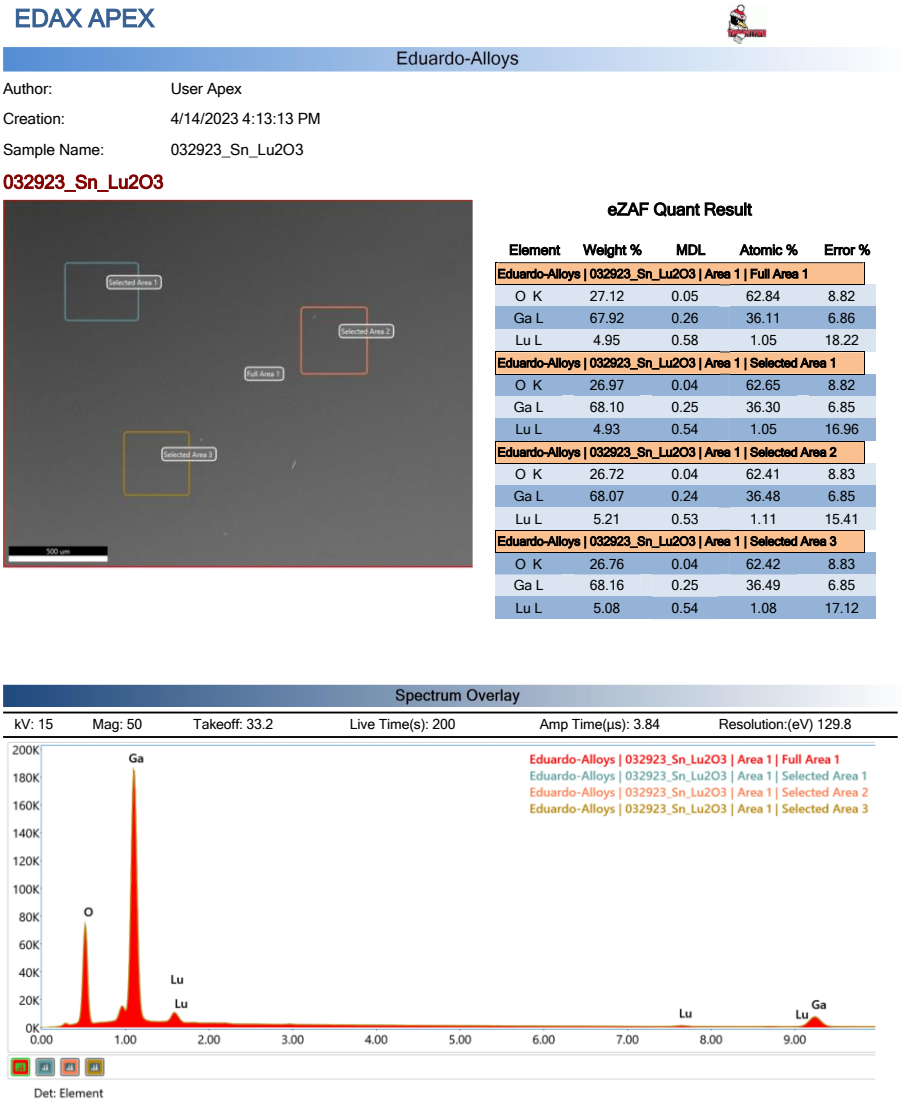

Figure 5.54 EDS report Lu_2O_3 on Sn-doped Ga_2O_3 rf power: 20 W.

EDAX APEX

Eduardo-Alloys

Author: User Apex

Creation: 4/14/2023 4:32:40 PM

Sample Name: 033023A_Sn_Lu2O3

033023A_Sn_Lu2O3

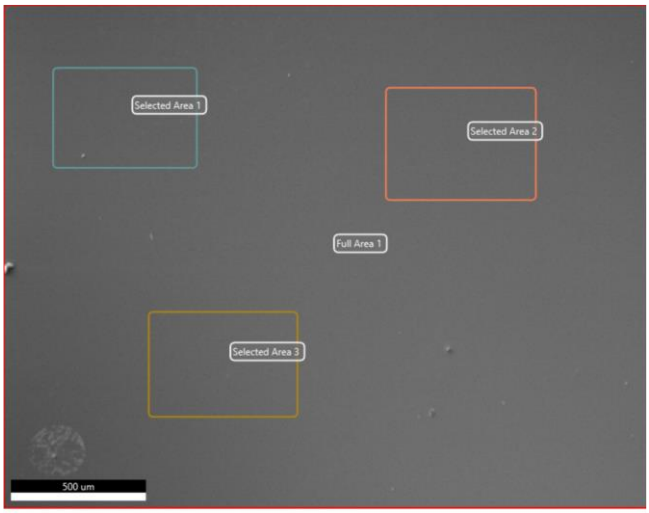

eZAF Quant Result

Element	Weight %	MDL	Atomic %	Error %
Eduardo-Alloys | 033023A_Sn_Lu2O3 | Area 1 | Full Area 1				
O K	25.05	0.05	61.65	8.94
Ga L	63.26	0.25	35.72	6.87
Lu L	11.69	0.57	2.63	9.27
Eduardo-Alloys | 033023A_Sn_Lu2O3 | Area 1 | Selected Area 1				
O K	25.17	0.05	61.72	8.93
Ga L	63.48	0.25	35.73	6.86
Lu L	11.36	0.56	2.55	9.01
Eduardo-Alloys | 033023A_Sn_Lu2O3 | Area 1 | Selected Area 2				
O K	24.88	0.04	61.45	8.91
Ga L	63.28	0.24	35.88	6.86
Lu L	11.84	0.56	2.68	8.78
Eduardo-Alloys | 033023A_Sn_Lu2O3 | Area 1 | Selected Area 3				
O K	25.17	0.05	61.75	8.93
Ga L	63.40	0.24	35.69	6.87
Lu L	11.43	0.57	2.56	9.35

Spectrum Overlay

kV: 15 Mag: 50 Takeoff: 33.2 Live Time(s): 200 Amp Time(µs): 3.84 Resolution:(eV) 129.8

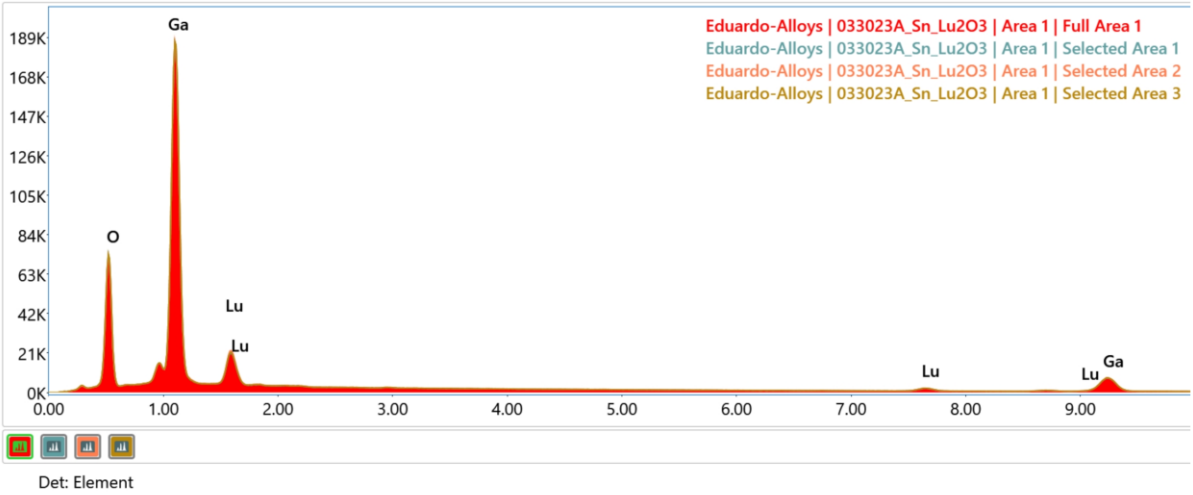

Figure 5.55 EDS report Lu_2O_3 on UID Ga_2O_3 rf power: 30 W.

EDAX APEX

Eduardo-Alloys

Author: User Apex

Creation: 4/14/2023 4:49:22 PM

Sample Name: 033023B_Sn_Lu2O3

033023B_Sn_Lu2O3

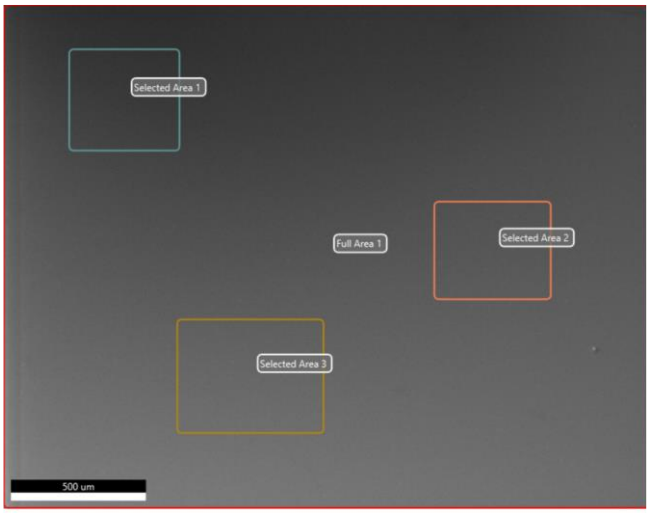

eZAF Quant Result

Element	Weight %	MDL	Atomic %	Error %
Eduardo-Alloys | 033023B_Sn_Lu2O3 | Area 1 | Full Area 1				
O K	19.05	0.06	61.76	9.30
Ga L	31.81	0.20	23.67	7.04
Lu L	49.14	0.71	14.57	4.77
Eduardo-Alloys | 033023B_Sn_Lu2O3 | Area 1 | Selected Area 1				
O K	19.08	0.06	61.88	9.30
Ga L	31.58	0.19	23.50	7.04
Lu L	49.34	0.70	14.63	4.70
Eduardo-Alloys | 033023B_Sn_Lu2O3 | Area 1 | Selected Area 2				
O K	18.91	0.06	61.49	9.30
Ga L	32.09	0.19	23.95	7.03
Lu L	49.00	0.71	14.57	4.76
Eduardo-Alloys | 033023B_Sn_Lu2O3 | Area 1 | Selected Area 3				
O K	18.96	0.06	61.71	9.32
Ga L	31.58	0.21	23.58	7.04
Lu L	49.46	0.74	14.71	4.86

Spectrum Overlay

kV: 15 Mag: 50 Takeoff: 33.2 Live Time(s): 200 Amp Time(µs): 3.84 Resolution:(eV) 129.8

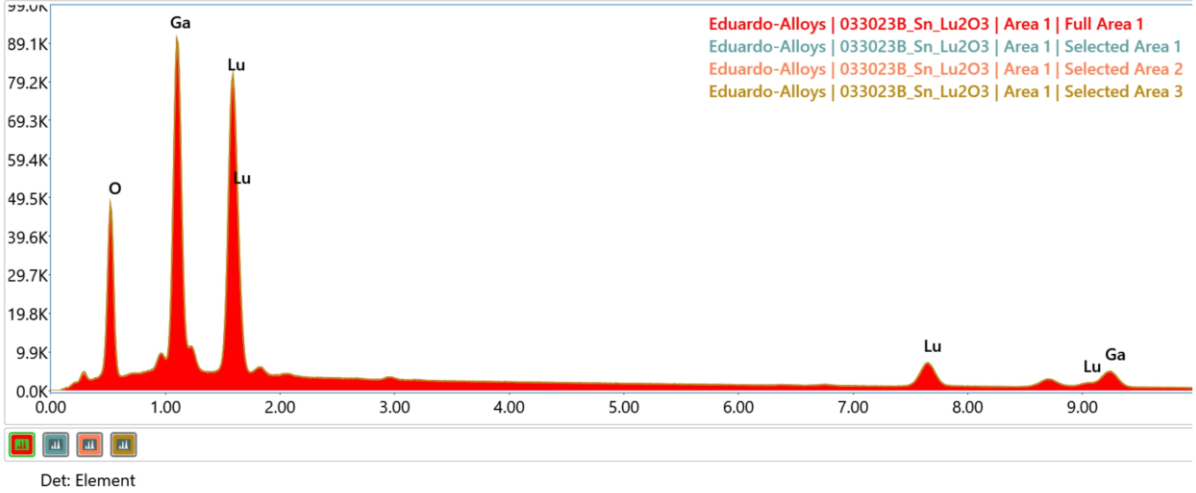

Figure 5.56 EDS report Lu_2O_3 on UID Ga_2O_3 rf power: 80 W.

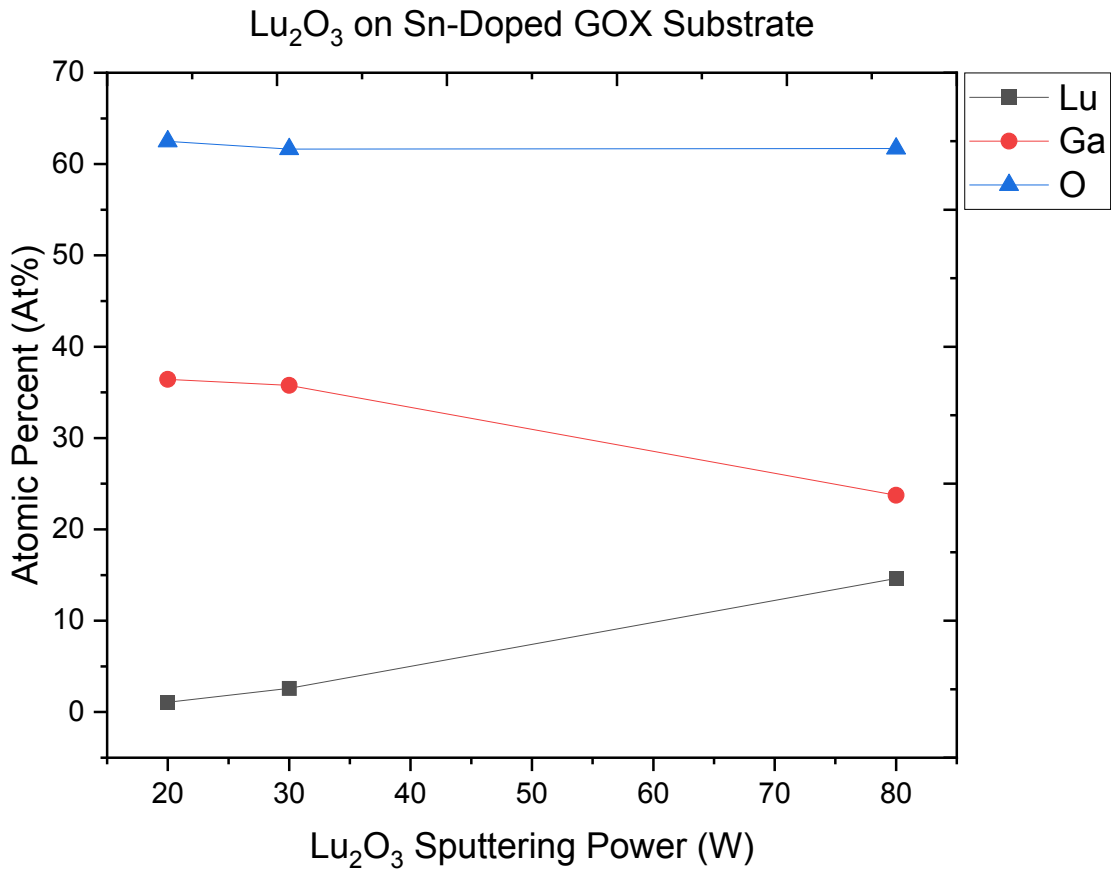

Figure 5.57 Atomic percent of Lu, Ga, and O of films deposited on Sn-doped Ga_2O_3 as a function of the Lu_2O_3 rf power.

UV-Vis Spectroscopy. Transmittance of the Lu_2O_3/Ga_2O_3 alloy films deposited on the Sn-doped Ga_2O_3 substrate is shown in Fig. 5.58. This set of samples exhibited a transparency level ranging from 60% to 76% with the samples deposited at higher power being more transparent.

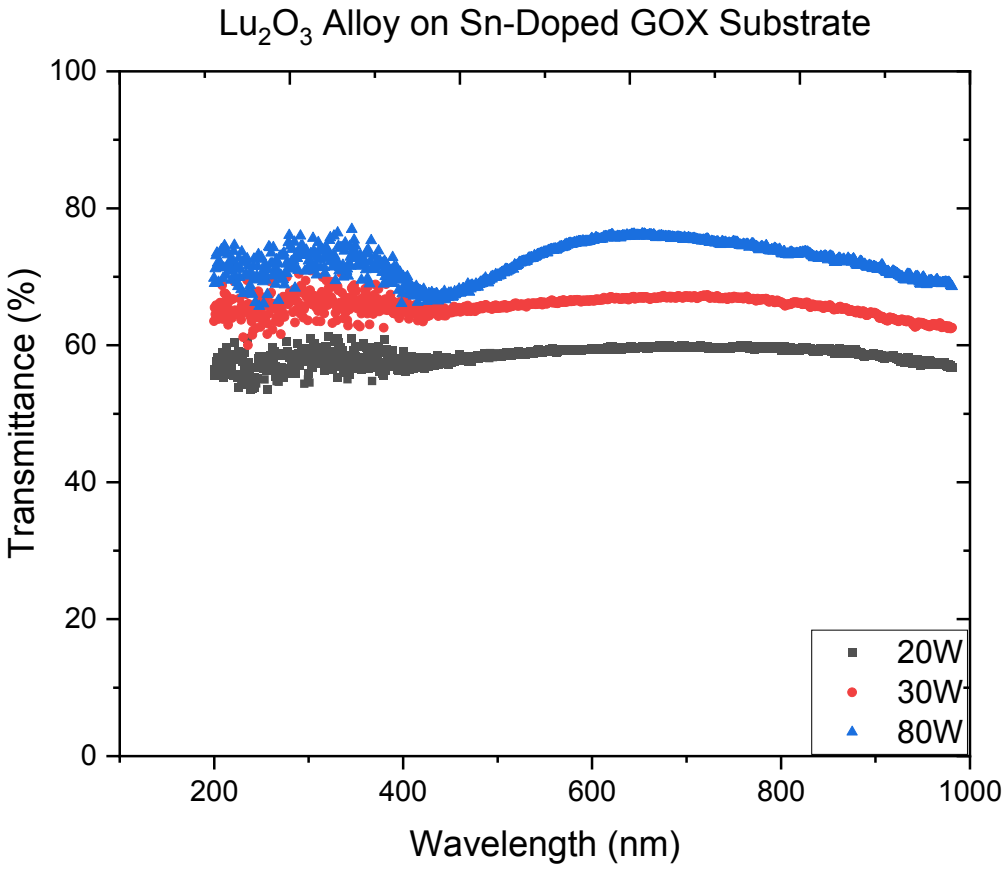

Figure 5.58 Transmittance of Lu_2O_3/Ga_2O_3 alloy films deposited on the Sn-doped Ga_2O_3 substrate.

Figure 2.59 (a) shows that the films also absorb in the UV region as expected for films co-sputtered with gallium oxide. Figure 2.59 (b) shows the energy plot used to extract the optical bandgap via a Tauc plot for Lu_2O_3/Ga_2O_3 films.

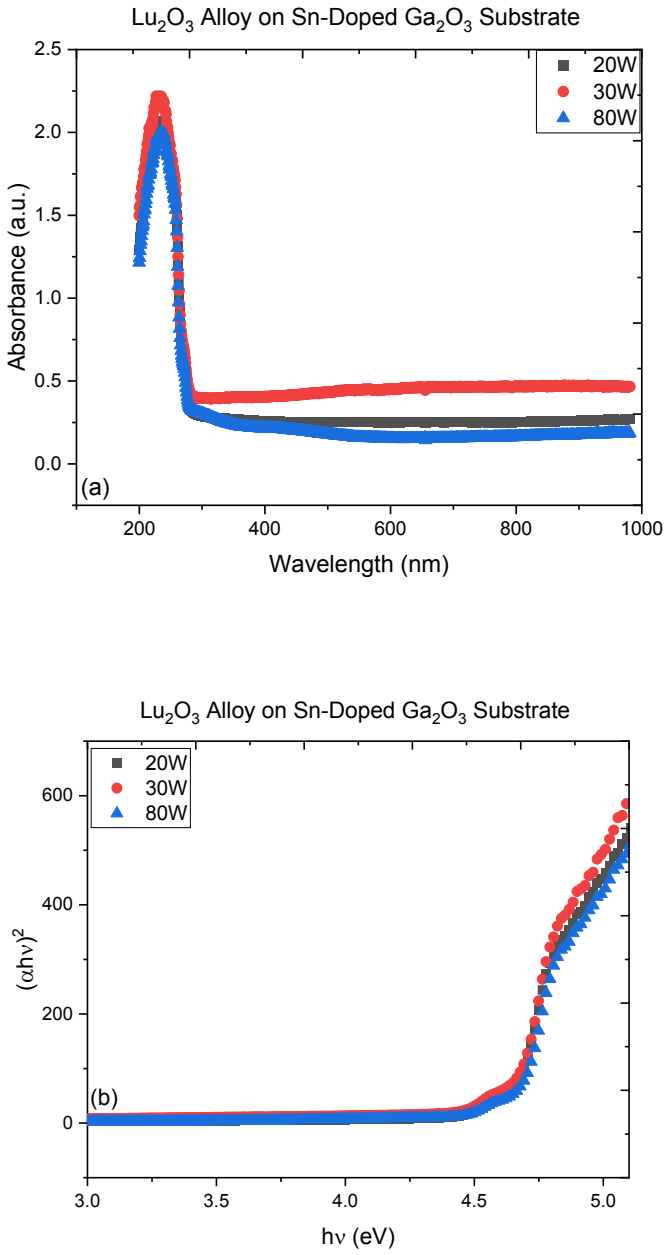

Figure 5.59 Absorbance (a) and energy plot (b) of Lu_2O_3/Ga_2O_3 alloy films deposited on the Sn-doped Ga_2O_3 substrate.

The optical bandgap for Lu_2O_3/Ga_2O_3 alloy films deposited on the Sn-doped Ga_2O_3 substrate is plotted as a function of the Lu_2O_3 rf power (Fig. 5.60). Similarly, the bandgap energy has a minor increase with increasing Lu_2O_3 rf power from 4.641 eV at 0W to 4.664 eV at 80 W.

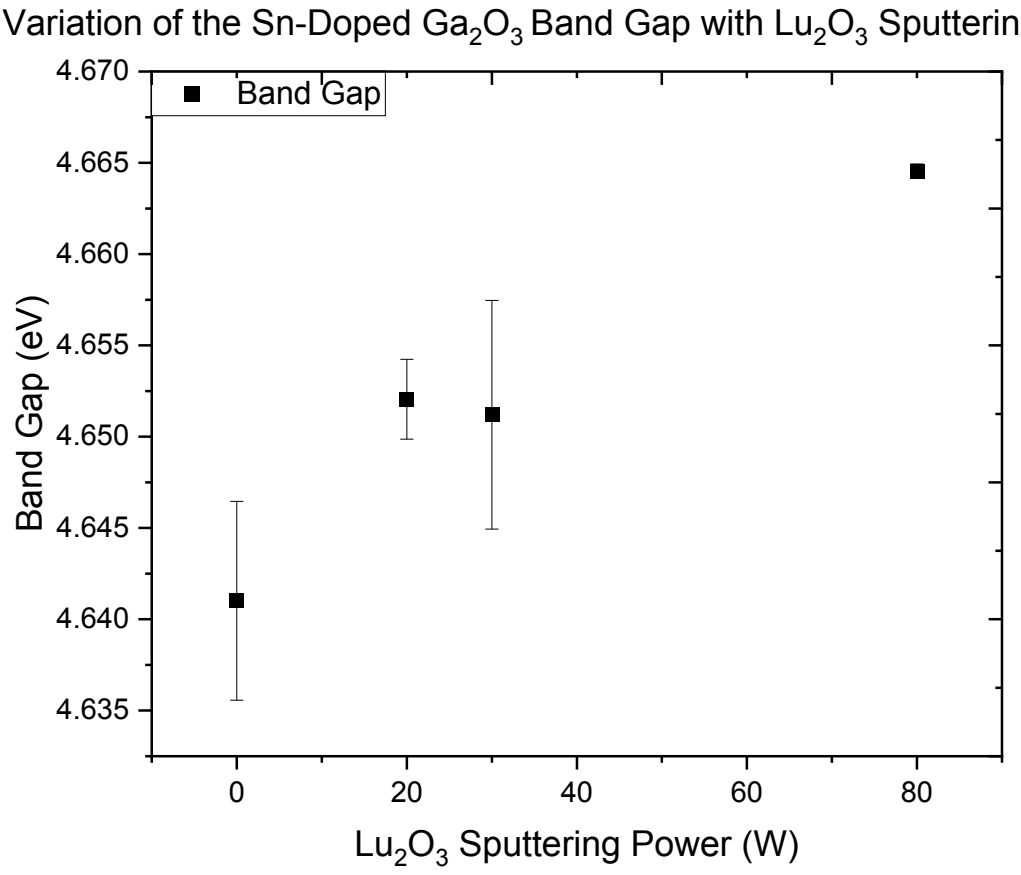

Figure 5.60 Bandgap energy vs Lu_2O_3 rf power for Lu_2O_3/Ga_2O_3 alloy films deposited on the Sn-doped Ga_2O_3 substrate.

5.5.5 Effects of B_2O_3 Sputtering Power Variation on Al_2O_3

XRD. X-ray diffraction of B_2O_3/Ga_2O_3 alloy films deposited on Al_2O_3 substrate data is presented in Fig. 5.61. The sample containing no B_2O_3 showed two dominant peaks consistent with ($\bar{2}$ 0 1) planes of Ga_2O_3. As the B_2O_3 rf power of is increased, the films become amorphous, and the Ga_2O_3 XRD peaks vanish. The sample deposited at 80 W shows a peak at 42.6° which belong to the substrate (0001) sapphire.

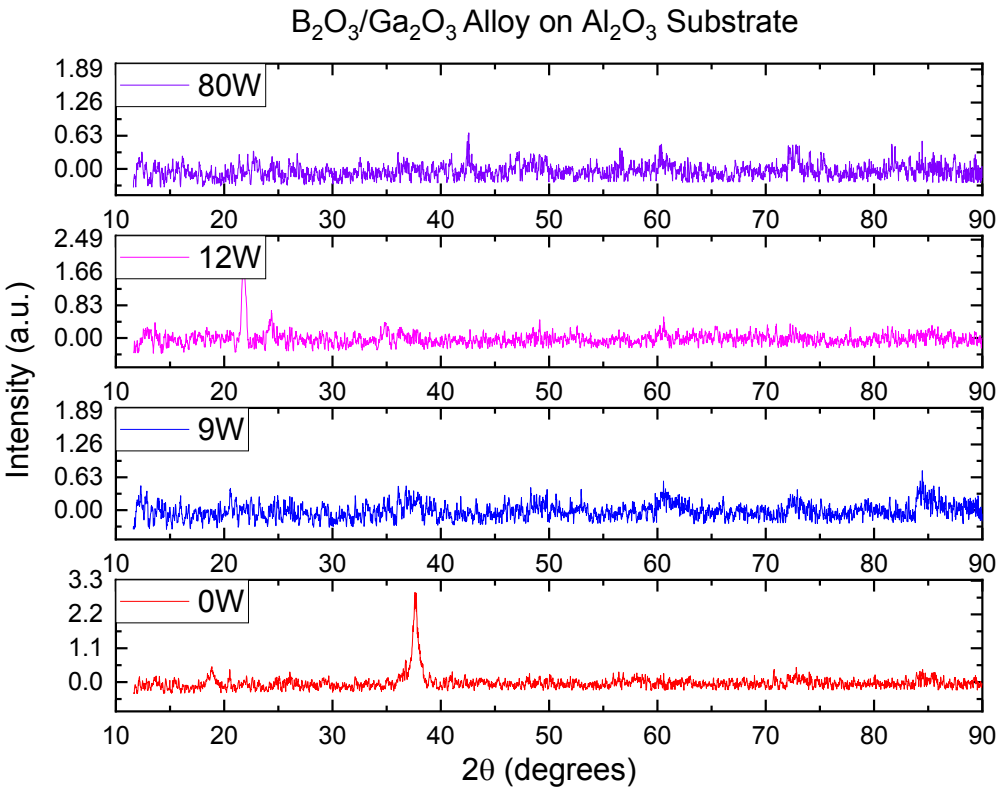

Figure 5.61 B_2O_3 alloy on Sn-dope Ga_2O_3 substrate XRD.

EDS. Energy dispersive spectroscopy shows the atomic percent of boron in the films varies across all samples and with no visible trend as the rf power of B_2O_3 increases (Fig. 5.62-5.65). This can be attributed to the variation in the film thickness and the evaporation of boron. Boron oxide can react with atmospheric moisture and carbon dioxide. When exposed to moisture in the air, B_2O_3 can slowly absorb water and form boric acid (H_3BO_3) [224].

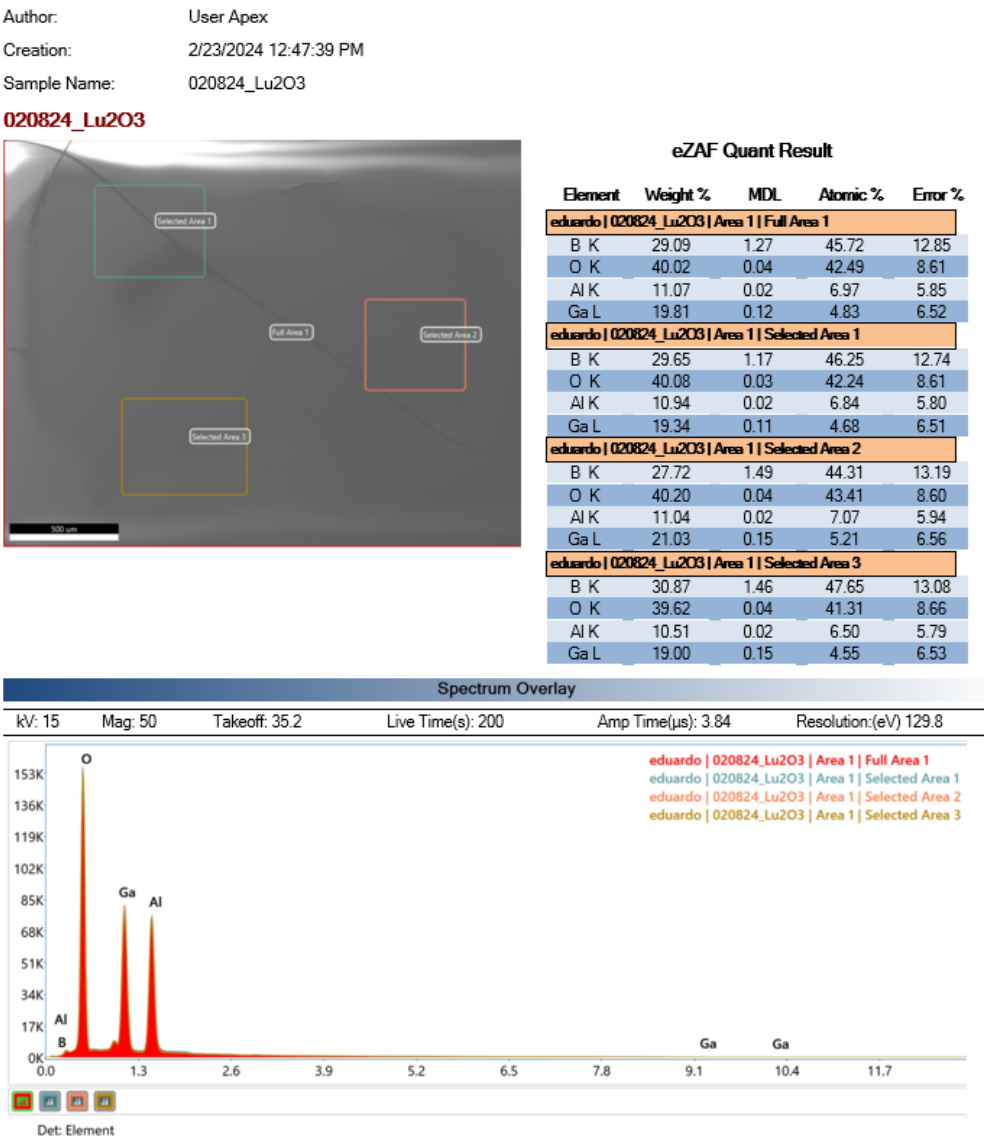

Figure 5.62 EDS report B_2O_3 on Al_2O_3 rf power: 0 W.

Author: User Apex

Creation: 2/23/2024 2:16:48 PM

Sample Name: 021524_B2O3

021524_B2O3

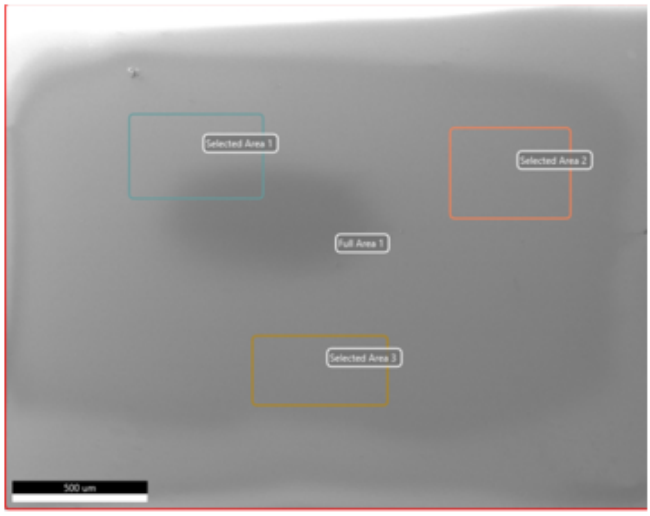

eZAF Quant Result

Element	Weight %	MDL	Atomic %	Error %
eduardo | 021524_B2O3 | Area 1 | Full Area 1				
B K	0.00	0.00	0.00	0.00
O K	45.12	0.05	74.75	8.12
Al K	7.27	0.05	7.14	7.74
Ga L	47.61	0.23	18.10	6.95
eduardo | 021524_B2O3 | Area 1 | Selected Area 1				
B K	0.00	0.00	0.00	0.00
O K	45.23	0.05	75.45	8.11
Al K	5.90	0.05	5.84	7.97
Ga L	48.87	0.23	18.71	6.97
eduardo | 021524_B2O3 | Area 1 | Selected Area 2				
B K	0.00	0.00	0.00	0.00
O K	44.62	0.06	75.36	8.14
Al K	5.17	0.05	5.18	8.01
Ga L	50.21	0.25	19.46	6.96
eduardo | 021524_B2O3 | Area 1 | Selected Area 3				
B K	0.00	0.00	0.00	0.00
O K	44.83	0.06	75.50	8.14
Al K	5.19	0.05	5.18	8.11
Ga L	49.97	0.28	19.31	6.98

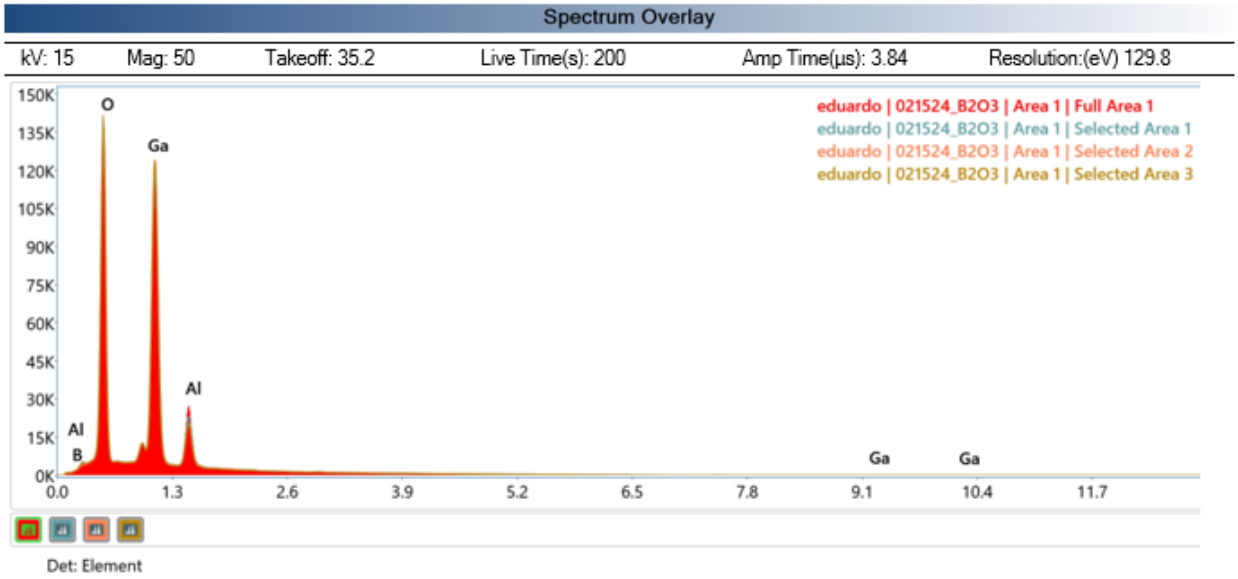

Figure 5.63 EDS report B_2O_3 on Al_2O_3 RF power: 9 W.

Author: User Apex

Creation: 2/23/2024 2:40:47 PM

Sample Name: 021624_B2O3

021624_B2O3

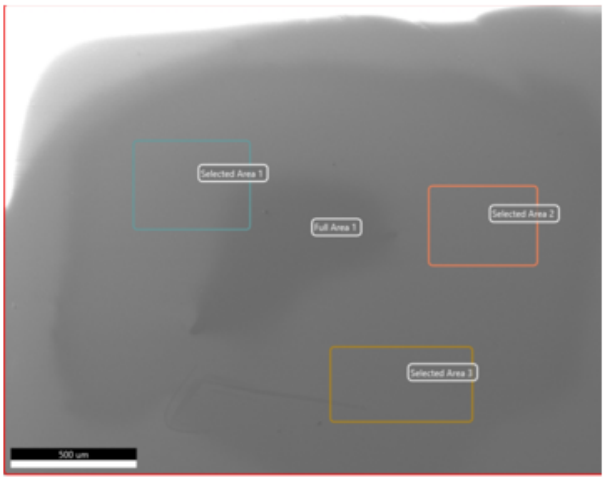

eZAF Quant Result

Element	Weight %	MDL	Atomic %	Error %
eduardo | 021624_B2O3 | Area 1 | Full Area 1				
B K	0.00	0.00	0.00	0.00
O K	45.84	0.05	75.50	8.09
Al K	6.73	0.05	6.57	7.77
Ga L	47.42	0.23	17.92	6.97
eduardo | 021624_B2O3 | Area 1 | Selected Area 1				
B K	38.97	1.04	58.31	11.82
O K	34.23	0.04	34.61	8.84
Al K	2.34	0.02	1.40	6.72
Ga L	24.47	0.11	5.68	6.38
eduardo | 021624_B2O3 | Area 1 | Selected Area 2				
B K	30.73	1.43	50.20	12.55
O K	36.80	0.04	40.61	8.70
Al K	2.39	0.02	1.56	7.22
Ga L	30.09	0.14	7.62	6.54
eduardo | 021624_B2O3 | Area 1 | Selected Area 3				
B K	31.74	1.51	51.25	12.57
O K	36.43	0.04	39.74	8.72
Al K	2.63	0.02	1.70	7.08
Ga L	29.20	0.14	7.31	6.52

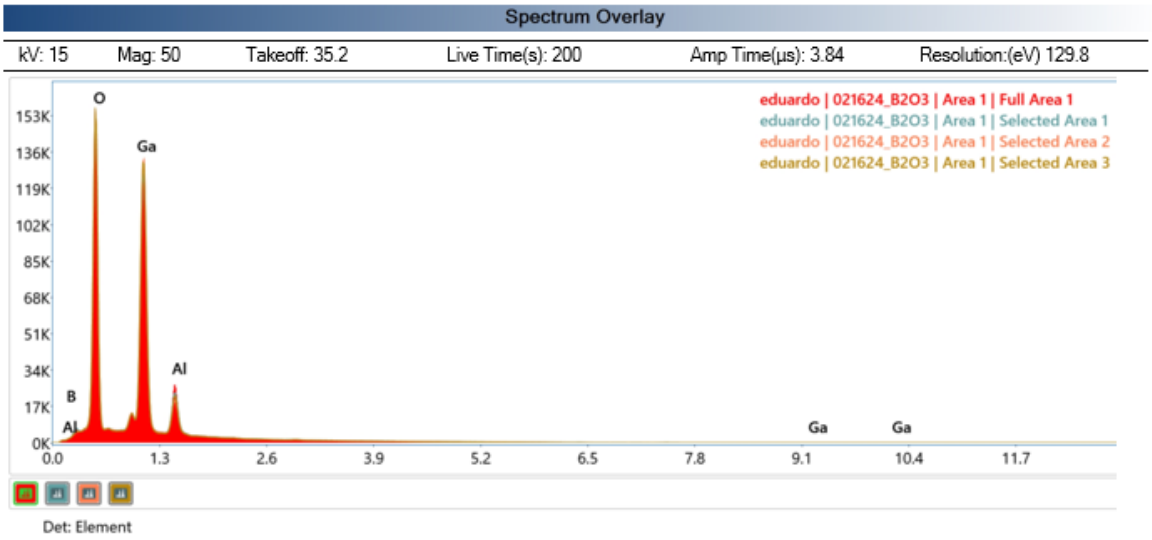

Figure 5.64 EDS report B_2O_3 on Al_2O_3 rf power: 12 W.

Author: User Apex

Creation: 2/23/2024 3:02:15 PM

Sample Name: 021224_B2O3

021224_B2O3

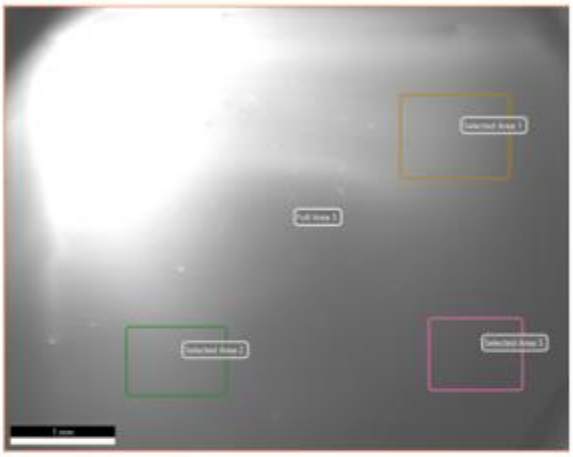

eZAF Quant Result

Element	Weight %	MDL	Atomic %	Error %
eduardo | 021224_B2O3 | Area 1 | Full Area 1				
B K	19.07	0.86	29.52	13.83
O K	47.70	0.02	49.89	8.26
Al K	33.19	0.02	20.59	4.11
Ga L	0.03	0.05	0.01	14.76
eduardo | 021224_B2O3 | Area 1 | Full Area 2				
B K	18.90	0.82	29.28	13.66
O K	47.89	0.02	50.12	8.25
Al K	33.19	0.02	20.60	4.11
Ga L	0.02	0.05	0.01	16.66
eduardo | 021224_B2O3 | Area 1 | Full Area 3				
B K	19.92	0.96	30.64	14.18
O K	47.44	0.02	49.31	8.30
Al K	32.43	0.02	19.99	4.13
Ga L	0.21	0.05	0.05	9.84
eduardo | 021224_B2O3 | Area 1 | Selected Area 1				
B K	17.43	1.15	27.32	14.96
O K	48.43	0.03	51.29	8.23
Al K	34.00	0.02	21.35	4.14
Ga L	0.14	0.06	0.03	13.38
eduardo | 021224_B2O3 | Area 1 | Selected Area 2				
B K	21.18	1.11	32.25	14.44
O K	47.17	0.03	48.53	8.33
Al K	31.41	0.02	19.16	4.13
Ga L	0.24	0.05	0.06	9.40
eduardo | 021224_B2O3 | Area 1 | Selected Area 3				
B K	19.14	1.15	29.65	14.83
O K	47.56	0.03	49.77	8.29
Al K	33.07	0.02	20.52	4.14
Ga L	0.23	0.06	0.06	9.65

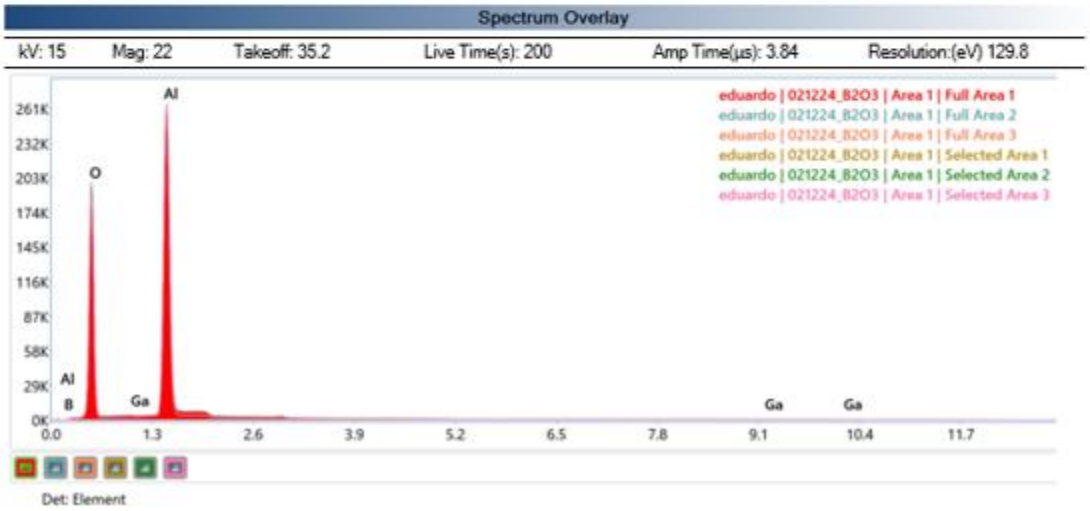

Figure 5.65 EDS report B_2O_3 on Al_2O_3 rf power: 80 W.

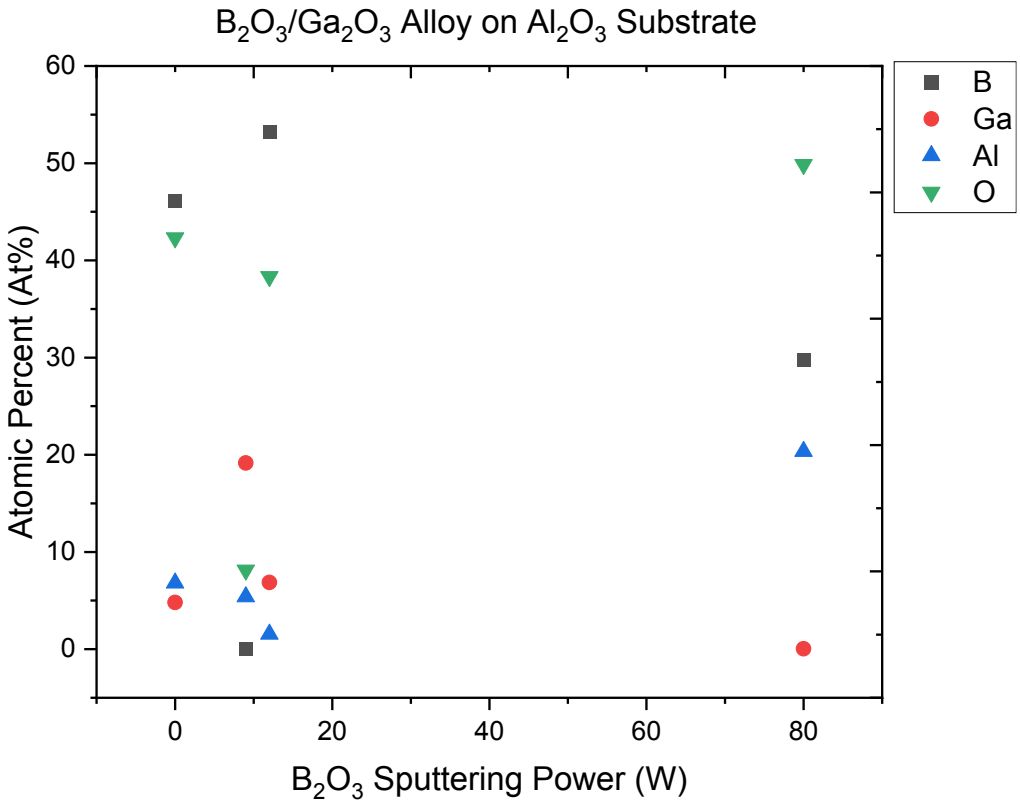

Figure 5.66 Atomic percent of B, Ga, and O of films deposited on Al_2O_3 as a function of the B_2O_3 rf power.

UV-Vis Spectroscopy. The transmittance of the B_2O_3/Ga_2O_3 alloy films on Al_2O_3 substrate is depicted in Fig. 5.67. The transparency significantly improved with double-side polished substrates, achieving a transmittance percentage of 98% in the visible spectrum range. Comparatively, the samples co-sputtered with B_2O_3 exhibited stronger absorption than the Ga_2O_3 film alone (0 W sample). The film deposited at 80 W did not include Ga_2O_3 and remained highly transparent throughout the spectrum. The bandgap of these films fluctuated around 5.0 eV, slightly higher than Ga_2O_3 with a bandgap of 4.9 eV, while the film containing pure B_2O_3 displayed a lower bandgap of 4.7 eV.

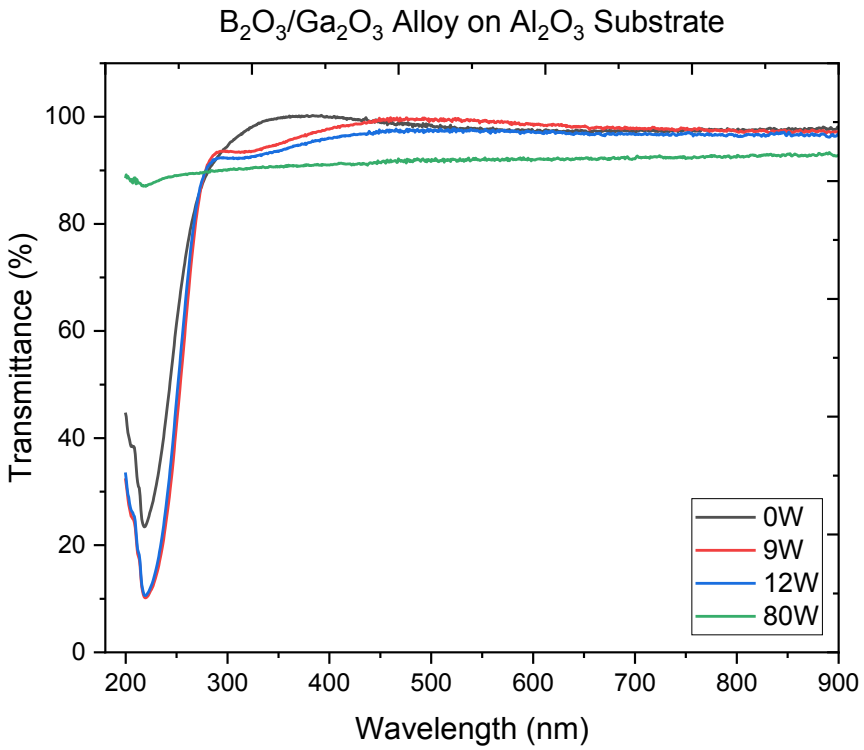

Figure 5.67 Transmittance of B_2O_3/Ga_2O_3 alloy films deposited on the Al_2O_3 substrate at various B_2O_3 rf powers.

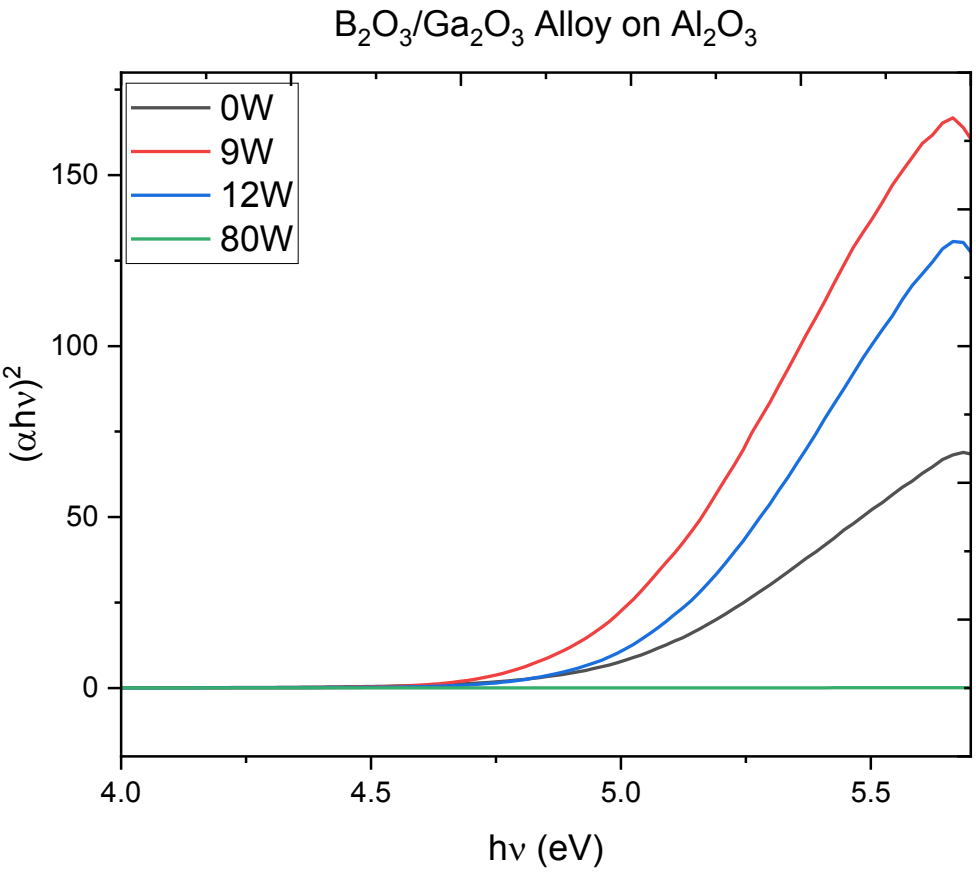

Figure 5.68 Energy plot of B_2O_3/Ga_2O_3 alloy films deposited on the Al_2O_3 substrate at various B_2O_3 rf powers.

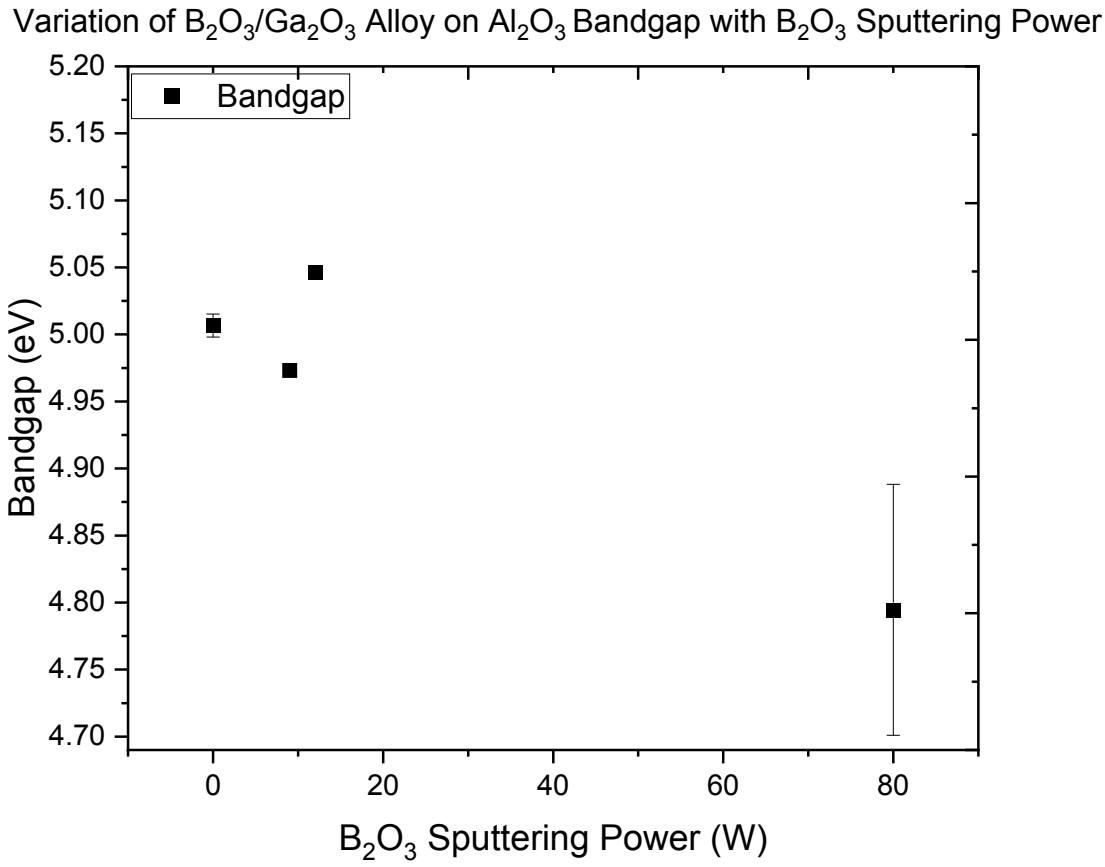

Figure 5.69 Bandgap energy vs B_2O_3 rf power for B_2O_3/Ga_2O_3 alloy films deposited on Al_2O_3 substrate.

5.5.6 Effects of Lu_2O_3 Sputtering Power Variation on Al_2O_3

XRD. X-ray diffraction data for Lu_2O_3/Ga_2O_3 alloy films on Al_2O_3 substrate are illustrated in Fig. 5.70. The sample deposited at 0 W represents pure Ga_2O_3 on Al_2O_3 and serves as the reference for the XRD graph. At 9 W, the crystal structure of $(\bar{2}01)$ Ga_2O_3 remains preserved. However, increasing the rf power to 12 W results in an amorphous film. Additionally, the sample deposited at 50 W, consisting solely of Lu_2O_3, exhibits two major peaks at 21.7° and 29.8°, corresponding to cubic Lu_2O_3 [225]. These peaks were not observed in films deposited on Ga_2O_3 substrate, indicating the potential for Lu2O3 crystallization on Al_2O_3.

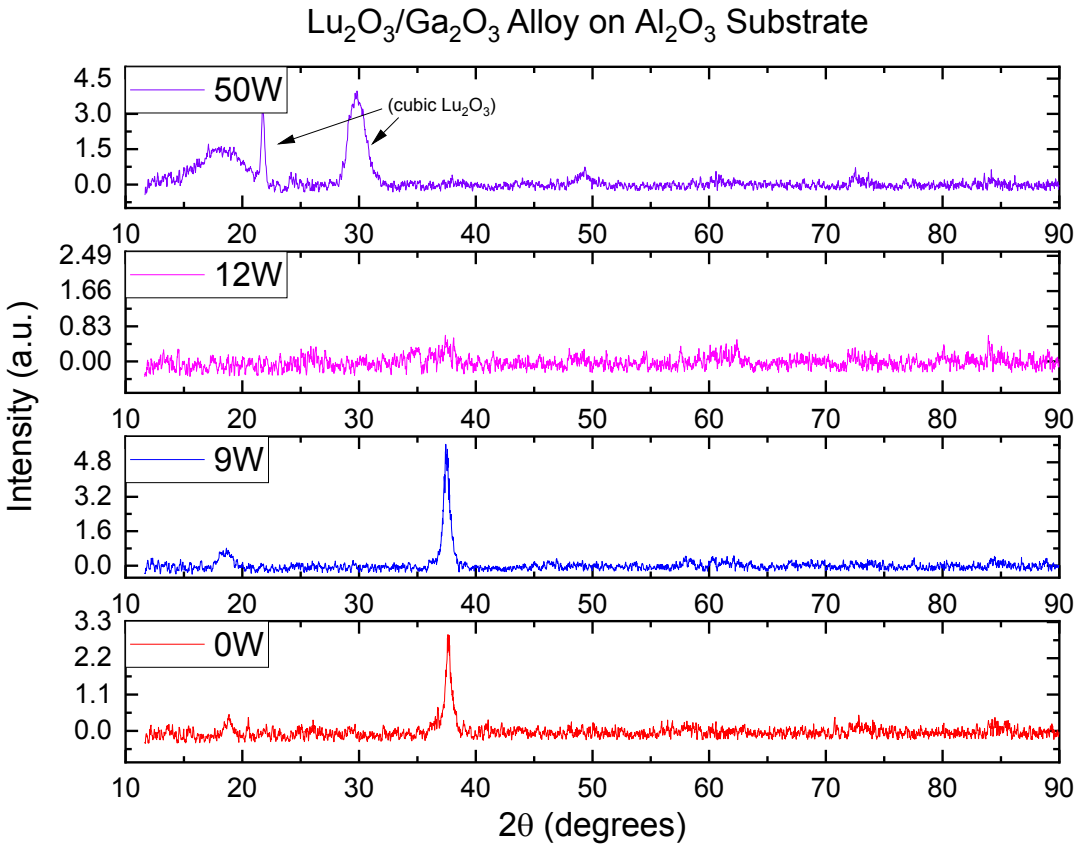

Figure 5.70 Lu_2O_3 alloy on Al_2O_3 substrate XRD.

EDS. Energy dispersive spectroscopy reports indicate the presence of Lu_2O_3 in the films (Fig. 5.71-5.74). The average atomic percentages of Lu_2O_3 obtained from three scanned areas were 0.07%, 0.12%, 0.04%, and 1.04% for rf powers of 0, 9, 12, and 50 W, respectively. A summary of these atomic percentages is plotted in Fig. 5.75 for all elements in the film as a function of Lu_2O_3 rf power. These values vary across all powers, likely due to the non-uniformity of the film throughout the sample.

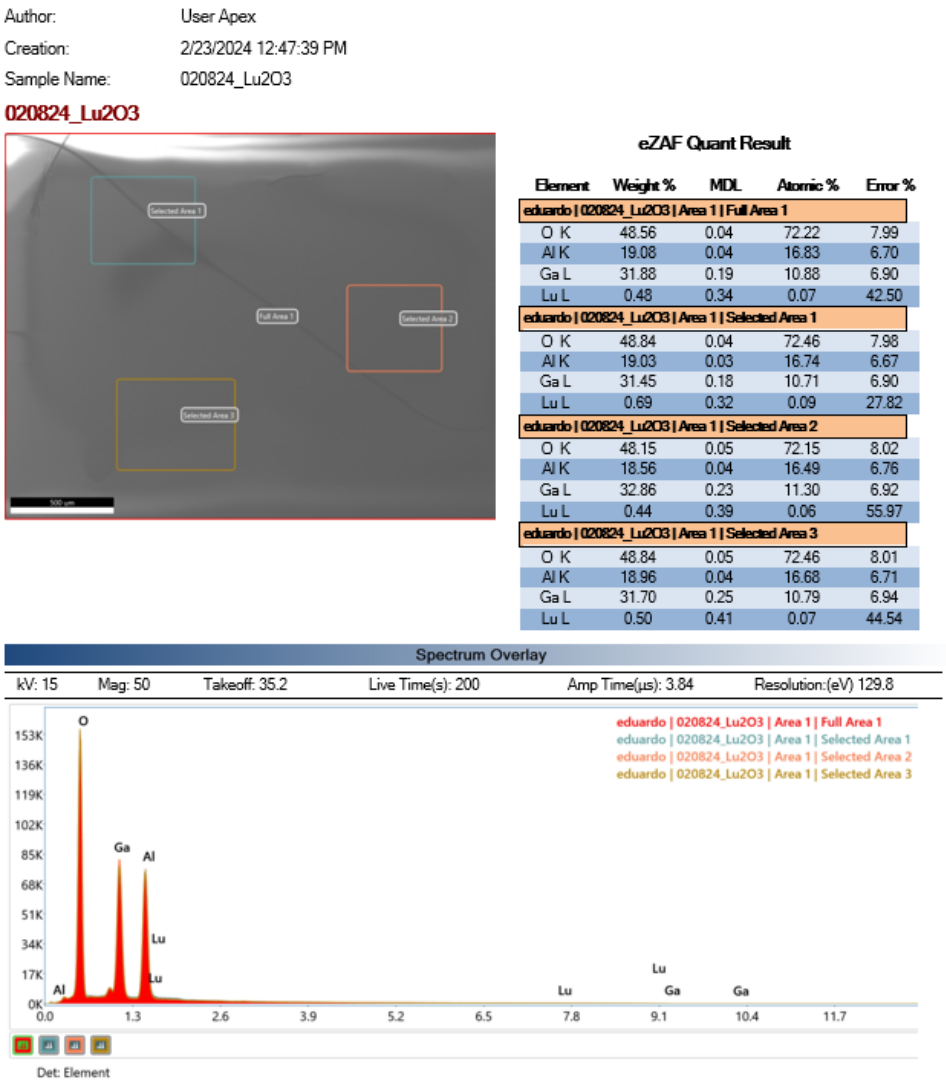

Figure 5.71 EDS report Lu_2O_3 on Al_2O_3 rf power: 0 W.

Author: User Apex

Creation: 2/23/2024 1:14:38 PM

Sample Name: 020624_Lu2O3

020624_Lu2O3

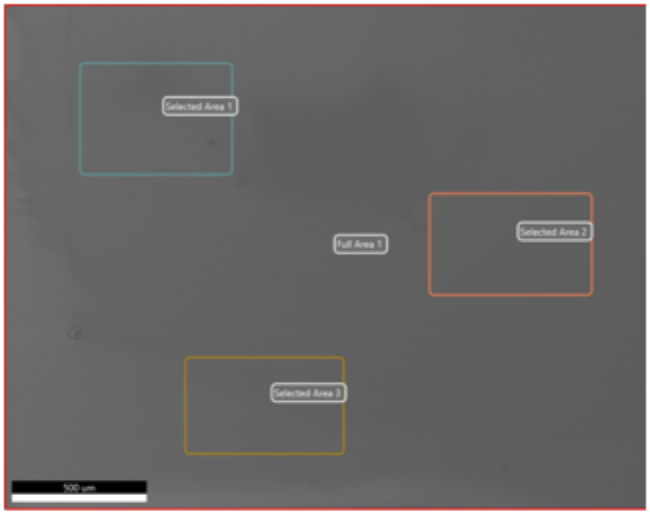

eZAF Quant Result

Element	Weight %	MDL	Atomic %	Error %
eduardo | 020624_Lu2O3 | Area 1 | Full Area 1				
O K	43.88	0.05	71.94	8.17
Al K	11.91	0.04	11.58	7.37
Ga L	43.55	0.23	16.38	6.89
Lu L	0.67	0.36	0.10	35.59
eduardo | 020624_Lu2O3 | Area 1 | Selected Area 1				
O K	43.55	0.05	72.50	8.18
Al K	10.11	0.05	9.99	7.49
Ga L	45.50	0.24	17.38	6.90
Lu L	0.83	0.32	0.13	27.41
eduardo | 020624_Lu2O3 | Area 1 | Selected Area 2				
O K	43.88	0.06	72.10	8.19
Al K	11.61	0.05	11.31	7.43
Ga L	43.64	0.28	16.46	6.91
Lu L	0.87	0.40	0.13	36.79
eduardo | 020624_Lu2O3 | Area 1 | Selected Area 3				
O K	43.92	0.06	72.22	8.19
Al K	11.32	0.05	11.04	7.46
Ga L	44.09	0.30	16.64	6.93
Lu L	0.67	0.42	0.10	39.34

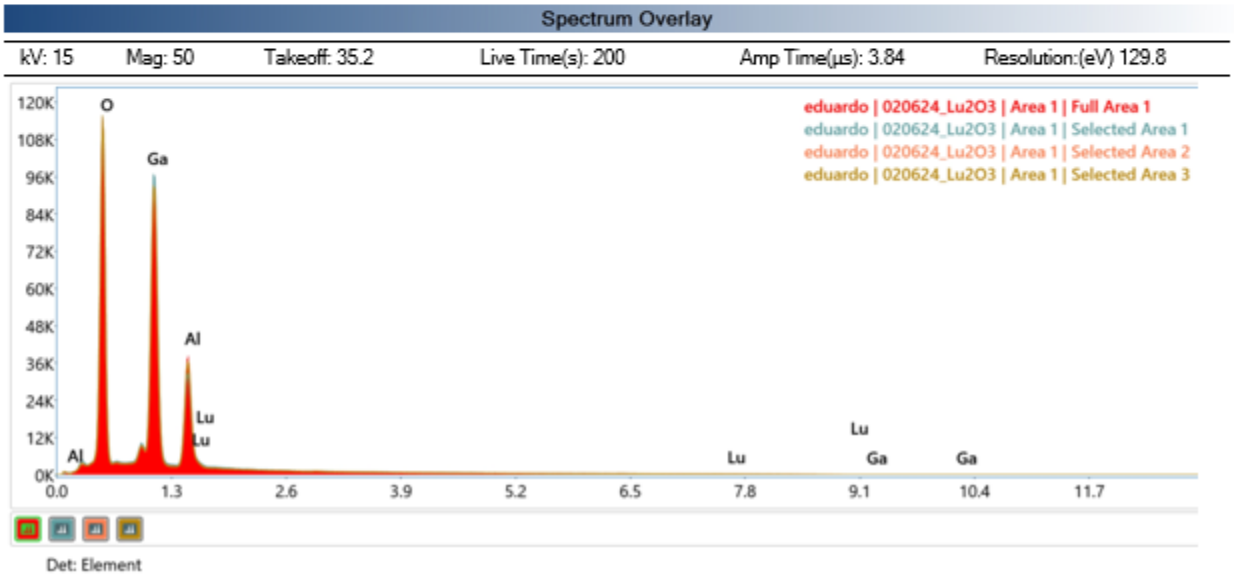

Figure 5.72 EDS report Lu_2O_3 on Al_2O_3 rf power: 9 W.

Author: User Apex

Creation: 2/23/2024 1:40:06 PM

Sample Name: 013024_Lu2O3

013024_Lu2O3

eZAF Quant Result

Element	Weight %	MDL	Atomic %	Error %
eduardo | 013024_Lu2O3 | Area 1 | Full Area 1				
O K	43.27	0.06	74.10	8.19
Al K	5.90	0.05	5.99	8.01
Ga L	50.58	0.28	19.88	6.94
Lu L	0.25	0.13	0.04	23.43
eduardo | 013024_Lu2O3 | Area 1 | Selected Area 1				
O K	43.21	0.07	74.92	8.20
Al K	4.09	0.06	4.21	8.41
Ga L	52.31	0.29	20.81	6.97
Lu L	0.39	0.12	0.06	27.64
eduardo | 013024_Lu2O3 | Area 1 | Selected Area 2				
O K	43.55	0.07	75.08	8.20
Al K	4.19	0.06	4.28	8.46
Ga L	52.11	0.32	20.61	6.98
Lu L	0.15	0.08	0.02	32.04
eduardo | 013024_Lu2O3 | Area 1 | Selected Area 3				
O K	43.05	0.08	74.91	8.23
Al K	3.79	0.07	3.91	8.59
Ga L	52.95	0.34	21.15	6.98
Lu L	0.21	0.11	0.03	36.26

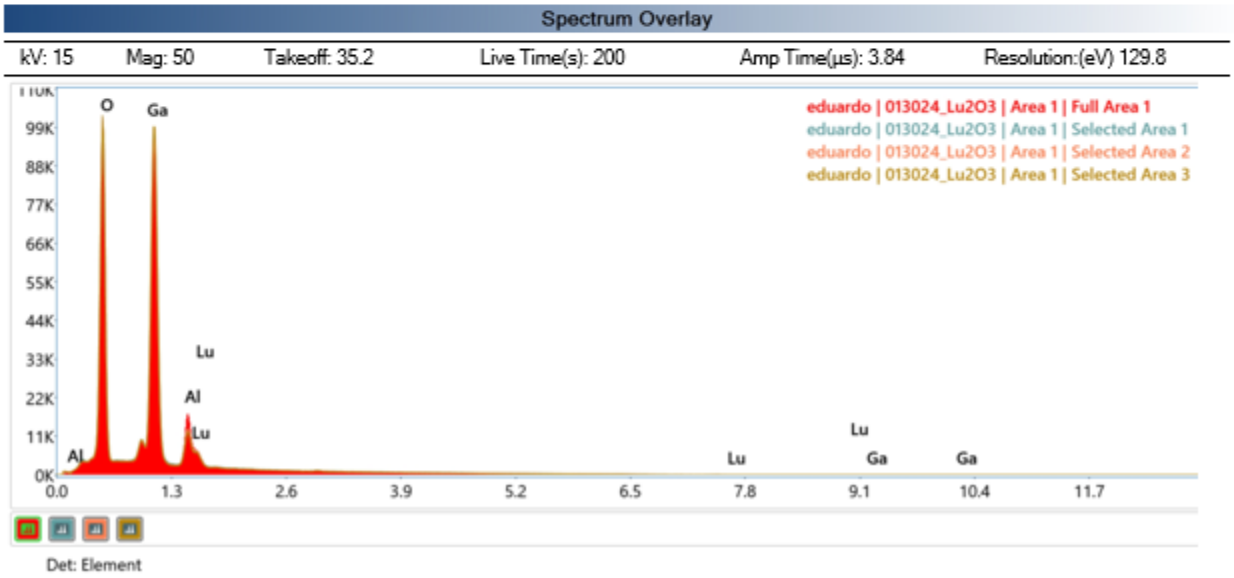

Figure 5.73 EDS report Lu_2O_3 on Al_2O_3 rf power: 12 W.

Author: User Apex

Creation: 2/23/2024 1:56:08 PM

Sample Name: 020924_Lu2O3

020924_Lu2O3

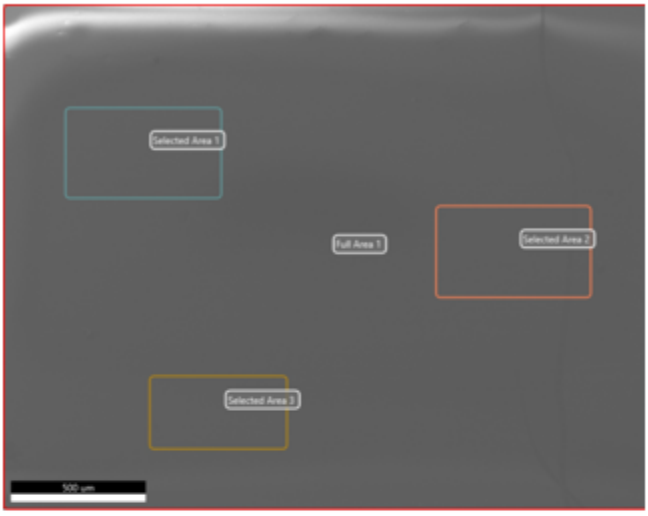

eZAF Quant Result

Element	Weight %	MDL	Atomic %	Error %
eduardo | 020924_Lu2O3 | Area 1 | Full Area 1				
O K	52.34	0.08	69.72	7.96
Al K	36.54	0.05	28.86	4.51
Ga L	0.36	0.15	0.11	20.88
Lu L	10.76	0.90	1.31	15.49
eduardo | 020924_Lu2O3 | Area 1 | Selected Area 1				
O K	53.65	0.08	70.33	7.90
Al K	36.59	0.05	28.45	4.51
Ga L	0.30	0.15	0.09	26.99
Lu L	9.46	0.93	1.13	17.44
eduardo | 020924_Lu2O3 | Area 1 | Selected Area 2				
O K	53.47	0.08	69.97	7.91
Al K	37.16	0.05	28.84	4.50
Ga L	0.39	0.16	0.12	19.16
Lu L	8.99	0.94	1.08	18.67
eduardo | 020924_Lu2O3 | Area 1 | Selected Area 3				
O K	54.58	0.08	70.45	7.86
Al K	37.25	0.05	28.52	4.51
Ga L	0.38	0.16	0.11	21.07
Lu L	7.79	0.99	0.92	19.30

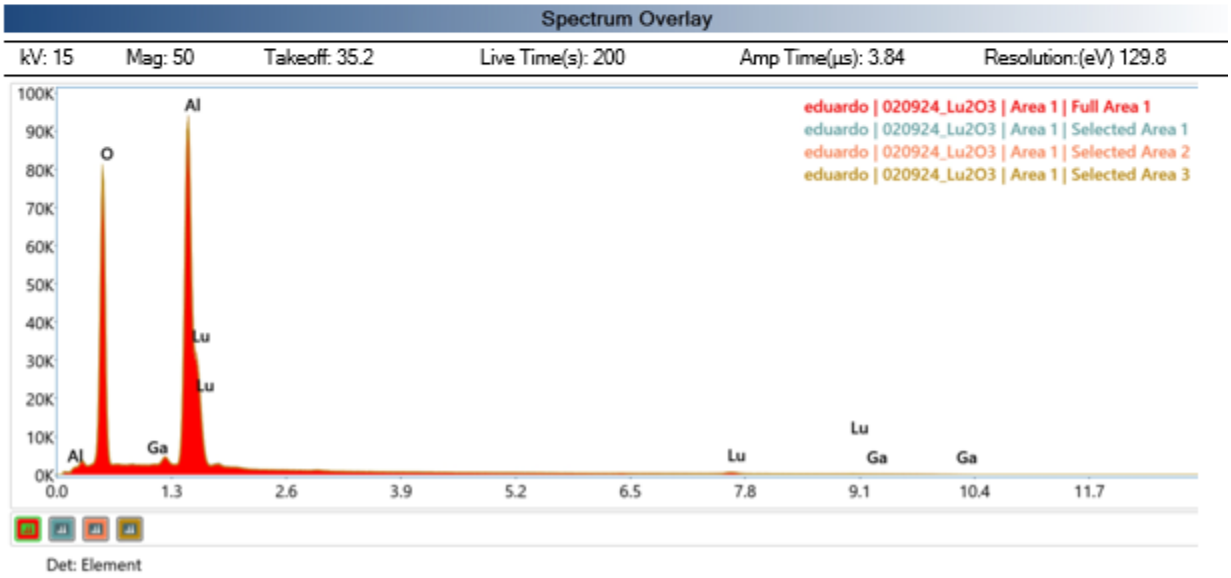

Figure 5.74 EDS report Lu_2O_3 on Al_2O_3 rf power: 50 W.

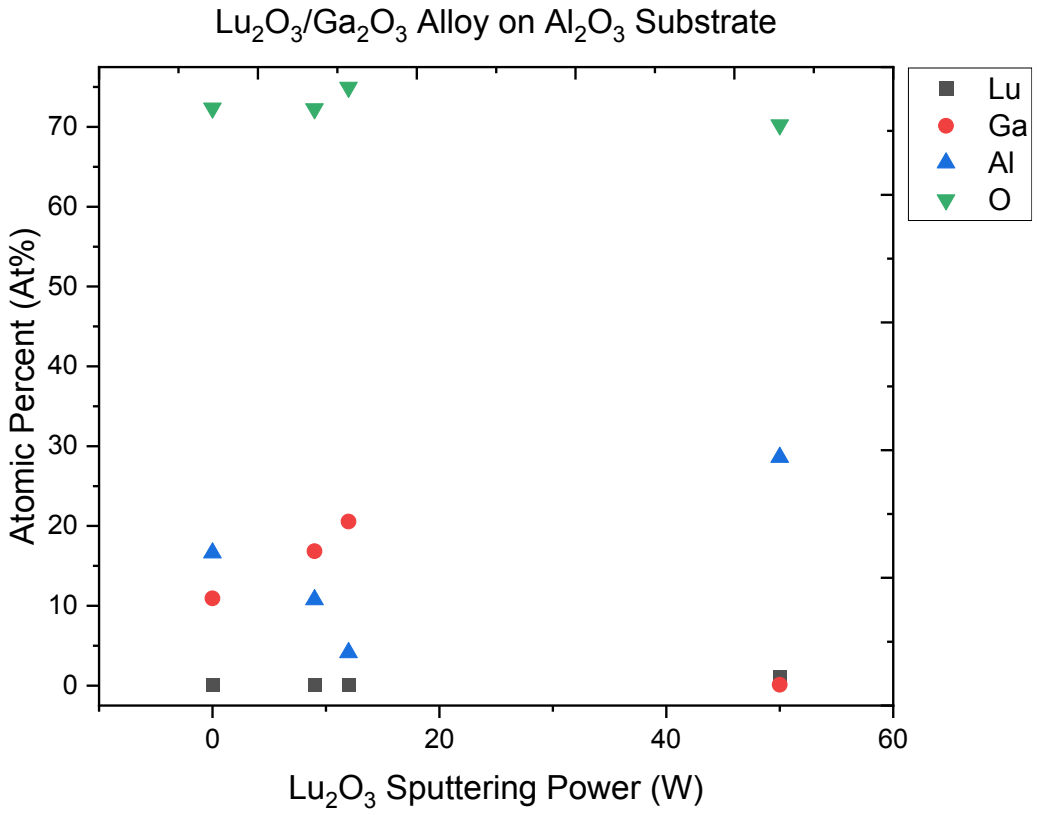

Figure 5.75 Atomic percent of Lu, Ga, and O of films deposited on Al_2O_3 as a function of the Lu_2O_3 rf power.

UV-Vis Spectroscopy. Figure 5.76 illustrates the transmittance characteristics of the Lu_2O_3/Ga_2O_3 alloy films deposited on an Al_2O_3 substrate. These films, co-sputtered with Lu_2O_3, demonstrated exceptional transparency, achieving a transmittance level of 99.97% within the visible spectrum range. In the UV region of the spectrum, all films exhibited absorption. Remarkably, films deposited with pure Lu_2O_3 exhibited an absorption peak at 215 nm in the UV region, consistent with the known absorption behavior of Lu_2O_3 in similar films documented in the literature [219]. The bandgap of the co-sputtered films, extracted from the energy plot shown in Fig. 5.77, remained around 5.0 eV, close to the sample deposited with pure Ga_2O_3. Nevertheless, the extracted bandgap for Lu_2O_3 was significantly higher when compared to the rest of the films with a value of 5.46 eV. The bandgaps for all films at various rf powers are plotted in Fig. 5.78.

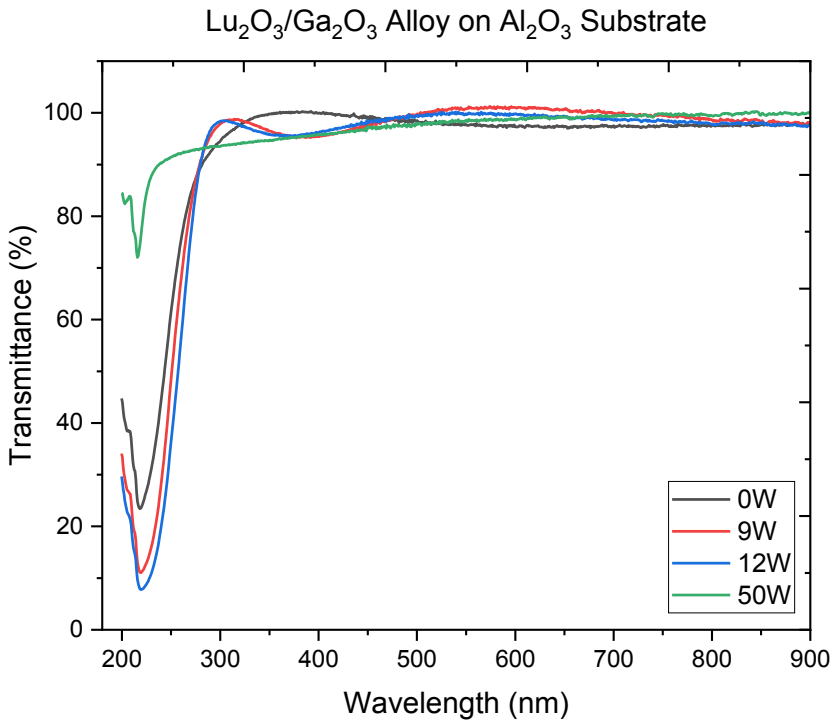

Figure 5.76 Transmittance of Lu_2O_3/Ga_2O_3 alloy films deposited on the Al_2O_3 substrate at various Lu_2O_3 rf powers.

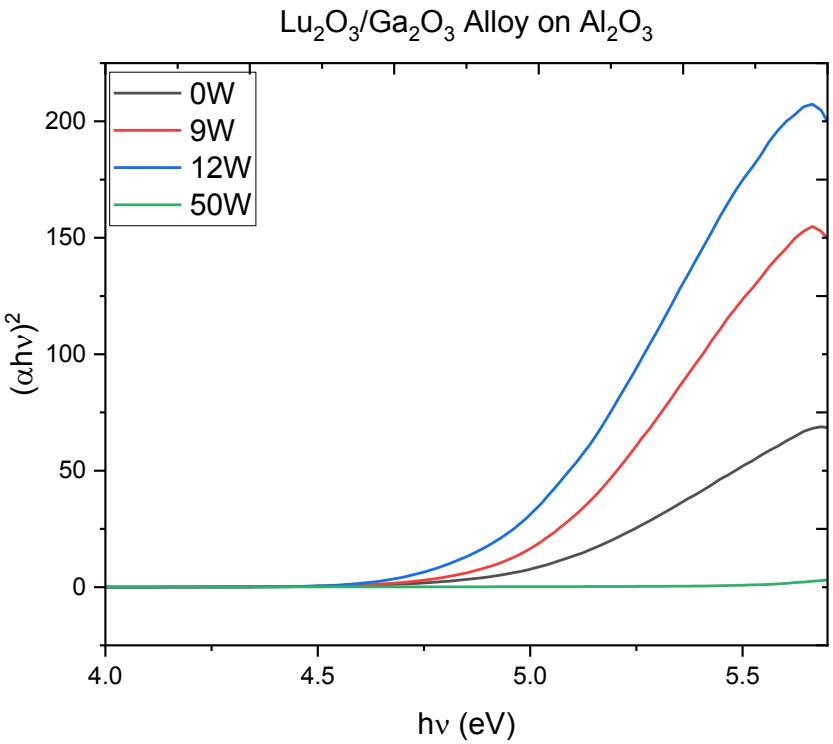

Figure 5.77 Energy plot of Lu_2O_3/Ga_2O_3 alloy films deposited on the Al_2O_3 substrate at various Lu_2O_3 rf powers.

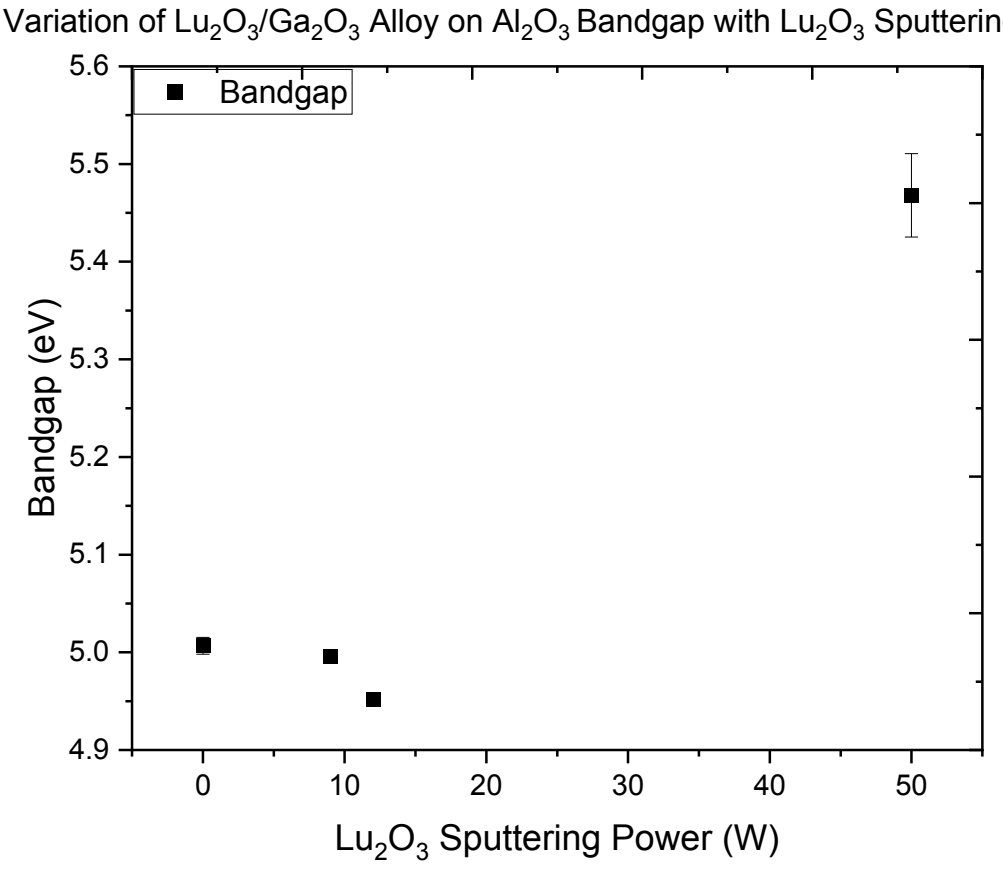

Figure 5.78 Bandgap energy vs Lu_2O_3 rf power for Lu_2O_3/Ga_2O_3 alloy films deposited on Al_2O_3 substrate.

5.6 Implementation of Devices on the Ga_2O_3

5.6.1 Introduction

This section encapsulates the culmination and practical application of the research findings presented in this dissertation, focusing on the construction of a simple yet critical component in semiconductor technology, the Schottky diode. Section 5.6.2 delves into the methodology employed for preparing samples and conducting experimental analyses to assess the electrical characteristics of metal contacts with Ga_2O_3. Subsequently, Section 5.6.3 elaborates on the electrical outcomes derived from the deposition of diverse metal contacts, with the overarching objective of attaining Ohmic contact behavior with Ga_2O_3. A comprehensive exploration of various conditions such as contact structure (layer thickness), deposition parameters, and annealing parameters to ascertain the optimal conditions for achieving Ohmic contact with Ga_2O_3. Additionally, Section 5.6.4 investigates the behavior of two Schottky metals, nickel (Ni) and molybdenum (Mo), when interfaced with Ga_2O_3 to explore their rectifying behavior and extract Schottky diode important parameters, namely, ideality factor, Schottky barrier height, and breakdown voltage.

5.6.2 Experimental Procedure

Figure 5.79 shows the setup used for depositing metal contacts to ($\bar{2}$ 0 1) Sn-doped (bulk concentration: 1.2E+18) Ga_2O_3 using sputtering deposition technique. The procedure for preparing Ohmic contacts on Ga_2O_3 substrates begins with meticulous cleaning steps to ensure surface purity and optimal contact conductivity. The substrates undergo sequential sonication in acetone for 10 minutes, followed by a similar process in isopropanol and then DI water, each for 10 minutes. Subsequently, the substrates are soaked in a 10 % hydrochloric acid (HCl) solution, rinsed with

DI water, and then immersed in boiling H_2O_2 at 85 °C for 5 minutes. After thorough rinsing with DI water, the substrates are blow dried to remove any residual moisture. This cleaning regimen is crucial for removing organic and inorganic contaminants and enhancing the adhesion and conductivity of the Ohmic contacts.

Next, photolithography techniques are employed to define the contact patterns, using a transmission line measurement mask (TLM), as shown in Fig. 5.80. The substrate is spin-coated with AZ 5214-E photoresist at 3,500 rpm for 1 minute and then soft baked at 110 °C for 1 minute. The desired pattern is then exposed using UV light for 30 seconds and developed in a 400k (4:1) developer solution for 6 seconds, resulting in the formation of the patter. Sputtering deposition is utilized to deposit the contact layers. Various layer structures, deposition temperatures, annealing temperatures and annealing atmospheres were studied for the formation of Ohmic contacts. Finally, liftoff is performed using acetone, which successfully removes the unwanted photoresist and leaves behind the metal layers in the defined contact pattern. This procedure ensures the fabrication of well-defined Ohmic contacts on Ga_2O_3 substrates, ready for subsequent electrical characterization, i.e., specific resistivity extraction. A summary of the various tests performed for the formation of Ohmic contacts is presented in Table 5.6.

For the final structure of the device a highly Sn doped layer needed to be deposited before the Ohmic contact layer to ensure the lowest specific resistivity. This film was deposited with conditions that were determined based on the findings from previous experiments involving homoepitaxial film deposition at 450°C (section 5.3) and the doping conditions established in section 5.4, which involved the use of a dc current of 5 mA for tin (Sn) deposition to ensure uniform doping of the film. Subsequently, the film undergoes annealing at 500 °C in an argon (Ar) atmosphere to further enhance its properties. An optimized Ohmic contact layer of 20 nm thick

titanium (Ti) layer, followed by an 80 nm thick gold (Au) layer was then deposited. The Ohmic contact deposition process is conducted at a pressure of 5.5 mTorr with an Ar flow rate of 10 sccm for both Ti and Au. The power settings are adjusted to 0.15A for Ti and 0.1A for Au to achieve the desired film thicknesses. The annealing was performed by RTP at 400 °C in Ar atmosphere for 6 min. Then, the front side of the substrate was mechanically polished with 1μm grade diamond polishing pad, followed by sequentially solvent cleaning. Lastly, 200 μm in diameter Schottky contacts of 50 nm (Ni)/ 50 nm (Au) or 50 nm (Mo)/ 50 nm (Au) layers were deposited on the front face. At this point, the device is ready for electrical measurement, the parameters of interest are the ideality factor (n), barrier height (Φ_B), and reverse breakdown voltage (V_{BR}) of the Schottky contact.

Figure 5.79 Setup for contact deposition using sputtering. The holder measures the deposition rate from which the film thickness is estimated.

5.6.3 Ohmic contacts

To achieve an effective ohmic contact that minimizes conduction losses in power devices, it is optimal to have a low specific contact resistivity (R_s) of 10^{-5} Ohm-cm^2 or lower [94]. To investigate the formation of Ohmic contacts to Ga_2O_3, various metal structures and compositions were assessed, including Ti, TiB_2, and W_2B_5. These metal contacts were shielded from oxidation using an 80 nm thick layer of Au. Among the metals studied, Ti (20 nm)/Au(80 nm) layers exhibited favorable Ohmic behavior when deposited at room temperature in an Ar atmosphere, followed by annealing at 400 °C in Ar for 6 minutes. The resulting specific contact resistivity was measured at 2.62×10^{-4} Ohm-cm^2. It is noteworthy that the lowest specific contact resistivity reported to date was achieved by Bhattacharyya et al. using the MOVPE method, with a value of 8.30×10^{-7} Ohm-cm^2 [104]. Table 5.6 summarizes various Ohmic contacts evaluated with controlled parameters and resulting behavior.

Table 5.6 Summary of Ohmic Contacts and parameters.

Name	Structure (nm)	Dep. Temp. (°C)	Dep. Gas	Ann. Temp. (°C)	Ann. Gas	Ann. Time (min)	R_s (Ohm-$cm^{2)}$	Behavior
041819	Ti(20)/Au(80)	25	Ar	400,500, 600	Ar	1	-	Non-Ohmic
042519	Ti(20)/Au(80)	25	Ar	400,450	Ar	1	-	Non-ohmic
051719A	Ti(20)/Au(80)	25	Ar	400	Ar	2,4,6	-	Ohmic
051719B	Ti(20)/Au(80)	25	Ar	400	Ar	6	2.62654 E-4	Ohmic
052119A	Ti(20)/Au(80)	25	Ar	-	-	-	-	Hall (Ohmic)
052119B	TiB_2(20) /Au(80)	25	Ar	-	-	-	-	-
052319	Ti(20)/Au(80)	25	Ar	400	Ar	2	-	Hall (Ohmic)
052319A	TiB_2(20) /Ti(10)/ Au(80)	25	Ar	200-600	Ar	2	-	Pseudo ohmic @500°C
052319B	TiB_2(20) /Ti(10)/ Au(80)	25	Ar	450,500, 550	Ar	0.5		550°C is Ohmic
052319C	TiB_2(20) /Ti(10)/ Au(80)	25	Ar	-	-	-	-	Scratched
052319D	TiB_2(20) /Ti(10)/ Au(80)	25	Ar	200-700	N_2	2		600°C is linear
052619A	W_2B_5(50)/ Ti(10)/Au(70)	25	Ar	200				Not Ohmic
053019	Ti(200)/ Au(80)	25	Ar	410	Ar	5	-	Not Ohmic
060319	Ti(100)/ Au(80)	25	Ar	400,410	Ar	2(400), 5(410)	-	Not Ohmic
060419	Ti(100)/ Au(80)	400(Ti) 25(Au)	Ar	400-800	Ar	5	2.6913E-4	Ohmic at 800°C
070220B	Ti(20)/Au(80)	400(Ti) 25(Au)	Ar	400	Ar	6,5,		Ohmic

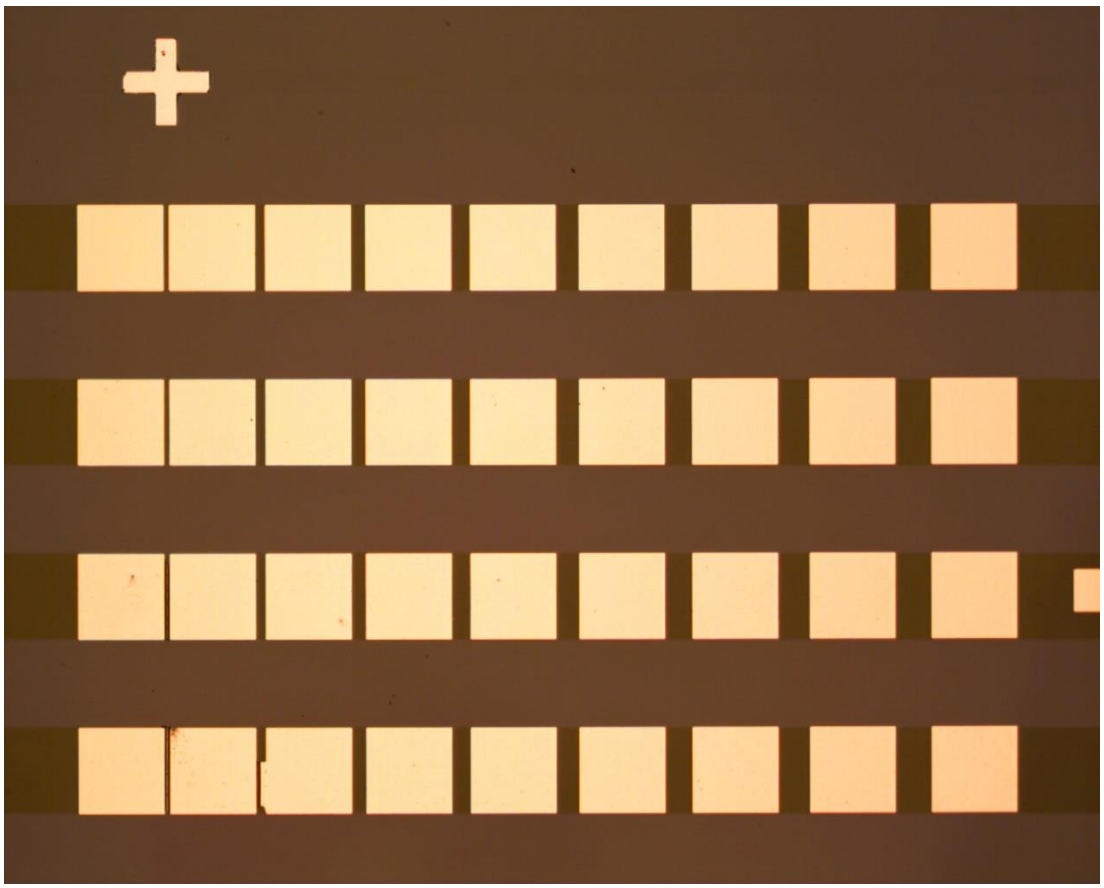

Figure 5.80 Transmission line measurement pattern for specific contact resistivity measurement using TLM method.

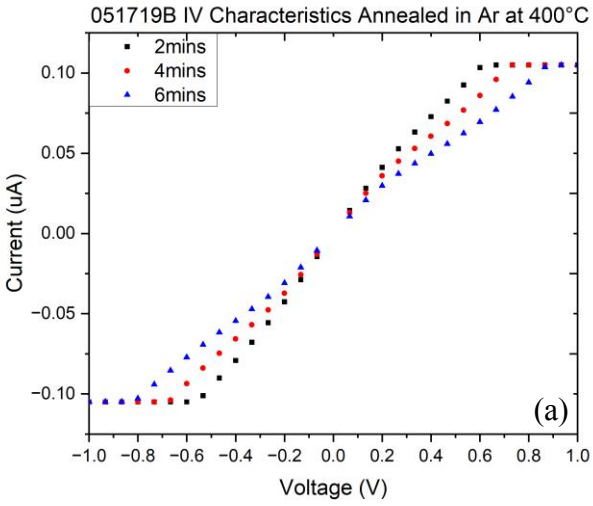

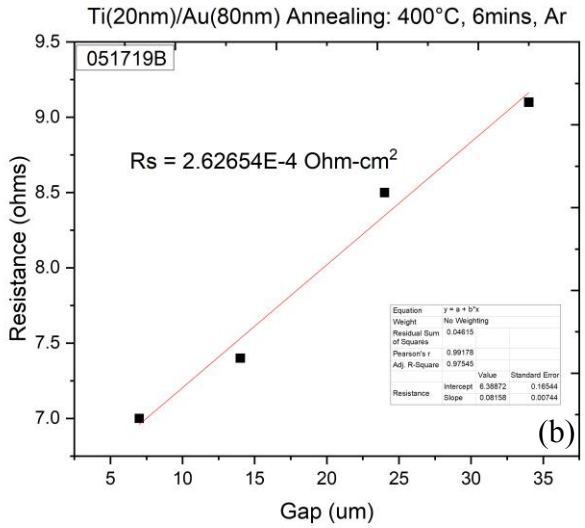

Figure 5.81 (a) IV curve of Ohmic contacts Ti(20 nm)/Au(80 nm) and (b) extracted specific contact resistivity from TLM method.

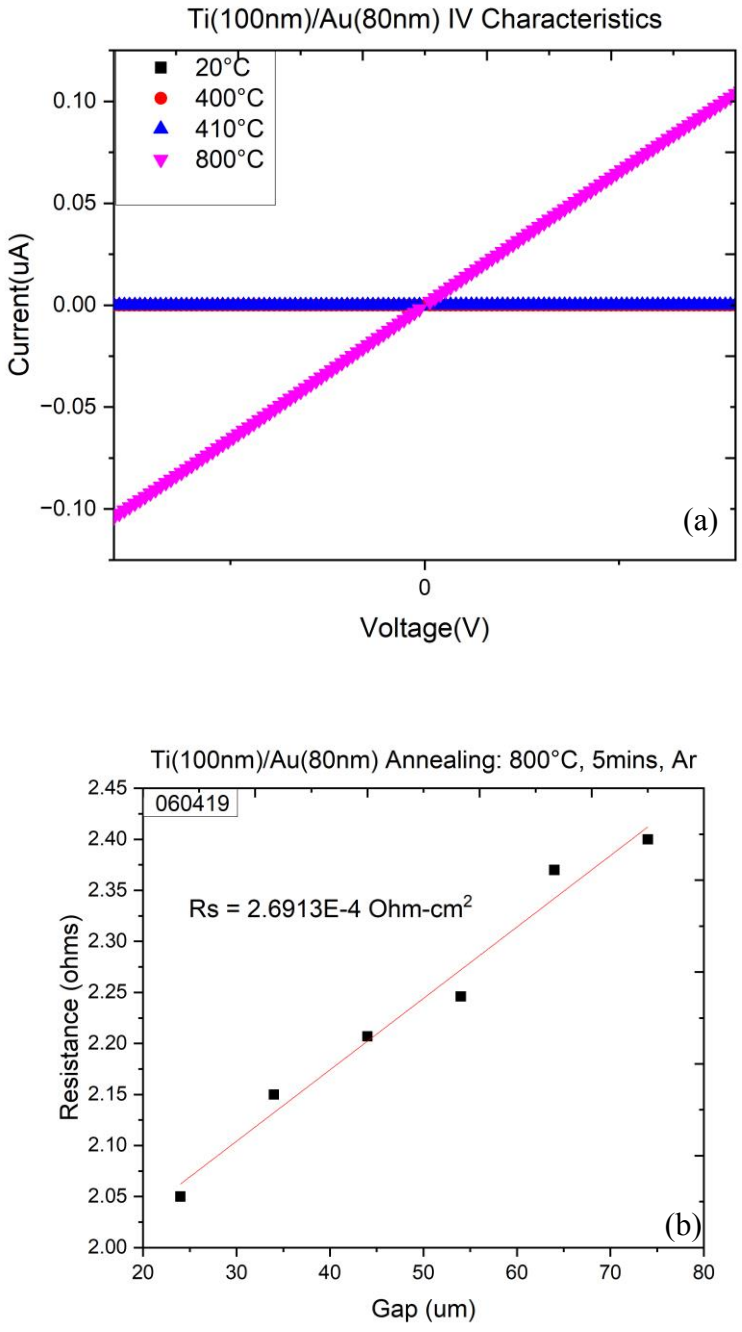

Figure 5.82 (a) IV curve of Ohmic contacts Ti(100 nm)/Au(80 nm) and (b) extracted specific contact resistivity from TLM method.

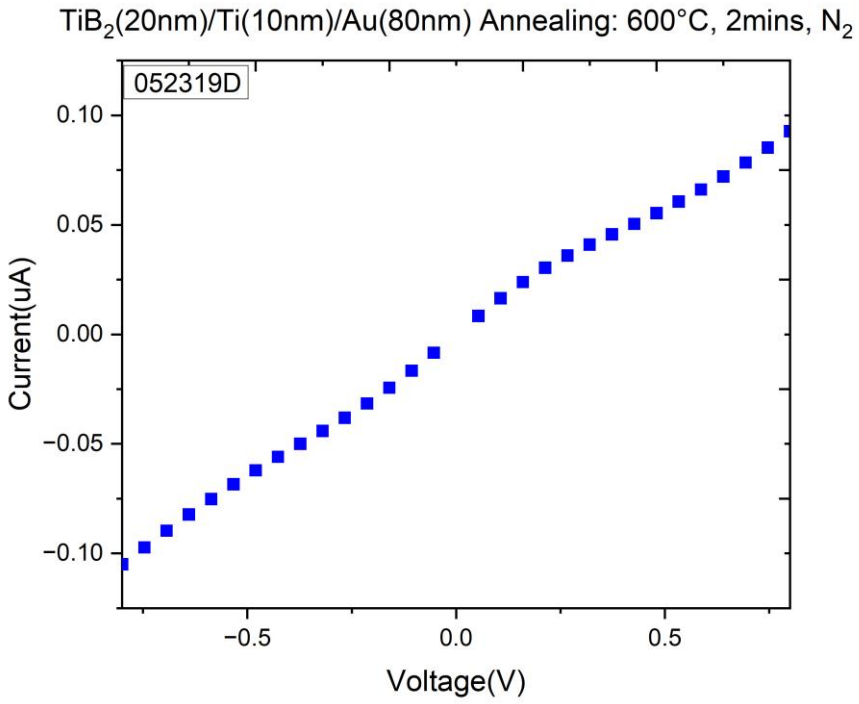

Figure 5.83 IV curve of Ohmic contacts TiB_2(20 nm)/Ti(10 nm)/Au(80 nm) showing pseudo ohmic behavior.

5.6.4 Schottky Barrier Diode Demonstration

Figure 5.84 displays a close view of the Schottky contacts applied to Ga_2O_3, featuring a pattern comprising one hundred circular pads with a diameter of 200 μm each. Table 5.2 outlines the prepared samples, denoted as SBD1, SBD2, SBD3, and SBD4, representing four samples fabricated, each containing 100 Schottky diodes. Additionally, labels C1, C2, and C3 are assigned to specific diodes for measurement purposes. Among the four samples, two had Ohmic contacts deposited on the mechanically polished side performed at YSU, while the other two had Ohmic contacts applied to the surface polished by the manufacturer. Figure 5.85 illustrates the structure of the fabricated Ga_2O_3-based Schottky barrier diode, using the optimized rf sputtered layers and contacts investigated in the previous sections.

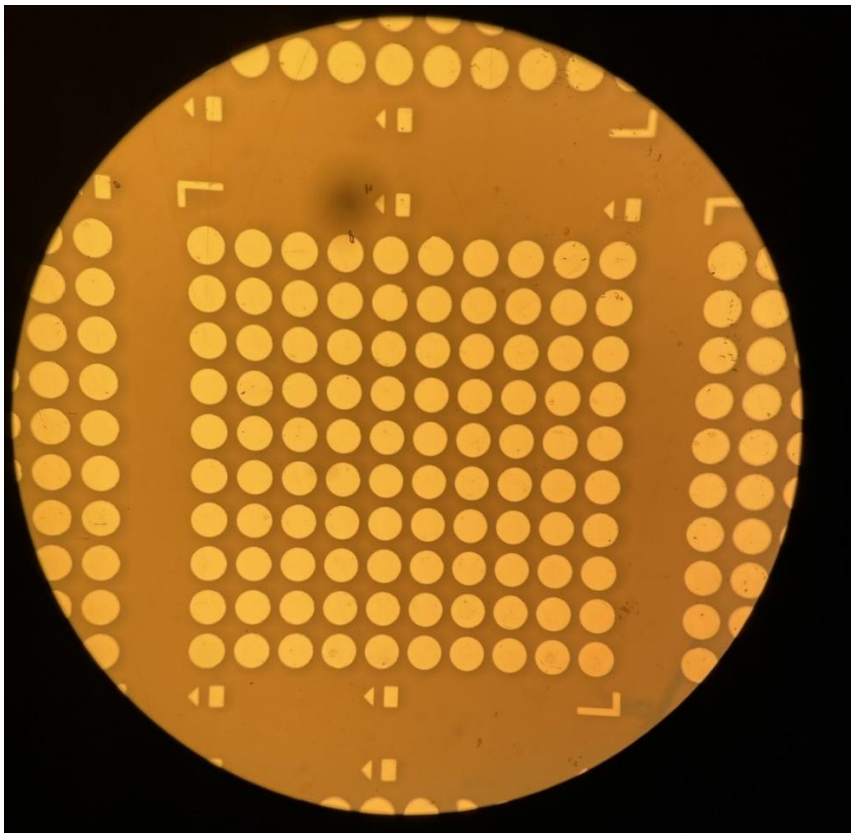

Figure 5.84 Schottky barrier diode pattern.

Table 5.7 Fabricated Schottky contacts.

Name	Ohmic contact Ti/Au (20 nm/80 nm)	Schottky Contact (50 nm/50 nm)	Doping (200 nm)
SBD 1 (072923)	Default Side	Ni/Au	5 mA
SBD 2 (073123)	Default Side	Mo/Au	5 mA
SBD 3 (072923)	Polished side (YSU)	Ni/Au	5 mA
SBD 4 (073123)	Polished side (YSU)	Mo/Au	5 mA

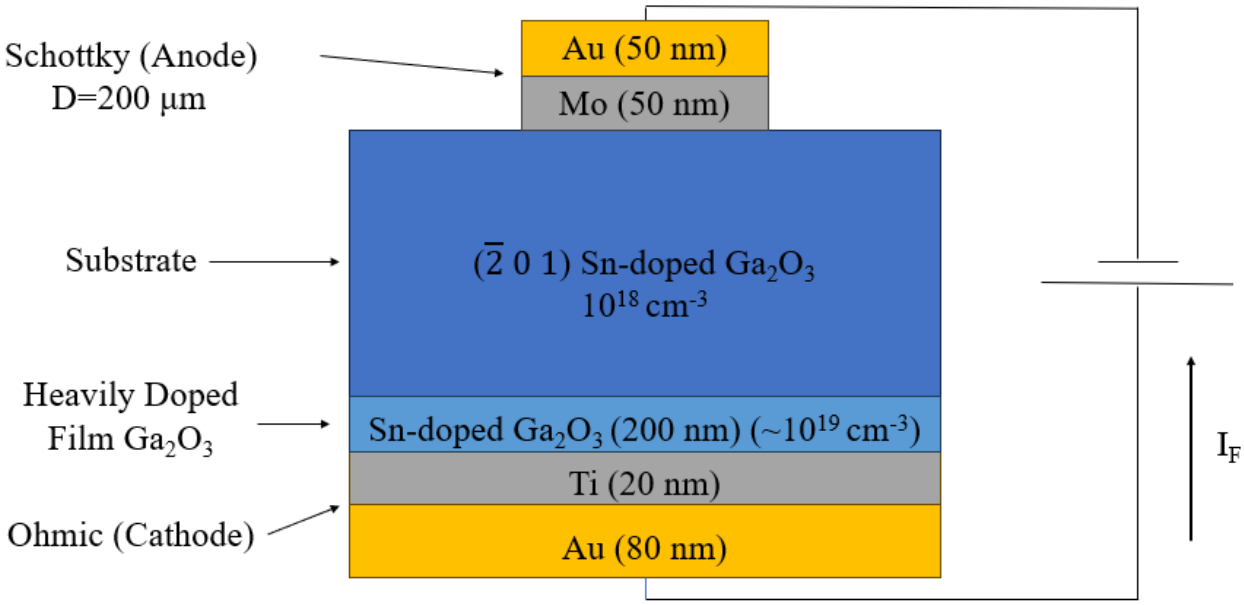

Figure 5.85 Ga_2O_3-based SBD with Mo/Au Schottky and Ti/Au Ohmic contacts.

5.6.4.1 Forward Bias Measurements

Table 5.8 summarizes the obtained ideality factors and barrier heights for the fabricated diodes. These measurements were performed in the forward and reverse bias of the device with an applied voltage from 0 to 5 V (Fig. 5.86-5.89). An ideal Schottky diode has ideality close to unity and a large barrier height. For each sample, the best measurement is highlighted on the table. The lowest ideality factor and largest Schottky barrier height obtained was from the SBD4_C34 sample deposited with Mo(50)/Au(50) Schottky contacts and had a value of n = 1.05047 and 1.21571 eV, respectively. Ideality factors reported in the literature for Ga_2O_3 range from 1.1 to 1.5 with barrier heights ranging from 0.6 eV to 1.2 eV [226]. The ideality factor obtained for the diodes fabricated with Mo Schottky contacts showed improved ideality. Both values vary according to substrate orientation, doping concentrations, metal contact used and its structure, and deposition conditions, but shows that the fabricated devices are in range.

Table 5.8 Summary ideality and barrier height.

Name	Ohmic Contact (nm)	Sn Dopant dc Current (mA)	Schottky Contact (nm)	Ideality	Barrier Height (eV)
SBD1_C1	Ti(20)/Au(80)	5	Ni(50)/Au(50)	1.27	1.12
SBD1_C2	Ti(20)/Au(80)	5	Ni(50)/Au(50)	1.20	1.14
SBD1_C24	Ti(20)/Au(80)	5	Ni(50)/Au(50)	1.54	0.96
SBD1_C35	Ti(20)/Au(80)	5	Ni(50)/Au(50)	1.59	0.96
SBD1_C38	Ti(20)/Au(80)	5	Ni(50)/Au(50)	2.36	0.93
SBD1_C86	Ti(20)/Au(80)	5	Ni(50)/Au(50)	1.76	0.98
SBD2_C1	Ti(20)/Au(80)	5	Mo(50)/Au(50)	2.52	1.10
SBD2_C14	Ti(20)/Au(80)	5	Mo(50)/Au(50)	2.81	1.11
SBD2_C24	Ti(20)/Au(80)	5	Mo(50)/Au(50)	3.38	0.99
SBD2_C44	Ti(20)/Au(80)	5	Mo(50)/Au(50)	1.80	1.26
SBD2_C65	Ti(20)/Au(80)	5	Mo(50)/Au(50)	2.28	1.06
SBD2_C69	Ti(20)/Au(80)	5	Mo(50)/Au(50)	2.90	1.00
SBD3_C1	Ti(20)/Au(80)	5	Ni(50)/Au(50)	1.91	1.05
SBD3_C5	Ti(20)/Au(80)	5	Ni(50)/Au(50)	1.41	0.98
SBD3_C24	Ti(20)/Au(80)	5	Ni(50)/Au(50)	1.12	1.16
SBD3_26	Ti(20)/Au(80)	5	Ni(50)/Au(50)	1.20	1.05
SBD3_C35	Ti(20)/Au(80)	5	Ni(50)/Au(50)	1.32	1.00
SBD3_C45	Ti(20)/Au(80)	5	Ni(50)/Au(50)	1.31	1.03
SBD4_C1	Ti(20)/Au(80)	5	Mo(50)/Au(50)	1.04	1.19
SBD4_C12	Ti(20)/Au(80)	5	Mo(50)/Au(50)	1.08	1.19
SBD4_C23	Ti(20)/Au(80)	5	Mo(50)/Au(50)	1.05	1.22
SBD4_C25	Ti(20)/Au(80)	5	Mo(50)/Au(50)	1.06	1.20
SBD4_C34	Ti(20)/Au(80)	5	Mo(50)/Au(50)	1.05	1.21
SBD4_C99	Ti(20)/Au(80)	5	Mo(50)/Au(50)	1.16	1.21

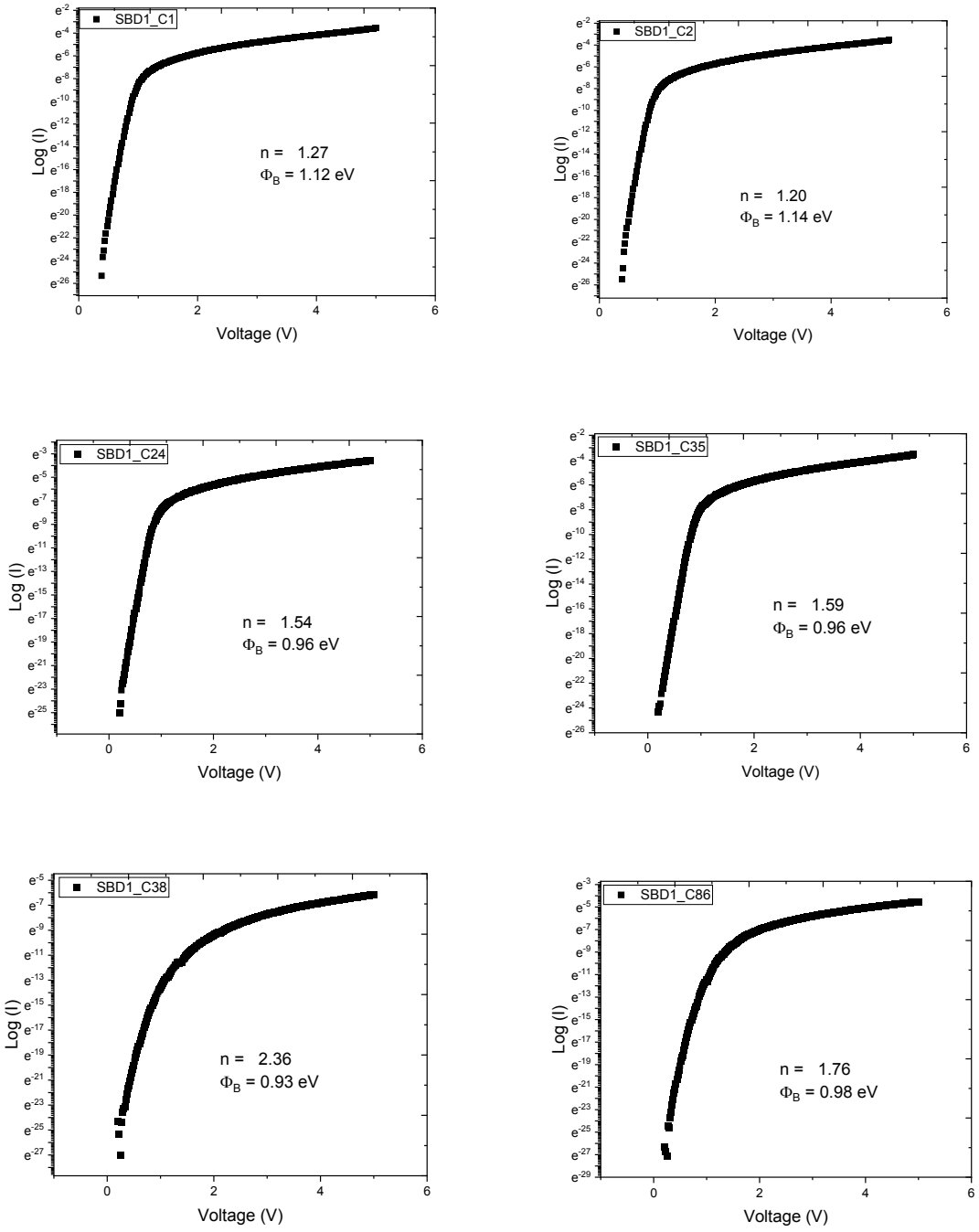

Figure 5.86 SBD1 forward bias characteristics.

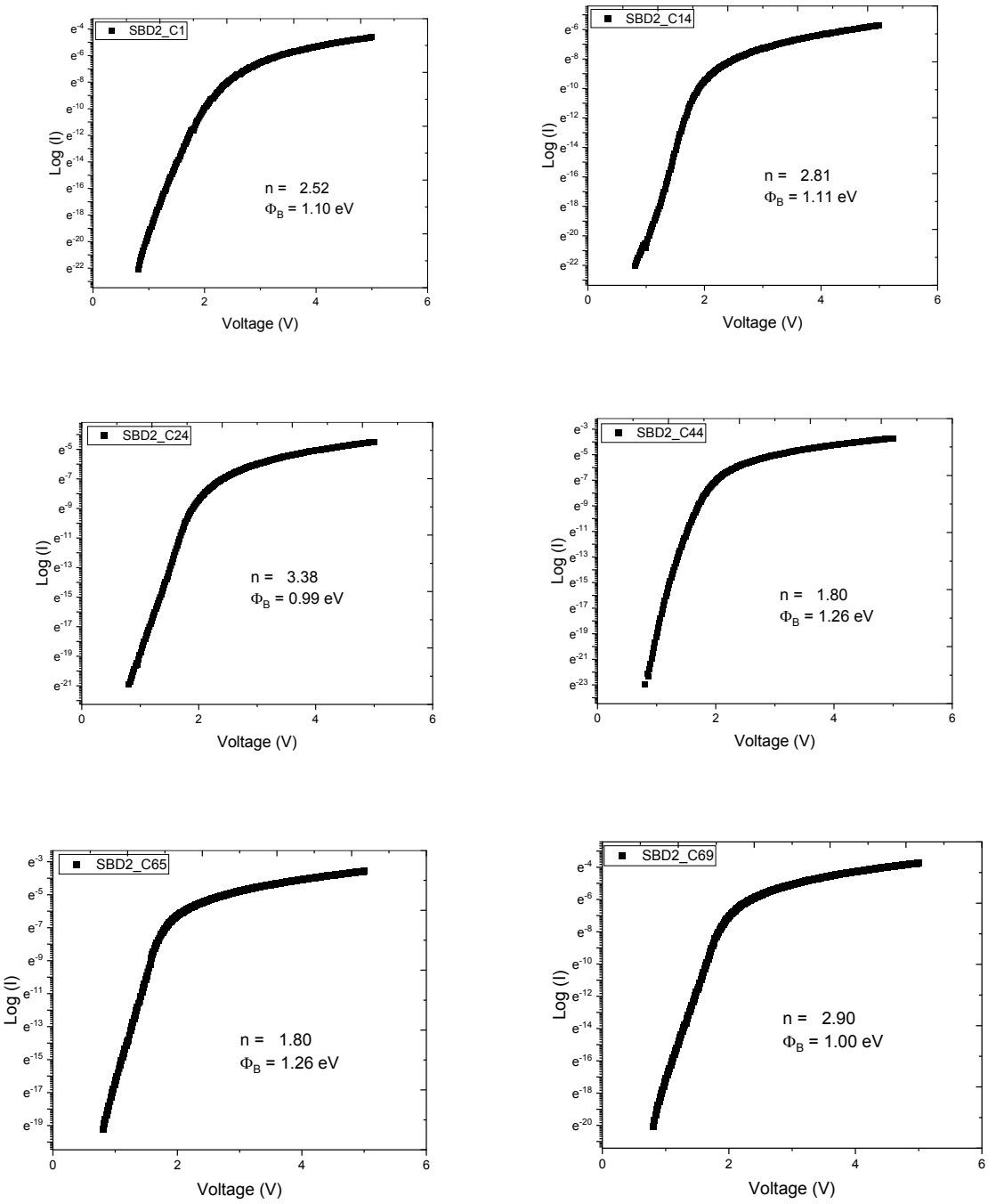

Figure 5.87 SBD2 forward bias characteristics.

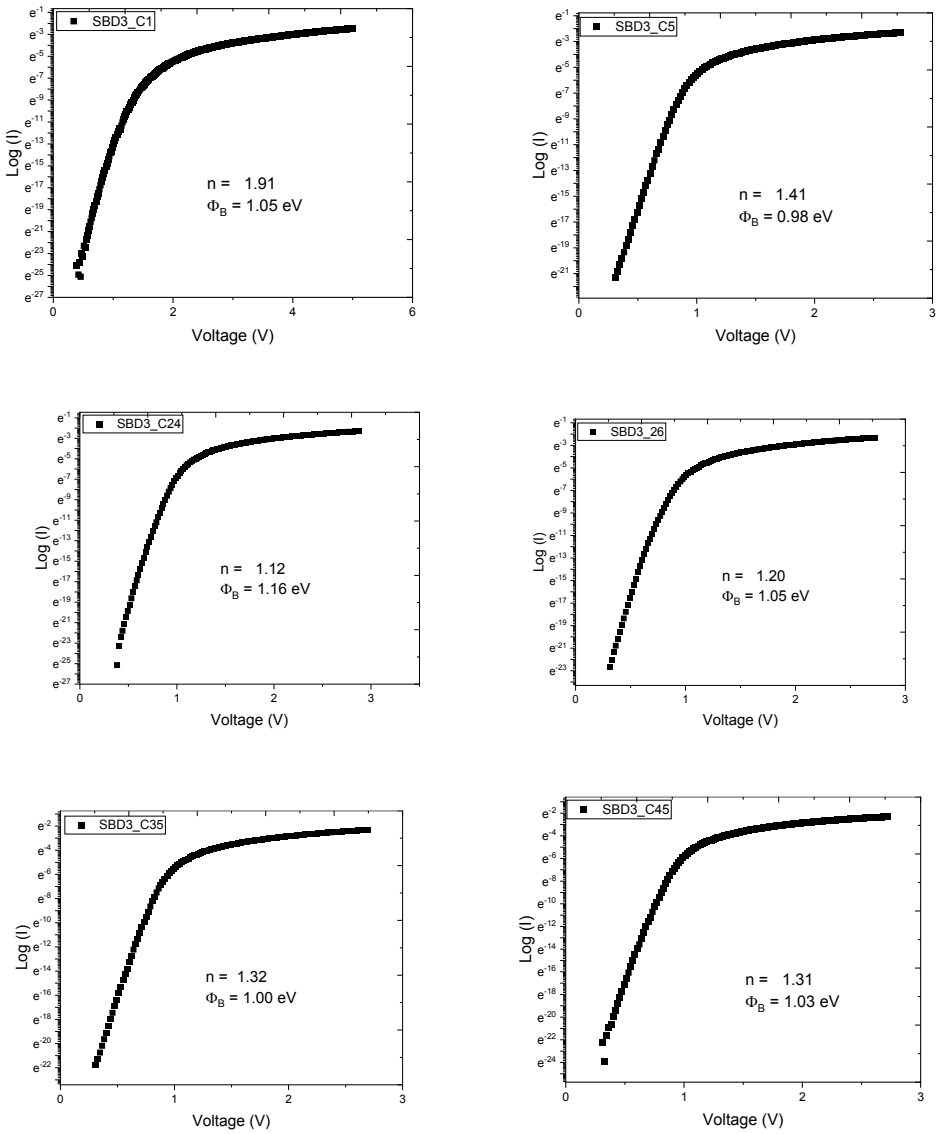

Figure 5.88 SBD3 forward bias characteristics.

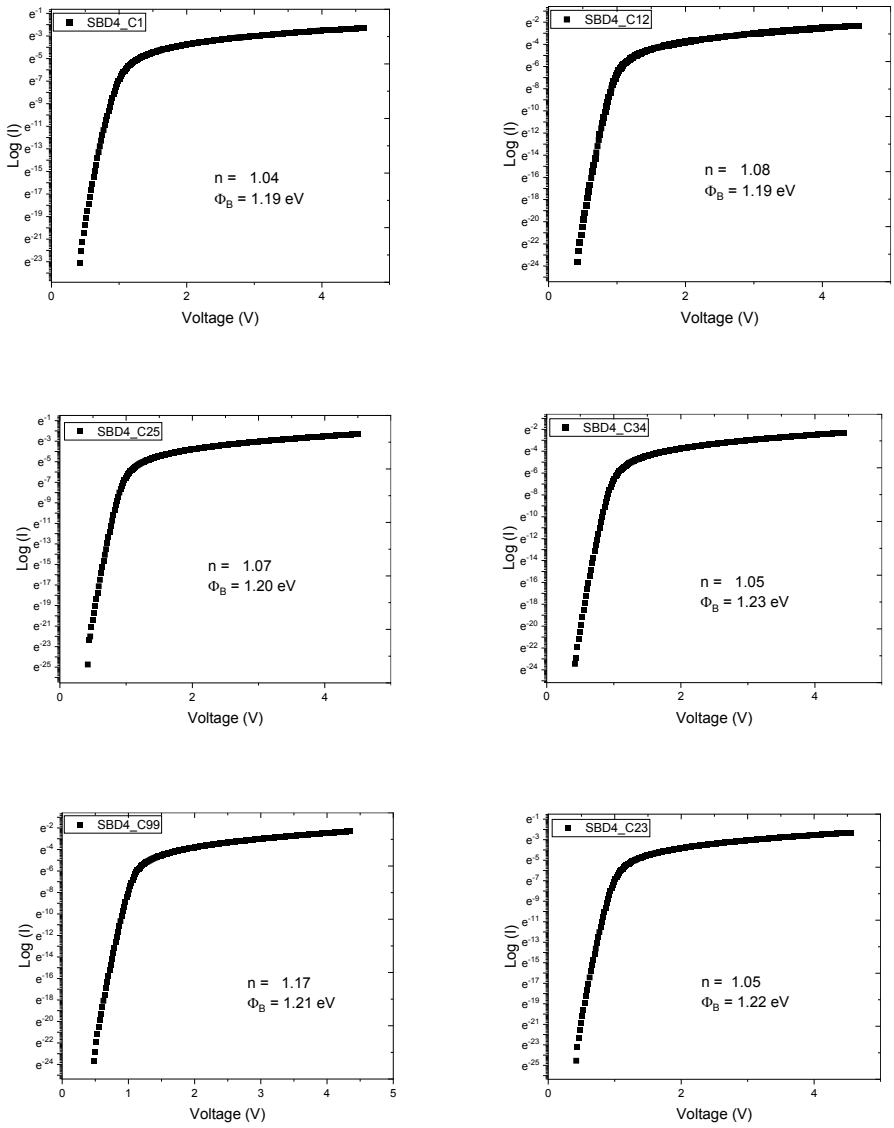

Figure 5.89 SBD4 forward bias characteristics.

5.6.4.2 Reverse Bias Measurements

Measurements of the breakdown voltage (V_{BR}) in the reverse bias were conducted for the four fabricated devices (Fig. 5.90-5.93). Each device was subjected to a reverse bias applied voltage up to 100 V, and the current was monitored until breakdown of the material occurred. This breakdown is indicated by a sudden increase in the current in the reverse bias polarization (Fig. 5.89). To estimate the voltage at which the device breaks down more accurately, the linear region of the increasing current was fitted with a linear regression (Figure 5.90 (b)). The breakdown voltage reported in the literature has a range from 40 V up to 1720 V [226]. The devices fabricated for this dissertation had a V_{BR} = 114.48 V as the largest value obtained. Again, these values can vary significantly with specific structure, substrate material orientation, metal contact, and deposition methods and parameters. Additionally, to achieve such a high V_{BR}, edge termination of the contacts is usually implemented. Nevertheless, the resulting device demonstrates and summarizes the utility of the optimized layers grown on Ga_2O_3 and contacts via rf sputtering deposition method.

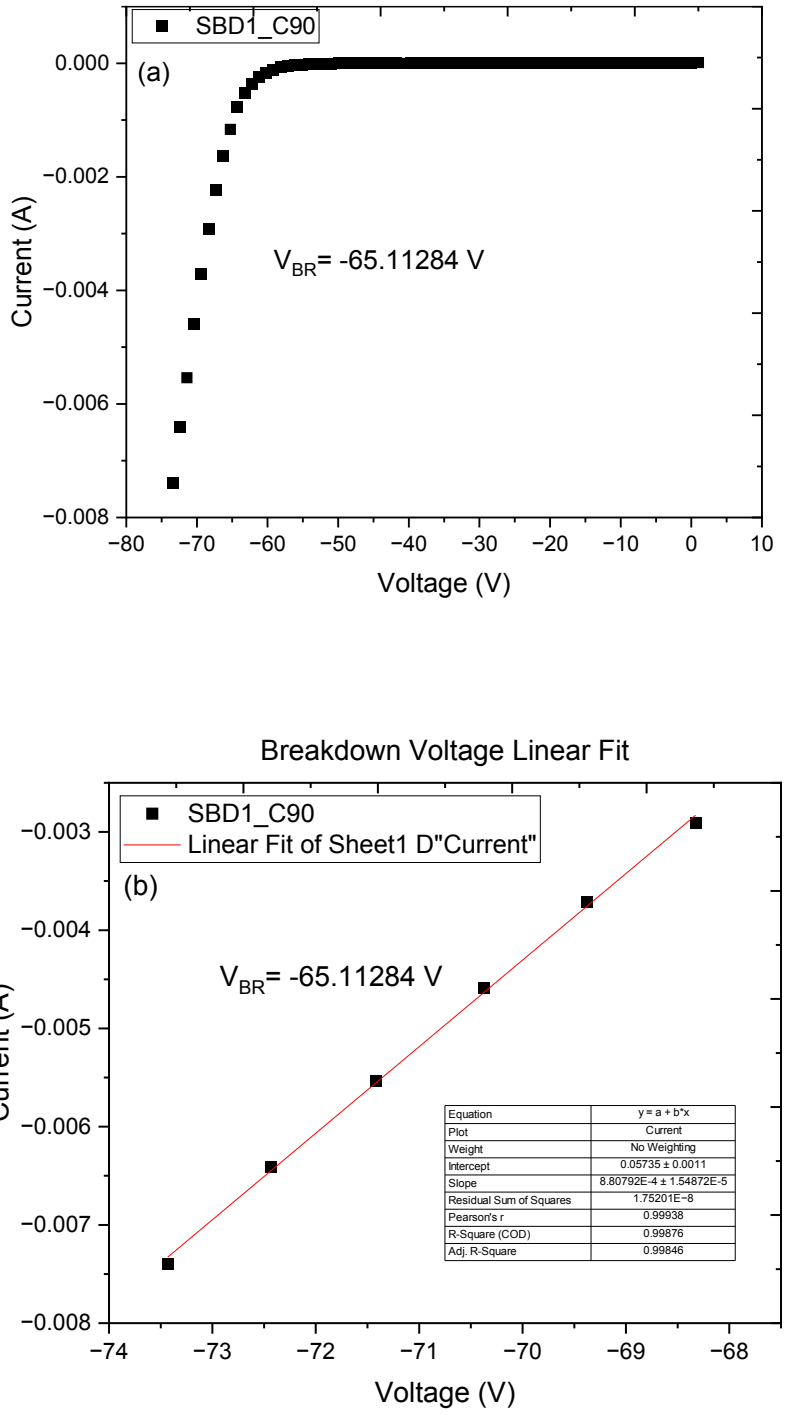

Figure 5.90 (a) SBD1 reverse bias characteristics, (b) V_{BR} linear regression.

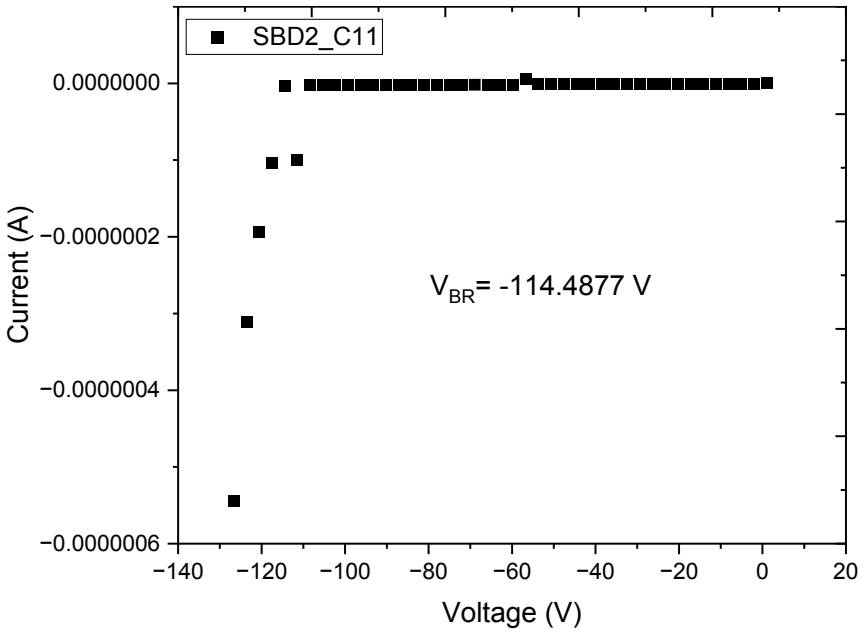

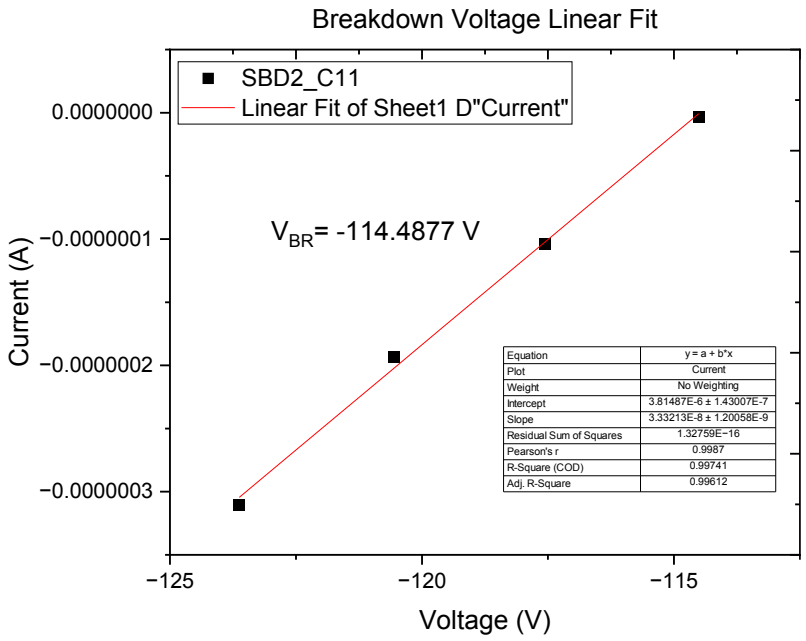

Figure 5.91 (a) SBD2 reverse bias characteristics, (b) V_{BR} linear regression.

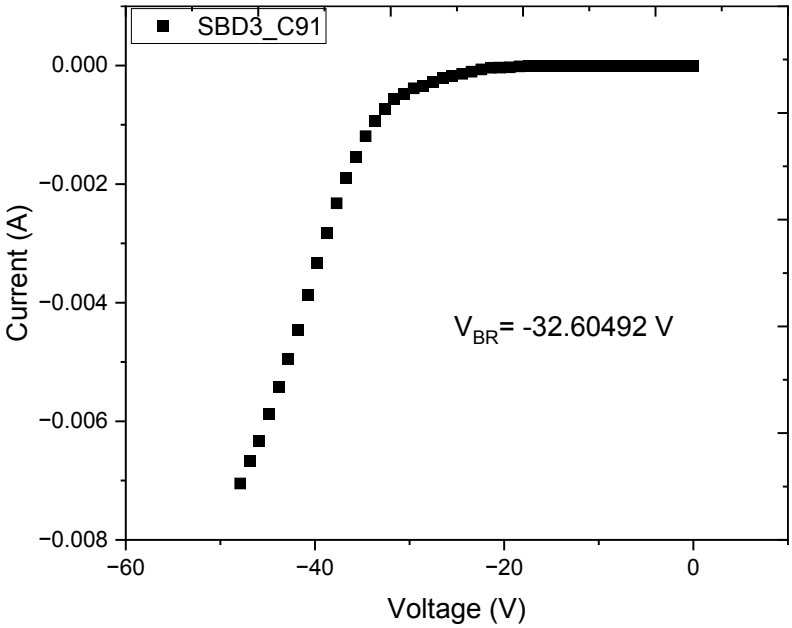

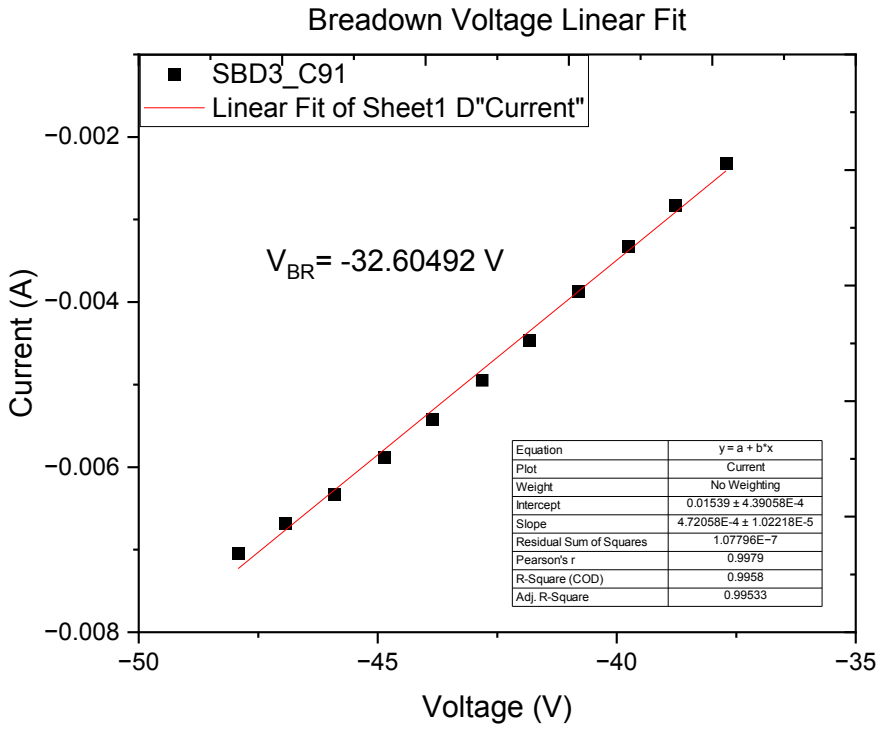

Figure 5.92 (a) SBD3 reverse bias characteristics, (b) V_{BR} linear regression.

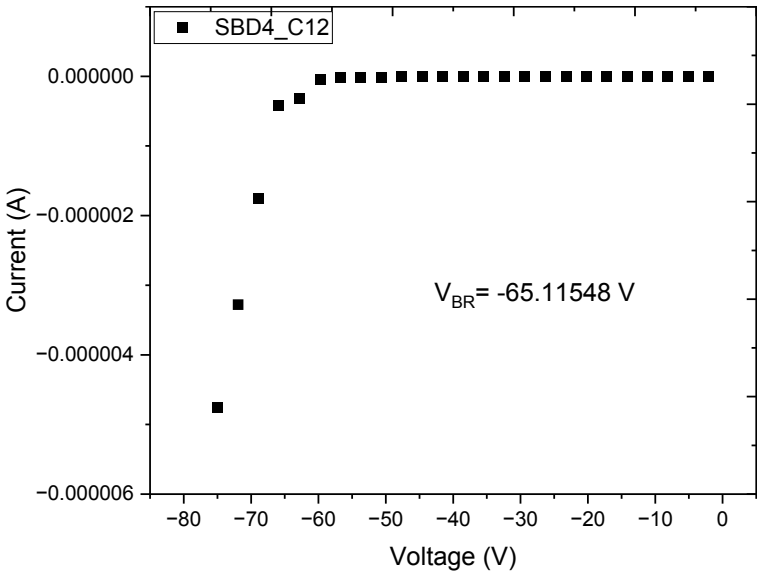

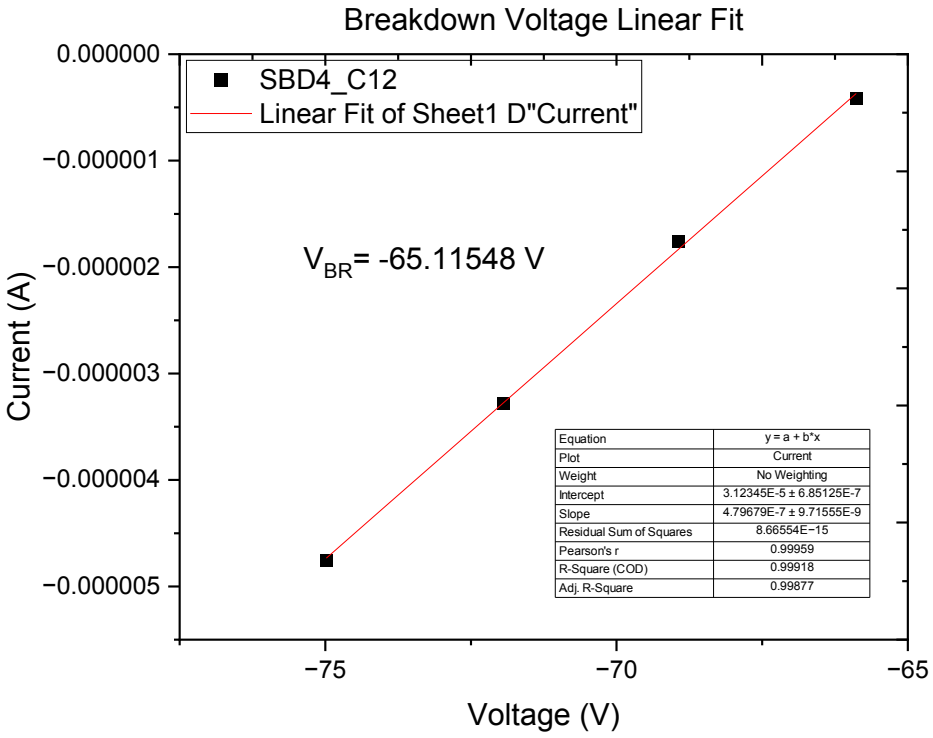

Figure 5.93 (a) SBD4 reverse bias characteristics, (b) V_{BR} linear regression.

6. Conclusion

6.1 Optimization of heteroepitaxial growth of Ga_2O_3 films on sapphire substrates

Ga_2O_3 thin films were deposited on c-plane sapphire substrates by rf magnetron sputtering under different substrate temperatures and different Ar/O_2 mixtures. The optimum substrate temperature for the films deposited in Ar, was found to be 400 ^oC, while that for the films deposited in 80% Ar + 20 % O_2 was 500 ^oC. The XRD scans of these films showed higher intensity diffraction peaks at 18.3^o, 37.1^o, 57.8^o belonging to $(\bar{2}\ 0\ 1)$, $(\bar{4}\ 0\ 2)$ and $(\bar{6}\ 0\ 3)$ planes of β-Ga_2O_3, respectively. Films deposited at other temperatures showed either amorphous or polycrystalline properties with additional XRD peaks. Post deposition annealing of these films at temperatures up to 900 °C in N_2 did not produce any further improvement in the crystalline quality of the films. The optical bandgaps of these films were found to decrease with increasing substrate temperature. For the films deposited in different Ar/O_2 mixtures, the bandgap reached a maximum value of 5.06 eV at a gas composition of 50% Ar + 50% O_2. Addition of increasing amounts of Sn dopants resulted in films with decreasing bandgaps, a consequence of renormalization effect.

6.2 Homoepitaxial Growth of Ga_2O_3 films on $(\bar{2}01)$ Ga_2O_3 substrate

The investigation into Ga_2O_3 films deposited homoepitaxially revealed several important findings. Firstly, it was observed that surface treatment prior to deposition led to the emergence of additional (100) β-Ga2O3 peaks, indicating alterations in the original crystal structure of the substrate. As a result, this surface treatment procedure was omitted from further experiments. Secondly, the optimal deposition temperature for homoepitaxial films on UID $(\bar{2}01)$ Ga_2O_3 substrate was determined to be 300 °C in Ar/O_2 (1% O_2), which did not exhibit additional planes from Ga_2O_3, ensuring structural integrity. Additionally, analysis using the Scherrer equation showed that the crystallite size of the $(\bar{6}03)$ Bragg peak of Ga_2O_3 remained around 40 nm,

indicating no significant broadening of peaks with increasing deposition temperature and maintaining crystal quality similar to that of the substrate. Furthermore, successful deposition was achieved on various substrate orientations, including (001)-, (010)-, and $(\bar{2}01)$-oriented Ga_2O_3, highlighting the versatility of the deposition process. Furthermore, XRD analysis demonstrated that only the homoepitaxial films deposited on (001)-, and (010)-Ga_2O_3, matched their respective substrates, but not the films deposited on the $(\bar{2}01)$-oriented substrate, suggesting the presence of faults domains in the films deposited on this orientation. Overall, these findings contribute valuable insights into optimizing the deposition process for homoepitaxial films on Ga_2O_3 and understanding the structural properties of gallium oxide films for potential applications in electronic devices and materials science.

6.3 Optimization of Doping of Ga_2O_3 Films Grown on $(\bar{2}01)$ Sn-Doped Ga_2O_3 Substrates

The use of Tin (Sn) dc currents ranging from 2 to 6 mA facilitated uniform doping of Ga2O3 films, as confirmed by EDS analysis which showed an increasing Sn atomic percent with higher dc currents, aligning with the desired doping levels. XRD data verified that the crystal quality of the films remained unaltered even after doping with Sn impurities, indicating the stability of the film structure. Hall effect measurements were taken after post-deposition annealing from 200 °C to 700 °C in Ar for 3 min, and provided crucial parameters such as bulk concentration, mobility, resistivity, and sheet resistance of the doped films at these temperatures. The bulk concentration exhibited a lower limit of 1 $x10^{15}$ cm^{-3} at 200 °C and reached a peak of 1 $x10^{19}$ cm^{-3} at 600 °C before dropping off. The mobility of the films was measured at 6.8 x 103 cm^2/Vs, notably different from the literature-reported value of 184 cm^2/Vs, indicating potential areas for further optimization. After comprehensive analysis, the optimal conditions for Ga_2O_3 Sn-doped films on $(\bar{2}01)$ Sn-doped Ga_2O_3 Substrates were determined to be 500 °C annealing temperature and a Sn

dc current of 5 mA. These optimized values serve as crucial parameters for the fabrication of the Schottky diode device, providing valuable insights into the doping process and the performance characteristics of Sn-doped gallium oxide films.

6.4 Optical Band Gap Tunning with Metal Alloys to Ga_2O_3

B_2O_3/Ga_2O_3 Alloy on ($\bar{2}$ 0 1) UID and Sn-doped Ga_2O_3. The initial mechanical polishing of ($\bar{2}01$) UID and Sn-doped Ga_2O_3 substrates resulted in a surface with an RMS of 1.5 nm, which although improved from the manufacturer's value of 0.26 nm, still poses challenges for optical transparency on the back side, particularly crucial for accurate optical measurements. Successful co-sputtering of B_2O_3 with Ga_2O_3 on both UID and Sn-doped Ga_2O_3 substrates was achieved, enabling the investigation of B_2O_3 alloy concentration effects using rf powers of 40, 50, and 80 W. The introduction of B_2O_3 at rf powers above 50 W led to the emergence of additional (100) Ga_2O_3 peaks in the XRD data, indicating alterations in the crystal structure. EDS analysis confirmed the presence of boron in the films, with increasing atomic percent observed as the rf power was increased, aligning with the intended alloying strategy. The B_2O_3/Ga_2O_3 films exhibited high transparency across the entire spectrum, albeit with noise in the UV region, and absorbance data confirmed UV absorption for films co-sputtered with Ga_2O_3. Interestingly, the optical bandgap showed a slight decrease with B_2O_3 rf power, from 4.64 eV at 0 W to 4.62 eV at 50 W, followed by an increase to 4.65 eV at 80 W. These subtle changes in optical properties highlight the intricate interplay between alloy composition and deposition conditions, underscoring the importance of precise control in alloy film fabrication for tailored optical applications.

In the case of co-sputtered B_2O_3 on Sn-doped Ga_2O_3, introduction of B_2O_3 at 50 W rf power resulted in the emergence of additional (100) Ga_2O_3 peaks in the XRD analysis, indicating changes

in the original crystal structure. However, these peaks were relatively weak in the samples deposited at 80 W rf power, suggesting a minimal impact of the B_2O_3 concentration on the crystalline characteristics of $(\bar{2}01)$ Ga_2O_3. Similarly, EDS analysis confirmed the successful incorporation of boron into the films, with increasing atomic percent aligning with higher rf power levels as intended. The optical transparency of the B_2O_3/Ga_2O_3 films remained high across the entire spectrum, although some noise was observed in the UV region, possibly due to the absorption properties of the polished surface in that range. Absorbance data further supported this observation, highlighting absorption in the UV for films co-sputtered with Ga_2O_3. The bandgap of the films exhibited a subtle trend with increasing rf power. It decreased slightly from 4.64 eV at 0W to 4.62 eV at 40 W but then increased to 4.66 eV at 80 W. This complex behavior underscores the intricate relationship between B_2O_3 concentration, rf power, and optical properties, emphasizing the need for careful optimization in the deposition process for desired material characteristics.

The co-sputtering of Lu_2O_3 with Ga_2O_3 on $(\bar{2}01)$ UID Ga_2O_3 substrates was also explored across varying rf powers of 20, 30, and 80 W, shedding light on the influence of Lu_2O_3 alloy concentration on the resulting films. At a rf power of 20 W, the introduction of Lu_2O_3 led to the appearance of additional (100) Ga_2O_3 peaks in the XRD analysis, which then disappeared at the 80 W sample, indicating a minimal effect on the original crystal structure of Ga_2O_3. EDS analysis revealed an increase in Lu atomic percent, although Lu_2O_3 deposition at low rf power (20 W) proved challenging, with an observed atomic percent of 1.4%. Despite this, the transparency of the films remained relatively high at 70%, although with noise observed in the UV region. The absorption in the UV range and the bandgap of the films showed a slight increase from 4.641 eV at 0 W to 4.648 eV at 80 W, suggesting a need for further optimization with higher rf power to

achieve desired optical and electrical properties. Co-sputtering of Lu_2O_3 with Ga_2O_3 on $(\bar{2}01)$Sn-doped Ga_2O_3 XRD data indicated that additional (100) Ga_2O_3 peaks decreased beyond 20 W rf power, suggesting a small effect on crystal structure at higher Lu_2O_3 concentrations. EDS analysis further revealed an increase in Lu atomic percent, with values of 1.0%, 2.6%, and 14.6% observed at 20, 30, and 80 W, respectively. This highlights the ability to control Lu_2O_3 alloy concentration during co-sputtering processes. The transmittance of the films ranged from 60% to 70%, with noise observed in the UV region. Despite this, there was a minor increase in absorption in the UV range and bandgaps, rising from 4.641 eV at 0 W to 4.664 eV at 80 W.

B_2O_3/Ga_2O_3 Alloy on Al_2O_3. Lastly, the investigation into films co-sputtered with B_2O_3 and Lu_2O_3 along with Ga_2O_3 on Al_2O_3 substrates was investigated. Double-side polished Al_2O_3 substrates were utilized to address noise issues in the UV range caused by diffraction from a non-optically transparent surface. rf powers ranging from 0 to 80 W were explored for B_2O_3 alloy concentration, revealing amorphous films on Al_2O_3 and a fluctuation in bandgap around 5.0 eV. Additionally, rf powers from 0 to 50 W were studied for Lu_2O_3 alloy concentration, showing preserved crystal structure at lower powers and Lu_2O_3 cubic phase for pure sample, with a slight decrease in bandgap down to 4.95 eV at 12 W. In conclusion co-sputtering of B_2O_3 and Lu_2O_3 on these two surfaces demonstrated the potential for bandgap modification, although further optimization of film fabrication, i.e., film uniformity, is needed to fully harness these capabilities for optoelectronic devices and related applications.

6.5 Device Demonstration

The demonstration of gallium oxide-based Schottky barrier diodes using photolithography technique was achieved with optimized parameters found in this dissertation, namely, film and doping optimization, Ohmic contact optimization, Schottky contact optimization. A 10x10 diodes of 200 μm in diameter made with Ni/Au and Mo/Au (50 nm/50 nm) pattern was successfully deposited on $(\bar{2}01)$ Sn-doped Ga_2O_3 substrates. Among the fabricated diodes, the SBD4_C34 sample deposited with Mo(50 nm)/Au(50 nm) Schottky contacts exhibited the lowest ideality factor, with a value of n = 1.05047, indicating good electrical performance. Additionally, this sample showed the largest Schottky barrier height of Φ_B = 1.21571 eV, suggesting good rectifying behavior across the metal-semiconductor interface. Furthermore, the SBD2_C11 sample deposited with Mo(50)/Au(50) demonstrated the largest breakdown voltage (VBR = 114.48 V), highlighting its robustness and suitability for high-voltage applications. These findings underscore the potential of gallium oxide-based Schottky barrier diodes for diverse electronic and semiconductor device applications and summarize all optimization parameters found in this dissertation.

6.6 Future Work

Several avenues emerge from the findings of this dissertation. Firstly, further exploration could involve depositing homoepitaxial Ga_2O_3 films at various deposition temperatures and on different substrate orientations. This would provide a deeper understanding of the crystalline structure and properties of these films under different growth conditions. Additionally, investigating alloys with diverse substrate orientations while employing double-sided polished gallium oxide substrates could help alleviate issues related to noisy optical measurements, enhancing the accuracy of optical characterizations.

Furthermore, delving into ohmic contacts with alternative metallization such as Hafnium, Borides, and ITO (Indium Tin Oxide) presents an intriguing direction. Different metallization schemes may offer unique advantages in terms of conductivity, stability, and compatibility with gallium oxide films, thus warranting comprehensive studies. Another crucial area for future research lies in the optimization of doping processes. Designing an optimization methodology to address multiple parameters derived from Hall effect measurements, such as bulk concentration, mobility, resistivity, and sheet resistance, would be instrumental. This optimization strategy could help achieve tailored doping profiles and enhance the overall performance of Sn-doped Ga_2O_3 films for various semiconductor applications.

List of Publications

i) Microstructure and Optical Properties of Sputter-Deposited Ga_2O_3 Films

This publication included section 5.1: Optimization of heteroepitaxial growth of Ga_2O_3 films on sapphire substrates. (2021) [168]

ii) Optical Bandgap Engineering of Ga_2O_3 via Lu_2O_3 and B_2O_3 Metal Alloy Deposition

This manuscript will include only section 5.5: Optical Band Gap Tunning with Metal Alloys to Ga_2O.

iii) Ohmic and Schottky Contacts for Ga_2O_3.

This manuscript will include only section 5.6: Implementation of Devices on the Ga_2O_3.

References

[1] S.B. Reese, Wide-Bandgap Electronics Analysis, (2019). https://research-hub.nrel.gov/en/publications/wide-bandgap-electronics-analysis (accessed March 19, 2024).

[2] B. Ozpineci, COMPARISON OF WIDE BANDGAP SEMICONDUCTORS FOR POWER APPLICATIONS, (n.d.).

[3] S.C. Binari, K. Doverspike, G. Kelner, H.B. Dietrich, A.E. Wickenden, GaN FETs for microwave and high-temperature applications, Solid-State Electronics 41 (1997) 177–180. https://doi.org/10.1016/S0038-1101(96)00161-X.

[4] N. Stath, V. Härle, J. Wagner, The status and future development of innovative optoelectronic devices based on III-nitrides on SiC and on III-antimonides, Materials Science and Engineering: B 80 (2001) 224–231. https://doi.org/10.1016/S0921-5107(00)00607-3.

[5] S.N. Mohammad, H. Morkoç, Progress and prospects of group-III nitride semiconductors, Progress in Quantum Electronics 20 (1996) 361–525. https://doi.org/10.1016/S0079-6727(96)00002-X.

[6] B.J. Baliga, Power semiconductor device figure of merit for high-frequency applications, IEEE Electron Device Letters 10 (1989) 455–457. https://doi.org/10.1109/55.43098.

[7] M. Higashiwaki, G.H. Jessen, Guest Editorial: The dawn of gallium oxide microelectronics, Appl. Phys. Lett. 112 (2018) 060401. https://doi.org/10.1063/1.5017845.

[8] S.J. Pearton, J. Yang, P.H. Cary, F. Ren, J. Kim, M.J. Tadjer, M.A. Mastro, A review of Ga2O3 materials, processing, and devices, Applied Physics Reviews 5 (2018) 011301. https://doi.org/10.1063/1.5006941.

[9] M. Higashiwaki, A. Kuramata, H. Murakami, Y. Kumagai, State-of-the-art technologies of gallium oxide power devices, J. Phys. D: Appl. Phys. 50 (2017) 333002. https://doi.org/10.1088/1361-6463/aa7aff.

[10] K. Sasaki, M. Higashiwaki, A. Kuramata, T. Masui, S. Yamakoshi, MBE grown Ga2O3 and its power device applications, Journal of Crystal Growth 378 (2013) 591–595. https://doi.org/10.1016/j.jcrysgro.2013.02.015.

[11] C.-Y. Huang, R.-H. Horng, D.-S. Wuu, L.-W. Tu, H.-S. Kao, Thermal annealing effect on material characterizations of β-Ga2O3 epilayer grown by metal organic chemical vapor deposition, Applied Physics Letters 102 (2013) 011119. https://doi.org/10.1063/1.4773247.

[12] Y. An, L. Dai, Y. Wu, B. Wu, Y. Zhao, T. Liu, H. Hao, Z. Li, G. Niu, J. Zhang, Z. Quan, S. Ding, Epitaxial growth of β-Ga2O3 thin films on Ga2O3 and Al2O3 substrates by using pulsed laser deposition, J. Adv. Dielect. 09 (2019) 1950032. https://doi.org/10.1142/S2010135X19500322.

[13] H.C. Kang, Heteroepitaxial growth of multidomain Ga2O3/sapphire(001) thin films deposited using radio frequency magnetron sputtering, Materials Letters 119 (2014) 123–126. https://doi.org/10.1016/j.matlet.2014.01.030.

[14] S. Jiao, H. Lu, X. Wang, Y. Nie, D. Wang, S. Gao, J. Wang, The Structural and Photoelectrical Properties of Gallium Oxide Thin Film Grown by Radio Frequency Magnetron Sputtering, ECS Journal of Solid State Science and Technology 8 (2019) Q3086–Q3090. https://doi.org/10.1149/2.0161907jss.

[15] A.K. Saikumar, S.D. Nehate, K.B. Sundaram, Review—RF Sputtered Films of Ga2O3, ECS J. Solid State Sci. Technol. 8 (2019) Q3064. https://doi.org/10.1149/2.0141907jss.
[16] M. Lorenz, M.S.R. Rao, T. Venkatesan, E. Fortunato, P. Barquinha, R. Branquinho, D. Salgueiro, R. Martins, E. Carlos, A. Liu, F.K. Shan, M. Grundmann, H. Boschker, J. Mukherjee, M. Priyadarshini, N. DasGupta, D.J. Rogers, F.H. Teherani, E.V. Sandana, P. Bove, K. Rietwyk, A. Zaban, A. Veziridis, A. Weidenkaff, M. Muralidhar, M. Murakami, S. Abel, J. Fompeyrine, J. Zuniga-Perez, R. Ramesh, N.A. Spaldin, S. Ostanin, V. Borisov, I. Mertig, V. Lazenka, G. Srinivasan, W. Prellier, M. Uchida, M. Kawasaki, R. Pentcheva, P. Gegenwart, F.M. Granozio, J. Fontcuberta, N. Pryds, The 2016 oxide electronic materials and oxide interfaces roadmap, J. Phys. D: Appl. Phys. 49 (2016) 433001. https://doi.org/10.1088/0022-3727/49/43/433001.
[17] S.B. Reese, T. Remo, J. Green, A. Zakutayev, How Much Will Gallium Oxide Power Electronics Cost?, Joule 3 (2019) 903–907. https://doi.org/10.1016/j.joule.2019.01.011.
[18] M. Higashiwaki, K. Sasaki, A. Kuramata, T. Masui, S. Yamakoshi, Gallium oxide (Ga2O3) metal-semiconductor field-effect transistors on single-crystal β-Ga2O3 (010) substrates, Applied Physics Letters 100 (2012) 013504. https://doi.org/10.1063/1.3674287.
[19] Z. Galazka, β-Ga2O3 for wide-bandgap electronics and optoelectronics, Semicond. Sci. Technol. 33 (2018) 113001. https://doi.org/10.1088/1361-6641/aadf78.
[20] Z. Hajnal, J. Miro, G. Kiss, F. Réti, P. Deak, R. Herndon, J. Kuperberg, Role of oxygen vacancy defect states in the n-type conduction of β-Ga2O3, JOURNAL OF APPLIED PHYSICS 86 (1999) 3792–3796. https://doi.org/10.1063/1.371289.
[21] O.M. Bordun, B.O. Bordun, I.Yo. Kukharskyy, I.I. Medvid, Photoluminescence Properties of β-Ga2O3 Thin Films Produced by Ion-Plasma Sputtering, J Appl Spectrosc 84 (2017) 46–51. https://doi.org/10.1007/s10812-017-0425-3.
[22] R. Roy, V.G. Hill, E.F. Osborn, Polymorphism of Ga_2O_3 and the System Ga_2O_3—H_2O, J. Am. Chem. Soc. 74 (1952) 719–722. https://doi.org/10.1021/ja01123a039.
[23] H.Y. Playford, A.C. Hannon, E.R. Barney, R.I. Walton, Structures of Uncharacterised Polymorphs of Gallium Oxide from Total Neutron Diffraction, Chemistry – A European Journal 19 (2013) 2803–2813. https://doi.org/10.1002/chem.201203359.
[24] J.P. Remeika, M. Marezio, GROWTH OF α-Ga2O3 SINGLE CRYSTALS AT 44 KBARS, Appl. Phys. Lett. 8 (1966) 87–88. https://doi.org/10.1063/1.1754500.
[25] S. Geller, Crystal Structure of β-Ga2O3, The Journal of Chemical Physics 33 (2004) 676–684. https://doi.org/10.1063/1.1731237.
[26] S.-D. Lee, K. Akaiwa, S. Fujita, Thermal stability of single crystalline alpha gallium oxide films on sapphire substrates, Physica Status Solidi c 10 (2013) 1592–1595. https://doi.org/10.1002/pssc.201300259.
[27] S.I. Stepanov, V.I. Nikolaev, V.E. Bougrov, A.E. Romanov, GALLIUM OXIDE: PROPERTIES AND APPLICA 498 A REVIEW, (n.d.).
[28] K. Yamaguchi, First principles study on electronic structure of β-Ga2O3, Solid State Communications 131 (2004) 739–744. https://doi.org/10.1016/j.ssc.2004.07.030.
[29] L. Binet, D. Gourier, C. Minot, Relation between Electron Band Structure and Magnetic Bistability of Conduction Electrons in β-Ga2O3, Journal of Solid State Chemistry 113 (1994) 420–433. https://doi.org/10.1006/jssc.1994.1390.
[30] E.A. Albanesi, S.J. Sferco, I. Lefebvre, G. Allan, G. Hollinger, Electronic structure of binary and ternary Ga or As oxides, Phys. Rev. B 46 (1992) 13260–13267. https://doi.org/10.1103/PhysRevB.46.13260.

[31] S. Yoshioka, H. Hayashi, A. Kuwabara, F. Oba, K. Matsunaga, I. Tanaka, Structures and energetics of Ga2O3 polymorphs, J. Phys.: Condens. Matter 19 (2007) 346211. https://doi.org/10.1088/0953-8984/19/34/346211.
[32] T. Lovejoy, R. Chen, E. Yitamben, V. Shutthanadan, S. Heald, E. Villora, K. Shimamura, S. Zheng, S. Dunham, F. Ohuchi, M. Olmstead, Incorporation, valence state, and electronic structure of Mn and Cr in bulk single crystal β–Ga2O3, Journal of Applied Physics 111 (2012). https://doi.org/10.1063/1.4729289.
[33] J. Åhman, G. Svensson, J. Albertsson, A Reinvestigation of β-Gallium Oxide, Acta Cryst C 52 (1996) 1336–1338. https://doi.org/10.1107/S0108270195016404.
[34] H. He, M.A. Blanco, R. Pandey, Electronic and thermodynamic properties of β-Ga2O3, Appl. Phys. Lett. 88 (2006) 261904. https://doi.org/10.1063/1.2218046.
[35] J.A. Kohn, G. Katz, J.D. Broder, Characterization of β-Ga2O3 and its Alumina Isomorph, θ-Al2O3*, American Mineralogist 42 (1957) 398–407.
[36] P. Kroll, R. Dronskowski, M. Martin, Formation of spinel-type gallium oxynitrides: a density-functional study of binary and ternary phases in the system Ga–O–N, Journal of Materials Chemistry 15 (2005) 3296. https://doi.org/10.1039/b506687e.
[37] H.H. Tippins, Optical Absorption and Photoconductivity in the Band Edge of $\ensuremath{\beta}\ensuremath{-}{\mathrm{Ga}}_{2}{\mathrm{O}}_{3}$, Phys. Rev. 140 (1965) A316–A319. https://doi.org/10.1103/PhysRev.140.A316.
[38] C. Janowitz, V. Scherer, M. Mohamed, A. Krapf, H. Dwelk, R. Manzke, Z. Galazka, R. Uecker, K. Irmscher, R. Fornari, M. Michling, D. Schmeißer, J.R. Weber, J.B. Varley, C.G.V. de Walle, Experimental electronic structure of In2O3 and Ga2O3, New J. Phys. 13 (2011) 085014. https://doi.org/10.1088/1367-2630/13/8/085014.
[39] M. Higashiwaki, K. Sasaki, A. Kuramata, T. Masui, S. Yamakoshi, Gallium oxide (Ga_2O_3) metal-semiconductor field-effect transistors on single-crystal β-Ga_2O_3 (010) substrates, Applied Physics Letters 100 (2012) 013504. https://doi.org/10.1063/1.3674287.
[40] J.L. Hudgins, G.S. Simin, E. Santi, M.A. Khan, An assessment of wide bandgap semiconductors for power devices, IEEE Transactions on Power Electronics 18 (2003) 907–914. https://doi.org/10.1109/TPEL.2003.810840.
[41] J.Y. Tsao, S. Chowdhury, M.A. Hollis, D. Jena, N.M. Johnson, K.A. Jones, R.J. Kaplar, S. Rajan, C.G.V. de Walle, E. Bellotti, C.L. Chua, R. Collazo, M.E. Coltrin, J.A. Cooper, K.R. Evans, S. Graham, T.A. Grotjohn, E.R. Heller, M. Higashiwaki, M.S. Islam, P.W. Juodawlkis, M.A. Khan, A.D. Koehler, J.H. Leach, U.K. Mishra, R.J. Nemanich, R.C.N. Pilawa-Podgurski, J.B. Shealy, Z. Sitar, M.J. Tadjer, A.F. Witulski, M. Wraback, J.A. Simmons, Ultrawide-Bandgap Semiconductors: Research Opportunities and Challenges, Advanced Electronic Materials 4 (2018) 1600501. https://doi.org/10.1002/aelm.201600501.
[42] Z. Galazka, β-Ga_2O_3 for wide-bandgap electronics and optoelectronics, Semiconductor Science and Technology 33 (2018) 113001. https://doi.org/10.1088/1361-6641/aadf78.
[43] H. Peelaers, C.G. Van de Walle, Brillouin zone and band structure of β-Ga2O3, Physica Status Solidi (b) 252 (2015) 828–832. https://doi.org/10.1002/pssb.201451551.
[44] A.Q. Huang, New unipolar switching power device figures of merit, IEEE Electron Device Letters 25 (2004) 298–301. https://doi.org/10.1109/LED.2004.826533.
[45] K.D. Chabak, K.D. Leedy, A.J. Green, S. Mou, A.T. Neal, T. Asel, E.R. Heller, N.S. Hendricks, K. Liddy, A. Crespo, N.C. Miller, M.T. Lindquist, N.A. Moser, R.C. Fitch,

D.E. Walker, D.L. Dorsey, G.H. Jessen, Lateral β-Ga2O3 field effect transistors, Semicond. Sci. Technol. 35 (2019) 013002. https://doi.org/10.1088/1361-6641/ab55fe.
[46] P. Basnet, METAL OXIDE PHOTOCATALYTIC NANOSTRUCTURES FABRICATED BY DYNAMIC SHADOWING GROWTH, 2015. https://doi.org/10.13140/RG.2.1.2393.8408.
[47] T. Işık, Solar Cells review, 2015. https://doi.org/10.13140/RG.2.1.4298.6404.
[48] X. Wang, Z. Liu, Y. Zhi, S. Li, Z. Wu, P. Li, W. Tang, Preliminary study for the effects of temperatures on optoelectrical properties of β-Ga2O3 thin films, Vacuum 166 (2019) 79–83. https://doi.org/10.1016/j.vacuum.2019.04.059.
[49] Direct and indirect band gaps, Wikipedia (2022). https://en.wikipedia.org/w/index.php?title=Direct_and_indirect_band_gaps&oldid=1105981718 (accessed October 23, 2023).
[50] S. Arumugam, P. Murugesan, A. K P, S. Satyanarayna, K. Suraj, Plasma–metal junction, Physics of Plasmas 27 (2020) 023512. https://doi.org/10.1063/1.5125618.
[51] Metal-Semiconductor Contacts, in: Physics of Semiconductor Devices, John Wiley & Sons, Ltd, 2006: pp. 134–196. https://doi.org/10.1002/9780470068328.ch3.
[52] A. Ebong, N. Chen, Metallization of crystalline silicon solar cells: A review, 2012. https://doi.org/10.1109/HONET.2012.6421444.
[53] T. Kusaba, P. Sittimart, Y. Katamune, T. Kageura, H. Naragino, S. Ohmagari, S.M. Valappil, S. Nagano, A. Zkria, T. Yoshitake, Heteroepitaxial growth of β-Ga2O3 thin films on single crystalline diamond (111) substrates by radio frequency magnetron sputtering, Appl. Phys. Express 16 (2023) 105503. https://doi.org/10.35848/1882-0786/acfd07.
[54] S. Ghosh, H. Srivastava, P.N. Rao, M. Nand, P. Tiwari, A.K. Srivastava, S.N. Jha, S.K. Rai, S.D. Singh, T. Ganguli, Investigations on epitaxy and lattice distortion of sputter deposited β-Ga2O3 layers on GaN templates, Semicond. Sci. Technol. 35 (2020) 085024. https://doi.org/10.1088/1361-6641/ab9326.
[55] J. Yu, Y. Wang, H. Li, Y. Huang, W. Tang, Z. Wu, Tailoring the solar-blind photoresponse characteristics of β-Ga2O3 epitaxial films through lattice mismatch and crystal orientation, J. Phys. D: Appl. Phys. 53 (2020) 24LT01. https://doi.org/10.1088/1361-6463/ab7e67.
[56] M.-Q. Li, N. Yang, G.-G. Wang, H.-Y. Zhang, J.-C. Han, Highly preferred orientation of Ga2O3 films sputtered on SiC substrates for deep UV photodetector application, Applied Surface Science 471 (2019) 694–702. https://doi.org/10.1016/j.apsusc.2018.12.045.
[57] Halide vapor phase epitaxial growth of β-Ga2O3 and α-Ga2O3 films | APL Materials | AIP Publishing, (n.d.). https://pubs.aip.org/aip/apm/article/7/2/022504/1064094/Halide-vapor-phase-epitaxial-growth-of-Ga2O3-and (accessed November 4, 2023).
[58] M. Ogita, N. Saika, Y. Nakanishi, Y. Hatanaka, Ga2O3 thin films for high-temperature gas sensors, Applied Surface Science 142 (1999) 188–191. https://doi.org/10.1016/S0169-4332(98)00714-4.
[59] S. Mobtakeri, Y. Akaltun, A. Özer, M. Kılıç, E.Ş. Tüzemen, E. Gür, Gallium oxide films deposition by RF magnetron sputtering; a detailed analysis on the effects of deposition pressure and sputtering power and annealing, Ceramics International 47 (2021) 1721–1727. https://doi.org/10.1016/j.ceramint.2020.08.289.
[60] S.S. Kumar, E.J. Rubio, M. Noor-A-Alam, G. Martinez, S. Manandhar, V. Shutthanandan, S. Thevuthasan, C.V. Ramana, Structure, Morphology, and Optical Properties of

Amorphous and Nanocrystalline Gallium Oxide Thin Films, J. Phys. Chem. C 117 (2013) 4194–4200. https://doi.org/10.1021/jp311300e.
[61] R. Saha, S. Bhowmick, M. Mishra, A. Sengupta, S. Chattopadhyay, S. Chakrabarti, Impact of deposition temperature on crystalline quality, oxygen vacancy, defect modulations and hetero-interfacial properties of RF sputtered deposited Ga2O3 thin films on Si substrate, J. Phys. D: Appl. Phys. 55 (2022) 505101. https://doi.org/10.1088/1361-6463/ac9b69.
[62] H. Akazawa, Formation of various phases of gallium oxide films depending on substrate planes and deposition gases, Vacuum 123 (2016) 8–16. https://doi.org/10.1016/j.vacuum.2015.10.009.
[63] L. Dong, R. Jia, B. Xin, Y. Zhang, Effects of post-annealing temperature and oxygen concentration during sputtering on the structural and optical properties of β-Ga2O3 films, Journal of Vacuum Science & Technology A 34 (2016) 060602. https://doi.org/10.1116/1.4963376.
[64] M. Li, W. Mi, L. Zhou, J. Zhao, X. Chen, J. Tang, X. Li, G. Zhang, K. Zhang, C. Luan, X. Zhang, M. Xu, Effect of oxygen flow ratio on crystallization and structural characteristics of gallium oxide thin films, Ceramics International 48 (2022) 3751–3756. https://doi.org/10.1016/j.ceramint.2021.10.157.
[65] S. Kumari, N. Mottaghi, C.-Y. Huang, R. Trappen, G. Bhandari, S. Yousefi, G. Cabrera, M.S. Seehra, M.B. Holcomb, Effects of Oxygen Modification on the Structural and Magnetic Properties of Highly Epitaxial La0.7Sr0.3MnO3 (LSMO) thin films, Sci Rep 10 (2020) 3659. https://doi.org/10.1038/s41598-020-60343-5.
[66] S. Li, S. Jiao, D. Wang, S. Gao, J. Wang, The influence of sputtering power on the structural, morphological and optical properties of β-Ga2O3 thin films, Journal of Alloys and Compounds 753 (2018) 186–191. https://doi.org/10.1016/j.jallcom.2018.04.196.
[67] K. Takakura, D. Koga, H. Ohyama, J.M. Rafi, Y. Kayamoto, M. Shibuya, H. Yamamoto, J. Vanhellemont, Evaluation of the crystalline quality of β-Ga2O3 films by optical absorption measurements, Physica B: Condensed Matter 404 (2009) 4854–4857. https://doi.org/10.1016/j.physb.2009.08.167.
[68] and, and, Structural and optical properties of Zn-doped β-Ga2O3 films, J. Semicond. 33 (2012) 073003. https://doi.org/10.1088/1674-4926/33/7/073003.
[69] H. Altuntas, I. Donmez, C. Ozgit-Akgun, N. Biyikli, Effect of postdeposition annealing on the electrical properties of β-Ga2O3 thin films grown on p-Si by plasma-enhanced atomic layer deposition, Journal of Vacuum Science & Technology A 32 (2014) 041504. https://doi.org/10.1116/1.4875935.
[70] M. Bartic, C.-I. Baban, H. Suzuki, M. Ogita, M. Isai, β-Gallium Oxide as Oxygen Gas Sensors at a High Temperature, Journal of the American Ceramic Society 90 (2007) 2879–2884. https://doi.org/10.1111/j.1551-2916.2007.01842.x.
[71] S.-J. Chang, Y.-L. Wu, W.-Y. Weng, Y.-H. Lin, W.-K. Hsieh, J.-K. Sheu, C.-L. Hsu, Ga2O3 Films for Photoelectrochemical Hydrogen Generation, J. Electrochem. Soc. 161 (2014) H508. https://doi.org/10.1149/2.0471409jes.
[72] R. Sun, H.-Y. Zhang, G.-G. Wang, J.-C. Han, X.-Z. Wang, X.-P. Kuang, L. Cui, L. Jin, J.-L. Tian, Influence of annealing atmosphere on the structure, morphology and transmittance of N-incorporated Ga2O3 films, Superlattices and Microstructures 60 (2013) 257–262. https://doi.org/10.1016/j.spmi.2013.05.004.
[73] S. Jiao, H. Lu, X. Wang, Y. Nie, D. Wang, S. Gao, J. Wang, The Structural and Photoelectrical Properties of Gallium Oxide Thin Film Grown by Radio Frequency

Magnetron Sputtering, ECS Journal of Solid State Science and Technology 8 (2019) Q3086–Q3090. https://doi.org/10.1149/2.0161907jss.
[74] P. Marie, X. Portier, J. Cardin, Growth and characterization of gallium oxide thin films by radiofrequency magnetron sputtering, Physica Status Solidi (a) 205 (2008) 1943–1946. https://doi.org/10.1002/pssa.200778856.
[75] P.H. Megat Abdul Hedei, Z. Hassan, H.J. Quah, Effects of post-deposition annealing temperatures in argon ambient on structural, optical, and electrical characteristics of RF magnetron sputtered gallium oxide films, Journal of Materials Research and Technology 22 (2023) 795–810. https://doi.org/10.1016/j.jmrt.2022.11.150.
[76] Z. Cheng, M. Hanke, Z. Galazka, A. Trampert, Growth mode evolution during (100)-oriented β -Ga $_2$ O $_3$ homoepitaxy, Nanotechnology 29 (2018) 395705. https://doi.org/10.1088/1361-6528/aad21b.
[77] A. Fiedler, R. Schewski, M. Baldini, Z. Galazka, G. Wagner, M. Albrecht, K. Irmscher, Influence of incoherent twin boundaries on the electrical properties of β-Ga2O3 layers homoepitaxially grown by metal-organic vapor phase epitaxy, Journal of Applied Physics 122 (2017) 165701. https://doi.org/10.1063/1.4993748.
[78] H. Murakami, K. Nomura, K. Goto, K. Sasaki, K. Kawara, Q.T. Thieu, R. Togashi, Y. Kumagai, M. Higashiwaki, A. Kuramata, S. Yamakoshi, B. Monemar, A. Koukitu, Homoepitaxial growth of β-Ga2O3 layers by halide vapor phase epitaxy, Appl. Phys. Express 8 (2014) 015503. https://doi.org/10.7567/APEX.8.015503.
[79] K. Sasaki, M. Higashiwaki, A. Kuramata, T. Masui, S. Yamakoshi, Growth temperature dependences of structural and electrical properties of Ga2O3 epitaxial films grown on β-Ga2O3 (010) substrates by molecular beam epitaxy, Journal of Crystal Growth 392 (2014) 30–33. https://doi.org/10.1016/j.jcrysgro.2014.02.002.
[80] M.J. Tadjer, F. Alema, A. Osinsky, M.A. Mastro, N. Nepal, J.M. Woodward, R.L. Myers-Ward, E.R. Glaser, J.A. Freitas, A.G. Jacobs, J.C. Gallagher, A.L. Mock, D.J. Pennachio, J. Hajzus, M. Ebrish, T.J. Anderson, K.D. Hobart, J.K. Hite, C.R.E. Jr, Characterization of β-Ga2O3 homoepitaxial films and MOSFETs grown by MOCVD at high growth rates, J. Phys. D: Appl. Phys. 54 (2020) 034005. https://doi.org/10.1088/1361-6463/abbc96.
[81] B.A. Eisner, P. Ranga, A. Bhattacharyya, S. Krishnamoorthy, M.A. Scarpulla, Compensation in ($2^{-}01$) homoepitaxial β-Ga2O3 thin films grown by metalorganic vapor-phase epitaxy, Journal of Applied Physics 128 (2020) 195703. https://doi.org/10.1063/5.0022043.
[82] S. Lee, K. Kaneko, S. Fujita, Homoepitaxial growth of beta gallium oxide films by mist chemical vapor deposition, Jpn. J. Appl. Phys. 55 (2016) 1202B8. https://doi.org/10.7567/JJAP.55.1202B8.
[83] T. Oshima, N. Arai, N. Suzuki, S. Ohira, S. Fujita, Surface morphology of homoepitaxial β-Ga2O3 thin films grown by molecular beam epitaxy, Thin Solid Films 516 (2008) 5768–5771. https://doi.org/10.1016/j.tsf.2007.10.045.
[84] G. Wagner, M. Baldini, D. Gogova, M. Schmidbauer, R. Schewski, M. Albrecht, Z. Galazka, D. Klimm, R. Fornari, Homoepitaxial growth of β-Ga2O3 layers by metal-organic vapor phase epitaxy, Physica Status Solidi (a) 211 (2014) 27–33. https://doi.org/10.1002/pssa.201330092.
[85] R. Schewski, M. Baldini, K. Irmscher, A. Fiedler, T. Markurt, B. Neuschulz, T. Remmele, T. Schulz, G. Wagner, Z. Galazka, M. Albrecht, Evolution of planar defects during

homoepitaxial growth of β-Ga2O3 layers on (100) substrates—A quantitative model, Journal of Applied Physics 120 (2016) 225308. https://doi.org/10.1063/1.4971957.
[86] K.D. Leedy, K.D. Chabak, V. Vasilyev, D.C. Look, J.J. Boeckl, J.L. Brown, S.E. Tetlak, A.J. Green, N.A. Moser, A. Crespo, D.B. Thomson, R.C. Fitch, J.P. McCandless, G.H. Jessen, Highly conductive homoepitaxial Si-doped Ga2O3 films on (010) β-Ga2O3 by pulsed laser deposition, Applied Physics Letters 111 (2017) 012103. https://doi.org/10.1063/1.4991363.
[87] S. Müller, H. von Wenckstern, D. Splith, F. Schmidt, M. Grundmann, Control of the conductivity of Si-doped β-Ga2O3 thin films via growth temperature and pressure, Physica Status Solidi (a) 211 (2014) 34–39. https://doi.org/10.1002/pssa.201330025.
[88] Md.E. Islam, K. Shimamoto, T. Yoshimura, N. Fujimura, Low-temperature homoepitaxial growth of β-Ga2O3 thin films by atmospheric pressure plasma-enhanced chemical vapor deposition technique, AIP Advances 13 (2023) 115224. https://doi.org/10.1063/5.0178100.
[89] J. Zhang, B. Li, C. Xia, G. Pei, Q. Deng, Z. Yang, W. Xu, H. Shi, F. Wu, Y. Wu, J. Xu, Growth and spectral characterization of β-Ga2O3 single crystals, Journal of Physics and Chemistry of Solids 67 (2006) 2448–2451. https://doi.org/10.1016/j.jpcs.2006.06.025.
[90] K. Akaiwa, K. Kaneko, K. Ichino, S. Fujita, Conductivity control of Sn-doped α-Ga2O3 thin films grown on sapphire substrates, Jpn. J. Appl. Phys. 55 (2016) 1202BA. https://doi.org/10.7567/JJAP.55.1202BA.
[91] X. Du, W. Mi, C. Luan, Z. Li, C. Xia, J. Ma, Characterization of homoepitaxial β-Ga2O3 films prepared by metal–organic chemical vapor deposition, Journal of Crystal Growth 404 (2014) 75–79. https://doi.org/10.1016/j.jcrysgro.2014.07.011.
[92] E. Chikoidze, H.J. von Bardeleben, K. Akaiwa, E. Shigematsu, K. Kaneko, S. Fujita, Y. Dumont, Electrical, optical, and magnetic properties of Sn doped α-Ga2O3 thin films, Journal of Applied Physics 120 (2016) 025109. https://doi.org/10.1063/1.4958860.
[93] M. Higashiwaki, β-Ga2O3 material properties, growth technologies, and devices: a review, AAPPS Bull. 32 (2022) 3. https://doi.org/10.1007/s43673-021-00033-0.
[94] M. Mohamed, K. Irmscher, C. Janowitz, Z. Galazka, R. Manzke, R. Fornari, Schottky barrier height of Au on the transparent semiconducting oxide β-Ga2O3, Appl. Phys. Lett. 101 (2012) 132106. https://doi.org/10.1063/1.4755770.
[95] V.D. Wheeler, D.I. Shahin, M.J. Tadjer, C.R. Eddy, Band Alignments of Atomic Layer Deposited ZrO2 and HfO2 High-k Dielectrics with (-201) β-Ga2O3, ECS J. Solid State Sci. Technol. 6 (2016) Q3052. https://doi.org/10.1149/2.0131702jss.
[96] S.D. Nehate, A. Prakash, P.D. Mani, K.B. Sundaram, Work Function Extraction of Indium Tin Oxide Films from MOSFET Devices, ECS J. Solid State Sci. Technol. 7 (2018) P87. https://doi.org/10.1149/2.0081803jss.
[97] M. Higashiwaki, K. Sasaki, T. Kamimura, M. Hoi Wong, D. Krishnamurthy, A. Kuramata, T. Masui, S. Yamakoshi, Depletion-mode Ga2O3 metal-oxide-semiconductor field-effect transistors on β-Ga2O3 (010) substrates and temperature dependence of their device characteristics, Applied Physics Letters 103 (2013) 123511. https://doi.org/10.1063/1.4821858.
[98] M.-H. Lee, R.L. Peterson, Annealing Induced Interfacial Evolution of Titanium/Gold Metallization on Unintentionally Doped β-Ga2O3, ECS J. Solid State Sci. Technol. 8 (2019) Q3176. https://doi.org/10.1149/2.0321907jss.

[99] Y. Yao, R.F. Davis, L.M. Porter, Investigation of Different Metals as Ohmic Contacts to β-Ga2O3: Comparison and Analysis of Electrical Behavior, Morphology, and Other Physical Properties, Journal of Electronic Materials 46 (2017) 2053–2060. https://doi.org/10.1007/s11664-016-5121-1.
[100] M.-H. Lee, R.L. Peterson, Interfacial reactions of titanium/gold ohmic contacts with Sn-doped β-Ga2O3, APL Materials 7 (2019) 022524. https://doi.org/10.1063/1.5054624.
[101] M.-H. Lee, R.L. Peterson, Accelerated Aging Stability of β-Ga2O3–Titanium/Gold Ohmic Interfaces, ACS Appl. Mater. Interfaces 12 (2020) 46277–46287. https://doi.org/10.1021/acsami.0c10598.
[102] L.A.M. Lyle, T.C. Back, C.T. Bowers, A.J. Green, K.D. Chabak, D.L. Dorsey, E.R. Heller, L.M. Porter, Electrical and chemical analysis of Ti/Au contacts to β-Ga2O3, APL Materials 9 (2021) 061104. https://doi.org/10.1063/5.0051340.
[103] Y. Kim, M.-K. Kim, K.H. Baik, S. Jang, Low-Resistance Ti/Au Ohmic Contact on (001) Plane Ga2O3 Crystal, ECS J. Solid State Sci. Technol. 11 (2022) 045003. https://doi.org/10.1149/2162-8777/ac6118.
[104] A. Bhattacharyya, S. Roy, P. Ranga, D. Shoemaker, Y. Song, J.S. Lundh, S. Choi, S. Krishnamoorthy, 130 mA mm−1 β-Ga2O3 metal semiconductor field effect transistor with low-temperature metalorganic vapor phase epitaxy-regrown ohmic contacts, Appl. Phys. Express 14 (2021) 076502. https://doi.org/10.35848/1882-0786/ac07ef.
[105] T. Oshima, R. Wakabayashi, M. Hattori, A. Hashiguchi, N. Kawano, K. Sasaki, T. Masui, A. Kuramata, S. Yamakoshi, K. Yoshimatsu, A. Ohtomo, T. Oishi, M. Kasu, Formation of indium–tin oxide ohmic contacts for β-Ga2O3, Jpn. J. Appl. Phys. 55 (2016) 1202B7. https://doi.org/10.7567/JJAP.55.1202B7.
[106] P.H. Carey IV, J. Yang, F. Ren, D.C. Hays, S.J. Pearton, A. Kuramata, I.I. Kravchenko, Improvement of Ohmic contacts on Ga2O3 through use of ITO-interlayers, Journal of Vacuum Science & Technology B 35 (2017) 061201. https://doi.org/10.1116/1.4995816.
[107] J. Shi, X. Xia, H. Liang, Q. Abbas, J. Liu, H. Zhang, Y. Liu, Low resistivity ohmic contacts on lightly doped n-type β-Ga2O3 using Mg/Au, J Mater Sci: Mater Electron 30 (2019) 3860–3864. https://doi.org/10.1007/s10854-019-00669-7.
[108] L.A.M. Lyle, K. Jiang, E.V. Favela, K. Das, A. Popp, Z. Galazka, G. Wagner, L.M. Porter, Effect of metal contacts on (100) β-Ga2O3 Schottky barriers, Journal of Vacuum Science & Technology A 39 (2021) 033202. https://doi.org/10.1116/6.0000877.
[109] Y. Yao, R. Gangireddy, J. Kim, K.K. Das, R.F. Davis, L.M. Porter, Electrical behavior of β -Ga_2O_3 Schottky diodes with different Schottky metals, Journal of Vacuum Science & Technology B, Nanotechnology and Microelectronics: Materials, Processing, Measurement, and Phenomena 35 (2017) 03D113. https://doi.org/10.1116/1.4980042.
[110] A. Li, Q. Feng, J. Zhang, Z. Hu, Z. Feng, K. Zhang, C. Zhang, H. Zhou, Y. hao, Investigation of temperature dependent electrical characteristics on Au/Ni/β-Ga2O3 Schottky diodes, Superlattices and Microstructures 119 (2018) 212–217. https://doi.org/10.1016/j.spmi.2018.04.045.
[111] S. Oh, G. Yang, J. Kim, Electrical Characteristics of Vertical Ni/β-Ga2O3 Schottky Barrier Diodes at High Temperatures, ECS J. Solid State Sci. Technol. 6 (2016) Q3022. https://doi.org/10.1149/2.0041702jss.
[112] C. Fares, F. Ren, S.J. Pearton, Temperature-Dependent Electrical Characteristics of β-Ga2O3 Diodes with W Schottky Contacts up to 500°C, ECS J. Solid State Sci. Technol. 8 (2018) Q3007. https://doi.org/10.1149/2.0011907jss.

[113] D. Splith, S. Müller, F. Schmidt, H. von Wenckstern, J.J. van Rensburg, W.E. Meyer, M. Grundmann, Determination of the mean and the homogeneous barrier height of Cu Schottky contacts on heteroepitaxial β-Ga2O3 thin films grown by pulsed laser deposition, Physica Status Solidi (a) 211 (2014) 40–47. https://doi.org/10.1002/pssa.201330088.
[114] M.E. Ingebrigtsen, L. Vines, G. Alfieri, A. Mihaila, U. Badstübner, B.G. Svensson, A. Kuznetsov, Bulk β-Ga2O3 with (010) and (201) Surface Orientation: Schottky Contacts and Point Defects, Materials Science Forum 897 (2017) 755–758. https://doi.org/10.4028/www.scientific.net/MSF.897.755.
[115] K. Irmscher, Z. Galazka, M. Pietsch, R. Uecker, R. Fornari, Electrical properties of β -Ga $_2$ O $_3$ single crystals grown by the Czochralski method, Journal of Applied Physics 110 (2011) 063720. https://doi.org/10.1063/1.3642962.
[116] C. Hou, R.M. Gazoni, R.J. Reeves, M.W. Allen, Direct comparison of plain and oxidized metal Schottky contacts on β-Ga2O3, Applied Physics Letters 114 (2019) 033502. https://doi.org/10.1063/1.5079423.
[117] Q. He, W. Mu, H. Dong, S. Long, Z. Jia, H. Lv, Q. Liu, M. Tang, X. Tao, M. Liu, Schottky barrier diode based on β-Ga2O3 (100) single crystal substrate and its temperature-dependent electrical characteristics, Applied Physics Letters 110 (2017) 093503. https://doi.org/10.1063/1.4977766.
[118] M.J. Tadjer, V.D. Wheeler, D.I. Shahin, C.R. Eddy, F.J. Kub, Thermionic Emission Analysis of TiN and Pt Schottky Contacts to β-Ga2O3, ECS J. Solid State Sci. Technol. 6 (2017) P165. https://doi.org/10.1149/2.0291704jss.
[119] X. Xia, M. Xian, F. Ren, M.A.J. Rasel, A. Haque, S.J. Pearton, Thermal Stability of Transparent ITO/n-Ga $_2$ O $_3$ /n+-Ga $_2$ O $_3$ /ITO Rectifiers, ECS J. Solid State Sci. Technol. 10 (2021) 115005. https://doi.org/10.1149/2162-8777/ac3ace.
[120] X. Xia, M. Xian, C. Fares, F. Ren, M. Tadjer, S.J. Pearton, Temperature dependent performance of ITO Schottky contacts on β-Ga2O3, Journal of Vacuum Science & Technology A 39 (2021) 053405. https://doi.org/10.1116/6.0001211.
[121] C. Hou, R.M. Gazoni, R.J. Reeves, M.W. Allen, Oxidized Metal Schottky Contacts on (010) β -Ga2O3, IEEE Electron Device Letters 40 (2019) 337–340. https://doi.org/10.1109/LED.2019.2891304.
[122] S. Müller, H. von Wenckstern, F. Schmidt, D. Splith, F.-L. Schein, H. Frenzel, M. Grundmann, Comparison of Schottky contacts on β-gallium oxide thin films and bulk crystals, Appl. Phys. Express 8 (2015) 121102. https://doi.org/10.7567/APEX.8.121102.
[123] L. Du, Q. Xin, M. Xu, Y. Liu, W. Mu, S. Yan, X. Wang, G. Xin, Z. Jia, X.-T. Tao, A. Song, High-Performance Ga2O3 Diode Based on Tin Oxide Schottky Contact, IEEE Electron Device Letters 40 (2019) 451–454. https://doi.org/10.1109/LED.2019.2893633.
[124] H.N. Tran, P.Y. Le, B.J. Murdoch, M.W. Allen, C.F. McConville, J.G. Partridge, Temperature-Dependent Electrical Properties of Graphitic Carbon Schottky Contacts to β-Ga_2O_3, IEEE Transactions on Electron Devices 67 (2020) 5669–5675. https://doi.org/10.1109/TED.2020.3031883.
[125] L.A.M. Lyle, L. Jiang, K.K. Das, L.M. Porter, Schottky contacts to β-Ga2O3, in: S. Pearton, F. Ren, M. Mastro (Eds.), Gallium Oxide, Elsevier, 2019: pp. 231–261. https://doi.org/10.1016/B978-0-12-814521-0.00011-7.
[126] D. Li, W. Ching, Electronic structures and optical properties of low- and high-pressure phases of crystalline B2O3, Physical Review. B, Condensed Matter 54 (1996) 13616–13622. https://doi.org/10.1103/PhysRevB.54.13616.

[127] P. Darmawan, P.S. Lee, Y. Setiawan, J. Ma, T. Osipowicz, Effect of low fluence laser annealing on ultrathin Lu2O3 high-k dielectric, Applied Physics Letters 91 (2007) 092903. https://doi.org/10.1063/1.2771065.
[128] M. Perego, G. Seguini, G. Scarel, M. Fanciulli, X-ray photoelectron spectroscopy study of energy-band alignments of Lu2O3 on Ge, Surface and Interface Analysis 38 (2006) 494–497. https://doi.org/10.1002/sia.2268.
[129] P. Darmawan, P.S. Lee, Y. Setiawan, J.C. Lai, P. Yang, Thermal stability of rare-earth based ultrathin Lu2O3 for high-k dielectrics, Journal of Vacuum Science & Technology B: Microelectronics and Nanometer Structures Processing, Measurement, and Phenomena 25 (2007) 1203–1206. https://doi.org/10.1116/1.2749526.
[130] D. Zhang, W. Lin, Z. Lin, L. Jia, W. Zheng, F. Huang, Lu2O3: A promising ultrawide bandgap semiconductor for deep UV photodetector, Applied Physics Letters 118 (2021) 211906. https://doi.org/10.1063/5.0048752.
[131] K. Kaminaga, D. Oka, T. Hasegawa, T. Fukumura, New Lutetium Oxide: Electrically Conducting Rock-Salt LuO Epitaxial Thin Film, ACS Omega 3 (2018) 12501–12504. https://doi.org/10.1021/acsomega.8b02082.
[132] P. Mandal, U.P. Singh, S. Roy, Co-sputtering of Lu2O3, Eu2O3 and Ga2O3 for optoelectronics applications, IOP Conf. Ser.: Mater. Sci. Eng. 872 (2020) 012062. https://doi.org/10.1088/1757-899X/872/1/012062.
[133] M. Higashiwaki, K. Sasaki, A. Kuramata, T. Masui, S. Yamakoshi, Development of gallium oxide power devices, Physica Status Solidi (a) 211 (2014) 21–26. https://doi.org/10.1002/pssa.201330197.
[134] C.-H. Lin, Y. Yuda, M.H. Wong, M. Sato, N. Takekawa, K. Konishi, T. Watahiki, M. Yamamuka, H. Murakami, Y. Kumagai, M. Higashiwaki, Vertical Ga2O3 Schottky Barrier Diodes With Guard Ring Formed by Nitrogen-Ion Implantation, IEEE Electron Device Letters 40 (2019) 1487–1490. https://doi.org/10.1109/LED.2019.2927790.
[135] Field-Plated Lateral --Ga2O3 Schottky Barrier Diode With High Reverse Blocking Voltage of More Than 3 kV and High DC Power Figure-of-Merit of 500 MW/cm2 | IEEE Journals & Magazine | IEEE Xplore, (n.d.). https://ieeexplore.ieee.org/document/8453847 (accessed November 4, 2023).
[136] Shivani, D. Kaur, A. Ghosh, M. Kumar, A strategic review on gallium oxide based power electronics: Recent progress and future prospects, Materials Today Communications 33 (2022) 104244. https://doi.org/10.1016/j.mtcomm.2022.104244.
[137] Y. Yao, Growth, Characterization and Contacts to Ga2O3 Single Crystal Substrates and Epitaxial Layers, thesis, Carnegie Mellon University, 2017. https://doi.org/10.1184/R1/6719396.v1.
[138] M. Madou, C. Wang, Photolithography, in: B. Bhushan (Ed.), Encyclopedia of Nanotechnology, Springer Netherlands, Dordrecht, 2012: pp. 2051–2060. https://doi.org/10.1007/978-90-481-9751-4_342.
[139] M. Shaban, G. Attia, M.A.B. M. Kabatas, H. Hamdy, Synthesis and characterization of Tin oxide thin film, effect of annealing on multilayer film, (2014) 90–99. https://doi.org/10.19138/mtpr/(14)90-99.
[140] tds_az_5209e_photoresist.pdf, (n.d.). https://www.microchemicals.com/micro/tds_az_5209e_photoresist.pdf (accessed October 5, 2023).

[141] Photoresists AZ and MicroChemicals TI resists, (n.d.). https://www.microchemicals.com/products/photoresists.html (accessed October 6, 2023).
[142] C. Anderson, Neg + dark, neg + bright, pos + dark, pos + bright, (n.d.).
[143] Y. Tomm, P. Reiche, D. Klimm, T. Fukuda, Czochralski grown Ga2O3 crystals, Journal of Crystal Growth 220 (2000) 510–514. https://doi.org/10.1016/S0022-0248(00)00851-4.
[144] K. Shimamura, E. Villora, K. Muramatu, K. Aoki, M. Nakamura, S. Takekawa, N. Ichinose, K. Kitamura, Optoelectronic Single-Crystal Candidates for UV/VUV Light Sources(Crystal Growth Technology of Fluoride and Oxide Developed from the Viewpoint of Their Material and Functional Properties), 日本結晶成長学会誌 33 (2006) 147–154. https://doi.org/10.19009/jjacg.33.3_147.
[145] Z. Galazka, R. Uecker, K. Irmscher, M. Albrecht, D. Klimm, M. Pietsch, M. Brützam, R. Bertram, S. Ganschow, R. Fornari, Czochralski growth and characterization of β-Ga2O3 single crystals, Crystal Research and Technology 45 (2010) 1229–1236. https://doi.org/10.1002/crat.201000341.
[146] G.M. Wolten, A.B. Chase, Determination of the point group of β-Ga2O3 from morphology and physical properties, Journal of Solid State Chemistry 16 (1976) 377–383. https://doi.org/10.1016/0022-4596(76)90054-2.
[147] E.G. Víllora, K. Shimamura, Y. Yoshikawa, K. Aoki, N. Ichinose, Large-size β-Ga2O3 single crystals and wafers, Journal of Crystal Growth 270 (2004) 420–426. https://doi.org/10.1016/j.jcrysgro.2004.06.027.
[148] A.O. Chase, Growth of β-Ga2, O3 by the Verneuil Technique, Journal of the American Ceramic Society 47 (1964) 470–470. https://doi.org/10.1111/j.1151-2916.1964.tb14442.x.
[149] H.F. Mohamed, C. Xia, Q. Sai, H. Cui, M. Pan, H. Qi, Growth and fundamentals of bulk β-Ga2O3 single crystals, Jos 40 (2019) 011801. https://doi.org/10.1088/1674-4926/40/1/011801.
[150] N. Ueda, H. Hosono, R. Waseda, H. Kawazoe, Synthesis and control of conductivity of ultraviolet transmitting β-Ga2O3 single crystals, Appl. Phys. Lett. 70 (1997) 3561–3563. https://doi.org/10.1063/1.119233.
[151] Czochralski Process - an overview | ScienceDirect Topics, (n.d.). https://www.sciencedirect.com/topics/chemistry/czochralski-process (accessed October 9, 2023).
[152] Z. Galazka, R. Uecker, D. Klimm, K. Irmscher, M. Naumann, M. Pietsch, A. Kwasniewski, R. Bertram, S. Ganschow, M. Bickermann, Scaling-Up of Bulk β-Ga2O3 Single Crystals by the Czochralski Method, ECS J. Solid State Sci. Technol. 6 (2016) Q3007. https://doi.org/10.1149/2.0021702jss.
[153] H.E. LaBelle, A.I. Mlavsky, Growth of controlled profile crystals from the melt: Part I - Sapphire filaments, Materials Research Bulletin 6 (1971) 571–579. https://doi.org/10.1016/0025-5408(71)90006-7.
[154] H.E. LaBelle, Growth of controlled profile crystals from the melt: Part II - Edge-defined, film-fed growth (EFG), Materials Research Bulletin 6 (1971) 581–589. https://doi.org/10.1016/0025-5408(71)90007-9.
[155] B. Chalmers, H.E. LaBelle, A.I. Mlavsky, Growth of controlled profile crystals from the melt: Part III — Theory, Materials Research Bulletin 6 (1971) 681–690. https://doi.org/10.1016/0025-5408(71)90101-2.

[156] H. Aida, K. Nishiguchi, H. Takeda, N. Aota, K. Sunakawa, Y. Yaguchi, Growth of β-Ga2O3 Single Crystals by the Edge-Defined, Film Fed Growth Method, Jpn. J. Appl. Phys. 47 (2008) 8506. https://doi.org/10.1143/JJAP.47.8506.
[157] W. Mu, Z. Jia, Y. Yin, Q. Hu, Y. Li, B. Wu, J. Zhang, X. Tao, High quality crystal growth and anisotropic physical characterization of β-Ga2O3 single crystals grown by EFG method, Journal of Alloys and Compounds 714 (2017) 453–458. https://doi.org/10.1016/j.jallcom.2017.04.185.
[158] A. Kuramata, K. Koshi, S. Watanabe, Y. Yamaoka, T. Masui, S. Yamakoshi, High-quality β-Ga2O3 single crystals grown by edge-defined film-fed growth, Japanese Journal of Applied Physics 55 (2016) 1202A2. https://doi.org/10.7567/JJAP.55.1202A2.
[159] A. Kuramata, K. Koshi, S. Watanabe, Y. Yamaoka, T. Masui, S. Yamakoshi, Bulk crystal growth of Ga2O3, in: F.H. Teherani, D.C. Look, D.J. Rogers (Eds.), Oxide-Based Materials and Devices IX, SPIE, San Francisco, United States, 2018: p. 13. https://doi.org/10.1117/12.2301405.
[160] S. Zhang, X. Lian, Y. Ma, W. Liu, Y. Zhang, Y. Xu, H. Cheng, Growth and characterization of 2-inch high quality β-Ga_2O_3 single crystals grown by EFG method, J. Semicond. 39 (2018) 083003–5. https://doi.org/10.1088/1674-4926/39/8/083003.
[161] F.K. Shan, G.X. Liu, W.J. Lee, G.H. Lee, I.S. Kim, B.C. Shin, Structural, electrical, and optical properties of transparent gallium oxide thin films grown by plasma-enhanced atomic layer deposition, Journal of Applied Physics 98 (2005) 023504. https://doi.org/10.1063/1.1980535.
[162] S.-H. Yuan, S.-L. Ou, C.-C. Wang, S.-Y. Huang, C.-M. Chen, K.-Y. Lin, Y.-A. Chen, D.-S. Wuu, Effects of high substrate temperature during pulsed laser deposition on the quality of aluminum-doped gallium oxide and its photodetector characteristics, Jpn. J. Appl. Phys. 57 (2018) 070301. https://doi.org/10.7567/JJAP.57.070301.
[163] M. Orita, H. Ohta, M. Hirano, H. Hosono, Deep-ultraviolet transparent conductive β-Ga2O3 thin films, Applied Physics Letters 77 (2000) 4166–4168. https://doi.org/10.1063/1.1330559.
[164] R. Sun, G.-G. Wang, H.-Y. Zhang, J.-C. Han, X.-Z. Wang, L. Cui, X.-P. Kuang, C. Zhu, L. Jin, Microstructure, surface morphology and optical properties of N-incorporated Ga2O3 thin films on sapphire substrates, Journal of Alloys and Compounds 580 (2013) 517–521. https://doi.org/10.1016/j.jallcom.2013.06.132.
[165] Z. Wu, G. Bai, Q. Hu, D. Guo, C. Sun, L. Ji, M. Lei, L. Li, P. Li, J. Hao, W. Tang, Effects of dopant concentration on structural and near-infrared luminescence of Nd3+-doped beta-Ga2O3 thin films, Applied Physics Letters 106 (2015) 171910. https://doi.org/10.1063/1.4919586.
[166] K. Takakura, S. Funasaki, I. Tsunoda, H. Ohyama, D. Takeuchi, T. Nakashima, M. Shibuya, K. Murakami, E. Simoen, C. Claeys, Investigation of the Si doping effect in β-Ga2O3 films by co-sputtering of gallium oxide and Si, Physica B: Condensed Matter 407 (2012) 2900–2902. https://doi.org/10.1016/j.physb.2011.08.061.
[167] V. Kalygina, A. Almaev, V. Novikov, Y. Petrova, Solar-Blind UV Detectors Based on β-Ga2O3 Films, Semiconductors 54 (2020) 682–686. https://doi.org/10.1134/S1063782620060093.
[168] E. Vega, S.B. Isukapati, T.N. Oder, Microstructure and optical properties of sputter-deposited Ga2O3 films, Journal of Vacuum Science & Technology A 39 (2021) 033412. https://doi.org/10.1116/6.0000938.

[169] T. Oshima, T. Okuno, S. Fujita, Ga2O3 Thin Film Growth on c-Plane Sapphire Substrates by Molecular Beam Epitaxy for Deep-Ultraviolet Photodetectors, Jpn. J. Appl. Phys. 46 (2007) 7217. https://doi.org/10.1143/JJAP.46.7217.
[170] E.G. Víllora, K. Shimamura, K. Kitamura, K. Aoki, Rf-plasma-assisted molecular-beam epitaxy of β-Ga2O3, Applied Physics Letters 88 (2006) 031105. https://doi.org/10.1063/1.2164407.
[171] K. Sasaki, A. Kuramata, T. Masui, E.G. Víllora, K. Shimamura, S. Yamakoshi, Device-Quality β-Ga2O3 Epitaxial Films Fabricated by Ozone Molecular Beam Epitaxy, Appl. Phys. Express 5 (2012) 035502. https://doi.org/10.1143/APEX.5.035502.
[172] D. Guo, Z. Wu, P. Li, Y. An, H. Liu, X. Guo, H. Yan, G. Wang, C. Sun, L. Li, W. Tang, Fabrication of β-Ga_2O_3 thin films and solar-blind photodetectors by laser MBE technology, Opt. Mater. Express, OME 4 (2014) 1067–1076. https://doi.org/10.1364/OME.4.001067.
[173] Reaction kinetics and growth window for plasma-assisted molecular beam epitaxy of Ga2O3: Incorporation of Ga vs. Ga2O desorption | Applied Physics Letters | AIP Publishing, (n.d.). https://pubs.aip.org/aip/apl/article-abstract/108/7/072101/1021448/Reaction-kinetics-and-growth-window-for-plasma?redirectedFrom=fulltext (accessed October 12, 2023).
[174] P. Mukhopadhyay, W.V. Schoenfeld, Tin gallium oxide solar-blind photodetectors on sapphire grown by molecular beam epitaxy, Appl. Opt., AO 58 (2019) D22–D27. https://doi.org/10.1364/AO.58.000D22.
[175] W. Mi, J. Ma, Z. Zhu, C. Luan, Y. Lv, H. Xiao, Epitaxial growth of Ga2O3 thin films on MgO (110) substrate by metal–organic chemical vapor deposition, Journal of Crystal Growth 354 (2012) 93–97. https://doi.org/10.1016/j.jcrysgro.2012.06.022.
[176] W. Mi, X. Du, C. Luan, H. Xiao, J. Ma, Electrical and optical characterizations of β-Ga2O3:Sn films deposited on MgO (110) substrate by MOCVD, RSC Adv. 4 (2014) 30579–30583. https://doi.org/10.1039/C4RA02479F.
[177] Y. Zhang, F. Alema, A. Mauze, O.S. Koksaldi, R. Miller, A. Osinsky, J.S. Speck, MOCVD grown epitaxial β-Ga_2O_3 thin film with an electron mobility of 176 $cm^2/V\,s$ at room temperature, APL Materials 7 (2019) 022506. https://doi.org/10.1063/1.5058059.
[178] W.R. Grove, LXXIX. On the electro-chemical polarity of gases, The London, Edinburgh, and Dublin Philosophical Magazine and Journal of Science 4 (1852) 498–514. https://doi.org/10.1080/14786445208647172.
[179] Physics and technology of magnetron sputtering discharges - IOPscience, (n.d.). https://iopscience.iop.org/article/10.1088/1361-6595/abb7bd/meta (accessed October 16, 2023).
[180] H.F. Fruth, CATHODE SPUTTERING, A COMMERCIAL APPLICATION, Physics 2 (2004) 280–286. https://doi.org/10.1063/1.1745055.
[181] E. Kay, Magnetic Field Effects on an Abnormal Truncated Glow Discharge and Their Relation to Sputtered Thin-Film Growth, Journal of Applied Physics 34 (2004) 760–768. https://doi.org/10.1063/1.1729530.
[182] W.D. Westwood, Glow discharge sputtering, Progress in Surface Science 7 (1976) 71–111. https://doi.org/10.1016/0079-6816(76)90002-2.
[183] G.S. Anderson, Wm.N. Mayer, G.K. Wehner, Sputtering of Dielectrics by High-Frequency Fields, Journal of Applied Physics 33 (2004) 2991–2992. https://doi.org/10.1063/1.1728549.

[184] J.S. Chapin, Sputtering process and apparatus, US4166018A, 1979. https://patents.google.com/patent/US4166018A/en (accessed October 16, 2023).
[185] M. Ohring, The Materials Science of Thin Films, (n.d.).
[186] P. Hishimone, H. Nagai, M. Sato, Methods of Fabricating Thin Films for Energy Materials and Devices, in: 2020. https://doi.org/10.5772/intechopen.85912.
[187] Radio Regulations, ITU (n.d.). https://www.itu.int:443/en/publications/ITU-R/Pages/publications.aspx (accessed October 16, 2023).
[188] E. Ahmadi, O.S. Koksaldi, S.W. Kaun, Y. Oshima, D.B. Short, U.K. Mishra, J.S. Speck, Ge doping of β-Ga2O3 films grown by plasma-assisted molecular beam epitaxy, Appl. Phys. Express 10 (2017) 041102. https://doi.org/10.7567/APEX.10.041102.
[189] N.K. Kalarickal, Z. Xia, J. McGlone, S. Krishnamoorthy, W. Moore, M. Brenner, A.R. Arehart, S.A. Ringel, S. Rajan, Mechanism of Si doping in plasma assisted MBE growth of β-Ga2O3, Applied Physics Letters 115 (2019) 152106. https://doi.org/10.1063/1.5123149.
[190] A. Mauze, Y. Zhang, T. Itoh, E. Ahmadi, J.S. Speck, Sn doping of (010) β-Ga2O3 films grown by plasma-assisted molecular beam epitaxy, Applied Physics Letters 117 (2020) 222102. https://doi.org/10.1063/5.0027870.
[191] S. Chen, Z. Chen, W. Chen, Z. Fei, T. Luo, J. Liang, X. Wang, G. Wang, Y. Pei, Metal–organic chemical vapor deposition of ε-Ga 2 O 3 thin film using N 2 O as a precursor, CrystEngComm 25 (2023) 2871–2876. https://doi.org/10.1039/D3CE00078H.
[192] A. Waseem, Z. Ren, H.-C. Huang, K. Nguyen, X. Wu, X. Li, A Review of Recent Progress in β-Ga2O3 Epitaxial Growth: Effect of Substrate Orientation and Precursors in Metal–Organic Chemical Vapor Deposition, Physica Status Solidi (a) 220 (2023) 2200616. https://doi.org/10.1002/pssa.202200616.
[193] A.F.M.A.U. Bhuiyan, Z. Feng, L. Meng, H. Zhao, Tutorial: Metalorganic chemical vapor deposition of β-Ga2O3 thin films, alloys, and heterostructures, Journal of Applied Physics 133 (2023) 211103. https://doi.org/10.1063/5.0147787.
[194] A.F.M. Anhar Uddin Bhuiyan, Z. Feng, J.M. Johnson, Z. Chen, H.-L. Huang, J. Hwang, H. Zhao, MOCVD epitaxy of β-(AlxGa1−x)2O3 thin films on (010) Ga2O3 substrates and N-type doping, Applied Physics Letters 115 (2019) 120602. https://doi.org/10.1063/1.5123495.
[195] P. Ranga, A. Bhattacharyya, A. Rishinaramangalam, Y.K. Ooi, M.A. Scarpulla, D. Feezell, S. Krishnamoorthy, Delta-doped β-Ga2O3 thin films and β-(Al0.26Ga0.74)2O3/β-Ga2O3 heterostructures grown by metalorganic vapor-phase epitaxy, Appl. Phys. Express 13 (2020) 045501. https://doi.org/10.35848/1882-0786/ab7712.
[196] G.F. Harrington, J. Santiso, Back-to-Basics tutorial: X-ray diffraction of thin films, J Electroceram 47 (2021) 141–163. https://doi.org/10.1007/s10832-021-00263-6.
[197] P.R. Jubu, F.K. Yam, K.M. Chahrour, Structural and morphological properties of β-Ga2O3 nanostructures synthesized at various deposition temperatures, Physica E: Low-Dimensional Systems and Nanostructures 123 (2020) 114153. https://doi.org/10.1016/j.physe.2020.114153.
[198] Which Electron Source is Best? - Nanoscience Instruments, (2023). https://www.nanoscience.com/blogs/which-electron-source-is-best/ (accessed October 17, 2023).

[199] N. Marturi, Vision and visual servoing for nanomanipulation and nanocharacterization in scanning electron microscope., (2013).
[200] Contact Atomic Force Microscopy - an overview | ScienceDirect Topics, (n.d.). https://www.sciencedirect.com/topics/chemistry/contact-atomic-force-microscopy (accessed October 18, 2023).
[201] Applied Spectral Knowledge | Spectrometers | Ocean Insight, (n.d.). https://www.oceaninsight.com/ (accessed October 18, 2023).
[202] tlm_measurements.pdf, (n.d.). https://gtuttle.net/fabrication/topics/tlm_measurements.pdf (accessed October 25, 2023).
[203] (18) (PDF) DC conductivity measurements in the Van Der Pauw geometry, (n.d.). https://www.researchgate.net/publication/3090303_DC_conductivity_measurements_in_the_Van_Der_Pauw_geometry (accessed October 18, 2023).
[204] Hall Effect, (n.d.). http://hyperphysics.phy-astr.gsu.edu/hbase/magnetic/Hall.html (accessed October 19, 2023).
[205] F. Orlandi, F. Mezzadri, G. Calestani, F. Boschi, R. Fornari, Thermal expansion coefficients of β-Ga2O3 single crystals, Appl. Phys. Express 8 (2015) 111101. https://doi.org/10.7567/APEX.8.111101.
[206] S. Nakagomi, Y. Kokubun, Crystal orientation of β-Ga2O3 thin films formed on c-plane and a-plane sapphire substrate, Journal of Crystal Growth 349 (2012) 12–18. https://doi.org/10.1016/j.jcrysgro.2012.04.006.
[207] Epitaxial growth of gallium oxide films on c-cut sapphire substrate, Thin Solid Films 589 (2015) 556–562. https://doi.org/10.1016/j.tsf.2015.06.034.
[208] T. Oshima, T. Okuno, N. Arai, Y. Kobayashi, S. Fujita, β-Al2xGa2-2xO3 Thin Film Growth by Molecular Beam Epitaxy, Jpn. J. Appl. Phys. 48 (2009) 070202. https://doi.org/10.1143/JJAP.48.070202.
[209] S. Kumar, C. Tessarek, S. Christiansen, R. Singh, A comparative study of β-Ga2O3 nanowires grown on different substrates using CVD technique, Journal of Alloys and Compounds 587 (2014) 812–818. https://doi.org/10.1016/j.jallcom.2013.10.165.
[210] J. Sun, W. Mi, D. Zhang, Z. Yang, K. Zhang, Y. Han, Y. Yuan, J. Zhao, B. Li, Synthesis of monoclinic structure gallium oxide film on sapphire substrate by magnetron sputtering, Optoelectronics Letters 13 (2017) 295–298. https://doi.org/10.1007/s11801-017-7065-y.
[211] C.V. Ramana, E.J. Rubio, C.D. Barraza, A. Miranda Gallardo, S. McPeak, S. Kotru, J.T. Grant, Chemical bonding, optical constants, and electrical resistivity of sputter-deposited gallium oxide thin films, Journal of Applied Physics 115 (2014) 043508. https://doi.org/10.1063/1.4862186.
[212] X. Zhang, L. Wang, X. Wang, Y. Chen, Q. Shao, G. Wu, X. Wang, T. Lin, H. Shen, J. Wang, X. Meng, J. Chu, High-performance β-Ga_2O_3 thickness dependent solar blind photodetector, Opt. Express, OE 28 (2020) 4169–4177. https://doi.org/10.1364/OE.385470.
[213] R. Sun, H.-Y. Zhang, G.-G. Wang, J.-C. Han, X.-Z. Wang, L. Cui, X.-P. Kuang, C. Zhu, L. Jin, Effect of thickness on the microstructure, surface morphology and optical properties of N-incorporated β-Ga2O3 films, Superlattices and Microstructures 65 (2014) 146–151. https://doi.org/10.1016/j.spmi.2013.11.004.
[214] E. Alfonso, J. Olaya, G.I. Cubillos, Thin Film Growth Through Sputtering Technique and Its Applications, in: 2012. https://doi.org/10.5772/35844.

[215] J. Pelleg, L.Z. Zevin, S. Lungo, N. Croitoru, Reactive-sputter-deposited TiN films on glass substrates, Thin Solid Films 197 (1991) 117–128. https://doi.org/10.1016/0040-6090(91)90225-M.
[216] J.E. Greene, J. -E. Sundgren, L. Hultman, I. Petrov, D.B. Bergstrom, Development of preferred orientation in polycrystalline TiN layers grown by ultrahigh vacuum reactive magnetron sputtering, Applied Physics Letters 67 (1995) 2928–2930. https://doi.org/10.1063/1.114845.
[217] I. Petrov, P.B. Barna, L. Hultman, J.E. Greene, Microstructural evolution during film growth, Journal of Vacuum Science & Technology A 21 (2003) S117–S128. https://doi.org/10.1116/1.1601610.
[218] K. Takakura, D. Koga, M. Yoneoka, T. Kudou, K. Hayama, K. Shigaki, H. Ohyama, Y. Kayamoto, M. Shibuya, H. Yamamoto, Optical property and crystallinities of Si doped β-Ga2O3 thin films, 1 (2009).
[219] V.I. Nikolaev, V. Maslov, S.I. Stepanov, A.I. Pechnikov, V. Krymov, I.P. Nikitina, L.I. Guzilova, V.E. Bougrov, A.E. Romanov, Growth and characterization of β-Ga2O3 crystals, Journal of Crystal Growth 457 (2017) 132–136. https://doi.org/10.1016/j.jcrysgro.2016.05.049.
[220] P. Marie, X. Portier, J. Cardin, Growth and characterization of gallium oxide thin films by radiofrequency magnetron sputtering, Physica Status Solidi (a) 205 (2008) 1943–1946. https://doi.org/10.1002/pssa.200778856.
[221] J. Zhang, J. Shi, D.-C. Qi, L. Chen, K.H.L. Zhang, Recent progress on the electronic structure, defect, and doping properties of Ga_2O_3, APL Materials 8 (2020) 020906. https://doi.org/10.1063/1.5142999.
[222] I. Hatipoglu, P. Mukhopadhyay, F. Alema, T.S. Sakthivel, S. Seal, A. Osinsky, W.V. Schoenfeld, Tuning the responsivity of monoclinic (In_xGa_1-x)_2O_3 solar-blind photodetectors grown by metal organic chemical vapor deposition, J. Phys. D: Appl. Phys. 53 (2020) 454001. https://doi.org/10.1088/1361-6463/aba313.
[223] E. Chikoidze, D.J. Rogers, F.H. Teherani, C. Rubio, G. Sauthier, H.J. Von Bardeleben, T. Tchelidze, C. Ton-That, A. Fellous, P. Bove, E.V. Sandana, Y. Dumont, A. Perez-Tomas, Puzzling robust 2D metallic conductivity in undoped β-Ga2O3 thin films, Materials Today Physics 8 (2019) 10–17. https://doi.org/10.1016/j.mtphys.2018.11.006.
[224] S. Balcı, N.A. Sezgi, E. Eren, Boron Oxide Production Kinetics Using Boric Acid as Raw Material, Ind. Eng. Chem. Res. 51 (2012) 11091–11096. https://doi.org/10.1021/ie300685x.
[225] J. Zeler, L. Jerzykiewicz, E. Zych, Flux-Aided Synthesis of Lu2O3 and Lu2O3:Eu-Single Crystal Structure, Morphology Control and Radioluminescence Efficiency, Materials 7 (2014) 7059–7072. https://doi.org/10.3390/ma7107059.
[226] X. Ji, C. Lu, Z. Yan, L. Shan, X. Yan, J. Wang, J. Yue, X. Qi, Z. Liu, W. Tang, P. Li, A review of gallium oxide-based power Schottky barrier diodes, J. Phys. D: Appl. Phys. 55 (2022) 443002. https://doi.org/10.1088/1361-6463/ac855c.